Swansea University
Prifysgol Abertawe

PROCESS AND MATERIALS EFFECT IN ORGANIC COATING OF ARCHITECTURAL STEELS

A Thesis presented,

By

Sara Lairah Mugabo

BEng (Hons) Chemical Engineering

M.Sc. Chemical Engineering

Submitted to Swansea University

In fulfilment of the program of Doctor of Engineering

September 2020

PREFACE

ABSTRACT

Coil roll coating is an industrially mature process to produce pre-coated steels at high speeds.30% sales by revenue for Tata steel colors, UK is attributed to the manufacture of architectural steels which is primarily used for composite panels for cladding systems. A research programme has been carried out which has examined the mechanisms by which the coating is picked up from the coating trough by the roll, with a reference to a defect where an insufficient coating is transferred leading to a defect named paint misses (PMD). A comprehensive study of a pair of coatings, one which demonstrated PMD and one which did not identify that their performance difference could be attributed to differences in rheology. The coating extensional viscosity and elasticity were identified as indicators of the behaviour. The identification of these primary rheological characteristics was corroborated through a blind test of a further pair of coatings where PMD had been observed on the coating line. The ability of the pickup roller to pull the coating from the trough and apparent wall slip (AWS) near the surface were identified as the dominant mechanisms. These mechanisms were also identified in a laboratory-scale simulation of the pickup cylinder rotating in the coating trough.

Model PVC coatings were manufactured where the pigment concentration and solvent level was varied independently to develop the further underlying relationship between material rheology and coating pick up. The Mooney analysis method used to examine the slip behaviour was found to be inadequate for describing the behaviour of the liquid coatings. The deviation between idealised and real behaviour increased as polymer and pigment mass fraction increased. The quantity of coating picked up by the roll was found to be difficult to measure accurately due to the presence of the ribbing phenomena, which was particularly evident on the commercial coating systems. Additionally, liquid coating pickup tended to reduce with roll speeds and decreased with increasing pigment fraction (and hence viscosity).

The study recommends an updated Quality Control (QC) system for checking the liquid coatings prior to being introduced to the process coating line.

DEDICATION

I dedicate this research work to my beloved mother, Mrs Maria Sarah Mugabo, for instilling in me the values of hard work, determination, the courage to dream big and kindness.

Thank you, mama!

ACKNOWLEDGEMENTS

Firstly, I would like to acknowledge my family; Mrs Maria Sarah Mugabo, Sammer Joyce Mugabo; Malachi Allan Muchiirawehondo, Makayla Maria Muchiirawehondo, Nuruh Kiyemba, Jannat Kiyemba and Halima Kiyemba, for standing with me throughout this chapter of my life.

Secondly, I owe a great deal of gratitude and appreciation to my academic supervisors, Dr Eifion Jewell and Dr Justine Searle, for the support and guidance without which I couldn't have reached this far. I am honoured and humbled to have met and worked with you.

Furthermore, I would like to thank Mr Joel Rousseau and Dr Jonathon Elvin for the support and industrial input you brought to this research project to ensure that the research work conducted is both industrially and academically relevant.

Furthermore, I would like to thank Swansea University, Materials and Manufacturing Academy (M2A), Tata steel Europe and the Engineering Physical and Science Research Council (EPSRC) for the financial support.

And finally, I would like to acknowledge WCPC (Welsh Coating and Printing Centre), AIM and SPECIFIC for letting me utilise their facilities and equipment to successfully conduct my research.

Thank you,

Sara Lairah Mugabo

Declarations

This work has not previously been accepted in substance for any degree and is not being concurrently submitted in candidature for any degree.

Signed: [redacted]

Date: 10/09/2020

This thesis is the result of my own investigations, except where otherwise stated. Other sources are acknowledged by footnotes giving explicit references. A bibliography is appended.

Signed: [redacted]

Date: 10/09/2020

I hereby give consent for my thesis, if accepted, to be available for photocopying and for inter-library loan, and for the title and summary to be made available to outside organisations.

Signed: [redacted]

Date: 10/09/2020

TABLE OF CONTENTS

TABLE OF FIGURES

TABLE OF TABLES

NOMENCLATURE

WORD	ABBREVIATION	UNITS
Anomalous layer thickness	δ_s	µm
Young's modulus	E_s	Pa
Average roll radius	R	m
Radius of Roll 1 (Rigid or deformable roll)	R_1	m
Radius of Rigid Roll 2	R_2	m
Roll speed ratio	S	-
Capillary number	Ca	-
Velocity of Roll 1	U_1	m/s
Velocity of Roll 2	U_2	m/s
Sliding speeds	V	m/min
Separation velocity	V_r	m/s
Infinitesimal small strain rate	$\partial\dot{\varepsilon}$	1/s
Strain rate	$\dot{\varepsilon}$	1/s
Infinitesimal small time	∂t	s
Contact angle	θ	degrees (^{0})
Phase angle	θ	degrees (^{0})
Young's modulus of roll 1	E_1	Pa
Young's modulus of roll 2	E_2	Pa
Local pressure	P	Pa
Film split ratio	H_{ratio}	-
Coating film thickness on the substrate.	H_{web}	µm
Coating film thickness on the applicator roll	H_{app}	µm

Coating film thickness on the pick -up roll	$H_{pick-up}$	µm
Minimum gap	$2H_o$	µm
Shear viscosity.	μ_s	Pas
Reynolds number.	Re	-
Characteristic time	λ_c	s
Viscous time scale	T_v	s
Shear rate	$\dot{\gamma}$	$1/s$
Extensional strain rate	$\dot{\varepsilon}$	$1/s$
Strain	ε	-
Surface tension of the dissolved solids	σ_{solids}	N/m
Surface tension of solvent	$\sigma_{solvent}$	N/m
Surface tension of a material	σ	N/m
Work of adhesion	WA	J/m^2
surface interface of liquid and solid	γ_{SL}	N/m
surface interface of liquid and vapour	γ_{Lv} i	N/m
surface interface of the solid and vapour	γ_{sv}	N/m
Density	ρ	Kg/m^3
Acceleration due to gravity	g	m/s^2
Process Flow Diagram	PFD	-
Computational Fluid Dynamics	CFD	-
Finite strip model	FSM	-
Large Amplitude Oscillatory shear	LAOS	-
Small Amplitude Oscillatory shear	SAOS	-
Viscous Modulus	G''	Pa
Elastic Modulus	G'	Pa
Frequency	Ꞷ	Hz

Strain	γ_0	-
Experimental time	t	s
Shear stress	σ	Pa
Shear strain	γ	
Prefactor constant	K_h	-
Low frequency elastic modulus	K'	Pa^n
Low-frequency viscous modulus	K''	Pa^n
Low-frequency complex viscosity	K^*	Pa^n
Power law index for loss modulus	n''	-
Power law index for elastic modulus	n'	-
Power law index for complex viscosity	n^*	-
Complex viscosity	μ^*	Pas
Power law flow index dynamic viscosity	n	-
Consistency	K	Pas^n
Apparent wall slip/stick	AWS	-
Slip coefficient	φ	-
Fluidity coefficient	χ	-
Slip length	β	µm
Gap separation	H	µm
Bulk shear rate	$\dot{\gamma}_{bulk}$	1/s
Slip layer shear rate	$\dot{\gamma}_{layer}$	1/s
Measured shear rate	$\dot{\gamma}_{ab}$	1/s
Apparent shear rate	$\dot{\gamma}_{app}$	1/s
Shear modulus	G	Pa
Slip velocity	v_s	m/s
Gradient	m	-
Function output	Y	-
Function input	X	-
N-Methyl-2-Pyrrolidone	NMP	-
Butyl Carbdol Acetate	BDA	-

Registration, Evaluation, Authorisation and Restriction of Chemicals	REACH	-
Kerosene	KJ	-
Polyisobutylene	PIB	-
Shear viscosity power exponent	a	-
Average roll speed law exponent	b	-
Flow rate through the nip gap per unit length is the	Q	m^3/s
Semi-gap width	H_O	µm
Dimensionless flow rate	λ	
Load power exponent	c	-
Rubber roll hardness power exponent	d	-
Roll radius power exponent	e	-
Apparent extensional viscosity	μ_{APP}	Pas
Paint misses defect	PMD	
Uniaxial extensional viscosity	μ_E	Pas
Bi-uniaxial extensional viscosity	μ_{APP}	Pas
Planar extensional viscosity	μ_{EB}	Pas
Strain	ε	-
Initial length	L_0	mm
Final length	L_f	mm
Initial filament radius	r_0	mm
Mid filament radius	r_{mid}	mm
Mid diameter	$D_{mid}(t)$	mm
Microns	μm	-
Volatile organic components	VOC	-
Bond number	Bo	-

CHAPTER ONE

INTRODUCTION

1.1 COIL COATING PROCESS AT TATA STEEL COLORS

This section of the thesis explains the steps involved in the coil coating process where multiple roll coaters are employed in the deposition of organic coatings on pre-treated steel substrates. Most of the information regarding Tata Steel Colors and the coil coating process was acquired from on-site plant tours at Tata steel Colors in Shotton and Walsall, and, correspondence with on-site staff.

Coil coating is a process of choice employed by Tata Steel Colors for manufacturing pre-coated steels for application in commercial construction (cladding systems), domestic appliances, bakeware and cookware, to mention but a few. The process is continuous and highly automated where a steel strip is roller coated with a layer of coating to obtain a uniform thickness of decorative, protective and functional coatings at medium and high operating speeds. Tata Steel Colors, formerly known as Corus, currently operates at line speeds of up to 120 meters per minute. The coil coating process, schematically described in fig. 1 – 1, goes through a range of operational units.

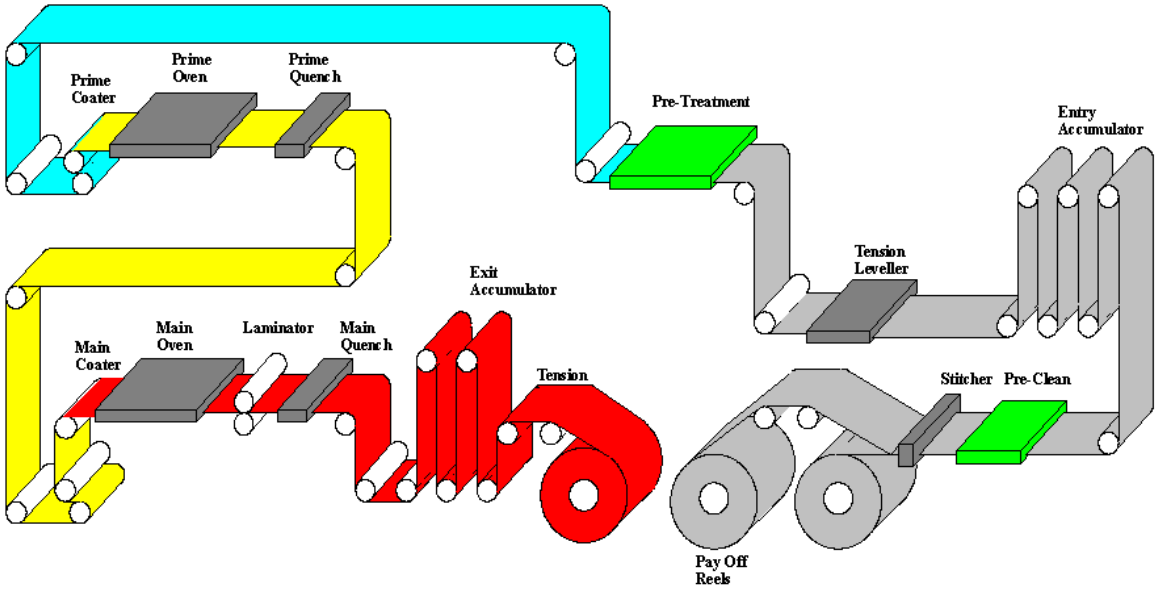

Fig. 1 - 1: Schematic of a coil coating process line employed by Tata Steel Colors at Shotton.

The entry strip employed in the manufacturing of architectural steels is pre-coated with a layer of a metallic coating through a hot-dip galvanised process (HDP), which enhances corrosion protective properties of the substrate by providing sacrificial corrosion protection from Zinc and, self - healing properties from aluminium oxide layer [1]. The type of hot-dip galvanised steel is dictated by the number of metal constituents and the alloys in the metallic coating that is deposited during the HDP unit. Below are the types of hot-dip galvanised steel substrates employed in the coil coating process: -

(1) A hot Dip Galv is a mixture of 99.8% zinc and 0.2% Aluminium mix.
(2) A Galvalloy ^{TM} or Galfan is a mixture of the other mix of 95.5% Zinc and 4.5% Aluminium [2].
(3) Galvalume or Zincalume is a mixture of 55% aluminium and 43.4% Zinc and 1.6% silicon [3].

Usually, hot Dip Galv is employed in the manufacture of pre-coated metals for cladding systems. The coil coating journey starts from the entry of a metallic coated steel at the pay - off reels where the substrate is fed to the downstream end of the process. The pay – off reels enable the unwinding of strip coils to the mechanical stitching unit.

Mechanical stitching or welding process unit follows the pay - off reel unit where the strip coil is joined to predecessors. This process can either be automated or manually operated and effectively monitored by operators.

The pre-cleaning process follows on from the mechanical stitching or welding unit to allow thorough cleaning and etching of the steel substrate. The pre-cleaning process is in two parts: chemical cleaning and hot water rinse. The chemical cleaning section is an alkaline cleaning process which employs sodium hydroxide (NaOH) or/ and potassium hydroxide (KOH) solution with a PH of 4 – 6 and dosed with a surfactant to enable thorough cleaning of the strip. The alkaline cleaning solution is kept below its cloud and oil saturation point, to allow optimal removal of detritus materials off of the strip surface.

Besides strip surface cleaning, the alkaline solution etches the surface to optimise the adhesion of the pre-treatment layer also known as the conversion coat, onto the strip surface at the downstream end of the process. Hot water rinse follows the chemical cleaning section to allow complete removal of the alkaline solution from the strip surface because the alkaline carry-over from the cleaning section neutralises the acidic conversion coating at the downstream end. It is therefore vital that a hot water rinse is

conducted to avoid the neutralisation process. Both the chemical and hot water rinse sections are operated within a temperature range of 50 – 100^0C for optimal results.

The accumulator follows on from the pre-cleaning section with the main aim of awarding mechanical stitching and the welding process unit enough time to attach the new substrate to its predecessor, without interrupting the continuity of the whole coil coating process. Therefore, the accumulator acts as the temporary storage section for the substrate.

Often substrates enter the coil coating process with variations in surface flatness due to pre-processes they have been subjected to; and therefore, if not corrected surface flatness-related defects such as "missed on edges" and "feathering" are manifested. Therefore, the tension leveller, positioned immediately after the accumulator to apply tension to the substrate and as a result variation in surface flatness are eradicated.

The deposition of the conversion coating follows the tension leveller via multi-roll coaters, though other methods such as dip coating were previously used. Based on the information obtained from the operators on the coating line, the nip gap between the applicator and pick-up roll, as opposed to line speeds, dictates the quantity of material deposited on to the substrate. The deposited layer in a liquid state is transformed into a solid-state via oven drying at temperatures of ~ 100 ^{0}C.

The conversion coat with a sub-micron thickness aids good adhesion of the primer coating onto the substrate. Previously a pre-treatment coating was a chrome VI containing conversion coating until the sunset date of 21/08/2017 imposed by Registration, Evaluation, Authorisation and Restriction of Chemicals (REACH) - a European Union regulation [4]. Currently, a chrome-free coating layer, either silicon or titanium-based pre-treatment is employed as a substitute to chrome VI containing a conversion coat.

The primer coater follows on from the pre-treatment coater where a layer of primer coating is deposited onto the pre-treated substrate. The primer coater is either operated in a reverse or forward roll coating configuration and, on both sides of the strip. It is worth noting that line speeds, nip gap settings, applicator and pick up roll speed ratio and paint viscosity play a crucial part in the quality and quantity of coating deposited on the surface. Primer coating, which is either acrylic or polyurethane resin-based coatings, has various functions. The layer provides good adhesion of the finish (top) coat on the pre-treated surface. Also, the layer provides anti-corrosive properties to the manufactured pre-coated steel due to the presence of corrosion inhibitors that are incorporated in the paint

formulation. The deposited layer in a liquid state is cured in the primer oven at the peak metal temperatures (PMT) of ~ 210 ^{0}C to obtain the optimal crosslinking density without burning the cured coating layer. However, line speeds dictate the level of cure of primer coating on the steel substrate because they dictate the residence of the coated strip in the primer oven. The thickness of a dry film of a primer coating layer range between 7 - 25 µm. Upon successful deposition and curing of the primer coating, the substrate is quenched in a water bath to reduce substrate temperatures, from the oven temperature to room temperature, followed by the removal of remnant water off the strip using squeegee rolls.

The application of the top coating layer onto the primer coated substrate follows on from the previous process unit. The top coating layer provides an extra corrosion barrier and, awards the steel panels the required aesthetic features. The process takes place in the main coater where a thicker layer of organic coating is applied using multi-roll coaters. The parameters that affect product quality during primer coating deposition also apply in the deposition of a top coating layer. The product end-use often dictates the type and size of topcoat and primer employed. For example, polyester resin-based coatings are often used for domestic appliances, whereas Poly (Vinyl Diflouride) based coatings (PVDF) and Poly (vinyl Chloride) based coatings (PVC) are usually employed for architectural steels [5] [6]. Table 1 - 1 summarises some of the pre-coated steels manufactured at Tata Steel Colors; each product has a delegated primer and topcoat type and layer thickness ranges employed.

Table 1 - 1: Pre - coated steel and primer type used

Pre-coated steel product	**Nominal topcoat thickness**	**Nominal primer thickness**	**Product application**
PE 15	15µm polyester resin-based coating	No primer	Internal products
PE 25	15–18µm polyester resin based coating	7–10µm polyester primer	Cheap exterior product
Prisma	25µm Polyurethane resin based coating	25µm Polyurethane primer	Branded products
HPS200	200µm PVC plastisol resin based top coating	7–10µm Acrylic primer	Branded products

The deposited wet layer of the top coating is cured in the main oven at a precise PMT; every coating has a specific PMT recommended by the paint formulators. Similarly, the primer oven, the degree of cure and quality of the top coating layer is dictated by the strip residence time in the main oven. It is worth noting that the Lower Exposure Limit (LEL) monitor is loaded in both the primer and main ovens. The LEL monitor measures the amount of volatile gases or solvents in the gas purge stream measured in percentage (%), and, the national limit of volatiles set into the atmosphere is 40%. Above 40% of the volatiles in the gas purge stream, the coil coating line is programmed to cease operation and strip will lift.

The auxiliary process units after the main oven include water quenching of the strip which is vital for reducing the strip temperature after passing through the main oven and, the squeegee roll which is vital for absorbing the remnant water on the strip.

The final process unit is the accumulator which is the storage unit responsible for allowing enough time for the strip to coil around the spool after being corrected for surface flatness and other defects. The final coated steel strip consists of various coating layers, as illustrated in fig. 1 – 2, with each layer adding functionality to the final product performance and appearance.

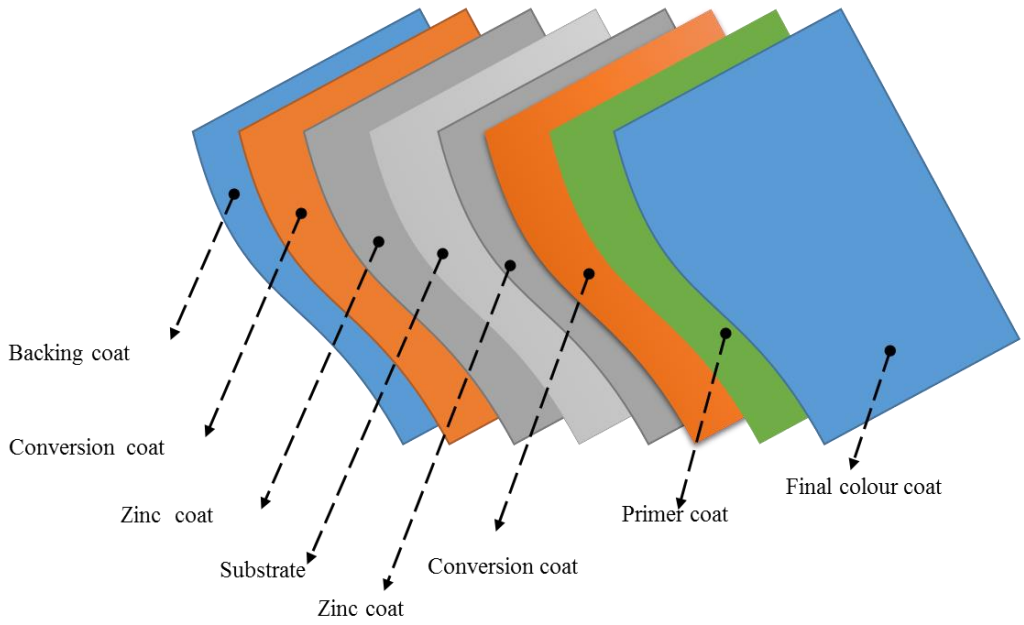

Fig. 1 - 2: Pre-coated galvanised steel manufactured at Tata Steel Colors.

The popularity of the coil coating process as a method of choice for manufacturing pre-coated steels for architectural and electrical goods, transcended in the 1950s with its

history traced back in the USA in the 1940s. However, it was only in the nearby history (the 1960s) that coil coating lines were made available in Britain and Europe at large. Currently, in Tata Steel Colors, there are two coil coating lines in Shotton (North Wales), and one coating line in Walsall -– presently sold to the William king group; two coating lines in Ijmuiden (Netherlands), two coil coating lines in Myriad (France), and finally one coil coating line in Turkey.

There have been tremendous technological advancements over the years that have led to improvements in process efficiency. This is evident in the production rates encountered in the current coil coating lines. For example, the line speeds at Tata Steel Colors in Shotton are operated at nominal speeds of 120 meters per minute (m/min), yielding 50 tonnes of coated steel in just an hour. In comparison to the 1940s coating lines, 1 tonne of pre-coated steel would be produced per hour.

Coil coating process mainly employs organic-solvent based coatings than water-based coatings because the former has better properties such as flowability at a wide range of line speeds during application. However, water-based coatings are more desired due to the reduced amount of volatile organic compounds (VOCs) emitted. VOCs are known to be harmful to human health. Therefore, VOC control units such as incinerators (oxidisers) are incorporated in the curing/ drying process to remove harmful substances through complete combustion of laden air to carbon dioxide and water. It is noteworthy that if water-based coatings are employed, the curing technique would be infrared ovens rather than incinerators [7].

Coil coating is an attractive technology over unit coating processes such as spray, curtain, amongst others for various reasons. One of the main reasons being the environmental benefits the technology offers. The deposition of solvent-based coatings on the substrate in a well-controlled environment reduces the amount of VOCs released to the environment, as required by the European Directive 2004/42/EC [8].

Furthermore, the economic advantages associated with the continuous coating process due to uninterrupted process runs reduces the amount of raw material input. Consequently, a reduction in the operating cost is obtained.

Lastly, the process produces less defective products because a high degree of surface uniformity and finish with the assured high-quality coating is achieved [9]–[11].

1.1.1 PROJECT AIMS AND OBJECTIVES

An introduction to the coil coating process and the process units involved have been described in detail in section 1.1. Each unit has the potential to leave surface defects on the manufactured pre-coated steel. However, the most encountered surface defects are believed to originate from the roll coating head, schematically described fig. 1 – 3, during the deposition of primer and top coating on the strip. Therefore, the initial research work focuses on understanding the rheological impact of the paint supply system on the final product through the development of temporal models.

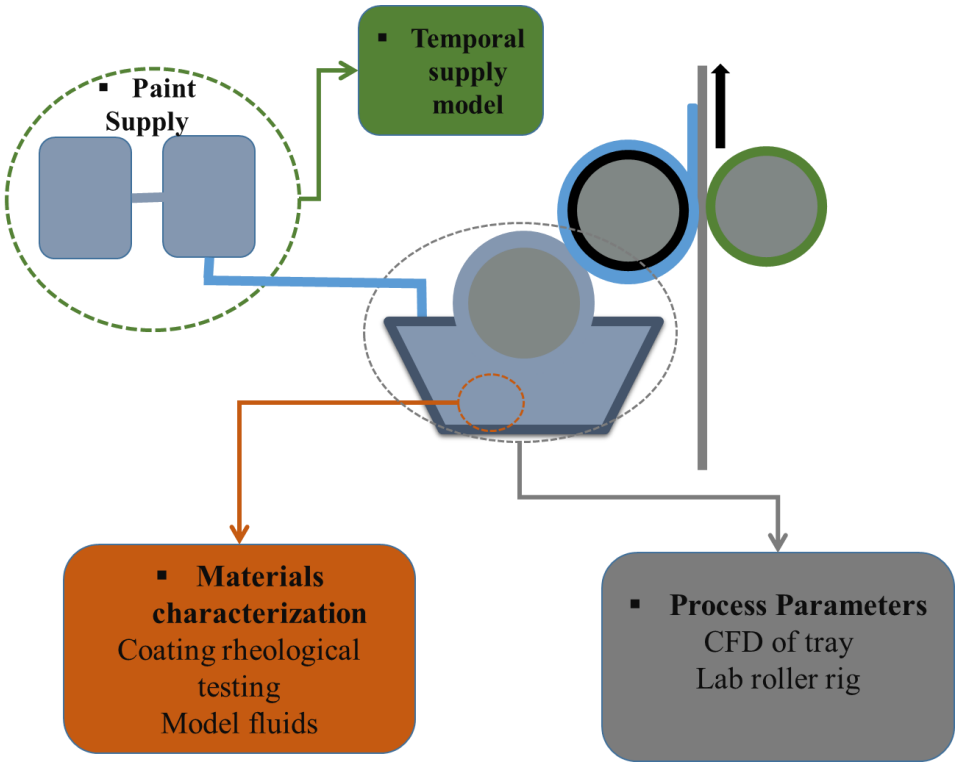

Fig. 1 - 3: Schematic of a coating head with a coating trough fed system

Having spoken to the operators following several site tours, operators reported that surface defects such as PMD and streaks were manifested on pre-coated steels following a curtain break of the coating on the pickup roll in the coating trough. Therefore, intensive materials characterisation work on coatings and the impact of rheological properties on the flowability of the coating in the coating tray was studied via lab simulation and Computation Fluid Dynamics (CFD) modelling.

Currently, in Tata Steel Colors, Shotton, Quality Control (QC) system of inward PVC coatings employed in the manufacture of pre-coated steels for architectural steels utilises a spindle rheometer rotated at a fixed rotational speed to obtain a single value viscosity

of 0.02 Pas. However, the QC has failed on numerous occasions to pick up subtle differences between coating batches. Consequently, liquid coatings that have proved to be less versatile in a high-speed roll coating environment have passed the inward QC test and later suffer surface defects.

Therefore, the aim and objectives of this project is a three-part: -

(1) To understand the effect of physical properties of liquid coatings, such as rheology and surface tension, on the final pre-coated steel.
(2) To understand the effect of operating parameters on pre-coated steels.
(3) To understand the interactions between the physical properties of liquid coatings and the operating parameters, using laboratory rig and computer simulations.
(4) Using the case study of PMD and the information developed in (1) to (3), develop an effective QC system to be employed at the coating line.

1.2 PROJECT MOTIVATION

Currently, process and material settings for manufacturing pre-coated coated steel for architectural steels are usually based on operator experience with little fundamental process understanding, and early rheological testing. This limited knowledge increases waste generation due to the defective coated products, and time-consuming process set-up runs that are conducted to achieve the required film build of organic coating on the substrate.

Considering a “cradle to gate” life cycle analysis of pre-coated steel, waste generation significantly increases the carbon footprint of the final product due to high fossil-based energy requirements, air emissions, water effluent and other environmental releases occurring in the extraction and manufacturing processes of raw materials. Also, the lack of process knowledge reduces process efficiency, increases operating costs and create difficulty when new materials and applications must be adopted.

Therefore, it is of high importance to understand a transient, free-surface flow, with deformable rolling/ sliding contact containing non-Newtonian and part volatile organic coatings, which is transferred from a liquid to a solid-state under controlled conditions.

1.3 THESIS STRUCTURE

CHAPTER ONE: Aims to provide project summary, industrial background, project aims and objectives, table of figures and table of tables.

CHAPTER TWO: literature reviews fundamental work conducted by predecessors; introduces fundamentals of roll coating process; reviews physical properties of liquid coatings and measuring techniques employed to characterise them; and investigates the impact of liquid coating physical properties in the manufacture of architectural steels

CHAPTER THREE: assesses the impact of base chemical composition and wetting of organic coatings on the onset of PMD

CHAPTER FOUR: assesses the impact of shear rheology on the onset of PMD.

CHAPTER FIVE: assesses the impact of extensional rheology of organic coatings on the onset of PMD

CHAPTER SIX: provides validation of the QC system developed based on the findings in chapter three to five

CHAPTER SEVEN: investigates the effect of pigment concentration on the rheological properties of PVC coatings

CHAPTER EIGHT: investigates the effect of solvent concentration on the rheological properties of PVC coatings

CHAPTER NINE: investigates the interaction of commercial coating properties and operating parameters in the coating trough during the pickup process

CHAPTER TEN: investigates the interaction of model PVC coating properties and operating parameters in the coating trough during the pickup process

CHAPTER ELEVEN: provides project discussions

CHAPTER TWELVE: Provides project conclusions, recommendations and future work

CHAPTER TWO

LITERATURE REVIEW

2.1 INTRODUCTION TO ROLL COATING PROCESS

Coil coating is the deposition of a thin film of liquid onto a continuous flexible substrate such as steel substrates using two or more gaps between rotating cylindrical rolls. The deposition technique belongs to a family of coating flows categorized under metered coating flow, where a boundary is created to reduce the extent of flow during material deposition onto a substrate [12],[13].

The process begins when a thick film of liquid coating is carried by the pick - up roll, through the metering nip gap where it is transferred to the applicator roll, and subsequently deposited onto the substrate via the transfer nip. By description, a metering nip gap is the gap separation located between the pick - up and applicator rolls, while the transfer nip gap is the gap separation positioned between the applicator and impression (pressure) rolls. The fundamental role of a pressure roll, positioned behind the substrate, is to pull the substrate along through the transfer nip gap to the subsequent process units.

At the exit of the metering nip gap, some of the coatings is retained on the pick - up roll and returned to the coating trough, whilst the rest is transferred to the applicator roll, where it is then completely deposited onto the substrate via the transfer nip. This is not strictly the obeyed at the transfer nip gap exit because the remnant layer of coating on the applicator roll is dictated by the roll coating configuration, that is to say-- either positive or negative roll coating regime

Fig. 2 – 1 schematically describes a transfer nip gap when two rotating cylindrical rolls are moving co-currently. Consider two cylindrical rolls, applicator and impression (pressure) rolls, with radius R_1 and R_2, rotating at velocities U_1 and U_2, respectively. The region of highest deformation rate is at the entrance to the nip gap; the region of the least deformation rate is at the “minimum gap” position, and the region of highest extension is at the exit of the transfer nip gap.

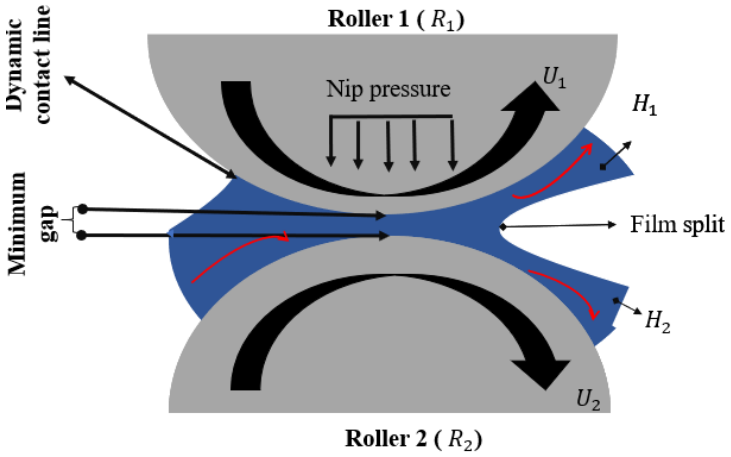

Fig. 2 - 1: Schematic of a transfer nip gap in positive gap setting

Where H_1 and H_2 is the transferred coating liquid on the pressure (or substrate) and remnant coating liquid on the applicator roll, respectively. The pressure and applicator rolls are rotating at surface speeds of U_1 and U_2, respectively.

When dealing with deformable roll coating process, the elastohydrodynamic effect is experienced. Due to the elastohydrodynamic action encountered within the nip gap, several pressure profiles in the transfer nip gap are obtained at each pressure roll revolution, especially pressure along the nip length. A review of elastohydrodynamic action is included on a further read of the thesis. Fig. 2 - 2 shows a typical pressure distribution curve in the transfer nip gap, for formulated coating colours with kaolin clay.

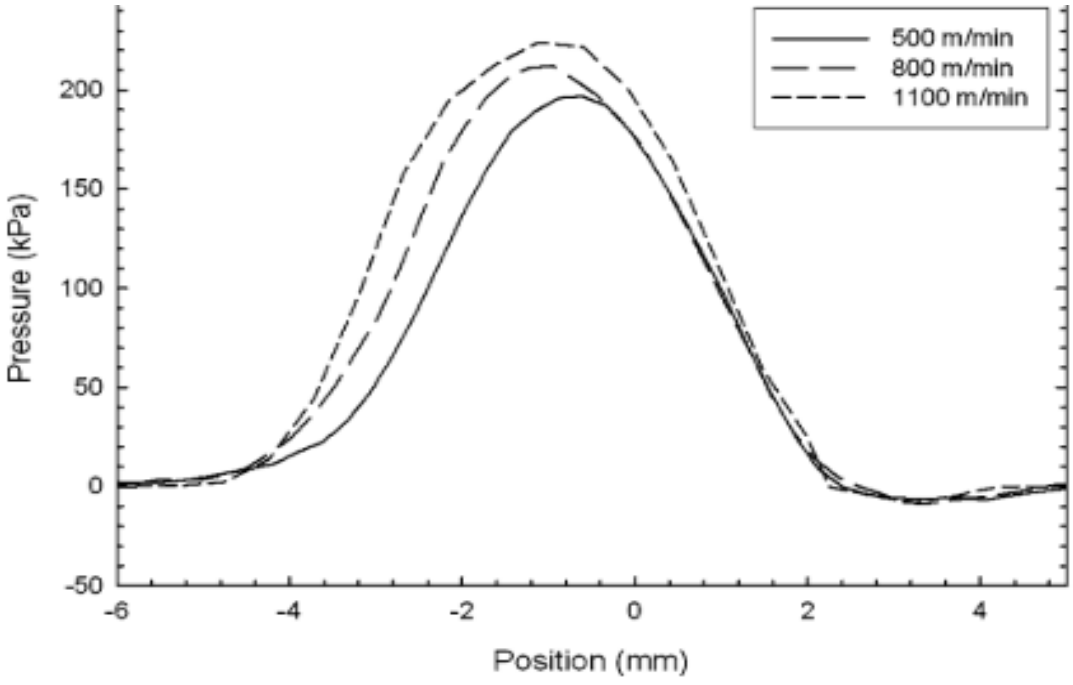

Fig. 2 - 2: Pressure variation along the nip gap adapted from [14]

Pressure variation in the nip gap are essential as they impact the stability of the coating film separation at the end of the nip gap and, the quantity of the coating transferred to subsequent nip gap or substrate. Extensive research work conducted by Ascanio, Carreau and Tanguy [14] on high-speed roll coating with complex rheology fluids highlighted that the maximum peak heights were observed for high solid content coatings at high roll coating speeds. High solids content in a coating liquid is usually correlated to high extensional viscosity and viscoelasticity which subsequently contributes to the high-pressure exhibition in the nip gap especially at the middle point of the nip length.

Roll coating process possesses numerous advantages over other deposition techniques, and these include the possibility of coating a substrate with thin films using highly viscous fluids; less complex in operation; extremely versatile; inexpensive to build, install and maintain. However, the coating technique is limited to the uniform or cylindrical surfaces. Additionally, the coating is deposited onto the substrate has to contain relatively slow evaporating solvents as this prevents viscosity build-up on the rolls[15].

Roll coating configurations affect the quality appearance of the final product, and therefore carefully chosen for different products and coating properties. The two most commonly employed roll coating configurations are forward roll coating (direct roll coating) which operates in the forward/ contra-rotating mode; and reverse roll coating (indirect roll coating) which operates in a reverse mode/ co-rotating [7]–[19].

2.1.1. FORWARD ROLL COATING CONFIGURATION

Forward roll coating configuration operates in a forward mode in either a negative or positive gap setting, often employing deformable rubber sleeved rolls. The coating liquid flows between the two cylindrical roll surfaces where the liquid splits at the downstream meniscus to form two coating layers; one of which is completely deposited onto the moving substrate and the other is retained on the applicator roll and returned to the coating trough [19]. A continuous substrate passes in the transfer nip between the applicator and impression roll, which are rotated in a contra-rotating manner whilst pulling the substrate between them. The pick - up roll, which is partially immersed in a trough filled with a liquid coating continuously supplies the coating to the applicator roll and finally to the substrate. Under a rigid roll coating process, the applicator and pressure rolls are made of steel metals. However, deformable roll coating employs a hard-polyurethane elastomer

or Ethylene Propylene Diene Monomer Rubber (EPDM) on the applicator roll.

The deformable roll serves many purposes, among them include: to reduce sensitivity to mechanical tolerances such as roll run out and surface finish; prevents damage that could arise due to roll clash and risk of wear; achieve thinner films at higher production speeds; and avoids the onset of defects such as ribbing.

During modelling, forward roll coating configuration is characterised by the consistent rolling directions which have previously been discussed. Therefore, the velocity of the fluid within the system, especially within the nip gap, remains a consistent parameter. As such, its displacement can be considered from a one - dimensional viewpoint, meaning that the coordinates of displacement conditions focused on movement in one space coordinate (x-direction) with respect to the cartesian coordinates.

2.1.1.1.CLASSICAL AND MENISCUS FLOW REGIME

Coating film thickness transferred onto the substrate is controlled by various factors, including; coating properties, operating parameters, nip gap openings and roll coating configurations.

Furthermore, the quantity of coating fed into the nip gap majorly affects the transferred coating film thickness; therefore, the coating process is either operated in a classical (fully flooded) or a meniscus (starved or ultra - starved) regime under positive gap configurations. Fig. 2 - 3 shows the difference between classical (a) and meniscus (b) flow regime.

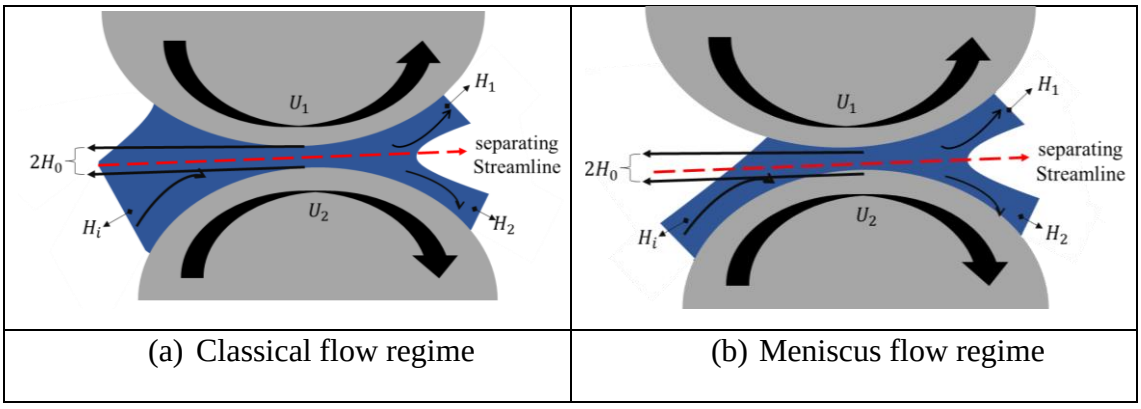

(a) Classical flow regime (b) Meniscus flow regime

Fig. 2 - 3: Schematic of a classical flow regime (a) and meniscus (b)

(a) The classical or fully flooded regime

A fully flooded flow regime is where a surplus of coating is fed into the nip gap. The applicator roll (bottom roll) delivers a liquid layer in the nip gap with a thickness, H_i, greater than the minimum gap, $2H_0$, ($H_i > 2H_0$) [20], which consequently split into H_1 and H_2 at the nip exit. The pressure roll (top roll) would then pull the coated strip along in the nip channel.

In a fully flooded regime, the roll surfaces form a converging channel at the nip region and as a result, variations in pressure within the nip gap are experienced. Variations in pressure are often attributed to the changing shape of the nip gap space. At the upstream end of the nip gap where the channel converges, the pressure increases drastically. At the downstream end of the nip gap where the channel diverges, the pressure drops below ambient such that the flow of the liquid between the roll surfaces is effectively one-dimensional. When modelling such a flow, the Reynolds equation can be employed to model the flow thereby determining pressure distribution. Although the model is constructed based on the assumption that the flow is one dimension, the reality is that the flow is multi-dimensional near the meniscus, and computational methods are thus required for a full analysis of the flow [21]. The dimensionless flowrate through the nip gap is therefore described mathematically using Eqn. (2 - 1) which is applies in a fully flooded feed condition. Various studies have shown that the dimensionless flow rate through the nip is roughly 1.34[22] [21]. Eqn. (2 – 2) describes an average velocity of roll speeds.

$$\lambda = \frac{\mathrm{Q}}{2\mathrm{H_o U}} \tag{2 - 1}$$

$$U = \left(\frac{|U_1| + |U_2|}{2}\right) \tag{2.- 2}$$

Where Q is the flow rate through the nip gap per unit length (m^3/s), H_O is the semi-gap width (μm), λ is the dimensionless flow rate, U is the average roll speeds (m/s).

Film split ratio between pressure and applicator roll during the flooded regime is calculated using Eqn. (2 - 3) and, thus employed to determine the film thickness deposited on the substrate, assuming gravity has a negligible effect on the process [22], [23].

$$H_{ratio} = \frac{H_1}{H_2} = \frac{S\,(S+3)}{(1+S)} \tag{2.- 3}$$

Where H_{ratio} is the film split ratio, H_1 is the film thickness on the substrate/pressure roll, H_2 is the film thickness on the applicator roll, H_i is the inlet film thickness, S is the speed ratio mathematically expressed in Eqn. (2 - 4)

$$S = (\frac{U_1}{U_2}) \tag{2.- 4}$$

(b) Meniscus or starved/ ultra-starved regime

When operating in a meniscus flow regime, a deficit of coating is fed into the nip gap, that is to say, $H_i < 2H_0$. Consequently, the downstream meniscus which is located close to the mid - nip, gives rise to a compact fluid domain referred to as the coating or fluid 'bead'. This feature contributes to the generation of a sub-ambient pressure field, with a profile that increases from the upstream to the downstream end. Unlike the flooded regime, the starved regime is a two-dimensional flow. The dimensionless flowrate of the meniscus flow regime is calculated using in Eqn. (2 - 5) below [22];

$$\lambda_i = \frac{H_i}{2H_o} \tag{2.- 5}$$

Gaskell *et al* [24] modelled the starved operating regime and states that both the dimensionless flowrate and the hydrodynamic pressure were found to be small. Such flow behaviour is attributed to the small modified capillary number - Eqn. (2 - 6). Note R is determined from Eqn. (2 – 7). In comparison to the classical regime, the upstream meniscus is located at the far end of the nip and therefore has a negligible effect on the pressure field.

$$Ca(\frac{R}{H_0})^{\frac{1}{2}} \leq 0.15 \tag{2.- 6}$$

$$\mathrm{R} = 2(\mathrm{R_1}^{-1} + \mathrm{R_2}^{-1})^{-1} \tag{2.- 7}$$

The film split ratio between the moving substrate and the applicator roll in a meniscus flow regime is calculated using Eqn. (2 - 8) and thus utilised to determine the film

thickness on the final product, assuming gravity has a negligible effect on the process [24].

$$H_{ratio} = \frac{H_1}{H_2} = S^{2/3} \qquad (2.- 8)$$

Gaskell *et al.*[22] expressed that in practice these two coating regimes are very different; the classical regime produces coating layer thicknesses of the order of the gap size, whereas the meniscus flow regime produces extremely thin coating layers of the order of a few tens of meters per minute thus concluding that the meniscus flow regime produces superior products than its counterpart.

2.1.2. REVERSE ROLL COATING CONFIGURATION

Reverse roll coating configuration is operated in a co-rotating mode where the coating liquid is either nip gap or a coating tray fed. Fig. 2 - 4 schematically illustrates the reverse roll coating configurations where two rolls are rotating in opposite directions.

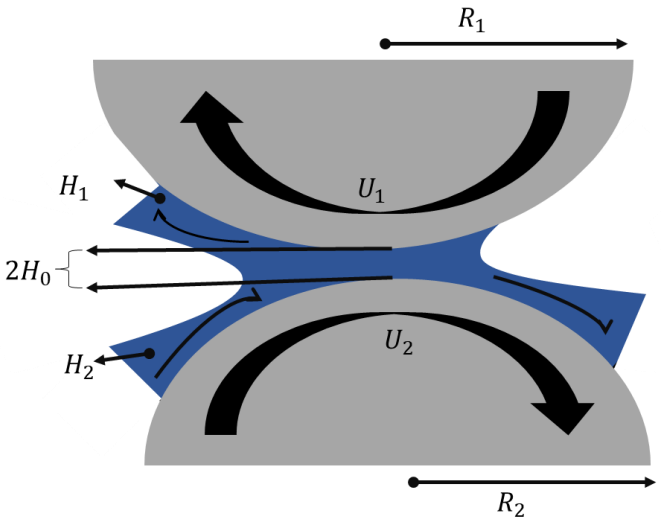

Fig. 2 - 4: Schematic of a reverse roll coating configuration

The technique is mostly employed in manufacturing of products such as magnetic and adhesive tape, OCS (one coat stucco), coated paper and paper board. A reverse roll coating configuration provides the advantage of achieving uniform thin film thickness (less than 25µm), at speeds ranging from 0.5 - 9 m/s, with liquid viscosity ranging between 0.002 - 50 Pas [25].

In reverse roll coating configuration and negative gap configuration, the deposited coating film is independent of fluid viscosity; however, the thickness of the coating layer is dependent of the metering/ transfer nip gap size and roll speeds.

In reverse roll coating, the flow is two dimensional, and therefore cannot be assumed to be one dimension even though this is the case in forwarding roll coating during the meniscus regime. Within the context of reverse roll coating, the rolling directions of the top and bottom rolls are opposite. As a direct consequence, the velocity of the fluid is more complex.

Firstly, because the velocity of the fluid is different at the inlet to the outlet. At the inlet, the fluid flow is considered only in the x-direction, similarly to the forward roll coating process. However, the fluid behaviour at the outlet is such that displacement is observed in complementary X and Y-axis displacement. Thus, highlighting the difference at the outlet between the reverse roll coating method to forward roll coating system.

Flow problem can thus be solved using a finite element method although some simple models such as those used in the work conducted by Coyle *et al* [19] can also be utilised. Greener and Middleman [26] report that the simple model works well due to a good agreement between results obtained theoretically and experimentally despite the simplicity of the simple lubrication model employed.

In roll coating process, thin-film thickness and uniformity of the applied coating layer is primarily dependant on the size of nip gap between the pick - up and applicator rolls; however, coating viscosity and roll speeds influence the thickness of coating layer deposited on the substrate or roll surface [27]. Coyle *et al* [19] expressed that the coating layer thickness is a function of Young's modulus, average roll speed and average roll radius at small deflection limits such as rigid roll coating process in Eqn. (2 - 9). Coating layer thickness at large deflection limits can similarly be derived from Eqn. (2 - 10).

$$\mathrm{H}_1 = \mathrm{R}(\mu_s \mathrm{U})\mathrm{W}^{-1}. \tag{2 - 9}$$

$$\mathrm{H}_1 = K_h\, {\mu_s}^a U^{-\mathrm{b}} W^c {E_s}^d\, R^e. \tag{2 - 10}$$

Where H_1 is the coating layer thickness (μm), W is the roll separating force (Pa), $\mathrm{E_s}$ is Young's modulus (Pa) and assumed to be constant, μ_s is the liquid shear viscosity (Pas),

U is the average roll speeds (m/min), a is the shear viscosity power exponent, b is the roll speed power exponent, c is the load power exponent, d is the rubber roll shore hardness power exponent, e is the roll radius power exponent and R is the average roll radius; Eqn. (2 – 10) is only valid for $K_h \approx 1.3$, and S ≤1.

However, various empirical models derived theoretically and experimentally for large deflection limits showed differences in prefactor and power exponent constants. It can only be speculated that the differences in the power exponent could be attributed to experimental conditions such as room temperature, rheological properties of the liquid, mechanical properties and operating parameters such as roll speeds and roll speed ratios, amongst others. Table 2 – 1 below shows the prefactor and power exponent constants of the predictive film thickness empirical model, experimentally derived, from the literature on Newtonian fluids.

Table 2 - 1: Empirical model constants from researched work

Authors and Source	Empirical model constants					
	K_h	a	b	c	d	e
Coyle *et al* [19] (Experimental study)	1	0.50	-0.50	-0.17	0.33	0.40
Coyle and Magnin [28] (Experimental study)	0.4	0.6	0.6	-0.3	-0.3	0.7
Johnson [29] (Experimentally)	0.42	0.55	0.55	0.39	-0.16	0.84

It was evident that the roll radius (e) and the load power exponent (c) varied greatly across three sources. However, shear viscosity (a) and roll speed power exponent (b) exhibited negligible changes across the literature sources possibly due to the Newtonian nature of the test liquids. Variation in roll radius and the load power exponent could be attributed to the difference in experimental rig dimensions (roll radius. Etc) and loads between rolls employed across the three researchers.

Johnson [29] further studied the effect of rheological properties on the derived constants in the empirical models by altering the concentration of polyisobutylene (PIB) polymer in the mixture containing solvent of kerosene (KJ) and polybutene. The results of the author's findings are summarised in Table 2 – 2 below, and as originally speculated, rheological properties have an impact on the empirical model constants.

Interestingly, the shear viscosity power-law exponent did not vary greatly despite the changing PIB concentrations of the test liquid. However, the prefactor (K_h) values decreased with increasing PIB concentration.

Table 2 - 2: Effect of Polymer concentrations on empirical model constants of Boger fluids

Test fluids	Empirical model constants					
	K_h	a	b	c	d	e
Newtonian	0.42	0.55	0.55	-0.39	-0.16	0.84
0.1 2% PIB	0.6	0.59	0.59	-0.48	-0.11	0.89
0.24% PIB	0.42	0.63	0.63	-0.58	-0.05	0.95
0.36% PIB	0.036	0.62	0.62	-1.05	-0.43	1.43
0.45% PIB	0.065	0.65	0.65	-1.07	-0.42	1.42
0.62% PIB	0.048	0.63	0.63	-1.08	-0.45	1.45

2.1.3. DEFORMABLE ROLL COATING WITH NEGATIVE AND POSITIVE GAP SETTINGS

Deformable roll coating is a commonly employed technique in the industry. Unlike rigid roll coating, industrial deformable roll coating configuration usually has a vertical arrangement of rolls. The lower roll is a rigid cylindrical roll which is partially immersed in a trough of the coating liquid, and the upper roll is comprised of a core metal covered in a deformable elastic (rubber) layer whose role is to meter the coating fluid[18].

The deformable layer with both viscoelastic and nonlinear properties is made up of elastomer/ rubber material [27]. The rubber cover undergoes deformation through a process called elastohydrodynamic action. Elastohydrodynamic action constitutes the flow of non- linear (non-Newtonian fluid) and the responsive deformation of rubber sleeve. The coating liquid at the converging end (upstream end) of the nip experiences high pressure which is enough to deform the rubber cover. Therefore, the flowrate, nip gap geometry, velocity and pressure profiles are altered.

Carvallo and Scriven[30] acknowledged the importance of understanding the flow in this situation to optimize the deformable roll coating process; however, the authors highlight the elastohydrodynamic action is not fully understood. Coyle [31] modelled and analysed the elastohydrodynamic action of the flow in forward deformable roll coating using a

simple one - dimensional elastohydrodynamic model with an assumption that the deformation of the roll is linear.

Large deflection limit is where the deflection of the roll surface dominates. This implies that roll coating is operated in large negative gaps settings at high applied load when a soft deformable roll is employed. The small deflection limit is the simplest of all, as the roll surface deflection is negligible due to a positive gap setting when a rigid-rigid roll coating process is employed [31].

The thickness of the deformable layer has a negligible effect on the final thickness of the coating layer on the substrate, provided that the contact width is smaller than the cover thickness, as proven by Cohu and Magnin [28]. However, Chong *et al* [18] and Gostling [32] state that the thickness of the deformable layer is effective at delaying the onset of ribbing when operating at higher roll speeds. This feature is attributed to the degree of the ‘‘stiffness’’ of rubber roll and thus making the roll more susceptible to larger deformations.

A plethora of models such as visco-capillary, lubrication approximation, a combination of springs and dashpots, to mention but a few and experimental work have been employed to analyse the deformation of the rubber cover during roll coating as this is believed to promote process optimization. Numerous authors including Chong *et al* [18] have attempted to characterise the rubber cover using loss modulus, G', elastic modulus, G'', and loss factor, $\tan(\delta)$, where the three components provide information about the energy distribution between the elastic and viscous energy. Earlier research on deformable roll coating such as work conducted by Carvalho and Scriven [27] [33] modelled the rubber deformation with both one-dimensional and plane-strain two-dimensional elastic models of the roll cover deformation. However, rubber and rubber-like materials used as roll covers were reported to behave not purely elastically. The authors comment that this behaviour was simply attributed to the stress history of the rubber cover.

2.1.3.1. NEGATIVE GAP CONFIGURATION

During negative gap configuration, the rigid and the deformable rolls are nipped together as shown in fig. 2 - 5. In this regime, the centre to centre distance is less than the sum of the two radii of the rolls. This consequently leads to the intersection of the rolls where the

rubber cover deforms due to this intersection. Deformable roll coating is mostly applied in fixed load and negative operating regimes.

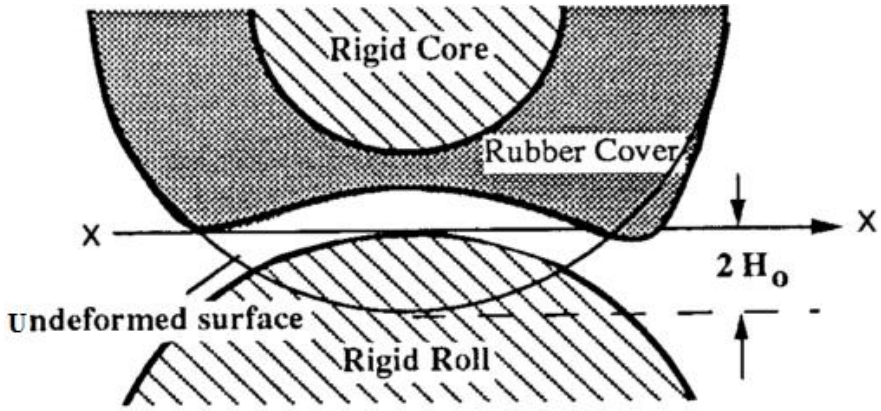

Fig. 2 - 5: Schematic of a forward roll deformable coating process in a negative gap regime, adapted from[27]

In practice, a reverse deformable roll coating configuration coupled with the negative regime is not widely employed mainly due to rubber layer tear; therefore, this configuration is not attractive on large scale operations as maintenance costs and system inefficiency are incurred.

Gosling *et al* [34] analysed the flow in negative gap setting using a finite strip model (FSM) and concluded that the layer properties (layer thickness and elasticity) of the rubber cover had similar effects on pressure profile and flowrate. However, the layer properties exhibited different effects on the position of the meniscus and layer swelling. Additionally, the layer properties showed a negligible effect on the elastic deformation of the flow within the contact region.

2.1.3.2. POSITIVE GAP CONFIGURATION

When a centre to centre distance exceeds the sum of the two roll radii, then the configuration is a positive gap regime, as schematically shown in fig. 2 - 6. Carvalho and Scriven [27] analysed the onset of ribbing using a deformable roll coating in a positive gap configuration and their findings show enhanced free - ribbing coating when using deformable roll coating as opposed to using rigid roll coating, thus enabling uniform film thickness at a faster-operating speed. There are similarities between deformable and rigid roll coating process when operating in a positive gap setting. Nonetheless, the subtle differences between the two cannot be ignored; for example, deformable roll coating configuration can be operated at higher speeds with delayed onsets of ribbing defect thus widening the operating window[27][18].

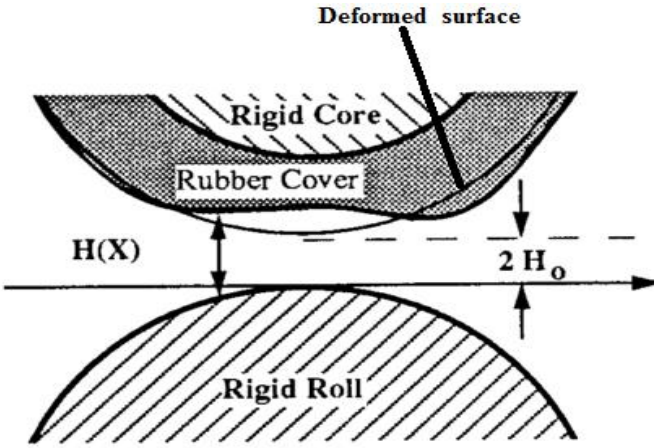

Fig. 2 - 6: Schematic of forward roll deformable coating in a positive gaps regime, adapted from [34]

2.2. COATING DEFECTS ENCOUNTERED DURING ROLL COATING PROCESS.

Section 2.1 of this thesis has reviewed various roll coating flows and the fluid dynamics associated with the process. However, coating defects affect the appearance of the final product. Therefore, this section reviews the most commonly encountered coating defects during the manufacturing of pre-coated steels.

Coating defects are a regular occurrence at the process coating line with millions of pounds annually lost in external and internal product rejects. Fig. 2 -7 shows the cost of external and internal product rejects due to surface defects encountered at Tata steel colors, Walsall.

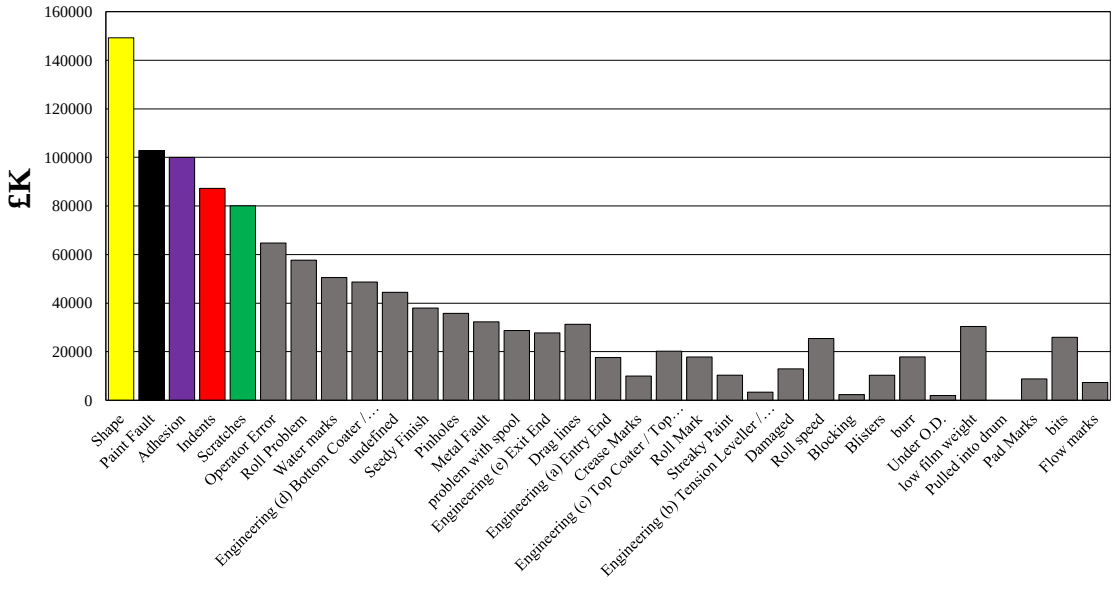

Fig. 2 - 7: Cost of defects to Tata steel Colors, Walsall, from January – August 2019

Unfortunately, elimination of coating defects has not advanced at the same rate as the technological developments of the roll coating process. Coating defects have not only persisted but increased in occurrence. A vast majority of defects can immediately be detected after application or curing process. Rectification of these defects at this stage of the process is usually impossible and yet their presence in the final product drastically increases scrap cost.

Numerous research work on coating defects such as cascading, fat edges, ribbing and many others, to determine operability window for a free - defect coating, has been conducted by various authors such as Yang *et al* [35], Lee *et al* [36] and Lopez *et al* [37], and have concluded that some defects are due to the physical properties of a liquid coating such as viscosity and, operating parameters such as roll and substrate speed. Therefore, if the levelling process before curing is insufficient to straighten out the defects, a compromise on the operating parameters might need to be considered and coating formulations might require improvement to alter liquid coating properties.

2.2.1. RIBBING

Ribbing defect is manifested as the non - uniform coating layer thickness across the coated substrate (in the axial direction of the rolls). As a result, a sinusoidal - like the appearance of the applied coating on the substrate is seen. Fig. 2 – 8 below shows the physical appearance of the coating defect.

Fig. 2 - 8: Pictorial description of ribbing coating defect

Forward roll coating is particularly susceptible to ribbing due to the diverging flow at the exit of the nip gap, coupled with high-speed coating lines and, small gap separations and large roll diameters.

The defect is known to occur as a consequence of an imbalance between surface tension forces (stabilising) and the viscosity (de-stabilising) present within the downstream nip gap where the de-stabilising forces dominate over the stabilising forces [16], [18], [27], [38]. The destabilising effect of viscosity can be expressed in terms of the Capillary number (Ca) (see Eqn. (2 - 11)) a dimensionless constant that governs the onset of the ribbing phenomena.

$$\mathrm{Ca} = \frac{\mathrm{U}\mu_S}{\sigma} \qquad (2 - 11)$$

Where U is the average speed (m/s), μ_S is the shear viscosity (Pa), and σ is the coating surface tension (N/m).

At low values of Capillary number where surface tension dominates the flow, the flow is uniform and stable at any speed ratios, thus surface tension is a stabilising force. At high capillary numbers where viscosity dominates the flow, a safe "operability window" exists: if the ratio of the line (web) speeds to the applicator roll speed, also known as the limiting wipe ratio during reverse roll coating, is within a specific range, ribbing phenomena cannot be exhibited. Outside of the wipe ratio range, a non- uniform flow exhibited as furrows and ridges are manifested. The wipe ratio is approximated at 1.2 and 1.6 for Newtonian and viscoelasticity, respectively [39]

Even though reverse roll coating configuration is not exempt from ribbing; the defect can easily be eliminated without utilising surface tension stabilising effect by simply increasing the line speeds and subsequently combating the de-stabilising effect of viscosity. This is a desirous method of eliminating ribbing in industrial reverse roll coating operations because the defect can be eradicated even when surface tension has negligible influence as a stabilising force. However, care must be taken not to drastically increase the line speed in comparison to the applicator roll speed as this increases the wipe ratio.

Chong and co-workers [18] experimentally investigated ribbing instabilities in the forward deformable roll coating both in positive and negative gap settings and, the authors report the ever so the presence of ribbing instabilities in the negative gap settings. However, the results exhibited a short wavelength of ribs when the coating speeds and thinner deformable cover on the applicator roll are used during negative gap settings. The

authors further reported that in positive gap settings the critical roll speeds at which ribbing was observed increased with operating at larger gap setting and using a thicker deformable roll cover.

2.2.2. MISTING

Misting is also one of the defects encountered due flow instabilities and filament splitting. The defect is manifested at the downstream end of the metering or transfer nip gap, in the form of liquid droplets are formed at high speeds. Misting has various consequences which include; health-related concerns to the operators through respiration; causes clean - up and cost-related issues and poor product quality Various mechanisms that explain the onset of misting have been reported.

Cavitation has been reported in the literature as one of the mechanisms that best describe misting formation. Here the pressure in the coating liquid decreases below its vapour pressure due to the tensile stresses that cause bubble formation and subsequently leading to bubble formation and mists [40][41][42]. The mechanism is correlated to *cobwebbing*, where the coating liquid forms filaments as the cylindrical rolls separate from the moving substrate. These filaments are known to look like cobwebs hence the name *cobwebbing*.

Misting effect can also be correlated to coating rheology. However, Fernando *et al* [43] report the absence of a correlation between misting, elastic modulus and higher shear viscosity. Nevertheless, the authors report a strong correlation between misting and extensional viscosity of coating fluids. The manifestation of misting phenomena manifests differently in non- Newtonian than Newtonian liquids. This statement is supported by Owens *et al* [40]. Ascanio *et al* [44] comment that Newtonian fluids are affected by misting when operating at high roll speeds and, using low viscous coating fluid. Therefore, the high solid content suspension is preferred for a mist free coating. Misting in Newtonian fluids happens when the septa break and generate the threads in a cylindrical shape (filaments) while being stretched by the rotating cylinders [40] [42]. In non-Newtonian fluids, the filament forms beads on the string structure while being stretched by the rotating cylinders. Operating parameters contribute to the onset of misting, to a certain degree; therefore when liquid coating properties cannot be improved, the operating parameters such as operating speed and roll speed ratios have to be reduced; otherwise, housekeeping practises such adequate shielding and airflow control methods can be employed as an alternative.

Eliminating this effect can be done either by reducing the rheological properties or running the pressure roll 3 – 5% faster than the line speed [45].

2.2.3. COATING DEBRIS

Coating debris (dirt) is one of the most encountered surface defects at the coating line. The defect is brought about by several factors which are traced back to paint formulation or housekeeping. In the context of paint formulation, the defect is more pronounced in solvent-based coatings. During the transformation of wet film coating to dry film coating, via curing or sintering process, some solvents such as N-Methyl-2-pyrrolidone (NMP) tend to condensate within the ovens to form char particulates (see fig. 2 - 9 (a)) which subsequently block the air knives. As a result, the air knives fail to supply enough heat to raise the required Peak metal temperature (PMT) on the substance to cure wet films. To tackle the issue of low PMT, the pressure of hot air through the air knives is drastically elevated which forces the char particulates to get deposited onto the coated substrate. At the exit of the oven, the cured coating film will exhibit random regions of deposited char particulates which lead to a coating defect called coating debris, as shown in fig. 2 - 9 (b).

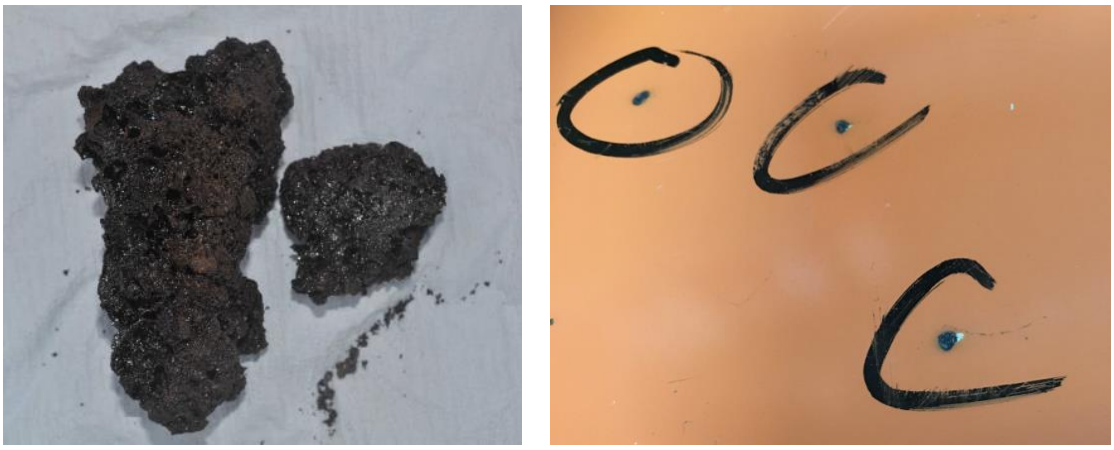

(a) Harvested char particulate (b) Coating debris defect

Fig. 2 - 9: Pictorial description of char particulates (a) and coating debris defect (b).

Therefore, regular oven maintenance and cleaning schedules are essential to solve both the problem of low PMT and condensate build- up in the air knives. Also, the use of alternative solvents that are unlikely to condensate such as NMP-free solvent-containing paints eliminate the coating defect. Alternatively, coating debris could be attributed to housekeeping where dirty chemical cleaning and rinsing tanks, and squeegee rolls could promote the deposition of detritus materials onto the bare substrate. Consequently, regions with deposited detritus materials have lower surface energy and therefore

deposited liquid coating flows away from these regions. Schoff [46] reviews surface defects in detail and, in his review, he discusses coating debris as “dirt”. The author states that detritus materials could also find their way onto the final product via supplied paint batches from the manufacturers. However, this problem is often eliminated by careful filtering process of the paint.

2.2.4. SOLVENT BOIL

Solvent boil defect is one of the major defects attributed to volatile solvents. Various acronyms have been associated with solvent boil, which includes but not limited to solvent pop, air entrapment, solvent pop, degassing, amongst others. The defect appears as bubbles on the surface that are randomly distributed across the coated substrate. Fig. 2 – 10 shows the manifestation of solvent boil defect on the final product.

Fig. 2 - 10: Pictorial description of Solvent boil

As a trapped solvent in the form of volatiles attempt to escape, the bubbles form on the surface of a coated strip. Information obtained from on-site visits at tata steel Shotton and Walsall suggested that high film build, incorrect solvent blend, a faster rate of flash off (high line speeds) through the ovens, and high substrate temperature are the main culprits of the onset of the defect reported. Therefore, to combat the manifestation of solvent boil, a reduction of the rate of cure to prevent skinning and promote solvent evaporation should be considered. Furthermore, as a recommendation to combat the defect, a mixture of compatible solvents should be employed, a reduction of film thickness during product manufacturing, and formulators should employ additives that act as boilinuse chips to release volatiles [45]. Mabbett *et al* [2] intensive work on highly absorbing pigments and near-infrared curing (NIR) of polyester/melamine coatings revealed that metallic and

black coatings were prone to solvent boil than white polyesters. This was attributed to the strong NIR absorption of carbon black pigments contained with black coatings and metallic coatings. The researchers studied alternative pigments with lower NIR absorption such as paliogen black pigments and, their findings showed that the alternative pigments were heated rapidly by the visible component of the NIR lamps emission. Additionally, the alternative pigments were costly as they contributed highly to the operating cost, and reduced corrosion control properties of the coated panels. It is noteworthy that even in convection curing, black coatings absorb heat and retain heat much better than white paints; therefore, promote the rate of cure faster than white coatings thus solvent boil defect.

2.2.5. FAT EDGES

Fat edges or picture framing is a surface tension gradient driven defect, where non-uniform surface tension distribution in the coating liquid causes thick edges on the sides of the coating width. Fat edges do not affect the coating protective purposes (anti-corrosive properties), however, the aesthetic features of the coated substrate are affected. The defect is usually observed during drying or curing where the solvent evaporates more rapidly at the edges than the bulk. Originally, the edges are thinner than the bulk of coating; however, during a faster rate of evaporation, the solvent is transported to the edges and the particles follow thereby causing differences in surface tension (see fig. 2 - 11).

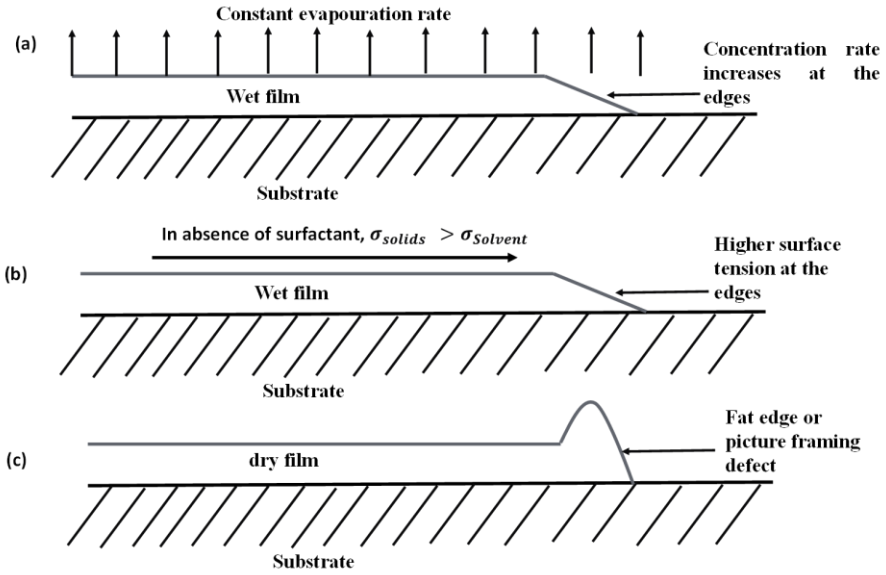

Fig. 2 - 11: Formation of picture framing or fat edge product defect schematically from image (a) – (c), where σ_{solids} is the surface tension of the dissolved solids and σ_{solids} is the surface tension of the solvent.

This mechanism is called the Marangoni effect. The drying process is limited by the evaporation of solvent from the wet film, where the agitation of the overlying gas or the heating of the film reduces the evaporation process [47]. This leads to diffusion interferences followed by surface tension gradients through the depth of the coating. As a result, particle concentration at the edges increases to form a higher surface tension region than the bulk and become extremely thick, doubling the nominal layer thickness. According to Kheshgi [48], the possible means of eliminating this defect is through controlling the rate of drying and the drying conditions, and also control the diffusivity of the components by controlling coating formulations.

2.2.6. PAINT MISSES DEFECT (PMD)

PMD, also known as Skips or Bare spots or Holidays, is a major defect encountered in the coil roll coating industry. As the name suggests, PMD is the appearance of uncoated areas on the substrate that appear in the form of “dry patches”. Fig. 2 – 12 shows the appearance of PMD on the final product.

Fig. 2 - 12: Pictorial description of PMD

The manifestation of the defect at roll coil coating process line is usually encountered with coatings which belong to the same family and believed to possess the same properties. However, one batch is more versatile than the other at a high-speed production line which could suggest a difference in paint formulation as the leading cause.

Observations made from plant- site visit support that some cases of dewetting have been attributed to poor surface cleaning of the substrate that leaves behind grease build up and dirt on the surface, that lowers the surface energy of the metal surface thus causing dewetting. Nevertheless, surfactant contribution in paint formulation cannot be ignored especially when two coatings of the same family and, believed to have the same formulation show differences in performance. Tricot [49] explains that though surfactants

aid to promote hydrophilic surfaces which are easier to wet, extremely hydrophilic surfaces could also be susceptible to hydrophobic substances that contaminate the surface thus promoting dewetting.

Unlike unfavourable interaction of the liquid film at the solid surface, rheology of a flowing liquid along the surface can play a part in the dewetting process of the coating film. Vilmin and Raphael [50] correlated dewetting mechanism to slip phenomena where entanglement between polymer chains allows for low chain polymers to slip onto the surface, provided that the surface is smooth with low friction effects. Al-Khayat [51] also writes that increasing molecular weight of the polymer chains results in increased entanglement, and subsequently increasing the bulk viscosity and friction forces of the flow along the surface. However, there exists a space to further understand the type of slip experienced in liquid flows that experience dewetting and, the relative contribution of slip to the total flow.

There are two mechanisms or geometries of the dewetting process discussed in the literature: spinodal and heterogeneous dewetting. Spinodal dewetting has been reported to manifest in unstable films, where the film instability initiates the formation of capillary waves with an amplitude that grows exponentially with time[51]. However, spinodal dewetting can only be observed for ultra-thin films, 10 nm or below.

Heterogeneous nucleation becomes the dominant mechanism of dewetting for thicker films of micron thickness. Heterogeneous dewetting by receding of the straight edge to form droplets has been well studied by Perscka *et al*'s work [52] and, the formation of hole mechanism has been in-depthly reported in [51][53].

2.3.RHEOLOGY OF COATING LIQUIDS DURING ROLL COATING

Research work on coating flows especially in roll coating process has been predominantly reported on Newtonian coating fluids. The reason being that at high shear rates non-Newtonian fluids behave more like Newtonian fluids. Nonetheless, complex coating liquids can recover their viscosity if the process is transient. Due to the transient nature of the coating processes and the complex nature of the coating liquids, it is therefore misleading to simply consider one value viscosity as the one determining factor of coating flows without considering coating rheology. Rheology, a term coined by Professor Bingham, is simply the deformation and flow of material. The term was adopted from the

Greek word “Rhein” which is interpreted as flow. Therefore, rheology is summarised as a branch of science that describes the response of a material when stress or strain is imposed [54].

This section of the thesis aims to review the rheology of coatings during the roll coating process due to the great influence of coating rheological properties on the appearance of the final product and process performance.

2.3.1. SHEAR RATE DEPENDENT VISCOSITY

Coating liquids during roll coating process are subjected to varying shear flow conditions; from instantaneous high shear rates of the order of magnitude of $10^4\ s^{-1}$ for 10 milliseconds through the nip gap, followed by low shear rates on the roll surface, through to instantaneous high shear rates characterised flow in the nip gap, and finally to the low shear rates characterised flow of the levelling process (order of magnitude of $10^{-2}\ s^{-1}$) before curing [5], [55]. Therefore, knowledge of coating rheological properties, surface tension and operating parameters would provide a preliminary step in counteracting the defects reviewed in section 2.2 of the thesis.

Rheological behaviour of coatings can be classified into two categories: Newtonian and non-Newtonian fluids. A review by Kazemian and colleagues [56] provides mathematical models employed in the analysis of different rheological behaviour. Newtonian fluids reveal a linear relationship between shear stress and shear rate, see Eqn. (2 - 12) [57]. Considering a simplified shear flow of a coating liquid between two plates, a stationary and moving plate, the coating liquid is expected to flow with a velocity profile as illustrated in fig. 2 – 13.

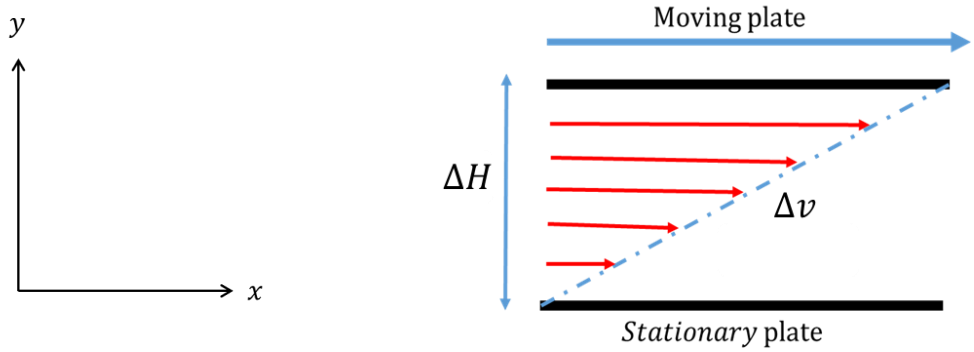

Fig. 2 - 13: A simple shear flow of a liquid

Therefore, the shear rate function in Eqn. (2 – 12) takes shape of the ratio differential velocity to layer thickness occupied in a gap space between the plates.

Generalised models such as those reported in Eqn. (2 - 12) to (2 – 13) are limited to flows that are steady-state in nature; however, the roll coating process is transient and, often liquid coatings employed during the process exhibit a different value viscosity dependent on the deformation rate they are subjected to.

$$\tau = \mu_s \dot{\gamma} \tag{2 - 12}$$

$$\tau = \mu_s \frac{\partial v_x}{\partial H} \tag{2 - 13}$$

Thus, a power-law non - Newtonian fluid that displays a non - linear relationship between shear stress and shear rate as shown in Eqn. (2 – 14) and (2 – 15), is often employed to predict coating performance in such as a transient process. The relationship between shear stress and shear rate is the viscosity function (consistency) during steady flow [58][59].

$$\tau = \mathrm{K}\dot{\gamma}^{\mathrm{n}}. \tag{2 - 14}$$

$$\mu_s = \mathrm{K}\dot{\gamma}^{(\mathrm{n}-1)} = \frac{\sigma_{xy}}{\dot{\gamma}_{xy}}. \tag{2 - 15}$$

Where τ is the shear stress (Pa), μ_s is the shear viscosity (Pas), K is the consistency (Pa^n) and, n is the flow index which determines the shear thickening (n > 1) and shear thinning behaviour (n < 1), x and y are cartesian coordinates in the x and y direction, respectively, v is the velocity component (m/s) and H is the layer thickness of the coating liquid (µm).

As mentioned therein, coatings employed in the roll coating process are mostly non – Newtonian, inferring that they are often shear thickening, shear-thinning, thixotropic and usually viscoelastic. Therefore, rheological characterisation before roll coating process is fundamental in describing the interactions between coating liquids properties and operating parameters. Armelin *et al* [60] conducted rheological characterisation of five different coatings: acrylic-based coating for varnish of steel, the alkyd-based coating used for a primer of steel plates, the chlorinated rubber-based coating used for a primer of steel plates, epoxy-based coating primer for steel plates and vinyl-based coating primer for steel plates, using a shear rate controlled rotational rheometer (Couette cell) fitted with a

Mooney - Ewart coaxial cylinder sensor. All five coating samples showed shear thinning behaviour. Except for chlorinated rubber coating, all tested coatings exhibited a thixotropic hysteresis loop, a property which is desired during storage to avoid sedimentation due to opposed yield stress to pigment settling but a nuisance during deposition. Armelin and colleagues' findings are a typical representative of the rheological behaviour of coatings employed at the coating line. And therefore, a fit for purpose Quality control test will be able to obtain this information, whilst a single value viscosity measurement will not provide this information.

Despite the ability of power-law non- Newtonian model to describe coating liquids rheological behaviour in comparison to the simplified Newtonian model, the power-law model fails to account for the constant viscosity often observed at very low shear rates. Therefore, models such as the Carreau and Cross model have been widely employed in numerous studies to account for this. Eqn. (2 - 16) below shows the Carreau model that accurately describes both low and high shear rates of the coating liquids, and consequently shows versatility for coatings liquids employed in transient processes, and therefore measurements are well fitted over a wide range of shear stress/ shear rate values[60]. Lopez and Rosen [57] findings support the versatility of the Carreau model in comparison to the power-law model.

$$\mu_s(\dot{\gamma}) = \mu_\infty + (\mu_0 - \mu_\infty)(1 + \lambda_c^2 \dot{\gamma}^2)^{\frac{n-1}{2}}, \qquad (2 - 16)$$

Where μ_∞ is the plastic viscosity (Pas), μ_0 is zero shear viscosity (Pas), n is the rheological flow index, λ_c is the characteristic time – scale at which the viscosity begins to drop off (S).

2.3.2. GAP SIZE VISCOSITY DEPENDENCE

Flow-through channels such as rotational rheometers, pipes, and nip – gaps between cylindrical roll - coaters, amongst others, is usually assumed to obey the no-slip boundary condition. A no-slip boundary condition is a widely accepted concept in rheology, tribology and fluid mechanics, with strong experimental evidence to support it. Under rheological characterisation, using a rotational parallel plate, a violation in the no-slip boundary condition is investigated by running a sweep – either shear rate, shear stress or dynamic oscillatory sweep at varying gap sizes between parallel plates. A gap size -

viscosity dependence of a material is an indication of the violation of the no-slip boundary condition [61][62]. The principle of the no-slip boundary condition is the continuity of the tangential velocity at the wall as a result of viscous fluids adhering to the solid surface [63]–[65].

A deviation from the no-slip boundary condition results in three different slip behaviours; True slip, negative AWS (wall stick) and positive AWS (wall slip).

Fig. 2 - 14 schematically describes the different velocity profiles achieved when the no-slip condition is violated during fluid flow of a liquid through two plates.

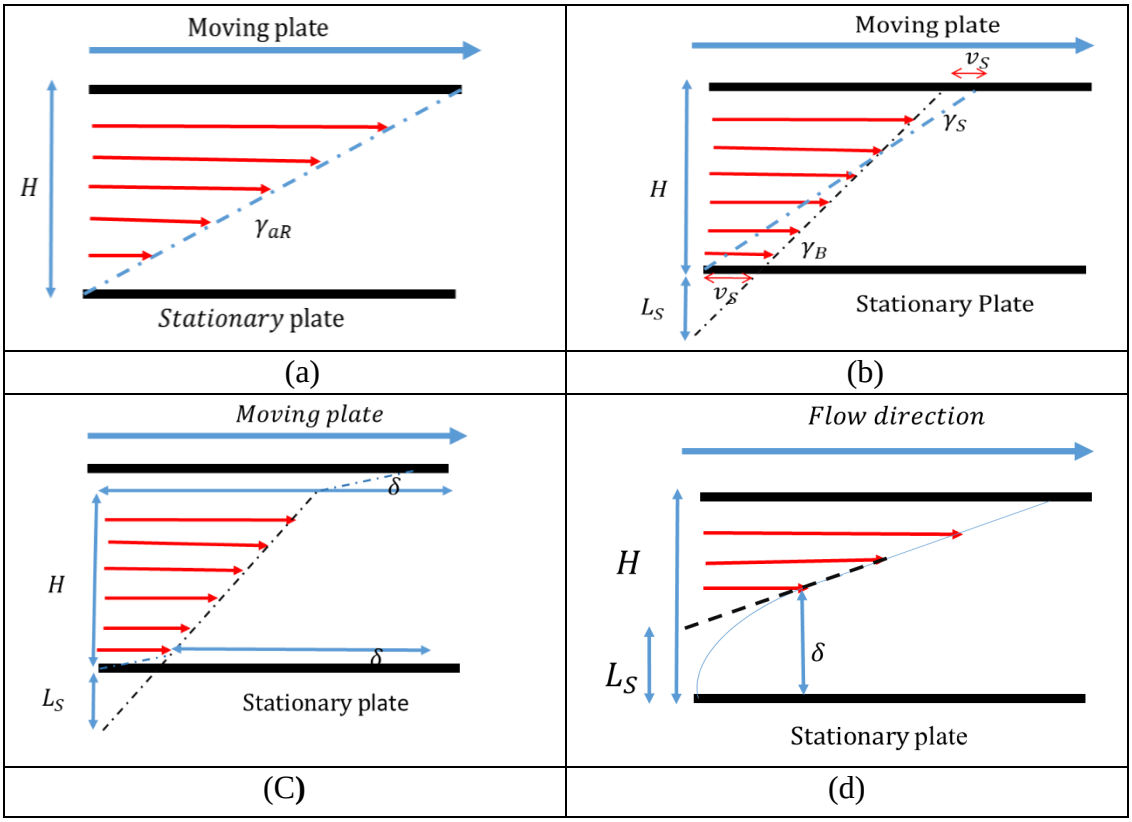

Fig. 2 - 14: Velocity profiles of flow through gap sizes of plates: Image (a) a simple shear flow, Image (b) a flow with true slip, Image (C) a flow with positive AWS (C) and Image (d) a flow with negative AWS.

Image (a) describes a simple shear flow that obeys the no-slip boundary condition. Image (b) illustrates true slip where there is a discontinuity in the velocity profile at the solid-liquid interface. Image (C) illustrates positive apparent wall slip where no-slip boundary conditions are not violated; however, there is an inhomogeneous thin layer of fluid adjacent to the solid surface, with low viscosity in comparison to the bulk fluid. Image (d) illustrates negative apparent wall slip; again, a no-slip boundary condition is not violated; however, there is inhomogeneous stagnation layer of solid particles adjacent to

the solid surface, with high viscosity in comparison to the bulk fluid.AWS types give an illusion of a no-slip boundary condition with the inconsistent rheological and physical behaviour of the test liquids across the gap size. Sochi, T [63] writes that apparent wall slip rather than true slip is the most viable mechanism for wall slip.

Durairaj *et al* [62] and Barnes [66] argue that wall slip is attributed to particle depletion from the solid surface and fluid interface into the bulk, and subsequently creating a lubricant layer (with lower viscosity) which prohibits adhesion of bulk fluid to the moving surface. Nevertheless, the authors state that despite the disadvantages associated with slip, the mechanism can prove essential in some processes that may not require adhesion such as pipe flow.

Slip length (L_S) by definition is the distance from the wall where the velocity profile is extrapolated from the bulk velocity[62][67][68]. Positive slip length estimates the distance from the plate (datum point) where the velocity profile of the flow, extrapolated from the bulk velocity, achieves the velocity equivalent to that of the plate into the wall, whilst negative slip length estimates the distance from the plate where the velocity profile of the flow, extrapolated from the bulk velocity, achieves the velocity equivalent to that of the plate in the fluid. True slip and positive apparent wall slip show a positive slip length while negative apparent wall slip exhibits negative slip length.

Numerous researchers have investigated slip presence by either gap - size viscosity dependence or geometry - size viscosity dependence. Both methods are known as Mooney analysis methods [7]. The Mooney analysis is a data analysis method developed by Mooney in 1931 [69][70][71] to determine slip velocities and subsequent slip properties subject to wall slip. The Mooney analysis method relies on varying the surface to volume ratio of dies/ plates and thus obtaining the resultant data pertaining to slip velocities as a function of shear stress or pressure.

For geometry size (diameter) - viscosity dependence method to be valid when using rotational rheometry, the ratio of the diameter to gap size (L/D) should be constant and thus maintaining the same stress. For both Newtonian fluids in Eqn. (2 – 17) and Non-Newtonian fluids in Eqn. (2 - 18) is often employed to determine wall slip behaviour. Apparent slip shear rate (total shear rate) is a contribution of slip velocity and rim (true) shear rate [61], [64], [72].

$$\dot{\gamma}_{ab} = \frac{4V_s}{R} + \dot{\gamma}_w \quad (2 - 17)$$

$$\dot{\gamma}_{ab} = \left(\frac{4n\,(k+3)}{3n+1}\right)\frac{4V_s}{R} + \frac{4n}{3n+1}\dot{\gamma}_w \quad (2 - 18)$$

Alternatively, slip analysis is conducted using gap - size viscosity dependence (the distance of rotating geometry from the stationary plate) and observing the change in viscosity as a function of gap size. Davies and Stokes [73] employed the latter method, following Eqn. (2 - 19) and Eqn. (2 - 20) on shear-thinning materials.

$$\dot{\gamma}_{ab} = \dot{\gamma}_{bulk}\left(1 - \frac{2\delta_s}{H}\right) + \frac{2\delta_s}{H}\dot{\gamma}_w \quad (2 - 19)$$

Also

$$V_s = 2\delta_s(\dot{\gamma}_w - \dot{\gamma}_{bulk}) \quad (2 - 20)$$

Where V_s is the slip velocity(m/s), $\dot{\gamma}_{bulk}$ is the bulk shear rate, $\dot{\gamma}_{ab}$ is the measured shear rate (1/s), H is the gap size (µm), $\dot{\gamma}_w$ is the shear rate at the wall (1/s), $\dot{\gamma}_{bulk}$ is the bulk shear rate (1/s) and δ_s is the anomalous layer thickness (µm).

A deviation from the no-slip boundary condition has its consequences during rheological characterisation, product quality and industrial processes. During rheological characterisation, slip effects on measured properties of test liquids are often assumed negligible since the mathematical equations in the background software fail to consider slip effects to the total flow. Nevertheless, Rides. M [74] argues that issues related to particle size relative to gap size must be put into consideration during rheological characterisations of test liquids. Davies and Stokes [73] state that rheological characterisation of structured fluids or Semi-solids is cumbersome due to particle confinement which further introduces discrepancies to the rheological studies.

Various researchers have reported methods of correcting for slip in experimental work. Amongst them include the Bagley correction often used during capillary rheometry. Ansari *et al* [75]reported a deviation from the Cox-Mertz rule of m-HDPEs of wide-range molecular weight distribution using a capillary rheometer. For the Cox-Mertz rule to be obeyed, the complex viscosity from the oscillatory rheometry and the shear viscosity flow

curve must be equal. The authors ascribed this occurrence to significant wall slip behaviour when the Mooney analysis method was used during oscillatory frequency sweeps in the LVE region revealed flow curve shifts at different die diameters. The author used the Bagley method to correct for any slip contributions to the total flow. A detailed review of the Bagley method for the correction of slip effects in pressure rheometers is well-reviewed by Puyvelde and Magnus [69]. The use of the Bagley correction factor can be time-consuming as each flow curve requires determination of the Bagley correction and, and the usage of at least three capillary dies of the same diameters but varying length to diameter ratios.

With regards to industrial processes such as Polymer extrusion in insulated cable manufacturing, is of pinnacle importance, the presence of slip, especially stick-slip, leads to rough surface finishes in the polymer extrusion process. Fig. 2 – 15 shows the product quality of polyethene extrudate in the presence and absence of slip. In the absence of slip, the extrudate product quality is smooth, and the opposite is true for the extrudate in the presence of slip.

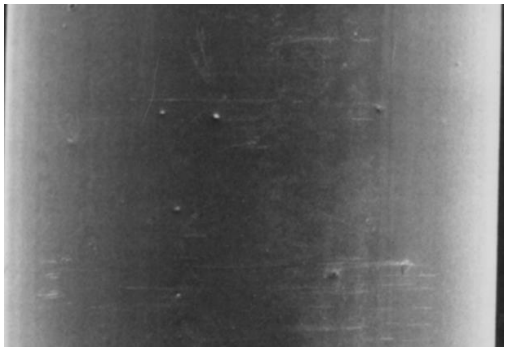

(a) -In the absence of slip

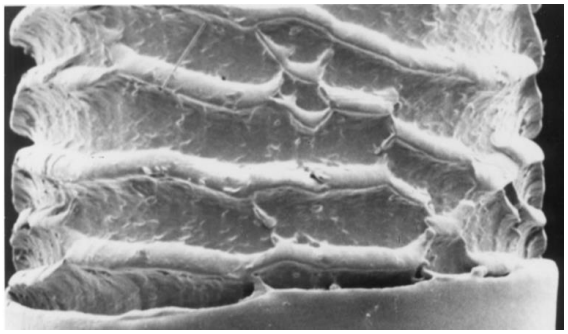

(a) In the presence of slip

Fig. 2 - 15: shows images of Polyethylene extrudate: (a)absence of slip tendencies (no-slip boundary extrusion of polyethene) and (b) Product quality in the presence of stick-slip, obtained from [76].

The direct impact of slip phenomena in the food industry is observed in quality control tests measurement methods. Cullen and co-workers [77] briefly addressed the concerns when dealing with conventional rheometers as they are prone to fouling which subsequently leads to measurement errors.

A plethora of research work on slip phenomena and its impact in rheological characterisation, polymer and food extrusion process, and paper industry is well understood and studied by various researchers. However, a limited study of slip

phenomena in the roll coating process is still not well known, though several surface defects encountered during the roll coating process, such as PMD and paint starvation is postulated to be an outcome of slip effects. While coil roll coating process is different from polymer and food extrusion process, similarities in the mechanism of slip manifestation could be identified and thus employed in the study of slip in roll coating process.

2.3.3. TIME DEPENDENCE RHEOLOGICAL PROPERTIES OF COATINGS

Coatings employed in roll coating process have been known to possess a time-dependent viscosity property. These properties are not only dependant on the change of viscosity with the shear rate but also the time length over which shear rate is applied. Therefore, the duration of the test or process will have a tremendous effect on the viscosity.

2.3.3.1.THIXOTROPIC OR RHEOPECTIC PROPERTIES OF COATINGS

Thixotropic behaviour, which is present in some shear-thinning materials, exhibits a gradual decrease in viscosity when a shear force is applied, and a gradual increase of viscosity upon cessation of shear force on the test material; whereas rheopectic materials exhibit an increase in viscosity at increasing external force and a gradual reduction in viscosity upon cessation of shear external. These properties are influenced by the intrinsic structure of the coating. However, when the applied shear stress is constant, these time-dependent materials show a Newtonian plateau, a point at which almost all the internal bonds have been broken. Ceased stress or shearing action causes the coating to gradually retain its original structure. Most of the referenced work on time-dependent viscosity materials in roll coating have been based either on thixotropic or Newtonian fluids. Lopez and Rosen [57], and Cohu and Magnin [6] reported thixotropic properties in the sample coatings mostly employed in manufacturing of pre-coated steel industries.

2.3.3.1.1. VISCOELASTICITY

Viscoelasticity influences the performance of the roll coating process in more ways than one. Amongst them include the appearance of the manufactured pre-coated steel; pumping requirements of the coating through the coating process; flexibility of the cured coating during deep drawing processes, amongst others. It is therefore of pinnacle importance to review viscoelasticity and the models employed to describe the behaviour. Thus far, there has been limited research on viscoelastic effects on coating flow during the roll coating process.

According to Scriven *et al* [78], high enough viscoelasticity in a liquid, categories it to polymer extrusion due to the strong tensile properties. However, this would lead to flow instabilities and non-uniformities in coating flows such as ribbing, *cobwebbing* and misting. Contrary to this argument, viscoelasticity promotes good adhesion onto steel substrates and allows a high quantity of coating pick up from the coating trough when operating under a classical/ fully flooded regime.

Additionally, viscoelasticity promotes the formation of a coating layer on steel surface by ceasing coating fluidity once applied onto the steel surface. There are various methods employed in the determination of viscoelasticity, but two of them are reviewed herein, namely; creep and stress relaxation test, and Dynamic Oscillatory rheometry.

(a) DYNAMIC LINEAR OSCILLATORY RHEOMETRY

Dynamic oscillatory rheometry is essential for determining the mechanical properties of the coating, and subsequently, determine their viscoelasticity within the linear viscoelastic region. The first step in conducting a dynamic oscillatory rheometry is to obtain a linear viscoelastic region and the critical strain by conducting an amplitude sweep. An amplitude sweep entails an application of a sinusoidal strain (or stress) at a constant frequency, and the resultant rheological properties (complex modulus, elastic and viscous modulus, critical strain and linear viscoelastic region) are obtained [79][47]

With the knowledge of LVR region, a frequency sweep is conducted to determine the mechanical properties where the frequency is varied whilst applying a constant strain (a critical strain or any strain value obtained with the linear viscoelastic region).

Complex modulus is a summation of the real and imaginary components of the modulus, also known as the elastic modulus, and viscous modulus, respectively. Similarly, complex modulus can be represented as the ratio of stress to strain in the Fourier transform nature as shown in Eqn. (2 -21) below[80].

$$G^* = \frac{\hat{\sigma}(\omega)}{\hat{\gamma}(\omega)} = G' + i\,G'' \qquad (2 - 21)$$

Frequency sweep relies on applying an oscillatory strain, mathematically represented in Eqn. (2 - 22) and the resultant oscillatory stress is determined, see Eqn. (2 - 23).

$$\gamma(\omega, t) = \gamma_0 \sin(\omega t + \theta(\omega)) \quad (2 - 22)$$

$$\sigma(\omega, t) = \sigma_0 \cos(\omega t) \quad (2 - 23)$$

Also;

$$\sigma(\omega, t) = \sigma_0 \cos\theta(\omega) \cos(\omega t) - \sigma_0 \sin(\omega t)\sin\theta(\omega))$$

Further mathematical description of complex modulus is composed of two "sinusoidal curves" and thus mathematically expressed in Eqn. (2 - 24)

$$G^*(\omega) = \frac{\sigma_0 \cos(\theta(\omega))}{\gamma_0(\omega)} + i\frac{\sigma_0 \sin(\theta(\omega))}{\gamma_0(\omega)} \quad (2 - 24)$$

Where G^* is the complex modulus (Pa), γ_0 is the amplitude strain (-), σ_0 is the oscillatory stress; $\theta$is the phase angle (^{0}), is the imaginary unit ($i = \sqrt{-1}$), G′ is the elastic modulus (Pa), G"is the viscous modulus (Pa) and ω is the frequency (Hz). Fig. 2 -16 shows an ideal viscous response with a phase angle of 90^0 on the right, and an ideal solid-like response on the left with a phase angle of 0^0. For liquid-like response, the stress and strain curves are always out of phase, whereas the stress and strain curves for a solid-like response is always in phase. For a viscoelastic response, $90^0 < \theta > 0^0$ [80].

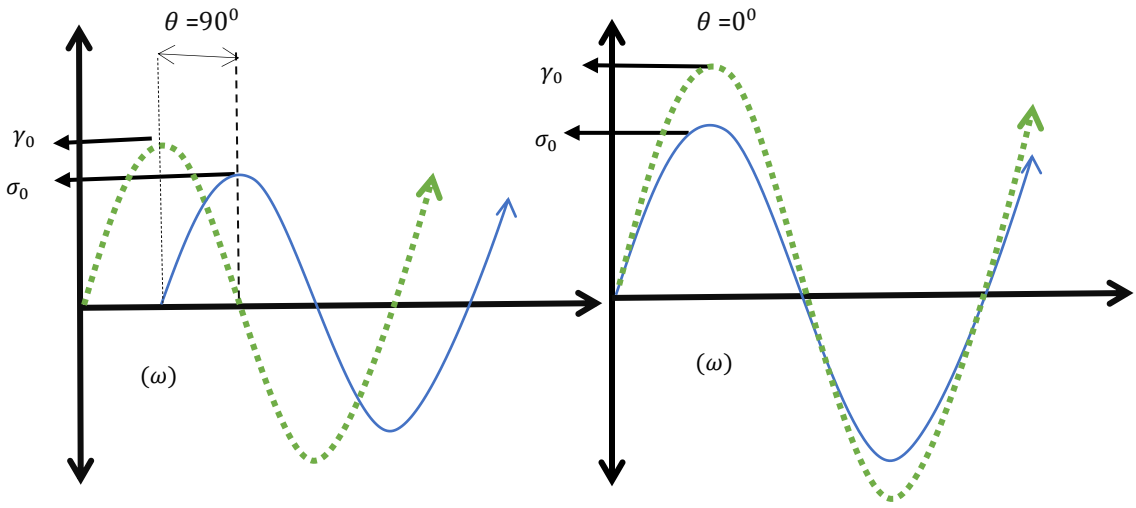

Fig. 2 - 16: Strain and stress response of an ideal viscous material (Left) and Ideal elastic material (Right)

(b). CREEP COMPLIANCE AND RELAXATION

Creep compliance and stress relaxation is a time-dependent test used to determine the viscoelastic properties of materials. Creep compliance and relaxation test requires an application of a known and constant of stress onto the material for a period, followed by instantaneously ceasing stress application. A strain response throughout the experimental time is recorded and used to analyse viscoelastic properties.

There are three responses to the imposed shear stress; Perfect elastic (solid-like) behaviour, perfect viscous (fluid-like) behaviour or a combination of the two properties (Viscoelastic) – meaning that the material displays both elastic and viscous behaviours based on the time scale [56].

a. Perfect elastic bodies

A perfect elastic body, represented by a mechanical model as spring, obeys Hooke's law, described by Eqn. (2 - 17), where the spring responds instantaneously to the applied force. Fig. 2 -17 shows a typical strain response of an elastic, where $t = 1$, $t = 2$and $t = 3$ represent rime at point 1, point 2 and point 3 respectively.

At the initial time $(t = 0)$, a force is applied on a material and the material responds instantaneously to the stress, up to a point of equilibrium. At $t = 1$, the force is ceased, and the body shows an instant reduction in strain to a point of recovery from deformation.

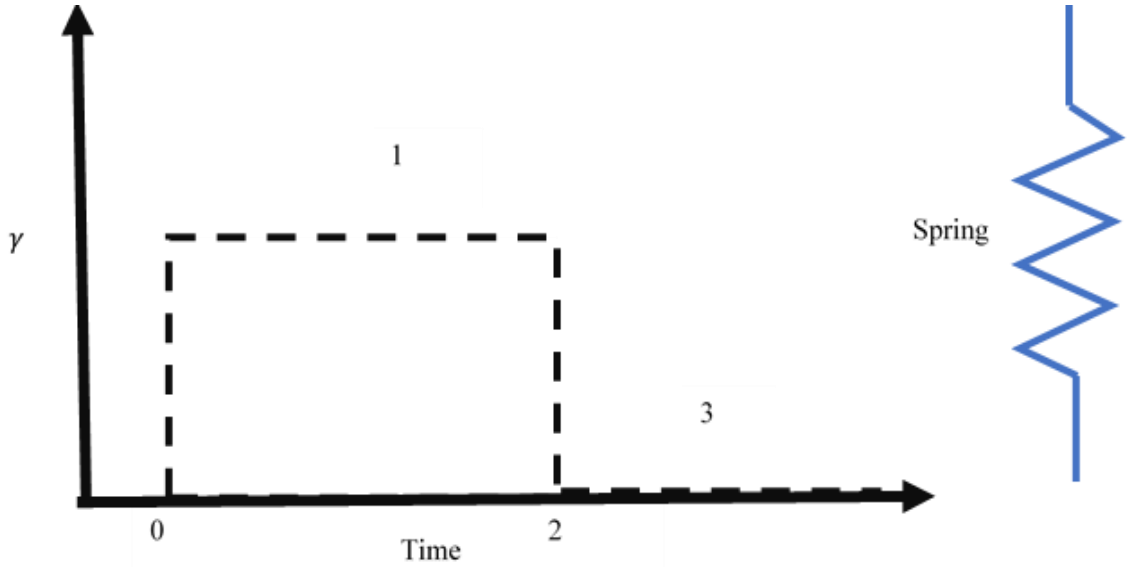

Fig. 2 - 17: Strain response of a perfect elastic body

$$\tau = G\gamma \qquad (2 - 25)$$

Where σ is the shear stress (Pa), G is the shear modulus (Pa), J is the creep compliance (Pa) and γ is the shear strain (-).

At *t =2*, stress application is ceased, and the material fully recovers from deformation. The strain response of a material is directly proportional to the applied stress, and elastic deformation is found to be reversible – meaning that the material's energy is not completely dissipated of as heat but stored in its elastic component and easily recoverable.

b. An ideal viscous behaviour

An ideal viscous body shows a delayed response in strain upon stress application. A mechanical model used to describe a viscous behaviour is a dashpot, shown in fig. 2 – 18 together with a viscous response. A viscous element response to the applied force is delayed by viscous resistance in the dashpot. The mechanical characteristics of a dashpot are described by the power-law Newtonian equation.

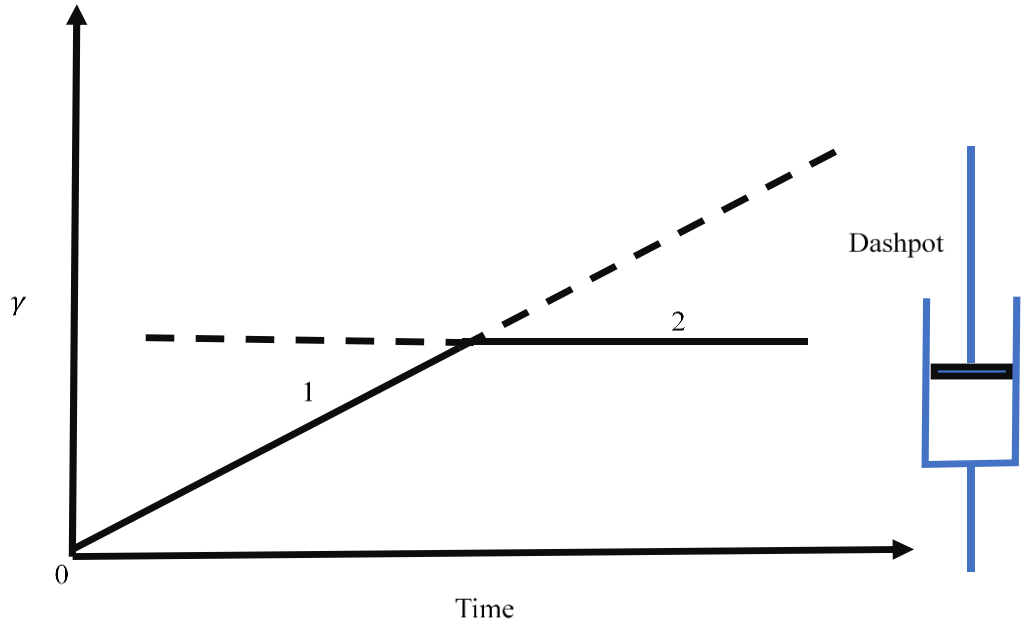

Fig. 2 - 18: Strain response of a perfect viscous body

At time *t = 1* there is delayed response to deformation but the material strains after a period. At *t = 2*, stress is ceased, and the material does not return to its original shape. This indicates that the energy stored within a material is dissipated through heat and the

material is permanently deformed. At $t = 3$, there is no recovery of the original shape even after shear stress cessation.

c. A viscoelastic body

A viscoelastic body displays both Viscous and Elastic behaviour, depending on the time scale. Therefore, a mechanical model used to describe this behaviour consists of both a spring (springs) and dashpot (dashpots). Depending on the experiment conducted, a plethora of models can be used to describe the material deformation.

For an experiment where constant applied stress (stress retardation) is applied and then ceased, a Kelvin-Voight model can be used where both Spring and dashpot are parallel, whereas an experiment where a constant strain is applied (Stress relaxation) may be represented using a Maxwell model. The response of many materials to constant stress (creep) or constant strain (stress relaxation) may differ from the simple Maxwell (single relaxation time) or Kelvin-Voight element (single retardation time). Therefore, a material response is determined using a Burgers model (See fig. 2 - 19), which utilizes multiple elements to describe the response. The strain response with time is feedback in the strain as a function of time, also known as compliance (J).

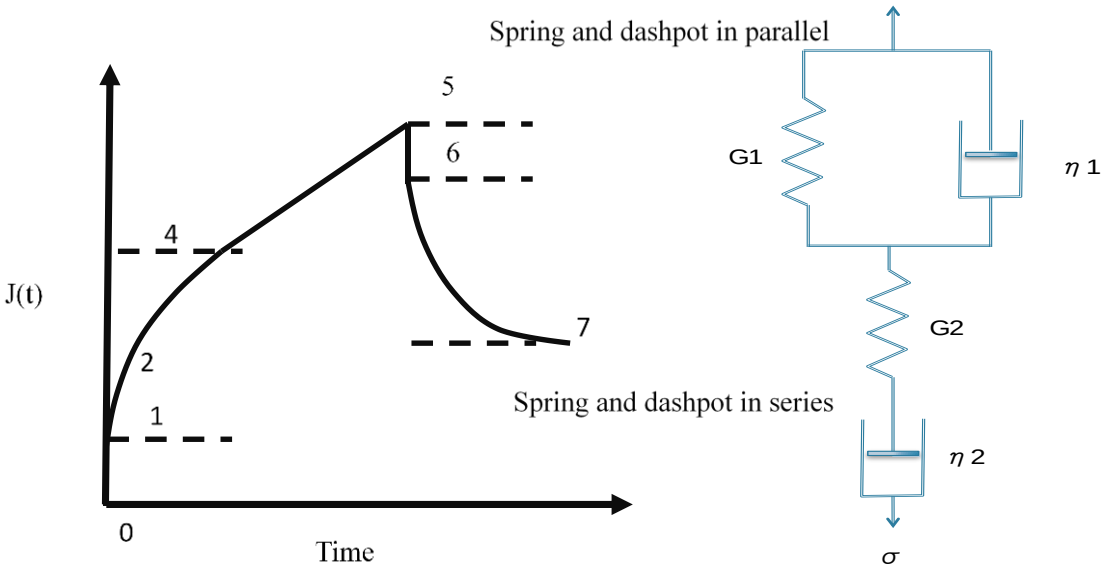

Fig. 2 - 19: Strain response of a viscoelastic fluid

2.3.4. SHEAR RHEOMETRIC TECHNIQUES FOR CHARACTERISING COATING

Rheological properties influence the coating performance at the coating line; therefore, good rheological characterisation techniques could be the difference between a defect-free performance from coating runs that suffer from defects. A rheometer is a device that creates a flow of the test liquid by applying stress and subsequently measuring the resultant deformation or deformation rate of the material. A rheometric technique is chosen purely based on the rheological properties that are required to be determined. Rheological properties such as steady-state shear viscosity, linear viscoelastic properties (elastic or elastic modulus), thixotropic properties, amongst others provide vital information on the intrinsic structure of the material and hence the performance of the coating when employed at the coating line.

Shear rheometry can be either drag or pressure flow driven. In the case of drag flow rheometry, a test liquid is placed between two solid surfaces. One surface is moved relative to another, thus creating shearing action in the fluid. The shearing action generates stress that acts parallel to the direction of the flow. The most commonly employed drag flow rheometers are Cone and plate, Parallel plate, Couette cells and the sliding cells [82]. However, parallel plate geometry and the cone and plate geometries are mostly employed to measure rheological properties of non-Newtonian fluids due to the small amount of sample required for running the experiment. Additionally, the ability of the equipment to measure viscoelastic properties of the samples (loss and elastic modulus) when an oscillatory torque or strain is applied, renders the two geometries vital for rheological characterisation. Albeit, a cone and plate geometry is the most preferred geometry over the parallel plate because it provides constant shear rate throughout the sample thus eliminating inaccuracies in data acquiring.

Pressure flow rheometry is when a fluid understudy is forced through a tube of constant cross-section and length under lamina flow conditions[83]. The flowrate is measured whilst keeping pressure drop fixed or measuring pressure drop and keeping the flow rate of the fluid fixed. The velocity gradient is maximum at the tube wall and zero in the centre of the flow. For this very reason, pressure-driven flows are non - homogeneous. Therefore, pressure flow driven rheometers are only used for measuring shear viscosity flow. The most prominent pressure-flow driven rheometers are capillary and slit

rheometers. The mathematical working principles of the drag and pressure-flow driven rheometric techniques have been reviewed by Glass and K. Pruf'homme [84]. Table 2 -3 summaries shear rheometric geometries often employed.

Table 2 - 3: Summary of shear flow rheometric geometries[85].

Geometry	Advantages	Disadvantages
Concentric cylinder (Couette or Searle method) rheometer	▪ Suitable for low viscous fluids (< 1000 Pas) ▪ Higher shear rates can be applied ▪ Couette method does not encounter secondary Taylor vortices that are encountered in the Searle method	▪ Narrow gap settings, ranging between 0.5 to 1, otherwise secondary flows will arise ▪ Not suitable for high viscous fluids ▪ Operating the equipment using the Searle method is prone to turbulent conditions when analysing low viscous fluids at high rotational speeds.
Cone and plate rheometer	▪ Shear is nearly uniform throughout the sample ▪ Possess a truncated tip to avoid friction interference with torque readings ▪ Shear rate is independent of the cone radius	▪ Limited ability to probe non-linear behaviour ▪ Inability to produce accurate data when operating at high shear rates ▪ Not suitable for fluids with large particles as slip effects might occur thus produce inaccuracy in the data collected
Parallel plate rheometer	▪ Sample preparation and loading is much easier with ▪ Suitable for high viscous fluid materials ▪ Ability to conduct small amplitude oscillatory shear tests	▪ Inability to probe non-linear behaviour shear rate ▪ Prone to solvent evaporation therefore solvent trap is used ▪ Nonhomogeneous flow therefore not suitable for measuring complex modulus as a function of both time and shear rate
Vane rheometer	▪ Suitable for materials that are prone to slip effects and settling ▪ Suitable for fluid materials with delicate structures	▪ Not suitable for measuring materials with yield stress values greater than 10 Pa[65]
Capillary rheometer	▪ Suitable for high shear rate tests ▪ Suitable for process simulations	▪ Measures only steady shear functions ▪ Yields nonhomogeneous flow therefore not suitable for measuring complex modulus as a function of both time and shear rate ▪ Not suitable for time-dependent measurement

2.4. EXTENSIONAL FLOW OF COATINGS

Even though the shear flow is most commonly encountered in our day to day lives, extensional flow dominates in an industrial environment. Therefore, this section aims to review extensional flow and its effect in the coating industry. Extensional viscosity is defined as the resistance of the fluid to the stretching motion [86], [87]. In the roll coating process, extensional flow is evident during film splitting between rolls; pick - up roll departure from the coating trough and film split between applicator roll and substrate.

There are three types of extensional flows, namely; Uniaxial, biaxial and planar extensional flow [88]. Fig. 2 – 20 schematically describes the three types of extensional flow; the un-deformed cubical material in fig. 2 – 20 (a) deforms under the three different extensional flows: Uniaxial (b) , (c) Bi-axial (C) l and Planar uniaxial (d).

<table>
<tr><td> 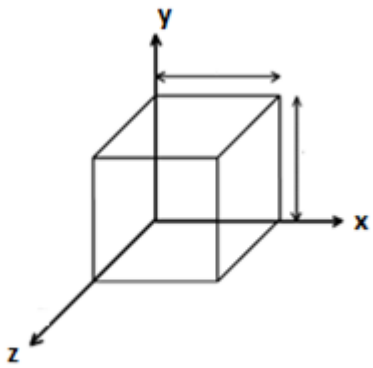
</td><td> 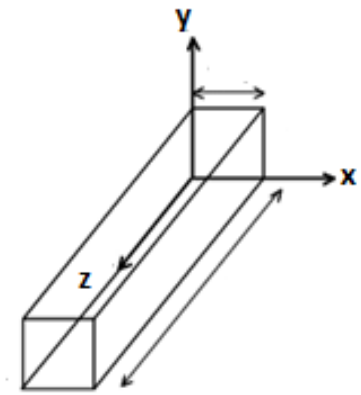
</td></tr>
<tr><td>(a) Un-deformed cubic material</td><td>(b) Deformed cubic material under uniaxial extensional flow</td></tr>
<tr><td> 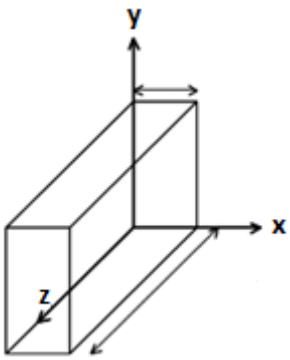
</td><td> 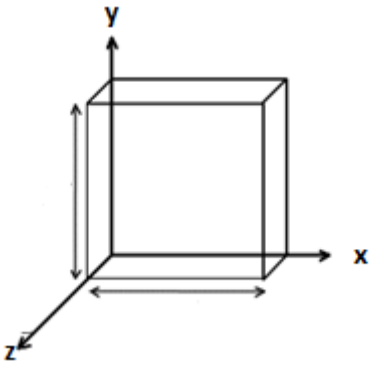
</td></tr>
<tr><td>(C) Deformed cubic material under biaxial extensional flow</td><td>(d) Deformed cubic material under planar uniaxial extensional flow</td></tr>
</table>

Fig. 2 - 20: Types of extensional flow. (a) Uniaxial (b) Bi-axial (c) Planar axial.

Under uniaxial extensional flow, volume conservation dictates the flow. Using an example of fig. 2 – 20 (b), a cubical material is reduced in the y and x-direction; while an extension in the z-direction is also seen. Therefore, uniaxial extensional flow is simply denoted as elongation of a fluid element in one direction [54], [61], [89].

Biaxial extensional flow exhibits extension in two dimensions, x and y directions, whilst showing a reduction in the z-direction. In-depth review and study of biaxial extensional flow has been reported in various manuscripts such as [81] [90][91] [92].

And finally, planar extensional flow, a cubical material is stretched with a resultant decrease in one dimensional, but the third dimension remains unchanged[84]. For example, the thickness of a cubical material under planar extension decreases but the width sustained.

In summary, a planar extension is the stretching of a material with no reduction in width. In this study, uniaxial extensional flow is studied because it reflects the film splitting process in the nip gap and material separation from the bulk.

Extensional viscosity of Newtonian fluids obeys trouton ratio, Eqn. (2 -26). In the case of non-Newtonian fluids such as coatings, trouton ratio varies greatly with deformation rate, process time and total deformation. In many cases μ_E is four times bigger than μ for planar Eqn. (2 - 27), and six times bigger for biaxial extensional flow Eqn. (2 -28). Under industrial conditions, extensional viscosity is of magnitude to 10^4 when compared to shear viscosity[93][91].

$$\mu_E = 3\mu_s \tag{2 - 26}$$

$$\mu_{EB} = 6\mu_s \tag{2 - 27}$$

$$\mu_{EP} = 4\mu_s \tag{2 - 28}$$

where μ_s, μ_E, μ_{EB} and μ_{EP} are the shea, uniaxial, biaxial, and planar extensional viscosity (Pas) of the fluid respectively.

Newtonian fluids are often restricted to shear and uniaxial or elongation viscosity; however, non - Newtonian fluids can potentially be deformed under all three types. High

values of extensional viscosity in polymer-containing materials are ascribed to the molecular conformation of the polymer molecules. Polymer chains exert less resistance to flow during the unravelling stage. Upon unravelling, the chains fully alignment chains in the direction of the applied stress yield greater resistance to the stretching flow, high extensional viscosity at high shear stress.

Three types of extensional viscosities can be achieved when a material is subjected to an external force, namely, Newtonian, tension thinning and tension thickening. Just like shear flow, Newtonian materials exhibit extensional rate-independent viscosity. Tension thinning materials exhibit extensional viscosity that decreases with increasing extensional strain rate. Conversely, tension thinning materials exhibit viscosity that increases with increasing extensional strain rate.

The flow fields in shear flow are different from those experienced in extensional flow due to the parallel streamlines under shear flow and converging streamlines under extensional flow. The effect of extensional flow is transient and can be desired or undesired. In roll coating process, high extensional viscosity has been reported to significantly contribute to the coating defects such ribbing [18], [32], [35], [57], fat edges[40], [43], cascading [16], sagging amongst others. James *et al* [94] and Fernando *et al* [43] analysed measurement of coating liquid using a filament stretching technique and the results showed a big correlation of misting to extensional flow.

2.4.1. EXTENSIONAL RHEOMETRIC TECHNIQUES FOR CHARACTERISING COATINGS FLUIDS

Advancements in extensional rheometry have been rather slow compared to shear rheometric techniques. Thus, it has been accepted that obtaining pure extensional viscosity of flow under laboratory conditions is cumbersome. For example, under uniaxial flow, filaments are seldom uniform thus introducing inaccuracy in collected data; stress along the length of the filament; and gravitational sagging when characterising low viscous materials due to their low viscous and capillary forces, pre-shearing of liquid coating before extensional part of the experiment, amongst others, introduces inaccuracies. Consequently, the measured extensional viscosity under controlled laboratory conditions is referred to as “transient extensional viscosity” due to the measurement errors that might be introduced during the testing process[95]. Furthermore,

short experimental time does not allow a steady-state viscosity to be achieved thus introducing in errors in the experimental data.

Various extensional rheometers have been employed for the study of extensional rheometry, and all of them fall into either constant force or constant stain rate extension rheometers. In this study, three t types of extensional rheometers were reviewed namely, Filament stretching extensional rheometer (FSR). Falling Mass extensional rheometer, and Capillary Break extensional rheometer (CaBER).

2.4.1.1 FILAMENT STRETCHING RHEOMETER (FSR)

FSR is a constant rate (controlled strain rate) rheometer and overcomes some of the drawbacks previously discussed. One of the advantages associated with FSR is that the equipment operates in a high viscosity range of 1 to 1000 Pas[96]. However, FSR is limited to relatively high viscosity or elastic fluids which are prone to sagging and bulging due to gravitational effects [88]

Fig. 2 – 21 shows a schematic of FSR equipment consisting two cylindrical plates with size diameters ranging from 3 - 5mm, supported by a bracket which is linked to a linear drive system.

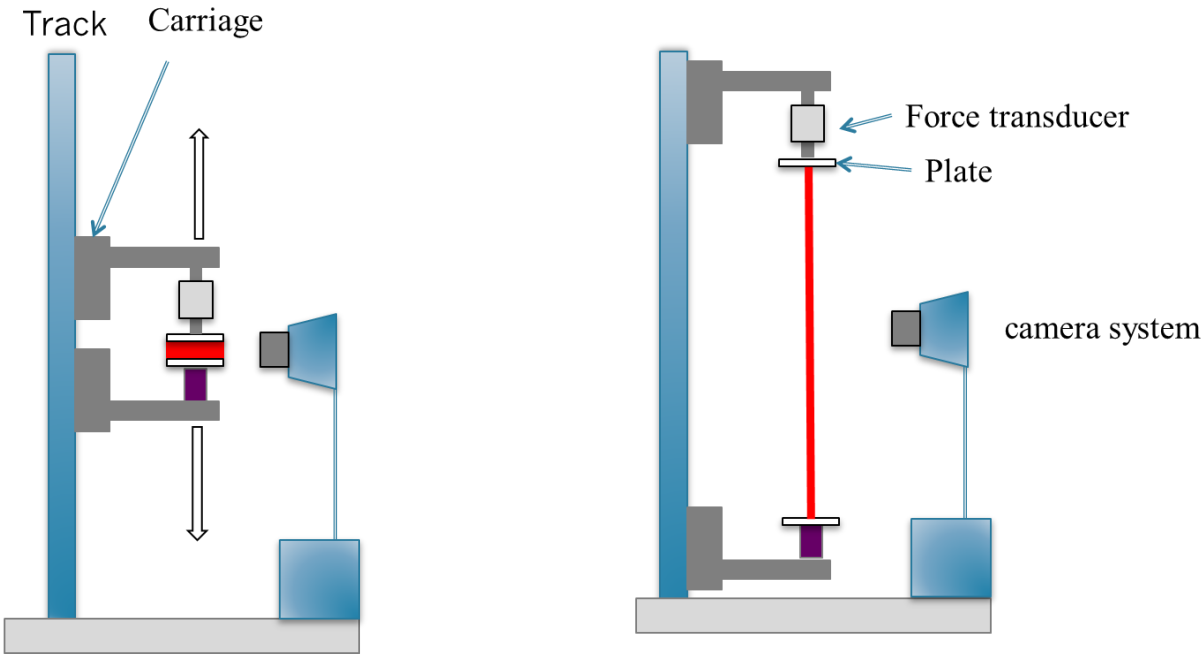

Fig. 2 - 21: Schematic of a filament stretching Extensional rheometer (FSR).

An optical measurement system (a high-speed camera or laser micrometer) is utilized to monitor changes in filament thinning diameter (radius) of the test fluid as a function of

time. A data acquisition system is required to capture the time-varying output of the transducer system and synchronizes this with the optical data from the camera. Once the diameter against time profile and the force against time profiles are known, apparent extensional viscosity can be calculated

In FSR, the two plates (bottom and top plate) are both separated, and a progressive filament thinning radius is monitored. And the motor system controls the separation of plates to produce a constant extensional rate.

2.4.1.2 CAPILLARY BREAK UP RHEOMETER (CaBER)

In CaBER equipment (fig. 2 – 22), the top plate is moved vertically by a known distance to allow separation and then held stationary. Progressive thinning of the filament radius is captured by a high-speed camera and then the mid-point diameter is measured from the captured images. With prior knowledge of surface tension and density apparent extensional viscosity is determined.

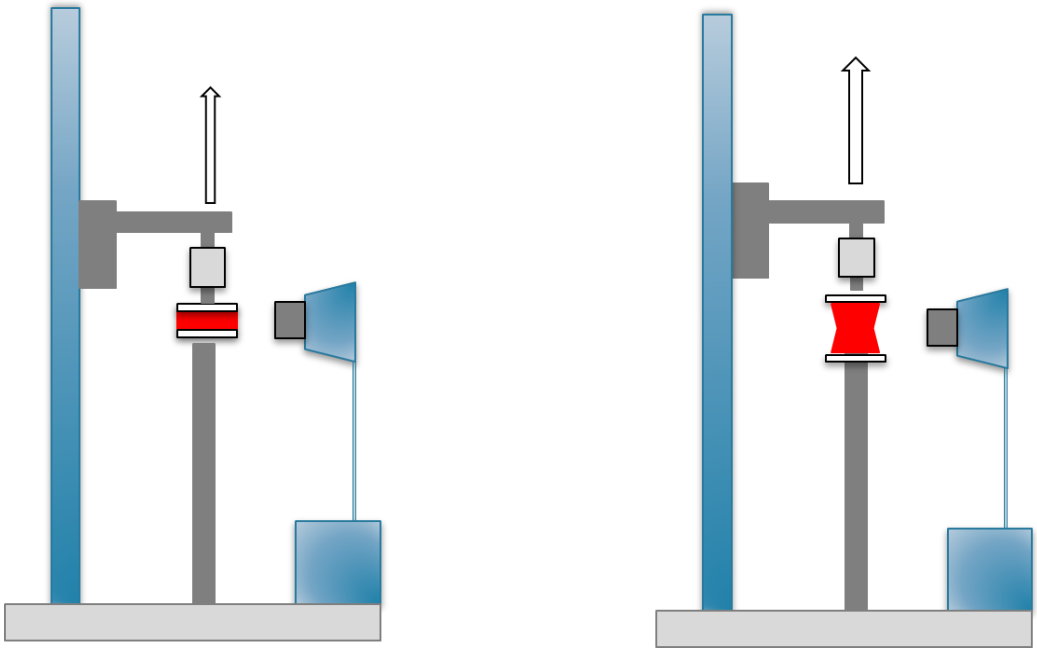

Fig. 2 - 22: Schematic of a Capillary Break Up tensional rheometer (CaBER).

One of the advantages associated with the CaBER equipment is that it is say to operate and measures large velocity gradients. The downsides of the rheometer include data interpretation is not straight forward, turbulence effect on obtained results at high flow rates; extreme strain rates; and flow instabilities in viscoelastic fluids. All the setbacks introduce errors in the obtained data. According to Nystrom *et al* [89], a CaBER is the

only extensional rheometer available on the market as the others are in-house built and designed for Polymer melts and dilute fluids. A CaBER tool consists of two cylindrical plates, a high-speed camera, a motor transducer.

2.4.1.3 FALLING MASS EXTENSIONAL RHEOMER

And finally, a falling mass extensional rheometer (fig. 2 – 23) falls under a constant force technique but strain rate varies. Similar to CaBER and FSR, falling mass consists of a high-speed camera, separation plates and a data acquisition tool. The working principles are the same as CaBER except that the bottom plate moves whilst the top late stays stationary.

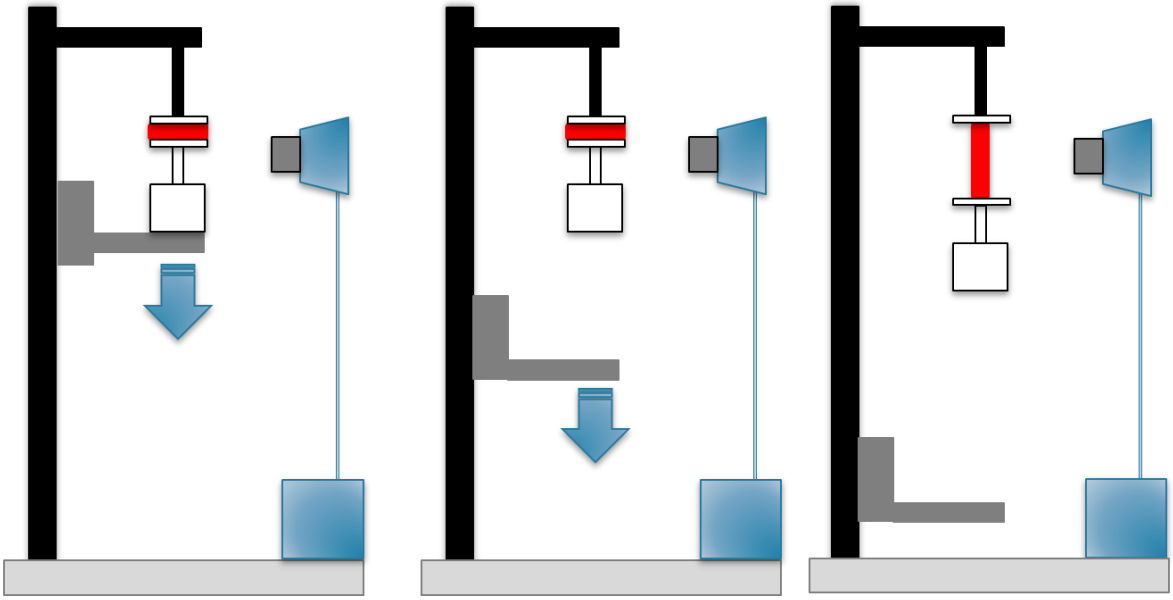

Fig. 2 - 23*:* Schematic of a Falling Mass extensional rheometer.

A sample is loaded between plates, and support is quickly retracted by letting the lower plate fall under the influence of gravity. The change in filament radius is captured by the high-speed camera[97].

2.4.2 EXTENSIONAL FLOW PARAMETERS

2.4.2.1 EXTENSIONAL STRAIN

From the reviewed extensional rheometers, the CaBER equipment is of interest in this study due to its ability to measure very low viscosity values. Therefore, the extensional parameters discussed therein pertain to the CaBER equipment.

During experimentation, the upper plate of the CaBER rheometer is moved upwards such that the inserted test fluid between the cylindrical plates is stretched. The resultant change in length is exponential and described using eqn. (2.- 29)

$$L(t) = L_0 \exp(\varepsilon_0 (t - t_0)) \quad (2 - 29)$$

The Hencky strain, ε_H, describes the logarithmic change in the material's characteristic length. Hencky strain can be derived through integration of the strain rate Eqn. (2 – 30), to obtain Eqn. (2 -31)[98]. Also note: $D_0 = 2r_0$ and $D_{mid}(t) = 2r_{mid}(t)$

$$\varepsilon_H = \int \dot{\varepsilon} \; dt \quad (2 - 30)$$

$$\varepsilon_H = 2\ln\left(\frac{D_0}{D_{mid}(t)}\right) \quad (2 - 31)$$

2.4.2.2 EXTENSIONAL STRAIN RATE

Time is very important during extensional flow; therefore, to include time, the rate of elongation, also known as strain rate, $\dot{\varepsilon}$, is determined using Eqn. (2 -32)[99].

$$\dot{\varepsilon} = -\frac{2}{D_{mid}(t)} \frac{dD_{mid}(t)}{dt} \quad (2 - 32)$$

2.4.2.3 APPARENT EXTENSIONAL VISCOSITY

A combination of strain rates and physical properties of the test liquid such as surface tension and density can be employed to determine apparent extensional viscosity, using Eqn. (2 – 33) [98].

$$\mu_E = -\frac{\sigma}{(dD_{mid}(t)/dt)} \quad (2 - 33)$$

Where μ_E is apparent uniaxial extensional viscosity (Pas), r_0 is the filament radius (m), r_i is the final filament radius (m), D_i is the final filament diameter (m), dt is the change in time (Secs), $\dot{\varepsilon}$ is the strain rate (1/s), $r_{mid}(t)$ is the filament radius is a function of time (m), V_r is the separation velocity (m/s), $D_{mid}(t)$ is the filament diameter is a function of time (m), D_0 is the initial filament diameter (m), r_0 is the initial filament radius (m), L_0 is the initial filament length (m) and L(t) is the filament length at length at time t.

2.5 SURFACE TENSION AND CONTACT ANGLE DURING IN ROLL COATING

Besides rheological properties, surface tension is a physical property of a coating liquid that influences the performance of the roll coating process by dictating wettability of coating on the roll surface and substrate. By definition, surface tension forces are interactions between liquid molecules at the surface of the liquid film created by the imbalance of forces between liquid molecules at the surface and those in the bulk. [85] [50].

Prior to coating adhesion on any surface, coating wetting is the preliminary step. Consequently, wettability is a function of surface tension of coating and surface energy of the substrate and is quantified through contact angle measurements. The dominance or inferiority of surface tension over surface energy dictates the value of contact angle and subsequently the degree of wettability.

The contact angle can be static and/ or dynamic, and dependant on the process, a suitable contact angle measurement can be employed. For example, the roll coating process is dynamic, and therefore dynamic contact angles are more representative of the roll coating process due to the dynamic mode of the process.

Fig. 2 -24 shows a series of droplets at various static contact angles. Drake and Shikhmurzaev [100] denote that the difference between the dynamic and static contact angle is that the former depends on both the flow geometry near the contact line and the contact-line speed, whereas the latter depends on the flow geometry only.

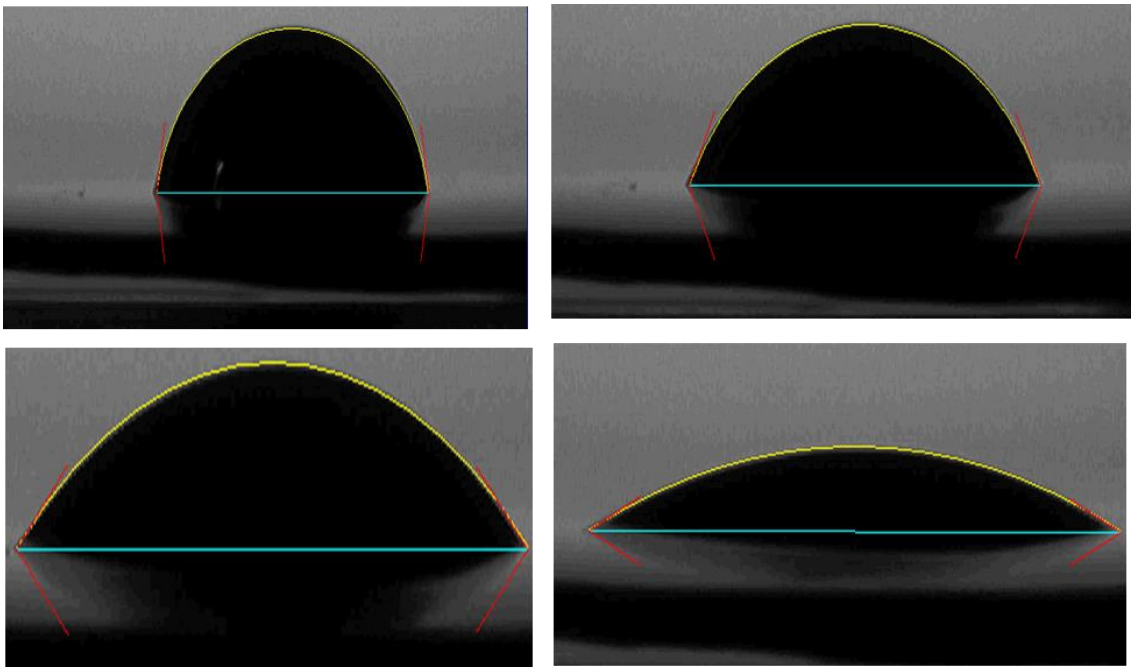

Fig. 2 - 24: Static contact angle using a sessile method - Contact angle < 90^0 (top right) and Contact angle > 90^0 (bottom right).

Great wettability is achieved at contact angle below 45^0 and therefore adhesive forces dominate over cohesive forces of liquid. Good wettability represented by contact angles between 45 – 90 ^{0} and therefore thee surface is known to be hydrophilic or "water loving". And finally, poor wettability is depicted as contact angle values between 90 – 180 ^{0}, and therefore cohesive forces of the liquid dominate over adhesive forces [85]. In such a case, the surface is known as hydrophobic or "water fearing".

At low static contact angle, the liquid droplets advance or spread on the substrate, depicting dominance of adhesive forces over cohesive forces. At a high contact angle, the droplet possesses retracting characters and thus depicting dominance of surface tension over surface energy of the substrate. Various researchers such as Bidwell and co-workers [101] conducted in-depth work on surface tension determination by a pendant drop method found that liquids with high surface tension show a more spherical droplet (retracting behaviour) in comparison to those with low surface tension.

The static contact angle is applicable under ideal conditions. However, in the roll coating process, the process is under dynamic conditions and their extra parameters or forces to consider during dynamic conditions

Several surface defects during coating are attributed to high surface tension and/ or surface tension gradient. Surface defects include fat edges, pinholes, PMD amongst

others. The surface tension of coating is highly dependent on the resin and surfactant concentration [102]; high concentration of surfactant reduces surface tension to a value that is below the surface energy of the substrate and hence obtaining a positive spreading coefficient.

The working principles of surfactants rely on the fact that they are micelles; they are aggregates of long molecules where one part of the molecule is soluble in the solvent and the other part is insoluble. This dual nature of surfactants enables molecules to concentrate on the surface of the coating. As a result, the soluble portion remains submerged in the coating whilst the part remains insoluble and in close contact with the air. The attempt of the aggregated molecules to line up causes a compressive force to act on the surface hence reducing surface tension.

Additionally, surfactants act as a dispersing agent in the coating formulation and subsequently prevent solids contained in a coating system from flocculating[103]. Weidner *et al* [102] caution that much care should be taken to avoid surfactant concentration gradients as this enhances the issues which were aimed to reduce in the first place.

2.5.1 SURFACE TENSION AND CONTACT ANGLE MEASURING TECHNIQUES FOR CHARACTERISING COATING

A plethora of commercial techniques for measuring surface tension have been employed; for example, Du Nouy ring, Wilhemy plate, oscillatory jet, the capillary rise, the falling curtain and the sessile or pendant drop techniques, to but mention but a few. The profile of a sessile (sitting) or a pendant (dropping) drop relies on the force balance between surface tension and gravity (weight). In static surface tension measurements, the pendant drop method uses an optical tensiometer to analyse the shape of the drop. The shape of the drop sitting or hanging from the needle attached to a syringe is determined using force balances; forces being surface tension and weight of the liquid. However, the Pendant drop technique generates faster than a sessile drop technique. None the less, the pendant and sessile method is still found to be more complex and tedious compared to the Whilhemy and Du Nouy ring method, despite their ability to obtain data faster and also work with high viscous fluids [104]. It is noteworthy to mention that a pendant drop predominantly employed to measure surface tension, while a sessile drop is employed to obtain contact angle measurements.

A prominent researcher, Thomas young [105], proposed that static angle of a liquid can be assumed as a drop sitting on a solid surface, and a mechanical equilibrium of the sitting liquid is maintained by three surface forces. The surface forces at the interface of solid and liquid, liquid and air, and air and solid. The mathematical and thermodynamic expression of Thomas young's relation in Eqn. (2 – 34) was further modified in to include reversible work of adhesion and ignores the contribution of surface tension and surface energy forces. The modified correlation known as the Young-Dupree correlation is presented in Eqn. (2 – 35)[51], [53].

$$\gamma_{\mathrm{Lv}} \cos\theta = \gamma_{\mathrm{SL}} - \gamma_{\mathrm{SV}} \qquad (2 - 34)$$

$$\gamma_{\mathrm{Lv}} (1 - \cos\theta) = \mathrm{WA} \qquad (2 - 35)$$

Where WA is the work of adhesion (J/m^2), γ_{SL} is the surface interface of liquid and solid (N/m), γ_{Lv} is the surface interface of liquid and vapour (N/m) and γ_{sv} is the surface interface of the solid and vapour (N/m).

2.6 COATING FORMULATIONS FOR APPLICATION IN COIL COATING PROCESS

Coatings employed in manufacturing of pre-coated steels are mainly for decorative and protective purposes of the substrate from the corrosive environment. However, there has been emerging industry for function coatings for various applications such as energy capturing coatings; self-cleaning coatings that mainly rely on nanoparticles, for instance, titanium dioxide containing coatings; fire resistance coatings; to mention but a few.

To achieve most of the intended purposes of coating, it is of great importance to understand that coating formulations are as important as the operating parameters employed during coating deposition onto the substrate. Coating formulations dictate the physical properties of the coatings and consequently affect the quality and functionality of the manufactured pre-coated steels. Coatings are formulated according to their intended purposes and are predominantly composed of pigments, binders, solvents, resins and additives.

There are two types of coatings; solvent and waterborne coatings. Waterborne coatings employ water is the main carrier driver of the coatings system. While solvent-borne coatings employ solvents such as N-Methyl-2-Pyrrolidone (NMP), Butyl Carbdol Acetate (BDA) and Petrosol to provide the flowability effect to the coating during processing. Waterborne coatings find their applications in coat porous materials, automotive, architectural sectors mainly because of their eco-friendly and low flammability properties. While solvent-borne coatings find their applications a vast number of products and industries, especially products that require extreme environments such as humid environments, agricultural cladding systems and many more. Fig. 2 – 25 show typical constituents of waterborne and solvent-borne base coating, respectively.

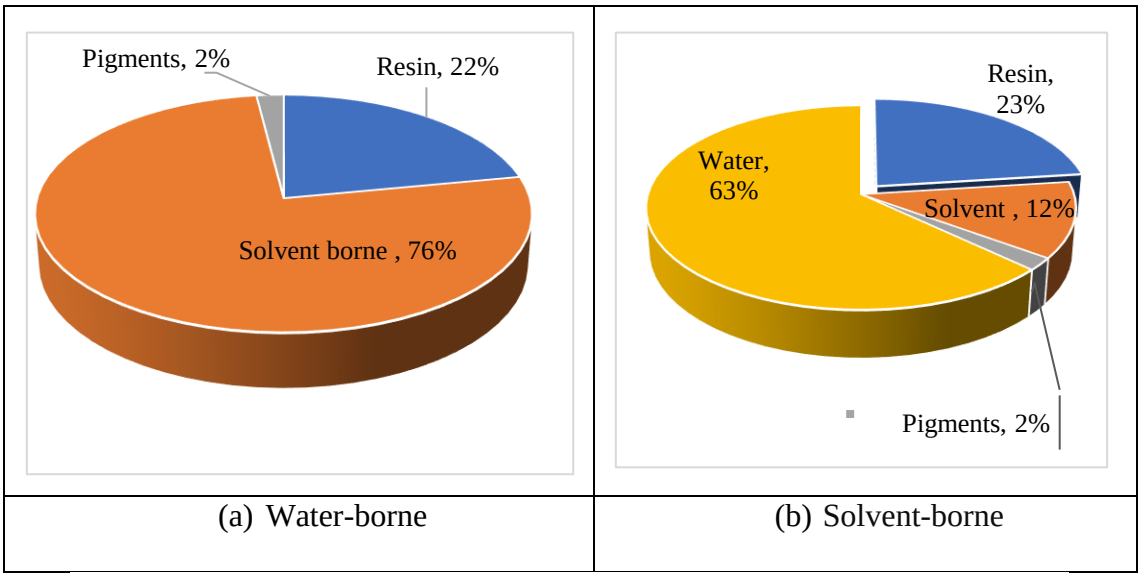

(a) Water-borne (b) Solvent-borne

Fig. 2 - 25: Constituents of a waterborne based coating (a) and Solvent based coatings (b)

Glass and Prud'homme [84] state that the main two components in any coating formulation are: binders that enhance the desired flow of coating during application and also provide mechanical integrity of the coated layer when transformed from a liquid into a solid-state; and the pigments that provide the aesthetic features and functionalities of coatings.

2.6.1. PIGMENTS

Pigments are one of the most important constituents of a coating that award great hiding power and chroma (colour intensity) to a coating. A higher the quantity of pigment in a coating not achieves colour strength but also rheologically modified. They are often organic pigments or mineral solids, and some pigments have photo-catalytic properties

and are therefore used in functional coatings to provide functional properties such as water purification and anti-corrosion properties. TiO_2 is one of the most commonly used pigments in coatings due to its great hiding power (white colour). A small quantity of this pigment provides great opacity. For example, in architectural coatings, 21% concentration of TiO_2 in latex is enough to yield optimal opacity. Due to the chromophore structure possessed by the TiO_2 pigments, a colour impression by absorption in the visible light spectrum is observed. Therefore, TiO_2 pigment is known to have a great refractive index. There exist alternatives to TiO_2 such as Feo, calcium, silica and or clay carbonate [84]. The inorganic pigments are reported to have a size range between 0.01 – 0.1 µm, and smaller than the organic pigment by 1 power of 10. However, small pigments require efficient dispersion for complete and even distribution into the coating formulation [106]

2.6.2. BINDERS OR RESINS

Binders also called resin to have a sole purpose of ensuring that coating constituents are homogeneously dispersed. Moreover, resins provide good adhesion of a coating to the substrate. The secondary purpose of resins includes the provision of high gloss level, toughness due to the polymeric structure, durability and flexibility. Resin is mainly made up of polymeric materials which enhance mechanical properties and toughness of the coating film upon curing. Goldschmidt and Steinberger [106] comment that binders are extenders and pigment-free components of the coating.

Polymeric resins are suitable for roll coating process; however, they must be amorphous with a low molecule weight (molecular weight ranging between 1,500 to 25,000 g/mol) [5]. Resins also enhance viscoelastic properties; at low shear rates coatings exhibits an increase in viscosity, and at high shear rates a shear-thinning behaviour is observed [104]. The shear-thinning behaviour is essential for ceasing flow ability once the coating has been applied on the substrate and therefore does not continue to flow.

Resins are categorised into four groups based on the drying or curing mechanism. These mechanisms include simple evaporation; single component catalysed/ cross-linked polymerization; two components catalysed/ cross-linked polymerisation and coalescence. Resins are further broken down into two types; natural or synthetic binders; with each type possessing different characteristics and applicability.

2.6.3 SOLVENTS

Solvents, also known as liquid carriers, are essential for coating fluidity. The liquid carriers used may be solvent or water-based hence the category names of coatings; a coating with a liquid carrier as water is known as a water-based coating, and the other with a liquid carrier as a solvent is known as a solvent-based coating [5].

The sole purpose of a liquid carrier is to bind together coating constituents, that is to say; pigments, binders and additives. Upon drying or curing, the solvent is evaporated leaving behind a dry film of coating on the substrate.

The choice of solvent is usually based on evaporation rates and flash temperatures. If the evaporation rate of the solvent is too high, the coating is likely to cure whilst the solvent has not completely evaporated from the wet film hence giving rise to a solvent pop or boil defect on the coating surface. Consequently, a good choice of solvent is essential for better control of evaporation rates.

2.6.4 ADDITIVES

Additives include rheological modifiers, UV stabilisers, amongst others. They enhance coating properties during and after coating deposition and drying/ curing process. Often a concentration of ~ 3% is added to bring about a drastic change in properties, such as coating fluidity, flexibility, colour intensity, amongst others [107]. The most commonly used additives are rheological modifiers, surfactants and plasticizers. Rheological modifiers improve the rheological or fluidity properties of coating to enhance the stability and operating window during roll coating. Plasticisers are often added to the formulation to improve the flexibility of the coating to enable the drying and curing process efficiency. The flexibility is achieved by separation of polymer chains and subsequently reducing the internal residual stress of coating. The internal residual stress is a function of the action of stress and stress relaxation process; therefore, it is essential to give sufficient relaxation time to the coating by drying the wet film of coating in mild operating temperatures and velocity of air.

And finally, surfactants are well known for reducing surface tension, hence improving the wettability and the spreading coefficient of the on the substrate. High surface tension and surface tension gradients may lead to defects such as pinholes and fat edges, therefore, surfactant addition can aid to combat defects mentioned therein. However, the

surfactant concentration gradient should be controlled as this may enhance the coating defects described above [108].

2.7. CONCLUSIONS

This chapter has highlighted various factors that can influence product quality during manufacturing of architectural steels, ranging from operating parameters such as line speeds, roller coating configurations, to mention but a few. While other researchers have mainly focused on operating parameters with regards to understanding the initiation of some of the defects encountered at the roller coating process, many have ignored the impact of the rheology, in particular the influence of slip phenomena, on the appearance of the final product and the processability of the liquid coating through various process units. Understanding the impact of slip during roller coating process would provide a greater understanding of material behaviour and subsequently eliminate some of the persistent defects encountered at the coating line. Therefore, this project's objective is to investigate the effects of material properties and operating parameters, and consequently devise a Quality Control test for in-ward goods at Tata steel colors, UK, based on the rheological understanding of liquid coating properties.

CHAPTER THREE:

ASSESSMENT OF THE "PAINT MISSES" DEFECT - PART 1: WETTING AND CHEMICAL CHARACTERISTICS

3.1. INTRODUCTION

"Paint misses" also known as PMD is a term used to describe a common defect encountered on the coating line at Shotton. This defect results in areas of the strip not being coated, exposing the underlying steel or base organic layer. This defect is known to be speed-related and it is believed that the defect originates from the coating trough following the operators' observation of a curtain break, near the coating trough, before the defect occurs. Operators' experience has identified that the defect can be eliminated by reducing the coating speed, but this has a direct subsequent reduction in the productivity and commercial profitability of the manufacturing process. The defect is reported to manifest itself apparently at random when machine controls and operating conditions are held constant. The origin of the defect has therefore been attributed to changes in the properties of the coating liquid material, as it often appears and disappears between nominally identical batches of material. In each instance, the batches of material pass the outward QC system at the paint supplier and the inward QC system at the Shotton plant.

As the liquid coating is a bespoke complex formulation, numerous chemical and physical properties can influence the manifestation of the defect on the final coated product. The strategy employed in identifying those key characteristics was to examine the process root causes to the issue and then to characterize the basic material properties of a batch of material which exhibited the defect and one that did not.

The aim of the study was three - fold;

1. To establish the cause of the defect such that possible remedies could be fed back to the paint formulators/manufacturers.
2. To investigate the underlying process physics relating to the flow of a complex fluid in shear and extension.
3. To develop a more robust QC system which could be used to more accurately determine batches of material which were liable to the defect.

Under ideal coating conditions, a continuous curtain is produced on the pick-up roll, as pictorially described in Fig. 3 – 1; however, the operators have identified that there is a breakup in this curtain is a sign that the defect is about to occur.

Fig. 3 - 1: The pick - up roll rotation in the coating trough with a coating curtain being formed when the process is operating

Three possible root causes of PMD and all were credited the physical properties of coatings, roll surface and substrate surface properties. The root causes are: -

(1). Failure of the liquid coating to wet chromated pickup roll surface and/ or substrate due to low surface energy of pick- up roll and/ or substrate.

(2). Low elongation viscosity and mechanical properties causing short critical breakup time of liquid coating film on chromated pick - up roll surface from the coating tray

(3). And finally, apparent wall slip (AWS) which promotes particles migration either from the bulk to the layer adjacent to the chromated pick - up roll wall (positive AWS/ wall slip), or particles migration from the bulk to the bottom surface of the coating trough (negative AWS/ wall stick).

The first outlined root cause; failure of coating to wet chromated pick - up roll surface and/ or primer coated substrate due to low surface energy of the surfaces or high surface tension of the liquid coating, was investigated by conducting contact angle measurements.

It is believed that enough wetting is the preliminary step in achieving coating adhesion to any surface. Otherwise true slip, as a result of poor wettability, takes effect thus leaving unpainted regions (PMD) on the roll surface and the substrate. Fig. 3.- 2 schematically shows the impact of good wetting (scenario 1) and poor wetting and hence true slip (scenario 2).

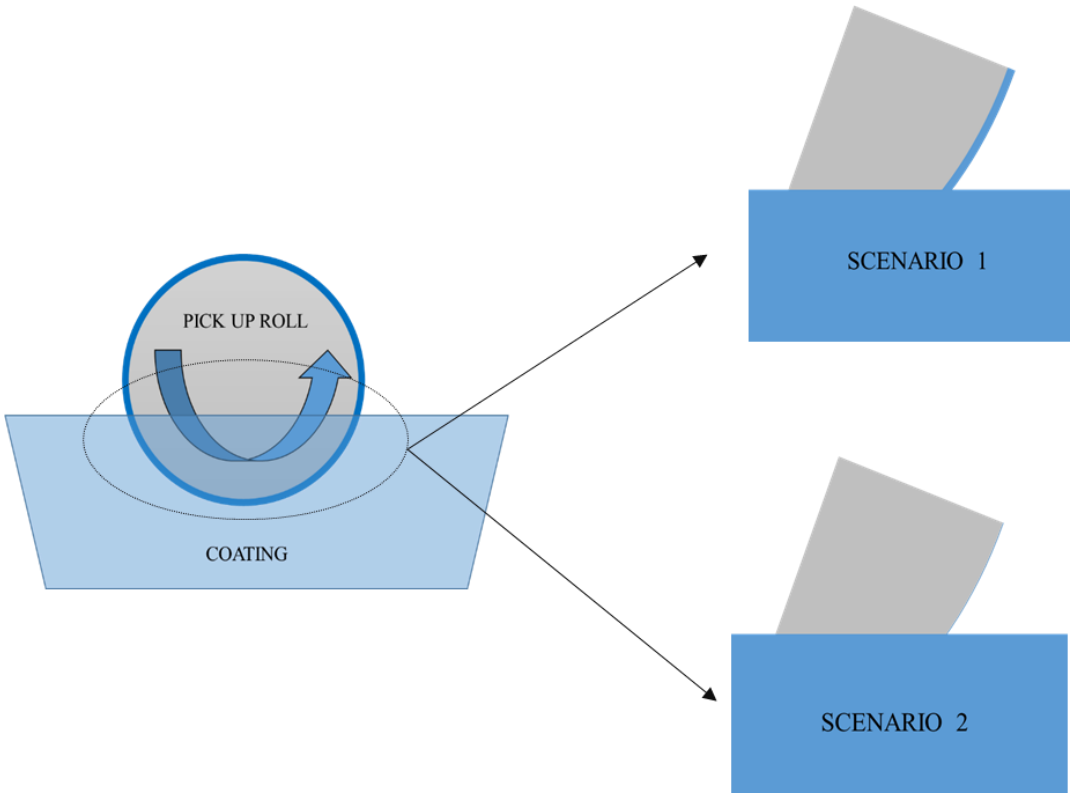

Fig. 3 - 2: Schematic of a pick - up roll rotating in the coating trough; a flow without true slip phenomena (scenario 1) and flow with true slip (Scenario 2).

Therefore, chapter three focuses on investigating the impact of wettability on the manifestation of PMD, through static and dynamic contact angle measurements on chromated pick - up roll surface and primer coated substrate. However, identifying differences in base chemical composition is the starting point to explain differences in wettability and consequently PMD. A range of chemical analysis techniques; from elemental analysis (EDX), and FT – IR studies, right through to thermal analysis was initially carried out.

3.2. MATERIALS AND METHODS

3.2.1. MATERIALS

3.2.1.1. COATINGS

Investigation of PMD was conducted on two commercial organic coatings which belonged to a family of PVC resin-based coatings, provided by AkzoNobel formerly known as BASF. The two coatings were dispatched in two different batches; however, they were believed to be the same in terms of formulation and therefore performance at the coating line. Under industrial conditions, the two coatings behaved differently, and this was manifested when line speeds and roll speeds were increased. Better coating denoted as Coating B, ran a defect-free performance at lines speed up to 90 m/ min, whereas Standard coating, denoted as Coating S, ran a defect-free performance at line speeds up to 70 m/min. Therefore, Coating B showed higher versatility than Coating S at the coating line.

3.2.1.2. METAL SURFACES

Investigation of wettability of coating was conducted on ECCS (electrochemically coated steel) surface to represent a chromated surface of the pick - up roll employed in the industry.

Investigation of wettability of coatings understudy on the substrate was conducted on a primer coated steel. There were two primer - coated steel substrates employed, ZA255 Polyurethane (PU) and ZA255 Acrylic - chromate-free primer, with dry film thickness (DFT) of primer of 5-8 µm. Primer - coated steel surfaces for this work were supplied by Tata Steel research centre, Warwick University.

3.2.2. METHODS

3.2.2.1. FOURIER TRANSFORM INFRARED (FT– R) SPECTROSCOPY

FT-IR analysis of PVC- resin-based coating was conducted using PerkinElmer FT-IR two-UATR apparatus, schematically shown in Fig. 3 – 3 below, provided by SPECIFIC laboratory at Swansea University.

Prior to each scan, the PerkinElmer apparatus (near the crystal Diamond) was thoroughly cleaned using Isopropanol. All experiments were conducted under ambient conditions.

Sample scans were run from 4000 – 515 cm^{-1}, with a resolution of 4 cm^{-1} and 4 accumulations per second. The experiment for each liquid coating was repeated three times.

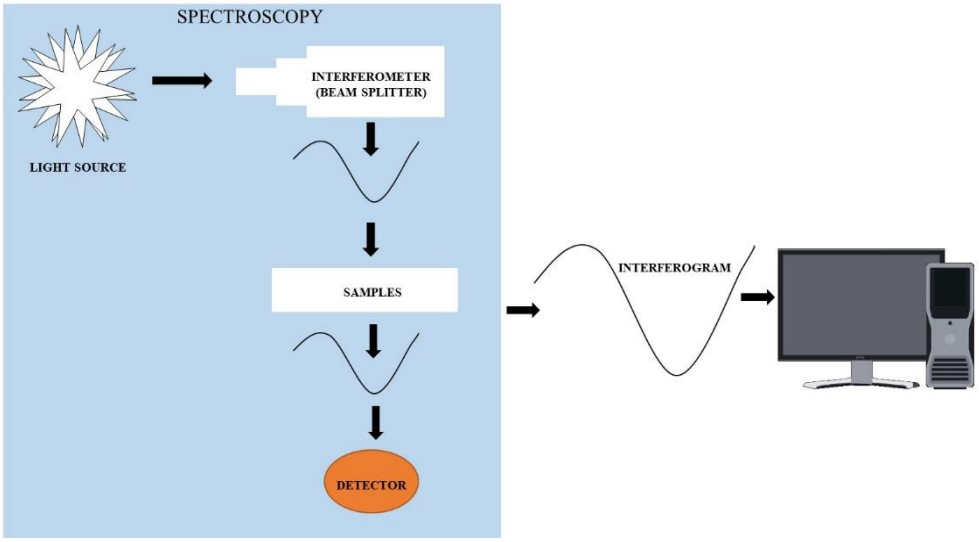

Fig. 3 - 3: PerkinElmer FT-IR two - UATR (serial number of 47443)

3.2.2.3. MICROSTRUCTURAL ANALYSIS

Microstructural analysis was conducted on cured coating films, to identify differences in particle size, shape and distribution between Coating B and S. The experiment was conducted using Zeiss SEM EVO LS25 with specifications of 3.49 nm resolution at 30 kV, < 7X to 1000000 X magnification, 0.2 to 30 kV accelerating voltage and pressure range of 10 to 3000 Pa, and provide by AIMS laboratory facility at Swansea University. In addition, microstructural analysis with the aim of studying and comparing quantities in elemental compositions of Coating B and S was conducted using Energy dispersive X-ray (EDX).

a. Sample preparation

Acrylic Primer coated substrate was blade coated with a PVC – resin-based topcoat (Coating B or Coating S). At the coating line, a deposition of ~ 200 µm of PVC topcoat wet film thickness is deposited on a primer coated substrate. In order to achieve, the same wet film thickness under laboratory settings, a 50 µm Plastic paper x 4 was used to estimate a 200 µm gap size between the substrate and the coating blade, and subsequently ensuring the deposition of a 200 µm wet film thickness.

The coated samples were subsequently cured in the Mathis oven, at 210 ^{0}C under a minimum exhaust airflow of 138 m^3 /h. It is worth noting that before material curing; the oven was left to heat up from room temperature to 210 ^{0}C for 10 minutes. The samples were let to cure for 60 seconds in the oven. Upon cooling, the samples were cut into 1 x 1cm dimensions followed by sample grinding on 500 and 200 grit under constant water supply, and surface polishing using a micron layer cloth and water-based diamond solution of 2 and 5µm.

Fig. 3 – 4 illustrates a blade coater (on the left) and a cured deposited topcoat (on the right).

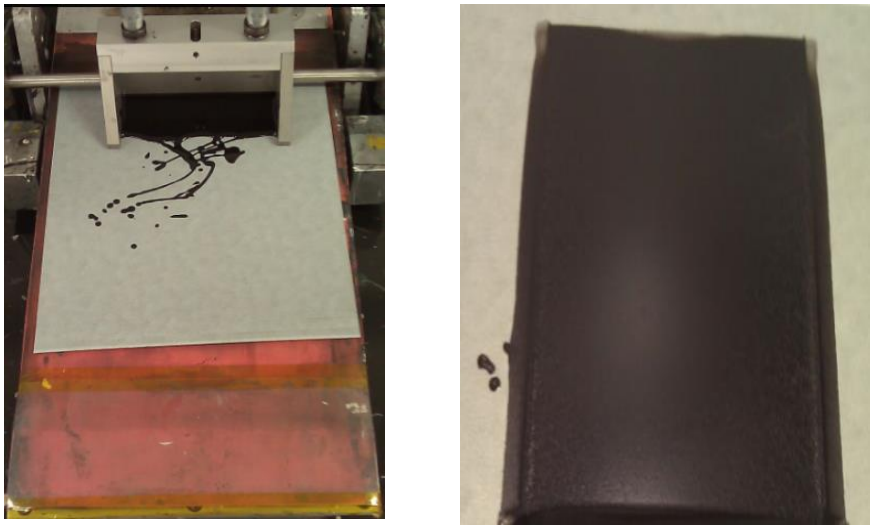

Fig. 3 - 4: Blade coating of PVC topcoat on acrylic primer-coated steel sample (on the left) and cured coating film (on the right).

Polished samples were sputter-coated by 15 nm layer thickness of Platinum due to the non-oxidising properties of the coating, using a rotary pump sputter coater (Q150T Quorum), ready for SEM and EDX analysis.

b. SEM and EDX analysis

SEM and EDX studies were conducted on the cross-section of the 1 X 1 cm coated steel sample. SEM studies were conducted under 1µm resolution, 9 mm working distance and 8.20 – 8.40 K magnification, 15 kV accelerating voltage and 40 PA.

EDX was conducted in the electron backscattering mode, and the analysis work was conducted under 20 kV accelerating voltage, energy range of 20 keV, working distance of 10 mm, and 2048 image scanning size and 5 seconds process time. The contribution of

Platinum to elemental composition analysis was ignored and thus subtracted away from the result.

3.2.2.4. THERMAL ANALYSIS

Organic coatings are multiphase systems; therefore, composition analysis via thermo-gravimetric and Differential thermal gravimetric analysis (TGA- DTG) method was employed. Fig. 3 - 5 shows a PerkinElmer Pyris 1 TGA equipment employed in this study.

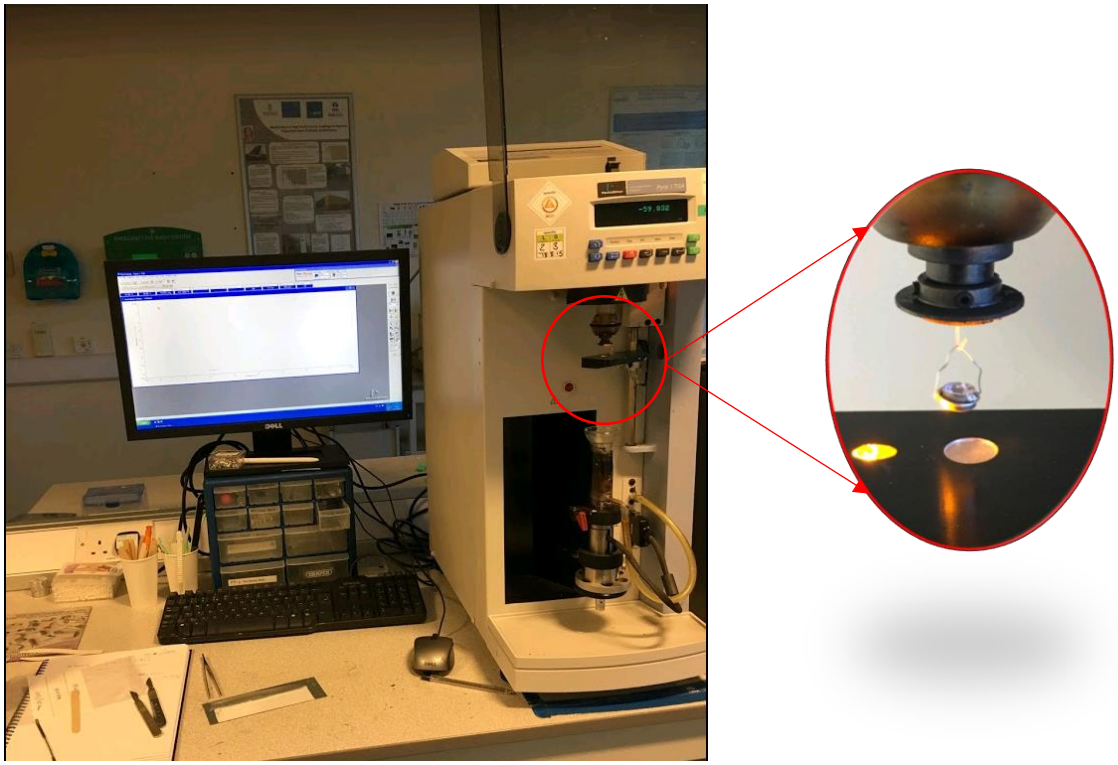

Fig. 3 - 5: PerkinElmer Thermogravimetric analyser (TGA - Pyris1)

Prior to heating scans, the furnace was thermally cleaned under isothermal conditions at 700 ^{0}C and 10 minutes. All heating scans were conducted under a nitrogen gas blanket, provided at a rate of 20 ml/min to avoid any oxidative reactions. A wet coating sample, with an initial weight of ~ 2 mg, was placed in a platinum pan and thermally heated from 28 - 600 ^{0}C at a heating rate of 2 ^{0}C/min.

The heating scans were repeated three times for both coatings, and a standard deviation of 2% was determined.

3.2.2.5. DENSITY MEASUREMENTS

Density measurements are a vital tool in determining the quantity of matter in a unit volume. Density measurements were conducted using a laboratory (analytical) weight scale with an accuracy of $\pm$0.001 mg and, a constant volume pipette (10 ml Syringe) with an accuracy of $\pm$0.01 ml, at room temperature of 21 ^{0}C. An empty 10 ml syringe was initially weighed. The syringe was then filled with 10 ml volume of a sample and weighed again. The normalised mass difference between an empty and filled syringe was calculated and employed as the density of the coating. The experiment was repeated three times for each coating.

3.2.2.6. SURFACE TENSION MEASUREMENTS

The defect under investigation, PMD, was believed to have originated from poor wettability of coating on the Pick-up roll and/ or the Primer-coated steel because the preliminary step prior to paint adhesion is good wettability. It is therefore of pinnacle importance to understand the effect of surface tension on the wettability of coating on chromated surface of the pick-up roll and Primer coated steel. Surface tension measurements using a pendant drop method was carried out using an optical tensiometer as shown in fig. 3. - 6. A high-speed camera was employed to capture a series pendant drop.

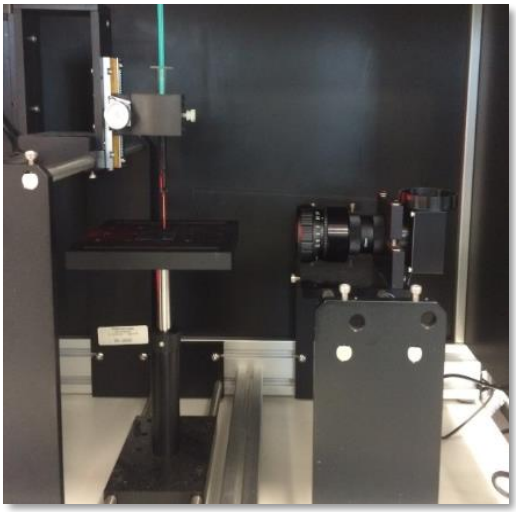

Fig. 3 - 6: FTA 32 Optical tensiometer

FTA 32 software was employed for data analysis; to determine surface tension from the captured images. Experiments were conducted at constant temperatures of 21 ^{0}C, using a ml syringe and 1.4 mm needle diameter.

Surface tension and contact angle measurements were conducted by dropping a 25 – 50 µl coating sample through the needle. A series of images were obtained using a high-speed camera were taken to monitor the change in the drop shape with time. FTA 32 software was employed to calculate surface tension and contact angle measurements from the captured series of images. It is worth noting that the software provides surface tension values at a specific gravity of 1. Therefore, prior knowledge of coating density was important to determine the specific gravity of coatings which was subsequently employed to determine the actual surface tension of coatings. Each experiment was repeated five times.

3.2.2.7. CONTACT ANGLE (WETTABILITY) MEASUREMENTS

a. Sample preparation of ECCS

Wettability of coating on ECCS was studied on two surfaces: a clean/dry ECCS surface and ECCS with a layer of coating (pre-wetted surface).

Under industrial conditions, a dead time of ~ 3 minutes, prior to coating deposition onto the substrate, was considered to pre-wet relevant units in the roll coating process. The pre-wetting process was therefore considered in the experimental work by assuming that a certain degree of coating on the pickup roll was expected. Therefore, wettability on both dry and pre-wetted ECCS was investigated.

ECCS was purchased with ~ 5 nm organic layer of Dioctyl Sebacate (DOS) and therefore required thorough cleaning. DOS oil was removed with fairy washing up liquid, water and a toothbrush as seen in fig. 3 – 7. Further cleaning was conducted with acetone to ensure that dirt and DOS oil have been cleaned.

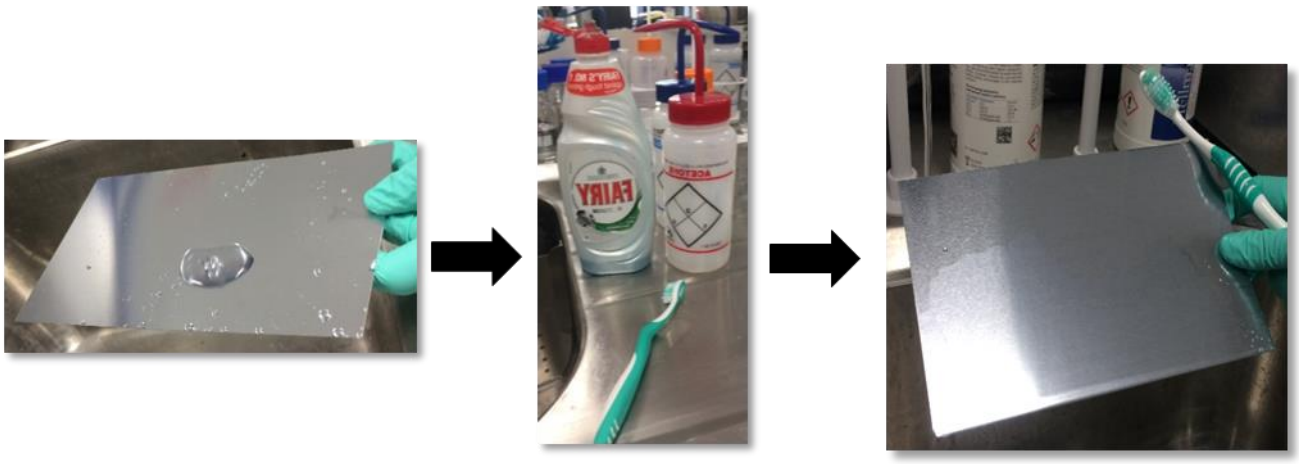

Fig. 3 - 7: Surface preparation for wettability study on ECCS.

A pre-wetted surface was prepared by dropping a 25 – 50 µl of coating sample and let to spread for 2 – 4 minutes to create a layer of coating for further investigation.

b. Primer-coated steel

Investigation of wettability via contact angle measurements was conducted on two primer - coated steel substrates, ZA255 Polyurethane (PU) and ZA255 Acrylic - chromate-free primer coated substrate, because the two primers coated substrates are the major substrate employed in the manufacturing of the PVC plastisol products for architectural use. Steel substrates contained a 2 µm zinc layer and a 5 - 8 µm dry film thickness of primer-coating. Primer - coated steel surfaces were supplied by Tata Steel research centre at Warwick University.

3.2.2.8. CONTACT ANGLE MEASUREMENTS USING A SESSILE METHOD.

Contact angle measurements were conducted using a sessile method. Fig. 3 - 8 shows a sessile drop for contact angle measurements. At the coating line, rolls and a substrate are in constant dynamic mode; therefore, to replicate this process a dynamic contact angle was obtained by capturing a series of images (video) showing the change of contact with time due to the spread-ability of a drop on a surface.

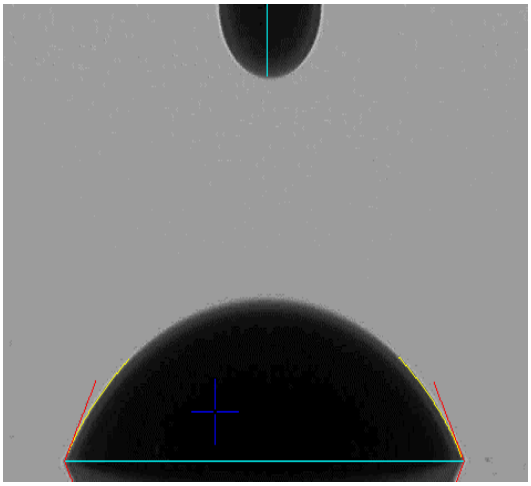

Fig. 3 - 8*:* A sessile drop method for contact angle measurements

To investigate dynamic contact angle on the pickup roll, information of roll speed - 70 m/min and 90 m/min - employed on the coating line, and roll diameter- 256 mm, was acquired from process technologists at Tata steel colors in Shotton. This information was

utilised to calculate the travel time of coating for 180 ^{0} (π rads) from the point of impact to the middle of the nip gap. Fig. 3 - 9 shows a schematic of roll coating process illustrating the journey taken by a drop of coating from the point of impact, A, to the midpoint of the nip – gap, B. A drop of coating would take 0.27 and 0.34 seconds at the pickup roll speeds of 90 m/min and 70 m/min, respectively, to travel from point A to point B on the pick roll diameter of 256 mm. A comparison of wettability of coating B and coating S deposited on dry and clean ECSS and, pre-wetted ECCS was conducted by obtaining contact angle values at the times obtained above.

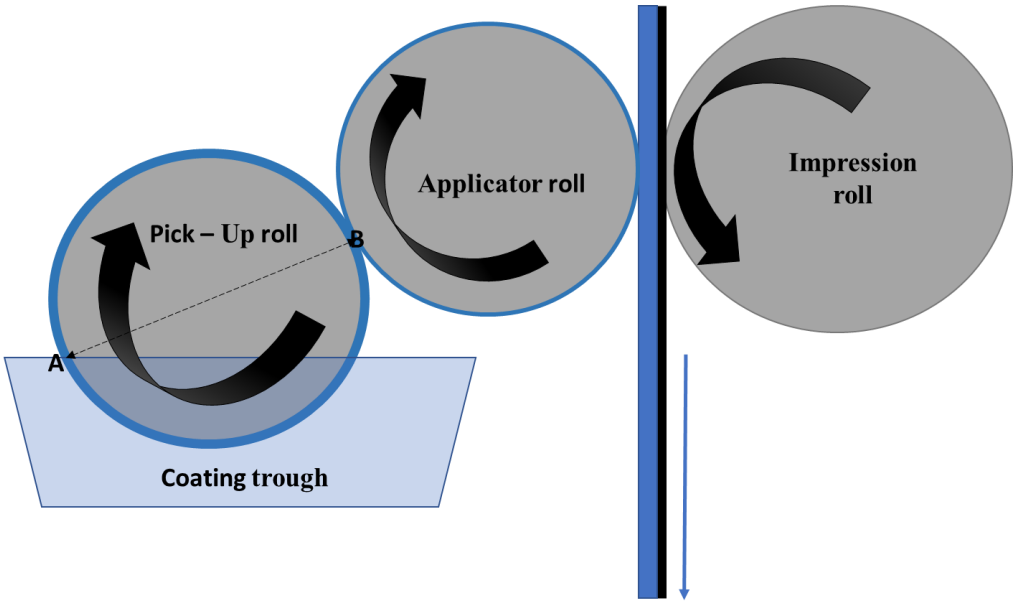

Fig. 3 - 9*:* Schematic of a reverse roll coating process showing the distance of travel of coating droplet from the point of impact, A, to the destination, B.

3.3. RESULTS

3.3.1. FOURIER TRANSFORM INFRARED SPECTROSCOPY (FT-IR) ANALYSIS

A comparison of absorbance spectra due to bond vibrations, conducted within the wavenumber range of 515 – 4000 cm^{-1} is presented in fig. 3 - 10. The presence of PVC resin was identified from symmetrical and non-symmetrical stretching of an alkane (C - H) at ~2926 cm^{-1} and 2852 cm^{-1}, respectively, CH_2 group deformation at ~ 1340 cm^{-1}, out of plane angular deformation of (ρCH) ~1250 cm^{-1}; out of phase trans deformation of (C - H) at ~960 cm^{-1}, and a stretch of (C - CL) at a wavenumber of 609 cm^{-1}. These findings correspond to those in literature by various researchers such as Balakit *et al*

[109], Beltrán and Marcilla [110] and Altenhofen da Silva *et al* [111], for PVC containing materials.

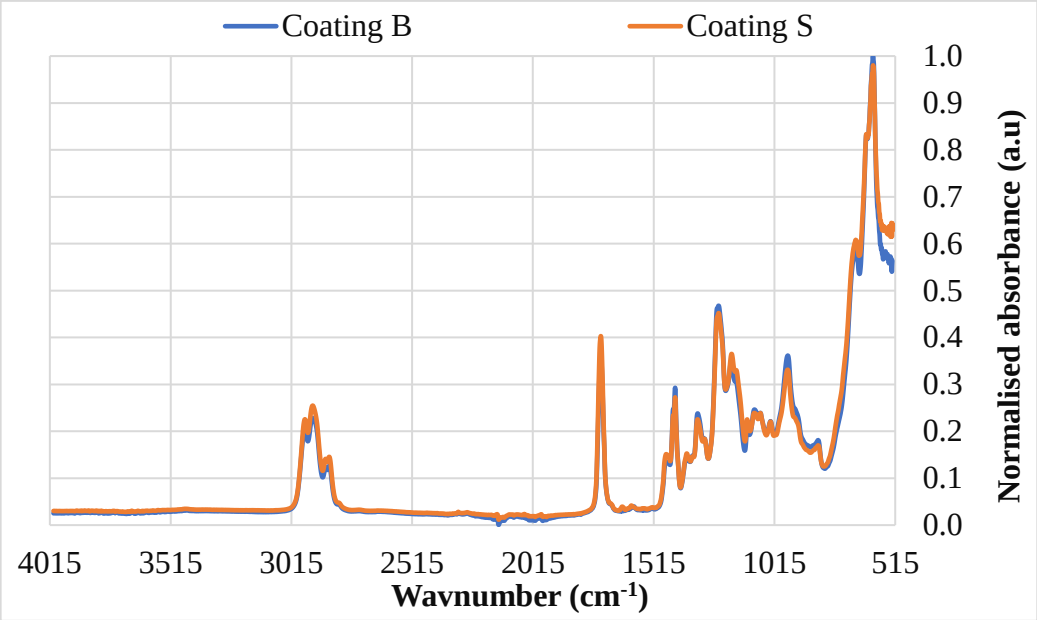

Fig. 3 - 10: FT - IR analysis of Coating B and Coating S, peaks normalised based on the C – CL vibrational bonds.

Additional peaks were observed in both coatings; a strong peak at ~1731 cm^{-1} attributed to the stretching of the carbonyl group (C = O) due to the presence of the alphatic ester; and finally a ~1423 cm^{-1} peak credited to a bending (O - H). These extra peaks were attributed to the presence of a plasticiser. Again, these findings were in line with Altenhofen da Silva *et al* [111] results, where the authors compared FT-IR spectral peaks of Pure PVC and plasticised PVC films in their work titled: The Polyvinylchloride (PVC) and natural rubber films plasticized with a natural polymeric plasticizer obtained through polyesterification of rice fatty acids.

Furthermore, the strong peaks observed at wavenumbers of 956, 1247 and 1427 cm^{-1} were ascribed to an asymmetric stretching of (B – O), and these results were also parallel to Babeela, Sabari Girisun and Vinitha's [112]work. The stretching of (B – O) bonds was credited to the presence of Barium diboron tetraoxides. And finally, C - CL intensities (absorption values) were the highest for both coating samples, depicting a higher abundance of C - CL than any other vibrational bonds in coatings.

FT-IR analysis showed a complete overlap of major absorbance peaks of Coating B and Coating S depicting that the polymer backbone and other organic components were the same in both coatings. The intensity of the major peaks was also observed to be the same,

depicting that the population of vibrational bonds was also similar. Therefore, the difference in the performance of the two batches was not credited to the difference in the organic composition of liquid coatings.

3.3.2. MICROSTRUCTURAL ANALYSIS AND EDX

FT–IR studies did not identify differences in vibrational bonds, and therefore did not give any insight into the difference between organic constituents between Coating B and Coating S. Thus, microstructural analysis and EDX studies were conducted on Coating B and Coating S to further understand the difference between inorganic constituents and microstructure.

Fig. 3 - 11 and 3 – 12 show the elemental composition of coating B and Coating S, respectively, obtained under backscattering mode. Microstructural and elemental analysis on a three-layered coated steel sample containing magiZinc, primer coating and top coating of Plasticeram Black was conducted to investigate the differences in the inorganic composition of coatings that could have impacted the performance of the liquid coatings under study.

It is worth noting that more than one spectrum on the specimen (top coating) - randomly picked, showed the same elements but different elemental weight values. It was, therefore, misleading to quantitatively compare Coating B and Coating S based on the elemental weight. Nevertheless, a comparison based on the qualitative study was employed for comparison purposes.

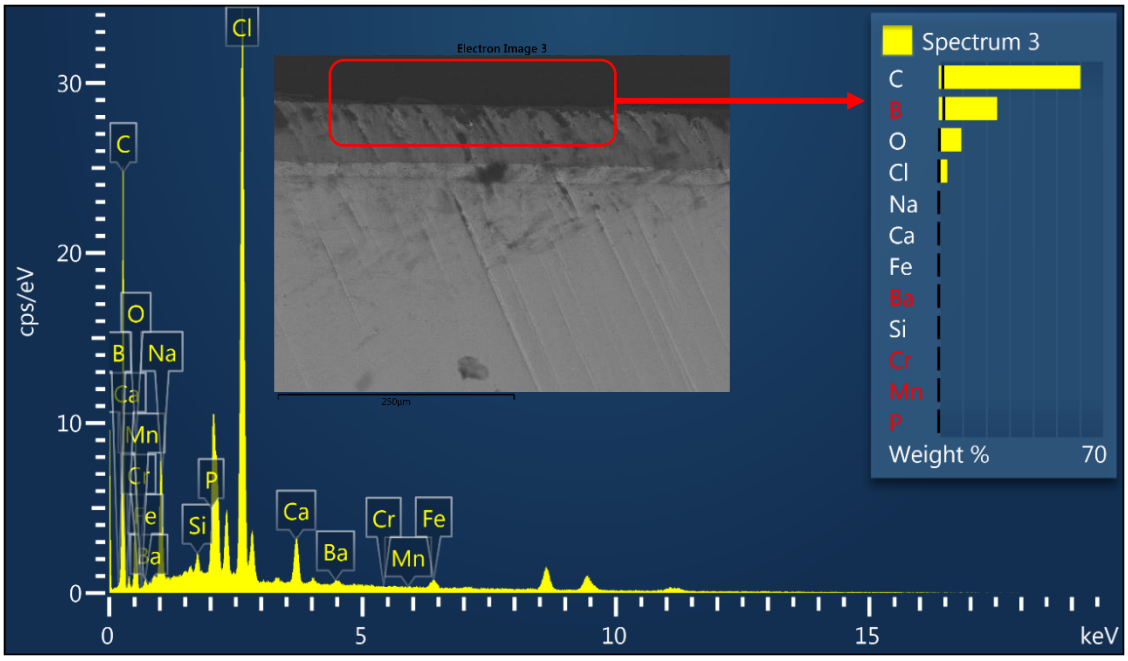

Fig. 3 - 11: Elemental EDX microanalysis of coated steel with Coating B as the topcoat.

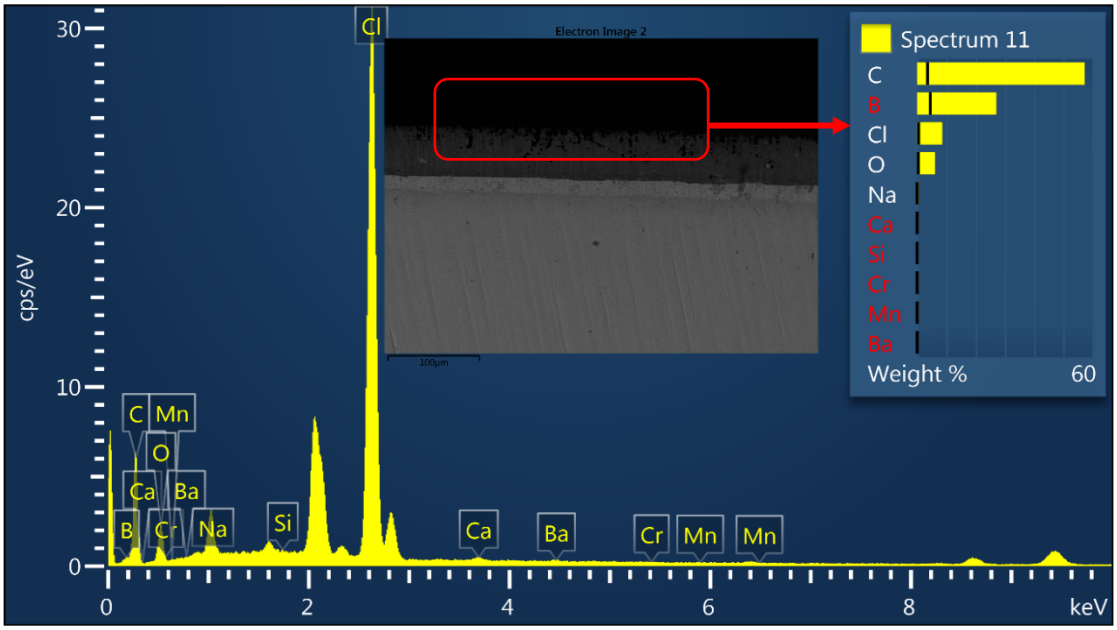

Fig. 3 - 12: Elemental EDX microanalysis of coated steel with Coating S as the topcoat.

EDX microanalysis of both coatings showed the same elements, with carbon (denoted as C) being the dominant element. Carbon was likely to have come from all constituents of the Coatings; from PVC resin to BDA/Petrosal solvent mixture and right through to carbon black pigment and other carbonaceous additives.

The presence of chlorine (denoted as Cl) in Coating B and Coating S was traced back to PVC resin. However, ~ 50% more carbon than chlorine in both coatings because carbon

was present in most of the individual constituents of the coatings, while chlorine was only traced back to PVC resin.

And finally, Boron (denoted as B) was the second-highest element observed in the elemental intensity graph, with ~25% in both coatings. The presence of Boron was credited to Barium diboron tetraoxide compound as stated in the formulator's MSDS. Barium diboron tetraoxide as an additive in coatings that is a strong thermal/ Stabiliser/ UV stabiliser and a rheological modifier. Negligible traces of Barium was detected in the elemental analysis results which are likely to suggest that small quantity of Barium in comparison to Boron. PVC is prone to low thermal stability, photodegradation, photooxidation, by attacking C – CL bond to form radicals. The mechanism of photodegradation and oxidation is reviewed in Yousif and Hassan's [109], [113]work. Therefore, Barium diboron tetraoxide acts as a stabiliser for a PVC system.

It proved a challenge to obtain information about particle size, size distribution and shape; therefore, a comparison based on microstructure analysis between coatings was not conducted. This was credited to the size of pigment particles employed in the coatings.

Based on EDX analysis and visual inspection of both coatings, it was believed that the pigments employed were carbon black. The typical size range of carbon black pigments is estimated between 50 – 80 nm as reported by Khankaew and Komasatitaya [114], and therefore too small to show in the micrographs using the Zeiss SEM EVO LS25 model.

3.3.3. THERMAL ANALYSIS (TGA - DTG) ANALYSIS

Complex fluids such as coatings consist of various constituents such as solvents (for solvent-borne coatings), fillers, dryers, pigments, polymers, amongst others. Fig. 3 - 13 shows a composition analysis of Coating B and S using the TGA - DTG tool. There were three degradation stages observed from the TGA - DTG curves for both coatings. The first stage was attributed to solvent mass loss, with Coating S exhibiting a higher percentage mass of solvent than its counterpart. The gradual change, as opposed to a fast decrease in the first mass loss stage, was attributed to the solvent blend and this was confirmed by the MSDS provided by the coating formulators. The solvent blend of BDA (Butyl Carbdol Acetate) and Petrosol were employed in this formulation.

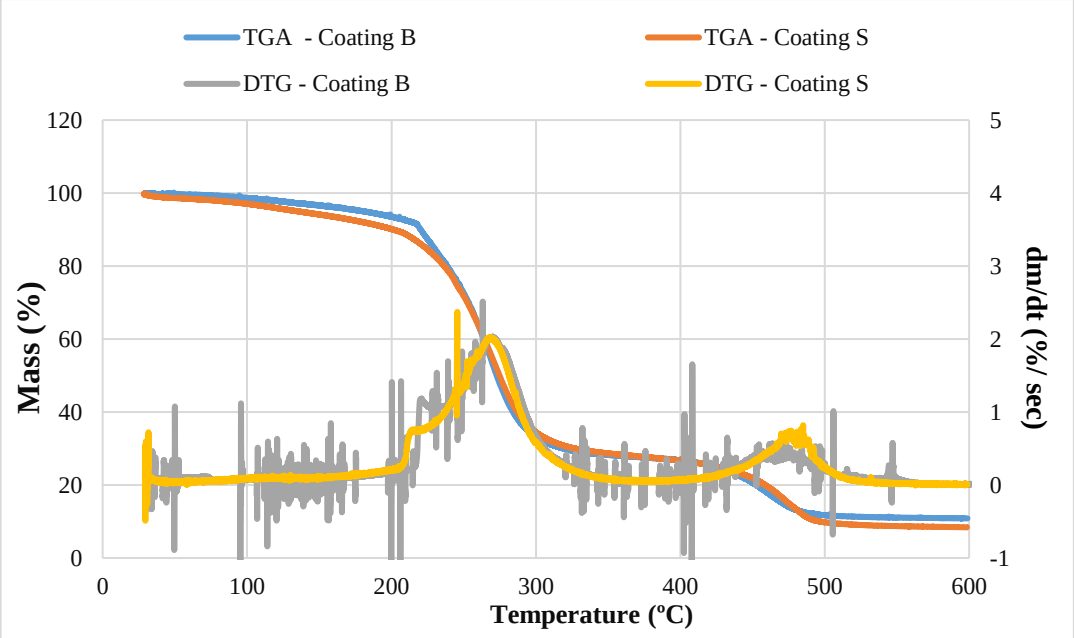

Fig. 3 - 13: Comparison of thermal degradation (primary axis) and rate of degradation (secondary axis) as a function of temperature for Coating B and Coating S

The second mass loss stage was attributed to the development of the polymer matrix and further scissoring of chlorine atoms from the PVC polymer back - borne. The main reaction was the dehydrochlorination of the polymer to form a de – HCL PVC (intermediates), which was further broken down into Polyene chain, and these findings are parallel to Yu *et al*[115] and Castro *et al* [116] work. Starnes Jr [117] analyses that the release of HCl acts as a catalyst in further decomposition of the PVC backbone, thus creating an autocatalytic process. However, the number of additives such as thermal stabilisers, fillers, pigments to mention but a few, hinder the autocatalytic process.

And finally, the third mass loss stage was credited to cracking and decomposition of polyene chains to form volatile components such as benzene and toluene, and other carbonaceous materials, leaving behind a final residual mass. The final residual mass was thus believed to contain char, pigments and fillers. The composition of final residual mass can only be obtained through the oxidative process (burning in the air) which was out of the scope of this research work, and therefore not pursued. A quantitative summary of composition analysis and degradation rates as a function of temperature are presented in Table 3 - 1 and Table 3 - 2, respectively.

Initial degradation temperature (IDT) for Coating B was higher than Coating S, depicting that Coating B has higher thermal stability than its counterpart. This was credited to the solvent blend where Coating B was likely to have a higher quantity of BDA with the

closed cup flash point of over116 ^{0}C or higher, than Petrosol with closed cup flash point of 90 ^{0}C or over.

Table 3 - 1: Summary of thermal degradation stages

Mass loss stages	**Coating s**		**Coating B**	
	Temperature range (^{0}C)	Mass (%)	Temperature range (^{0}C)	Mass (%)
Solvent (First Peak)	28 - 212	~ 11	28 – 220	~ 9
(De - chlorination) Second peak	212 - 300	~ 60	221 – 300	~ 64
Decomposition of Polyene (Third Peak)	400 - 473	~ 20	400 - 464	~ 16
Final residual Mass (contains char, Pigment and fillers)	~ 496	~ 9	~ 495	~ 11

Table 3 - 2: Summary of thermal properties from TGA- DTG curves

	Coating S	**Coating B**
Initial decomposition Temperature (IDT)	~ 28 ^{0}C	~ 50 ^{0}C
Maximum rate of decomposition temperature (MRDT)	~ 267 ^{0}C	~ 267 ^{0}C
$\boldsymbol{D_{1/2}}$ **(50% mass decomposition) temperature**	~ 276 ^{0}C	~ 276 ^{0}C

The maximum rate of decomposition (MRDT) was observed in the dehydrochlorination mass loss stage (stage two) for both coatings, inferring C- CL group has the highest composition in the binder and solvent mixture. MRDT was observed to be the same depicting that both coatings have the same binder content. This was verified with the TGA results, where the second mass loss stage for both coatings overlapped.

The third mass loss stage (polyene chains) showed a negligible difference in composition, and MRDT peak in DTG curves was the same for both coatings, confirming that the binder content and polymer backbone was the same for both coatings. The final residual mass attributed to solids content such as pigment and fillers showed almost the same quantity.

TGA-DTG analysis curves have provided a ground of comparison of Plasticeram black coatings. There were subtle differences in the composition of coatings; for example,

Coating B showed ~ 2% more final residual mass (solids) content than Coating S; however, Coating S showed ~ 2% more solvent content than Coating B. The differences in composition were negligible and therefore attributed to the experimental error tolerance. Experimental errors might have risen during sample loading - differences in the initial mass of the test liquid coating. Additionally, the TGA equipment is very sensitive to subtle movements and vibrations; therefore, any movement in the room could cause erroneous readings. This could also have contributed to the experimental errors.

The formulators of the coatings under study claimed that the difference in thermal stability was due to the high quantity of Barium diboron tetroxides which is also believed to be a UV/ thermal stabiliser and a rheological modifier. However, the FT – IR analysis results showed the same quantity of B - O bond intensities, depicting almost the same quantity of Barium diboron tetraoxides. This also further cemented findings from the composition analysis.

3.3.4. DENSITY AND SURFACE TENSION MEASUREMENTS

Surface tension describes the interaction between surface molecules of the liquid coatings. High surface tension depicts strong bonds holding surface molecules together and therefore requires high surface energy to overcome the strong surface bonds. Density describes the quantity of matter in a unit volume. Table 3 – 3 show surface and density values for Coating B and Coating S.

Table 3 - 3: Density and Surface tension measurement for Coating B and Coating S

	Density [kg/m^3]	**Surface tension [mN/m]**
Coating B	1294± 0.2	35± 0.6
Coating S	1193± 0.2	27±0.6

A ~ 8% difference in density values between Coating B and Coating S was seen, depicting a higher quantity of matter in a unit volume for Coating B than its counterpart. Higher solids content is often credited to various factors, among which include; surfactant concentration, type of surfactant, the concentration of the solvent, solvent, amongst others. However, the negligible difference in solids content and absorbance intensities were seen in TGA and FT - IR studies. Surface tension for Coating B was ~ 15 % higher than Coating S.

3.3.5. COATING WETTABILITY ON THE PICKUP ROLL

In order to achieve good/ superb wetting, the surface energy of the surface should be high enough to overcome the surface tension of a coating and this is represented in contact angle values. It was seen in fig. 3 – 14 that both Coating B and Coating S exhibited contact angle dependence on time on both pre-wetted and dry ECCS surfaces. However, Coating S showed a stronger contact angle dependence on time than Coating B. It was therefore deduced that at different time readings, and thus line/pick up roll speeds, different contact angle values can be obtained. Therefore, a comparison of wettability of both coatings on pre-wetted and dry ECCS surfaces was carried at the different pick – up roll speeds.

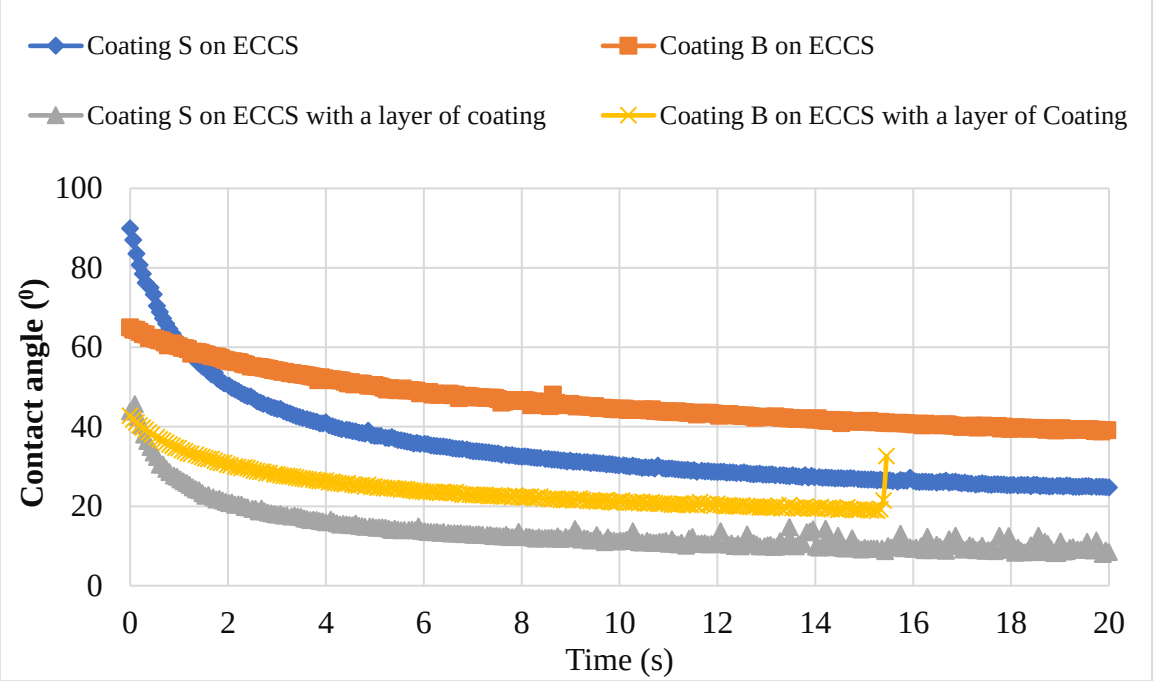

Fig. 3 - 14*:* Dynamic contact angle of coatings on different surfaces

Fig. 3 - 15 and 3 - 16, respectively, show contact angles of coating on dry ECCS and pre-wetted ECCS obtained from the dynamic contact angle measurements. On both dry and pre-wetted ECCS, contact angles for both coatings did not change greatly as a function of time depicting that pick - up roll speeds understudy had a negligible impact on the wettability of coating on the pick - up roll surface.

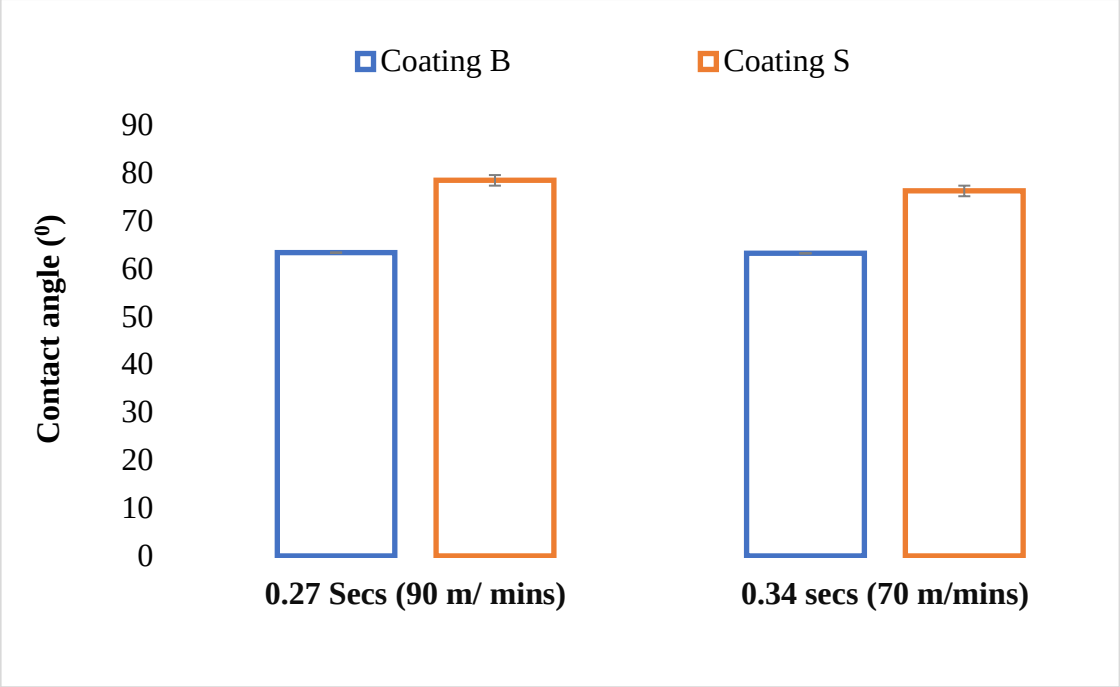

Fig. 3 - 15: Contact angle measurements of Coating S and Coating B on dry ECCS at pick - up roll speeds of 90 and 70 m/min.

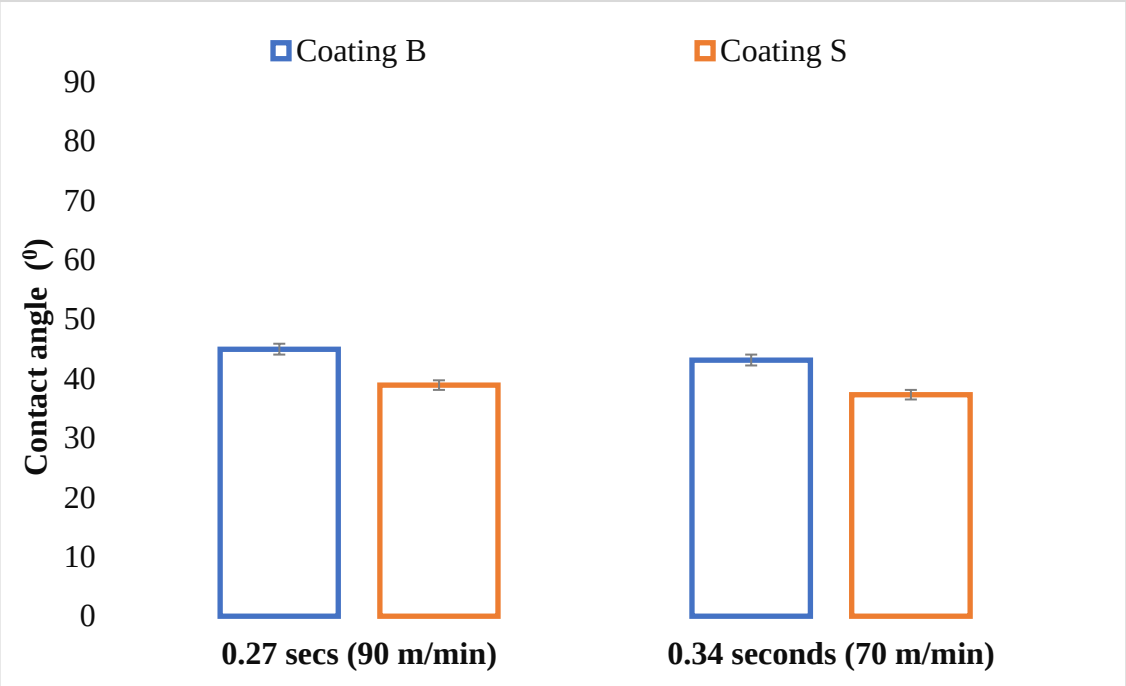

Fig. 3 - 16: Contact angle of Coating S and Coating B on pre-wetted ECCS surface at pickup roll speed of 90 and 70 m/min.

However, it was noticed that pre-wetted ECCS wetted better than dry ECCS surface for both coatings, due to the lower contact angle values, signifying that the downtime of ~ 3 minutes employed on the coating line significantly improves the wettability of coating on the pick-up roll. A reduction in contact angle by ~ 45 % was noticed, and this was credited

to the stronger effect of cohesive forces between coating layers than adhesive forces between dry ECCS and the deposited coatings.

On dry ECCS, Coating S showed ~ 19% higher contact angle values than Coating B at both pick - up roll speeds, depicting that coating B wets better than its counterpart, Coating S. On pre-wetted ECCS, Coating S exhibited ~ 13% lower contact angle than Coating B inferring better wettability for Coating S than Coating B when downtime of 3 minutes is employed.

3.3.6. COATING WETTABILITY ON A PRIMER COATED SURFACE

Having established that Coating S wets better than Coating B on a pre-wetted pick – up roll, it was deduced that PMD was not credited to poor wettability on the pick - up roll. Therefore, further investigation into wettability on primer - coated steel was carried out because the defect was likely to have been caused by poor wettability on the substrate. Fig. 3 - 16 shows dynamic contact angle of Coating B and Coating S on Polyurethane (PU) and Acrylic Primer-coated steel surface. It was seen that Coating S had a lower contact angle than coating B on both substrates. This further cemented that Coating S wets better than Coating B.

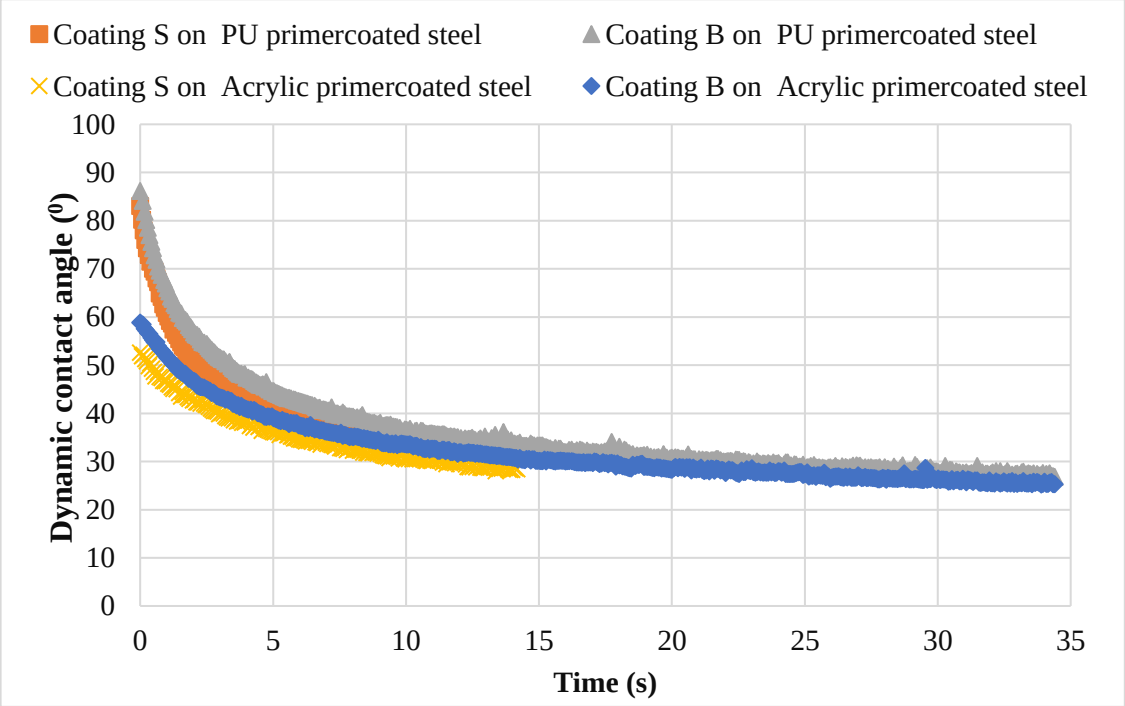

Fig. 3 - 17: Dynamic contact angle of Coating B and Coating S on both PU and Acrylic Primer coated steel

Additionally, the type of substrate employed affected the degree of wettability. It was evidenced that both coatings exhibited a lower degree of wettability on PU primer - coated steel than acrylic primer coated steel throughout the test time. This difference was significant at lower times and lessened as time increased. Above 10 seconds, static contact angle values were obtained. All static contact angle values for both coatings on PU and acrylic primer coated steel showed superb wetting due to the low contact angle values less than 45^0.

3.4. CONCLUSIONS

The aim of chapter three was to investigate and compare the wettability of Coating B and Coating S on a chromated pick- up roll surface and primer coated steel surface. With the information obtained from the chemical analysis part of this work, differences in wettability of coatings could thus be explained.

There were limitations encountered during microstructural analysis of coatings; SEM studies were unable to provide information about particle sizes, shapes and distribution of coating constituents. The limitations of the SEM to provide particle size and shape analysis was ascribed to the small sizes of carbon black pigments that could not be seen under EVOLS SEM equipment employed in this study. However, alternative optical methods such as Mastersizer equipment were also adapted but still failed to provide information of particle size and shape analysis because coating constituents adsorbed onto the agitator and therefore unable to disperse evenly in the dispersant. However, elemental analysis via EDX provided valuable information on inorganic composition in both coatings. Inorganic constituents were found to be similar in both coatings. It is worth noting that EDX studies were only employed for qualitative and not quantitative studies to identify differences in elements.

Coating B and Coating S exhibited the same vibrational bonds under FT -IR analysis. Negligible differences in mass composition under TGA - DTG studies were also found. The three chemical analysis tools, qualitatively, namely, TGA_DTG, FT-IR and EDX, were able to identify the presence of PVC resin; Barium diboron tetraoxides - a strong UV stabiliser and a strong rheological modifier; carbon black pigment; and the solvent mix of BDA/ Petrosol solvent.

Wettability of dry ECCS which acted as a representative of the pick - up roll showed about 19% better wettability of Coating B than Coating S was achieved despite of the fact the Coating B has higher surface tension than Coating S.

However, wettability on dry ECCS does not reflect real industrial conditions because the pick - up roll is maintained in a “pre - wetted” condition prior to coating deposition. Under industrial conditions, a dead time of ~3 minutes is factored in to allow the pick-up roll to become pre - wetted. Therefore, an investigation of wettability on pre - wetted pick - up roll surface was conducted. Coating S exhibited ~13% lower contact angle than Coating B at both roll speeds. This inferred that Coating S wets better than Coating B under pre-wet conditions. The difference in performance of both coatings was credited to the difference in surface tension where Coating S showed lower surface tension than Coating B, thus allowing easier distortion of the coating on a pre-wetted surface.

It was therefore deduced that wettability of a coating layer on the pick - up roll was not the root cause of PMD due to superb wetting achieved by both coatings. Further investigation of wettability of both coatings on primer - coated steel showed better wettability on PU than acrylic primer - coated steels depicting that surface type and conditions also play a part in the wetting on a liquid coating onto the surface.

In conclusion, wettability studies and chemical analysis did not provide an insight into the sources of PMD at Tata steel colors. Therefore, rheological assessment in the next chapter would provide further information on the root cause and the mechanism of PMD.

CHAPTER FOUR:

ASSESSMENT OF THE "PAINT MISSES" DEFECT - PART 2: SHEAR RHEOLOGY OF PLASTICERAM BLACK COATINGS

4.1. INTRODUCTION

Having established in chapter three that there exists a negligible difference in base composition, both qualitatively and quantitatively, further research work in rheological differences was pursued. It was suggested that insufficient blending of coating constituents such as blending of PVC resins and the plasticisers, or plasticised PVC resin and pigments during formulations could explain the difference in performance. Therefore, the effect of homogeneity on the quality and quantity of coating pick – up from the trough by the pick - up roll was investigated using the concept of Apparent Wall Slip (AWS). Fig. 4 - 1 schematically demonstrates the effect AWS on the quantity and quality of coating picked up from the coating trough. Scenario 1 illustrates Wall stick (Negative AWS) credited to phase separation, where a high-density layer manifests a high affinity towards the chromated pick – up roll surface. Consequently, this causes migration of solid particles/ pigments from the bulk to the pick – up roll surface. Scenario 1 has two consequences to the pick - up process;

(1) There is a development of a solid layer of coating on chromated pick - up roll that blocks the nip gap, thus creating competition of nip - gap space between fresh paint and the solid layer,
(2) There is a development of a solid layer due to phase separation of the coating that leaves behind the solvent at the bottom of the trough. Therefore, low quantity or intermittent liquid coating is picked up and transported to the downstream units.

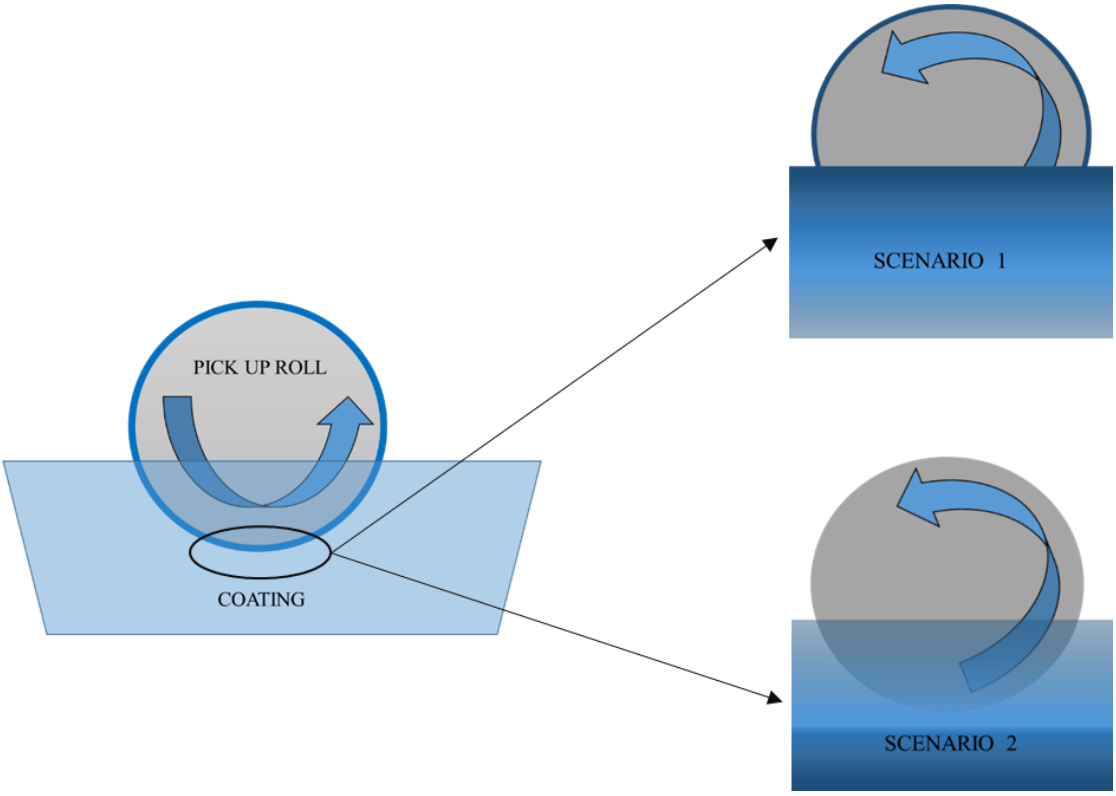

Fig. 4 - 1: Schematic of pick - up roll in the coating trough with negative AWS (scenario 1) and positive AWS (Scenario 2)

Scenario 2 shows a phase separation of coating where particles migrate from the bulk to the bottom of the coating trough. The layer adjacent to the roll surface is occupied with a low-density phase, mainly solvent, that acts as a lubricating layer between a particle - rich layer and the chromated pick – up roll surface.

Further shear rheological studies, in addition to slip investigation, were conducted to understand the flow behaviour of the two coatings through the coating trough and the nip gap. Currently, viscosity measurements at Tata Steel Colors at Shotton are conducted using a spindle rheometer to obtain a single viscosity value, within the range of 24 – 30 cp (0.024 – 0.03 Pas), and this is the inward goods Quality Assurance (QC) test. However, a single value of viscosity against a rotational speed per minute (RPM) does not depict a typical flow behaviour of coatings through the roll coating process. Therefore, shear rate dependent rheology of coatings was carried out to understand the difference in coating flow between batches, but also establish the mechanism by which PMD is manifested.

And finally, mechanical properties (dynamic oscillatory rheometry) and thixotropic tendencies were investigated. Viscoelastic materials with higher elastic components usually exhibit thixotropic properties through a transient process such as roll coating

process which subsequently affects the quality of the final product. Therefore, this chapter aims to investigate the correlation between shear rheology and PMD.

4.2. MATERIALS CHARACTERISATION

4.2.1 SHEAR RATE- DEPENDENT VISCOSITY

Steady-state flow curves were obtained using a Bohlin Geminin HR nano rotational rheometer, with a cone and plate geometry. The equipment was provided by the Welsh Coating and Printing Centre (WCPC) at Swansea University. Fig. 4 - 2 below illustrates a cone and plate rotational geometry, with a 40 mm diameter and 4^0 angle.

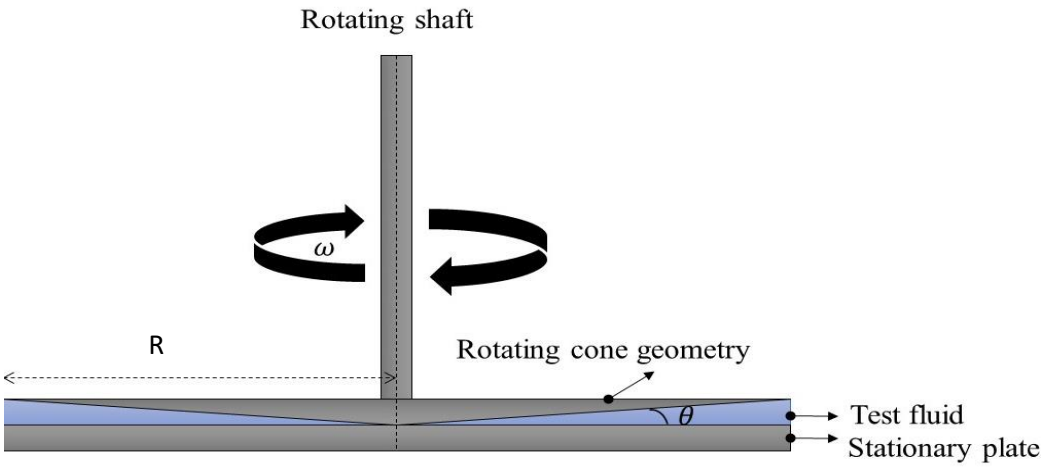

Fig. 4 - 2: Cone and Plate geometry employed in the of steady-state and dynamic flow rheology

A Bohlin Gemini HR nano rheometer operates within a torque range of 10mNm to 200mNm when operating under steady-state mode. However, if the system operates in a controlled stress and strain oscillation rheometry, the torque range is between 3mNm to 200mNm. The rheometer has various temperature control systems such as fluid circulator (temperature range between 40 - 250^0C) and a Peltier plate device (temperature range between -30^0C to 200^0C)

In the investigation of shear rate dependent viscosity, a coating sample was placed between a stationary and a truncated (cone) plate. The sample was sheared in a shear stress range of 10 – 990 Pa at 20 ^{0}C temperature. The cone geometry had dimensions of 40 mm diameter and 4^0. A pre-shearing regime of 0.001 s^{-1} for 5 seconds was applied to

ensure uniform starting conditions of the experiment within the coating sample. To avoid particles migration due to centrifugal forces, from affecting the accuracy of the collected data, experiments were conducted below a shear rate of 1200 s^{-1}.

4.2.2 THIXOTROPY

According to Pearson [118], thixotropy is a viscosity determined by the history of the rate-of-strain when complex fluids are subjected to non-constant shear rate. However, thixotropy could also be defined as a time-dependent property where a shear-thinning material exhibits less viscosity when subjected to constant stress value, over a period time. Time dependence property is beneficial in operating units within the roll coating process such as the storage units and levelling process to correct surface defects. However, the property has been reported by Olivier *et al* [55] to be a nuisance in a transient roll coating process.

4.2.2.1 THIXOTROPIC HYSTERESIS LOOP ANALYSIS

Thixotropic hysteresis loop analysis was conducted using a cone and plate geometry in fig. 4 - 2, with a 40 mm diameter and 4^0 angles. A sample was sheared in the range of shear stress of 0.01 – 990 Pa, and the data was presented as shear rate vs shear rate. Erroneous data was observed at high shear stress/ shear rate. The onset of erroneous data was monitored and data that exhibited this trend was credited to the destruction of the internal structure, and therefore not considered during analysis.

It is worth noting that the coating sample, before the elevated shearing forces, was subjected to a pre-conditioning step of shear rate value of 0.01 s^{-1} for 5 seconds.

4.2.2 DYNAMIC OSCILLATORY RHEOMETRY

Further rheological characterization of coating samples was conducted using dynamic oscillatory rheometry to study mechanical properties such as the elastic or viscous response of the material to the applied strain. Information about mechanical properties provides information on the intrinsic structure of coatings.

Dynamic oscillatory rheometry, that is to say; amplitude strain-controlled and frequency sweep, were conducted using a Bohlin Gemini HR Rotonetic drive 2 rheometer with a cone and plate geometry of dimensions 40 mm diameter and 4^0, schematically fig. 4 – 2, at 20 ^{0}C.

4.2.2.1 DYNAMIC AMPLITUDE STRAIN SWEEP

Prior to conducting a frequency sweep, a dynamic strain amplitude sweep was conducted to determine the linear viscoelastic region (LVR) for both coating samples and subsequently determining the critical strain value, γ_c.

Amplitude sweeps were conducted at constant temperatures of about 20^0 C, at an angular frequency of 1 Hz, and a stress range from 0.01 to 20 Pa using a linear setting. However, results were reported as Moduli as a function of strain. A delay time of 2 seconds between points and an integration time of 1 second was employed.

4.2.2.2 DYNAMIC FREQUENCY SWEEP

Upon determination of the LVR zone and thus the critical strain value, a dynamic frequency sweep was conducted in a frequency range between 0.1 to 15 Hz at 20^0C.

4.2.3 APPARENT WALL SLIP (AWS)

AWS was believed to have contributed to PMD due to phase separation of the coating system. To investigate this phenomenon, gap - size viscosity dependence was conducted and the shift in steady-state flow curves was monitored.

4.2.3.1 GAP SIZE VISCOSITY DEPENDENCE-

From section 2.5.1 in this chapter, a suitable choice of a parallel plate with a diameter of 40 mm was chosen and employed for further investigation of AWS. The experiment was conducted in a stress-controlled regime; a shear stress ramp between 10 - 990 Pa at 20 ^{0}C was conducted. The experiment was repeated for gap sizes of 100, 200, 300, 400, 500,600, 700, 800 and 900 µm, and the change in viscosity and the apparent shear rate was investigated to provide insight in AWS. It is noteworthy that a pre-shearing regime of 0.01 s^{-1} for 5 seconds was employed to allow the same starting conditions.

4.3 RESULTS

Investigation of shear rheology on coating performance is presented in this section, from steady state flow curves and right through to AWS. This section of the thesis provides findings and discussions obtained for the shear rheological methods reported herein

4.3.2 STEADY STATE FLOW CURVES

Shear rate viscosity dependence of Coating B and Coating S was investigated using steady-state flow curves. Fig. 4 – 3 compares apparent viscosity of Coating B and Coating S. There were two regions exhibited on the obtained rheograms; a shear rate dependent region also known as the power-law region; and shear rate-independent region, also known as a Newtonian plateau. The non-linear response of viscosity to shear rate represents a typical non- Newtonian fluid behaviour, specifically, a power-law pseudoplastic (shear thinning) tendency for both coatings. Shear-thinning behaviour was attributed to various configurations a polymer chain adopts at different shear rates. At low shear rates, a coil-like configuration was adopted due to complete alignment of the polymer chain, and this was seen for both coatings.

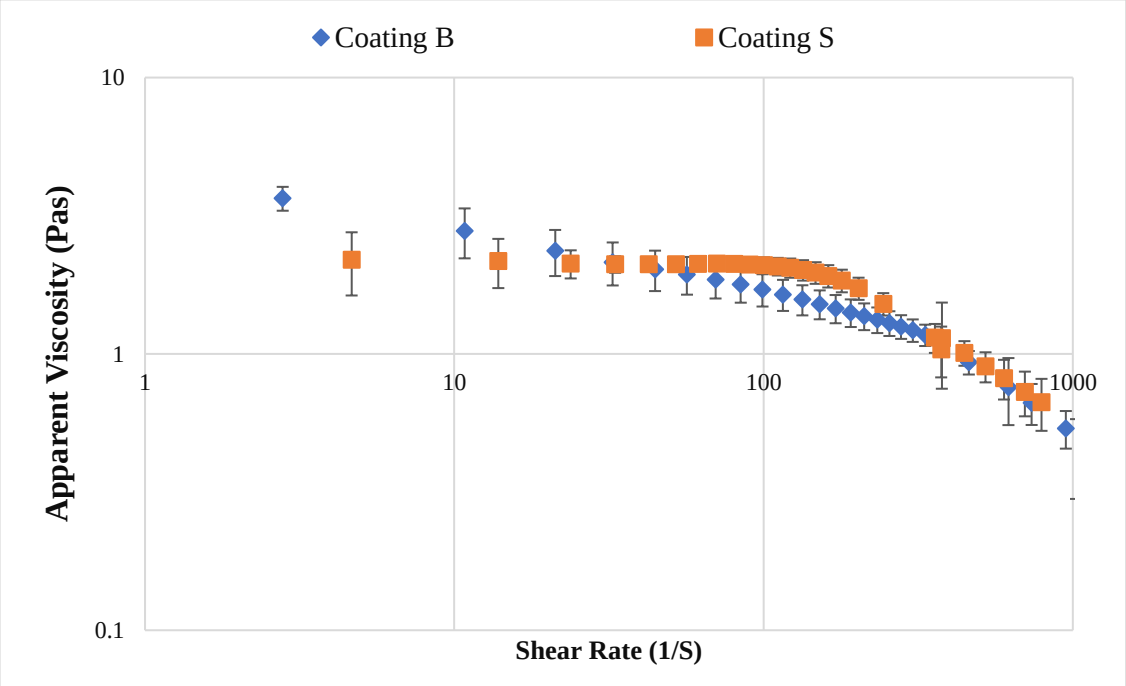

Fig. 4 - 3: Comparison of apparent viscosity against shear rate for Coating B and Coating S

A coil-like configuration persists until high enough shear rates are applied, hence showing higher resistance to flow which yields higher viscosity in the power-law region. At high enough shear rates, a Newtonian plateau was achieved by both coatings due to the stretched and fully aligned polymer chains. Within the Newtonian plateau, the rate of recovery and deformation were believed to be approaching equilibrium and the viscosity within this region was therefore independent of the shear force applied. As a result, a constant viscosity value was exhibited.

Shear rate dependent viscosity of Coating B was higher than that of Coating S in the power law region. Additionally, Coating B showed ~12% zero shear viscosity than Coating S possibly due to higher pigment concentration in coating B formulation.

Though Coating S showed higher viscosity in the Newtonian plateau, the error bars show that both coatings are likely to have the same Newtonian viscosity and that the differences between them could be ascribed to error tolerances of the experiment.

Additionally, erroneous data was observed at high shear rates than lower shear rates. This was also depicted as long error bars. This erroneousness in the data was likely to have come from particles migration from the gap separation between rotating and stationary plates of the rheometer, during experimentation, due to high centrifugal forces.

Given the small differences between the two materials, it is understandable why the current QC method which measures a single shear rate with a relatively broad band of tolerance of viscosity (couple with a low sensitivity instrument) is inadequate for highlighting differences between these materials. Thus, the first practical recommendation from the investigation is that the current QC methodology is a poor tool for inwards coating assessment.

4.3.3 THIXOTROPY

Thixotropy is a time-dependent property that can be a nuisance during coating deposition but beneficial during levelling at the upstream units. Thixotropy was investigated using the thixotropic hysteresis loop analysis method.

4.3.3.1 THIXOTROPIC HYSTERESIS LOOP ANALYSIS

Fig. 4 – 4 shows a comparison of the thixotropic hysteresis loops of Coating B and Coating S. The coatings under study portrayed a thixotropic loop depicting that both coatings are thixotropic. A reverse sweep did not follow the same flow path as the forward sweep, an indication of thixotropic tendencies.

During the forward sweep, shear forces destroy the primary structure through bond breakage and cause rearrangement of polymer chains. However, a secondary structure was formed during the reverse sweep where particles and polymer chains rebuild and create a weak gel-like structure, thus the reverse sweep does not follow the forward sweep.

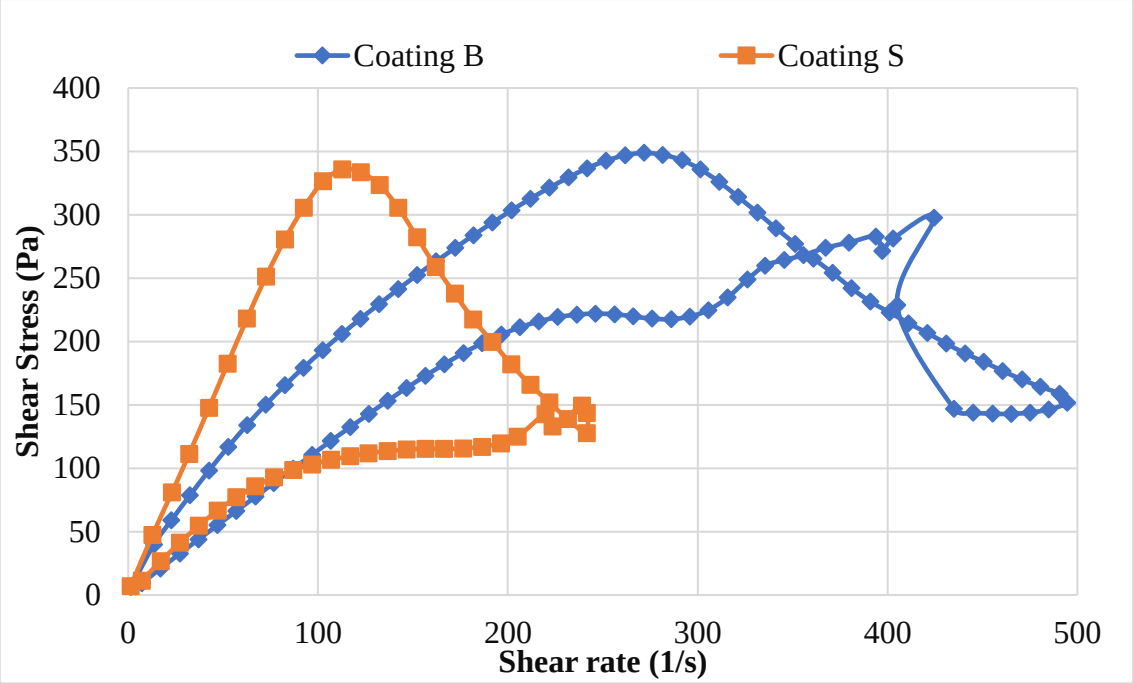

Fig. 4 - 4: Comparison of thixotropic analysis loop for Coating B and Coating S

A comparison of the degree of thixotropy of both coatings was carried out based on the magnitude of the area under the thixotropic loop hysteresis. The area of the thixotropic loop for Coating S and Coating B was calculated at ~ 29 $kPas^{-1}$ and ~ 33 $kPas^{-1}$, respectively, depicting that coating B is more thixotropic than Coating S.

Interestingly, both coatings exhibited a multiple hysteresis loop response at high shear rates, and this was credited to microstructural breakdown. The microstructural change as a result of break - down was correlated to flow stress build-up. It was suggested that above the critical shear stress, prior to the initiation of multiphase hysteresis, optimal alignment of particles and polymer chains was achieved. Above this point, structural breakdown progressed.

In addition, both coatings exhibited an increase in shear stress when the shear rate increased up to a critical shear stress value. At critical shear stress of ~ 396 Pa and ~ 388 Pa for Coating S and Coating B, respectively, shear stress gradually decreased although the shear rate was increased. This phenomenon was, again, observed by Huang and Lu, [119]. The authors attributed this behaviour to high elastic properties of the material where shear strengthening occurs in short time transient shearing.

It was deduced that both coatings experience and are affected by flow history differently. In the preconditioning units, including the storage units, and the entry to the coating head

(coating trough), Coating B is more thixotropic/ time-dependent than Coating S thus enabling high quantity of coating to pick up from the coating trough to the downstream units. However, during the levelling stage Coating S recovers faster than its counterpart, Coating B.

4.3.4 DYNAMIC OSCILLATORY RHEOMETER

Dynamic oscillatory rheology provides information about the intrinsic structure of the coatings and therefore the mechanical properties. Mechanical properties dictate fluid "memory" and ease of deformation of the material either under shear or extensional forces. The test was conducted in two parts; amplitude and frequency sweep.

4.3.4.1 AMPLITUDE SWEEP

Amplitude sweeps of Coating B and Coating S are presented in fig.4 - 5 and fig. 4 - 6, respectively.

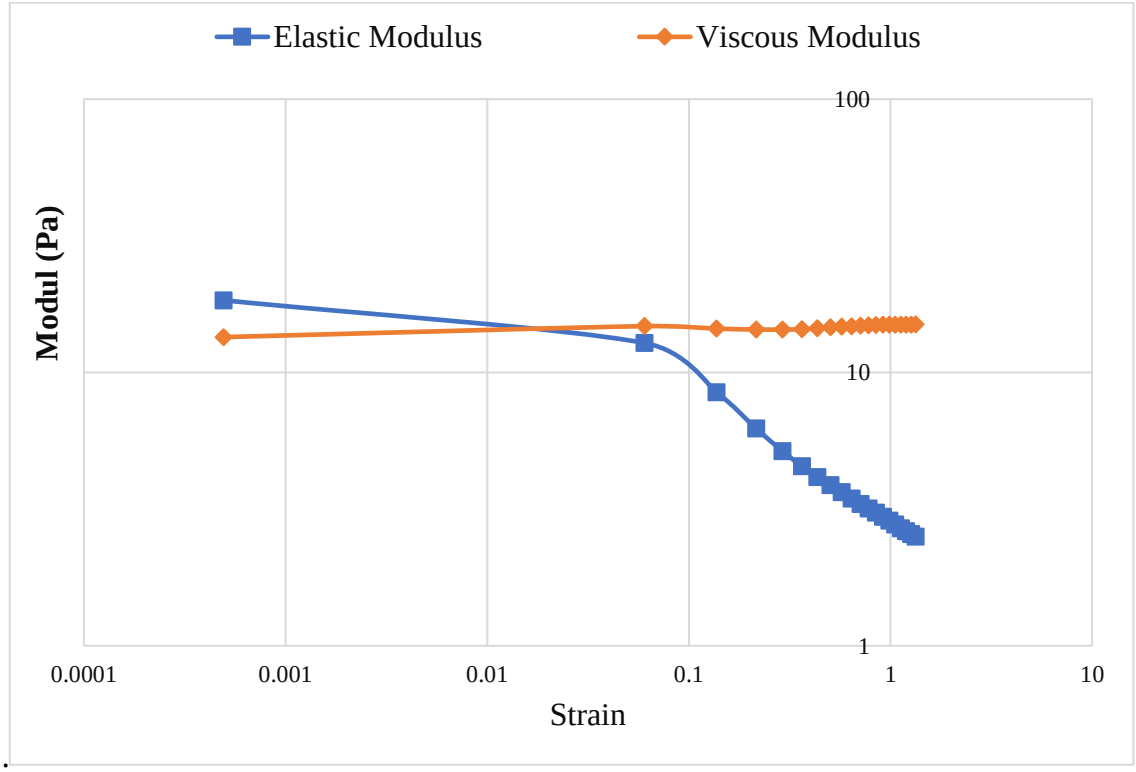

Fig. 4 - 5: Amplitude sweep of Coating B showing Elastic and Viscous modulus as a function of strain

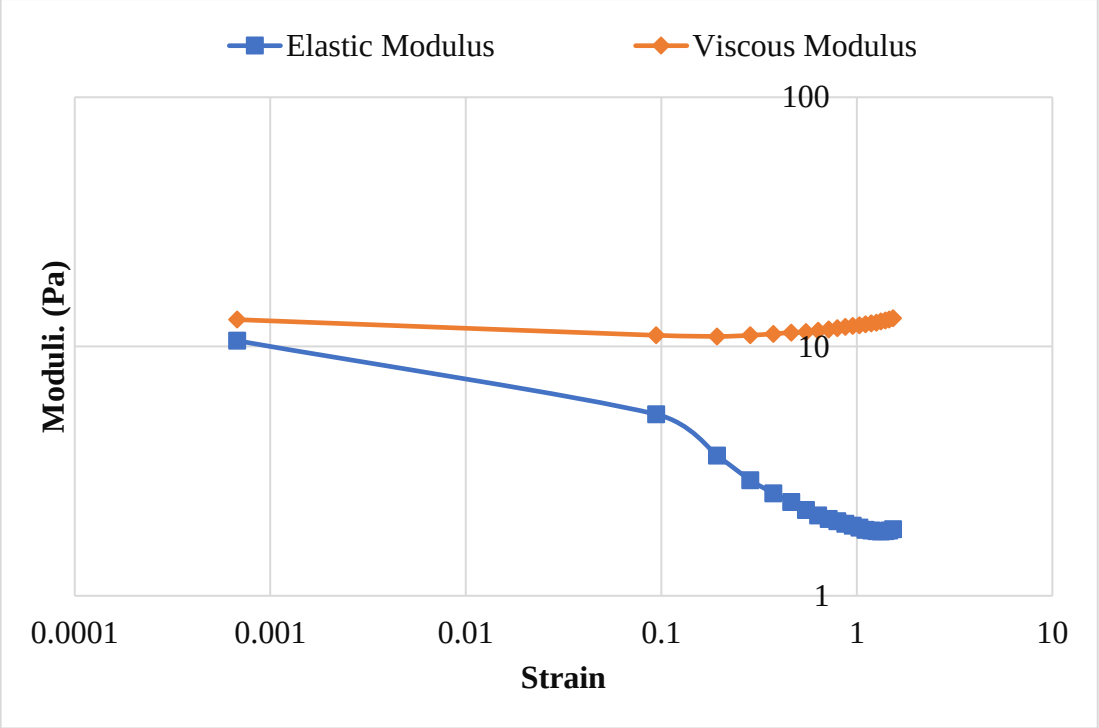

Fig. 4 - 6: Amplitude sweep of Coating S showing Elastic and Viscous modulus as a function of strain

Within the strain test range, there were two distinct regions observed in both the viscous and elastic moduli curves, namely: Small amplitude Oscillatory strain (SAOS) and Medium Amplitude Oscillatory strain (MAOS).

In the SAOS region, Coating B shows that the elastic modulus curve was higher than the viscous modulus curve. However, the viscous modulus curve was higher than the elastic response in the MAOS region, and this was credited to structural break down as the frequency increased and, therefore deformation increased. Coating S showed a different response; the viscous modulus was higher than the elastic modulus in both SAOS and MAOS regions.

Amplitude sweeps of both Coatings showed a decrease in the elastic modulus within the SAOS region thus presenting a challenge when obtaining the actual critical strain value for subsequent frequency sweep. This deviated from the expected response and the work reported in literature findings. In order to understand this anomaly, amplitude sweeps on a simpler liquid, Porcine based cold rolling oil, was conducted using both a linear and a logarithmic mode in the rheometer settings. The choice of a porcine – based cold rolling oil for this investigation was based on the fact the cold rolling is a homogeneous liquid; therefore, issues of phase separation were unlikely to affect my results. Additionally, the cold rolling oil is employed in a cold rolling process and shares similarities to roll coating

processes such as the experience of flow under high shear and extensional forces. Therefore, rheological analysis of cold rolling oils can be related to the roll coating process. Fig. 4 - 7 and fig. 4 - 8 show amplitude sweeps obtained during a linear and logarithmic mode, respectively.

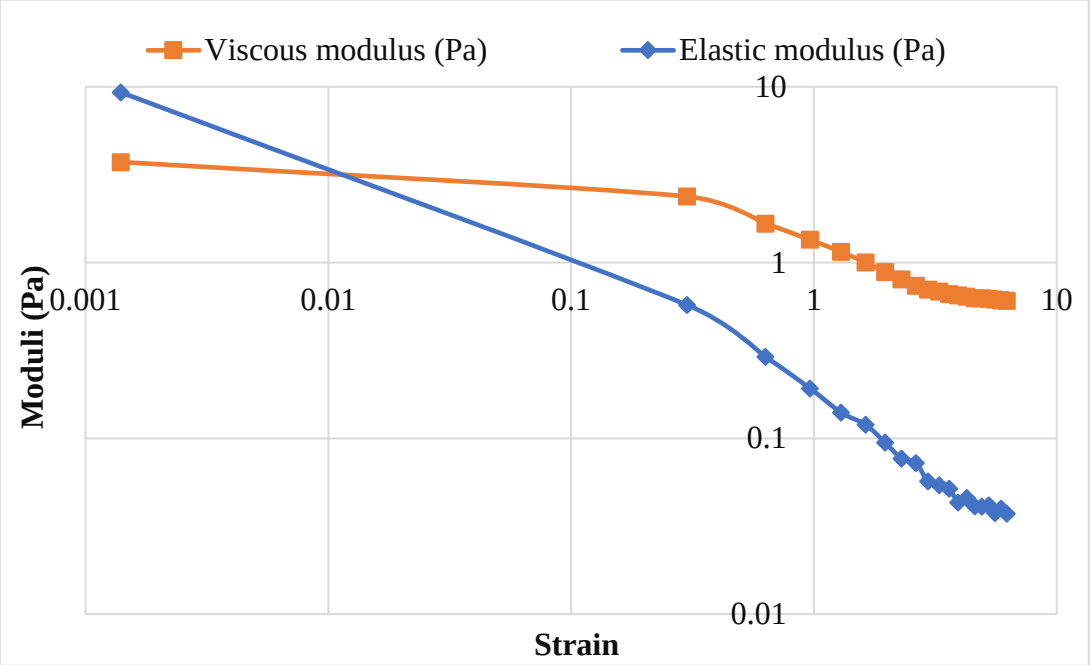

Fig. 4 - 7: Amplitude sweep of a Porcine – based cold rolling oil conducted in a linear mode setting.

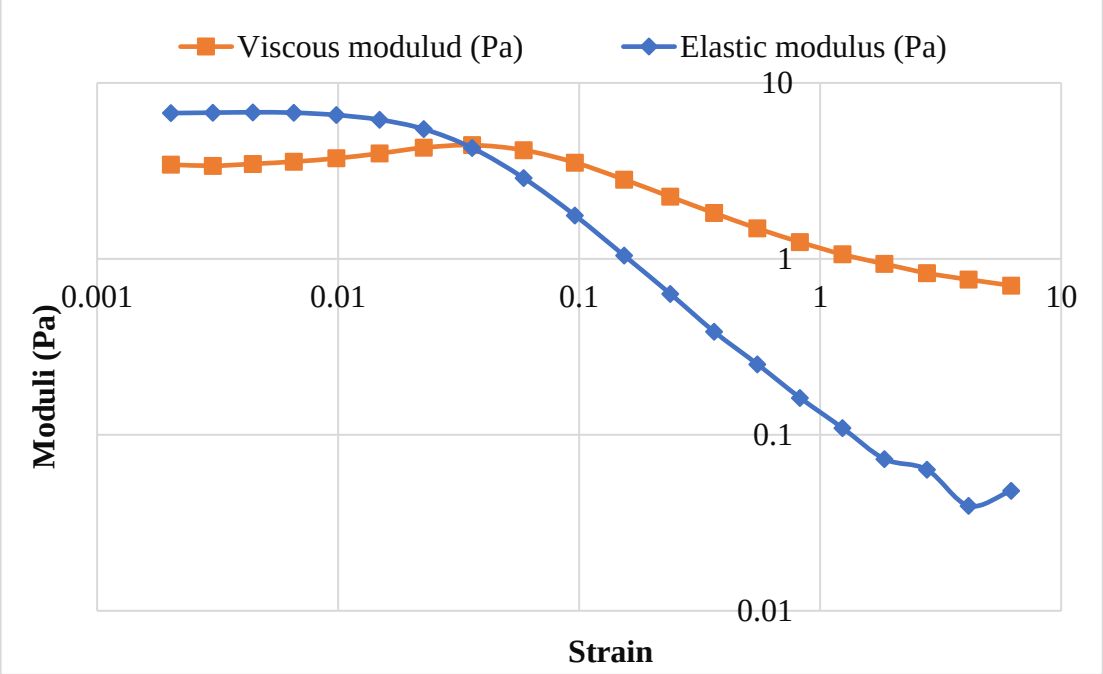

Fig. 4 - 8: Amplitude sweep of a Porcine – based cold rolling oil conducted in a logarithmic mode setting.

The amplitude sweep conducted in a linear mode setting showed a decrease in the elastic modulus curve within the SAOS region and, therefore bears resemblance to the response of Coating B and Coating S amplitude sweeps. Moreover, the amplitude sweep conducted in the logarithmic mode exhibited a linear response in the SAOS region, revealing a visible LVR region.

This inferred that the reduction of the elastic modulus in the SAOS region seen in the amplitude sweep of Coating B and Coating S was due to experimental artefact as opposed to a material response. Therefore, a strain value of 0.1 was employed for both coatings in subsequent experiments as this strain value was believed to be positioned within the LVR region and therefore possible to conduct a frequency sweep in the SAOS region.

4.3.4.2 FREQUENCY SWEEP

The strain value of 0.1 was therefore enough to prompt material response without breaking down the intrinsic structure of the material. Fig. 4 - 9 and Fig. 4 - 10 show frequency dependence of both elastic and viscous modulus for Coating B and Coating S, respectively. Firstly, both coatings showed that the viscous modulus was higher than the elastic modulus that behaved more liquid-like than solid-like. As frequency increased, erroneous data at frequency values > 15 Hz.

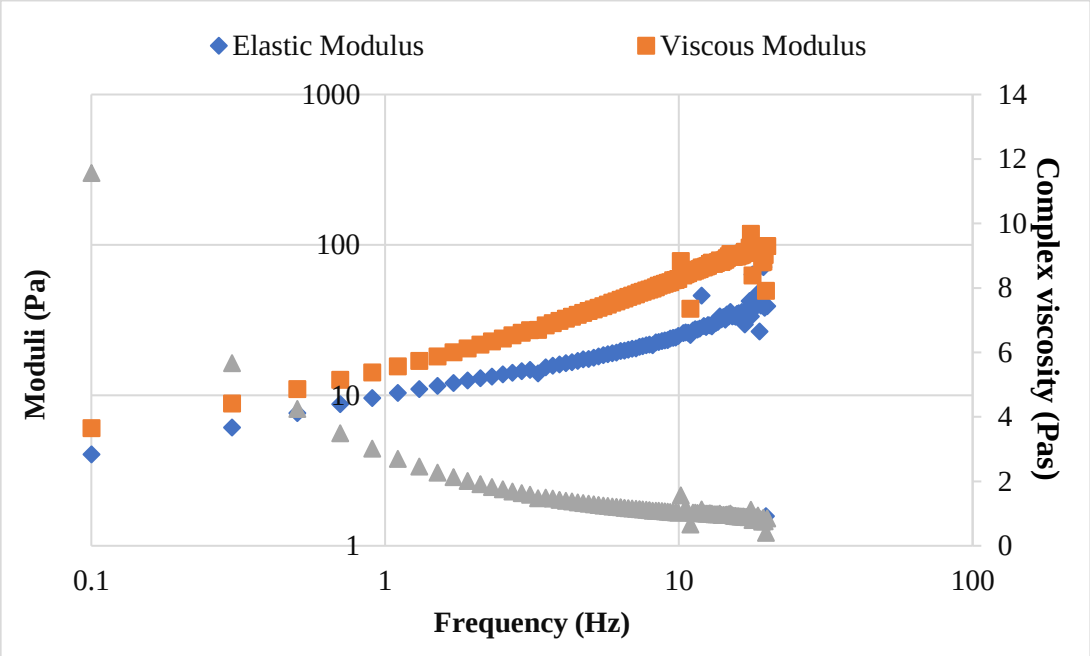

Fig. 4 - 9: Frequency sweep of Complex viscosity (Secondary axis- Pas), Elastic and Viscous modulus for Coating B (Primary axis – Pa)

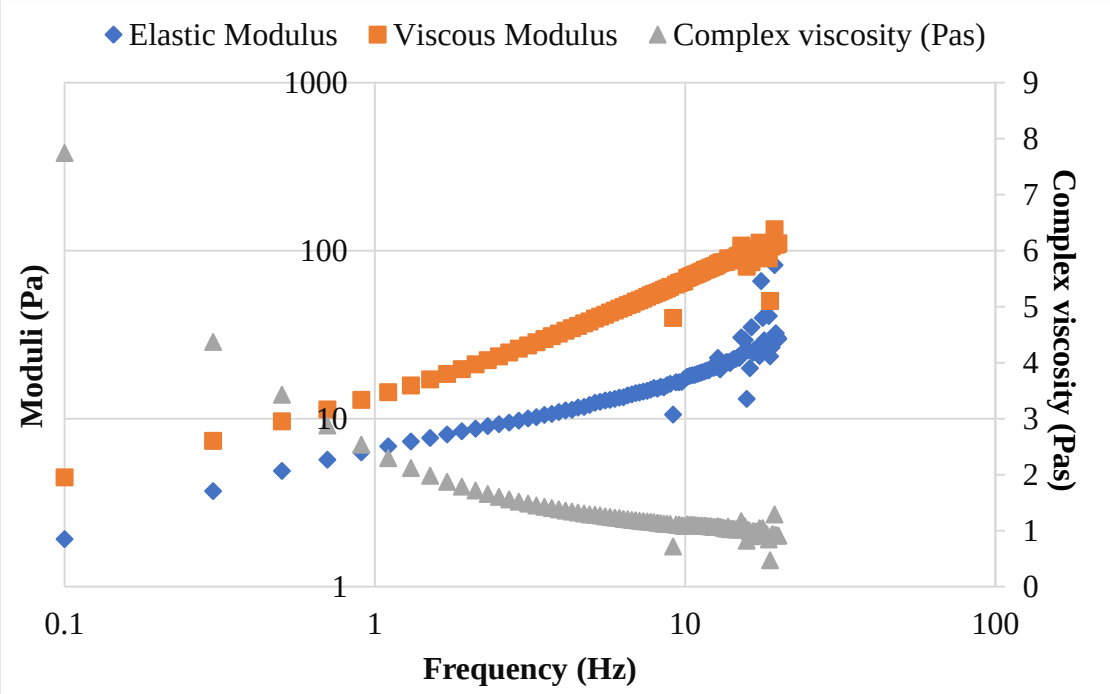

Fig. 4 - 10: Frequency sweep of Complex viscosity (Secondary axis- Pas), Elastic and Viscous modulus for Coating S (Primary axis – Pa)

The presence of erroneous data was credited to material deformation as deformation rate increased, and therefore proved a challenge to obtain a gel point of the coatings. It was also seen that increasing frequency increased both elastic and viscous modulus. This was credited to the recovery of material structure when reduced time (longer frequency) is applied the tested sample and enables the recovery of the gel-like properties. However, complex viscosity for both coatings decreased non - linearly and obeyed and power-law model due to increased deformation rate.

A comparison of elastic modulus for Coating B and Coating S in Fig. 4 - 11 showed that Coating B has higher solid-like properties than Coating S. Though negligible differences between coatings were seen through TGA-DTG studies, in chapter three, claims from the paint formulators that there was more Barium diboron tetraoxides in Coating B than Coating S which could rheologically have modified Coating B. A strong dependence of elastic modulus on frequency for both coatings reflected a weak (physical) gel-like structure for both coatings.

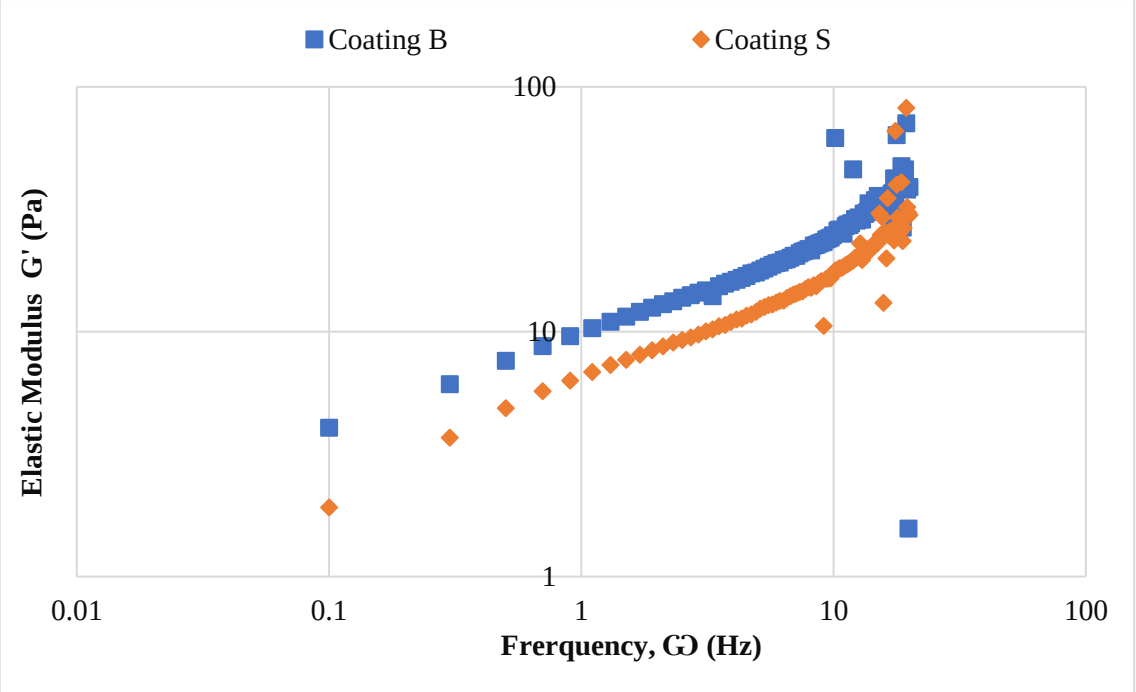

Fig. 4 - 11: Comparison of elastic modulus during the Frequency sweep for coating B and Coating S

Interestingly, viscous modulus curves in fig. 4 - 12 for Coating B and Coating S overlapped denoting a similarity in liquid-like properties for Coating S and Coating B.

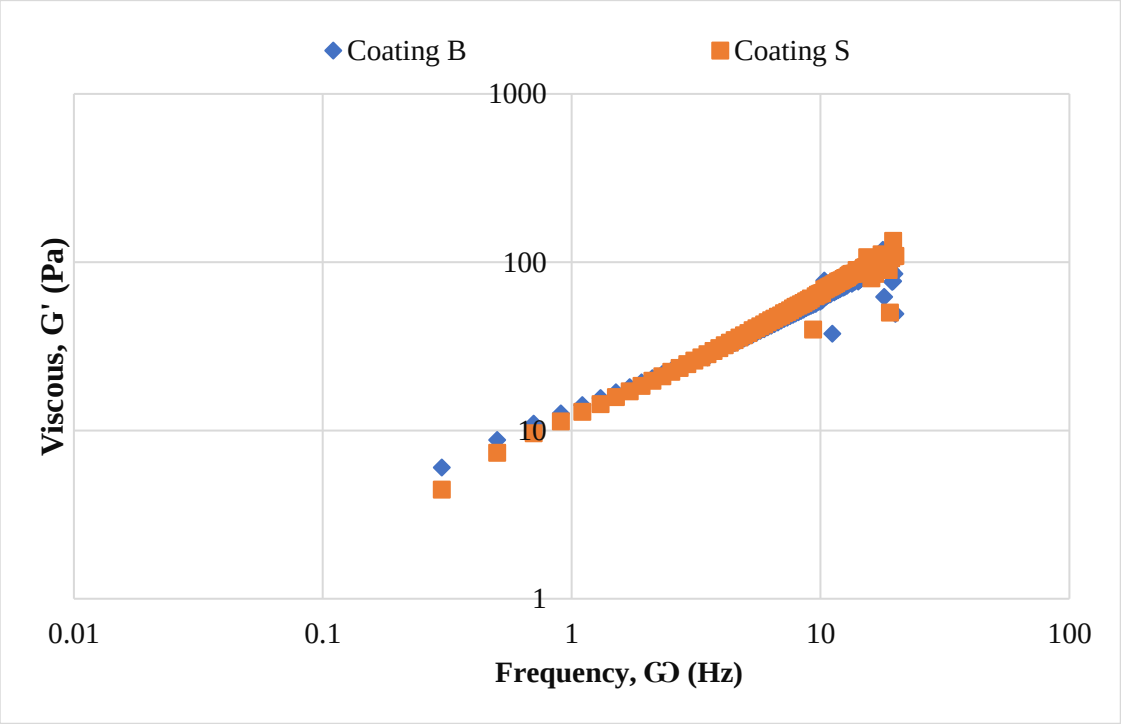

Fig. 4 - 12: Comparison of viscous modulus during the Frequency sweep for coating B and Coating S

Because Coating B showed both higher viscous and elastic modulus than Coating S, it was required to determine the ratio of viscous modulus to the elastic modulus also known

as phase angle for clarity that Coating B has higher solid-like properties than the counterpart, Coating S.

The phase angle in fig. 4 – 13, showed that Coating B had lower phase angle than Coating S throughout the test range inferring higher solid-like properties for Coating B. These findings were parallel and complementary to those obtained in fig. 4 -12.

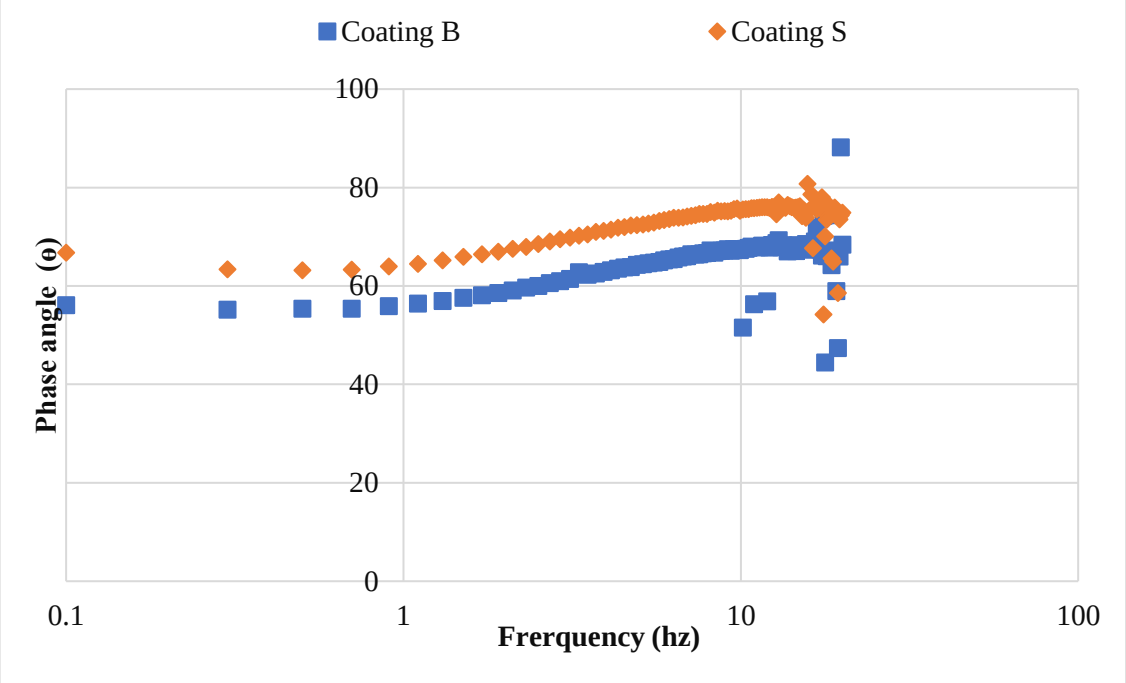

Fig. 4 - 13: Phase angle against Frequency sweep for coating B and Coating S

4.4 APPARENT WALL SLIP (AWS)

Positive and Negative AWS characteristics are known to affect fluid flow through channels, which often manifests itself during rheological characterisation. The presence of AWS is detected through systematic shifts between flow curves when variations of gap sizes between plates are adopted. Investigation of AWS was conducted through observing apparent viscosity/ shear rate- dependence on gap-size as discussed in chapter two.

4.4.1. APPARENT SHEAR RATE AGAINST SHEAR STRESS

Fig. 4 -14 and 4 - 15 represents steady-state flow curves obtained with a parallel plate geometry at gap sizes of 100 to 900 µm and, a cone and plate geometry. The curves showed a systematic shift when gap sizes varied. The shift in flow-curves was also observed when a parallel plate was switched to a cone and plate geometry. This inferred the presence of AWS.

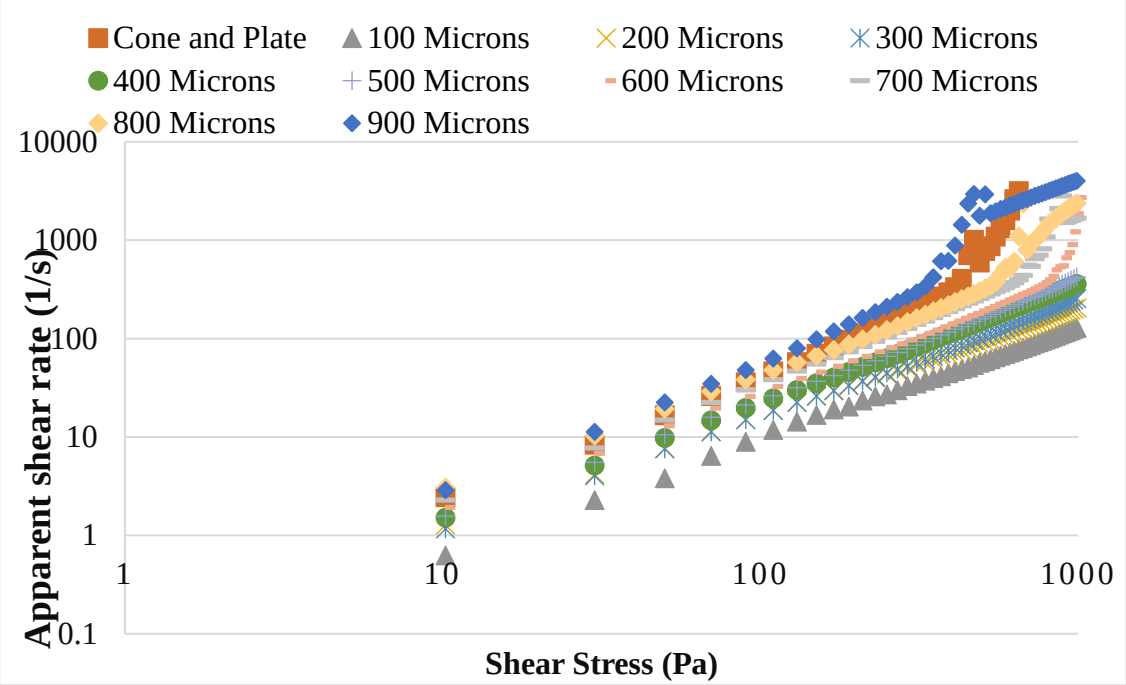

Fig. 4 - 14: Apparent shear rate against shear stress for Coating B

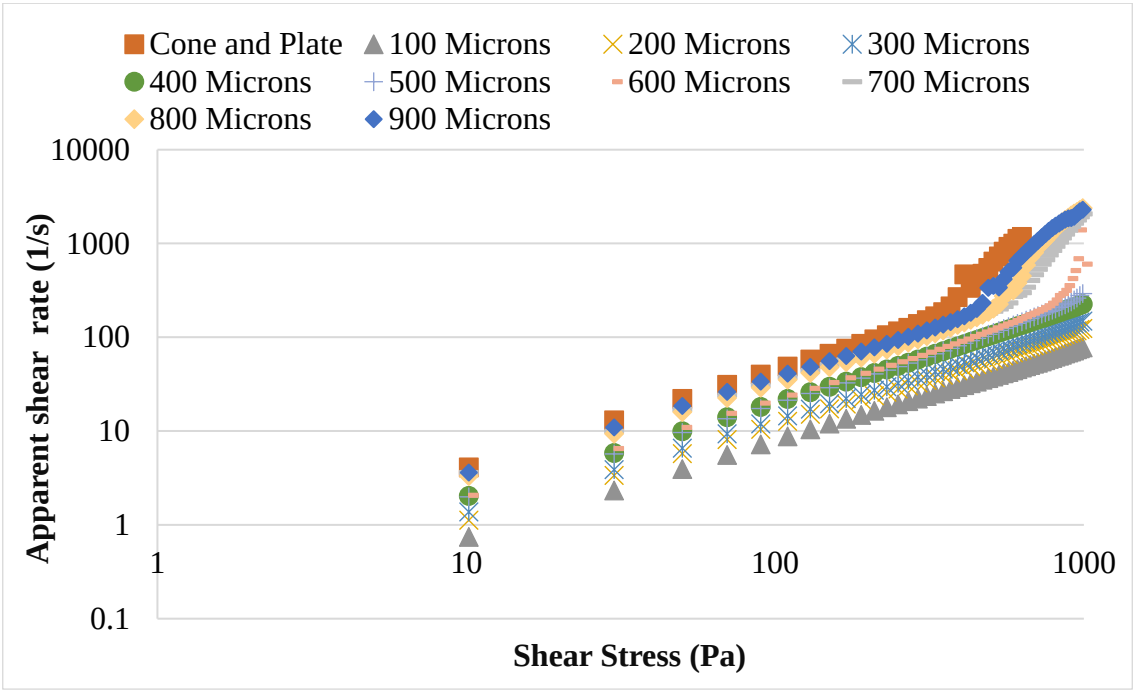

Fig. 4 - 15: Apparent shear rate against shear stress Coating S

Additionally, the flow curves at large gap sizes of a parallel plate geometry almost overlapped with that of the cone and plate geometry. It was further noticed that the obtained data of the apparent shear rate increased as the gap size increased, and this signified a reduction in viscosity when large gap sizes were adopted. However, Davies G.A and Stokes. J.R [73] findings on apparent wall slip using 0.15wt. % Carbogol

(microgel) showed a decrease of apparent shear rate with increased gap sizes, which was contrary to what was observed in this study on commercial coatings.

Penkavova *et al* [120] found aqueous kaolin suspensions to manifest both high flow curves of small gap size at low shear stress, and high flow curves of large gap sizes at high shear stress using cone-cone (KK) sensors. The authors suggested that when the flow curve of large gap sizes is higher than small gap sizes, there exists negative AWS and therefore development of a stagnant layer of the moving geometry. Similarly, when the flow curves of small gaps sizes are higher than large gap sizes, there exists positive apparent wall slip and hence the development of a slippery layer adjacent to moving geometry.

A linear relationship between apparent shear rate and shear stress (Newtonian behaviour) was seen for a gap size range of 100 - 500 µm. Above 500 µm, a non- Newtonian response was seen. This was attributed to large deformation rates experienced at small gap sizes and therefore the test sample reaches a Newtonian plateau faster at small gap sizes than at large gap sizes. It is worth noting that at gap sizes above 500 µm and the cone and plate geometry, the rheometer ceased rotation. A Bohlin Gemini HR nano rheometer operates within a torque range between 10nNm to 200mNm for a controlled stress and shear rate viscometer [121]. Therefore, failure of the rheometer to operate at high shear stress was credited to the fact that high torque/ shear rates were experienced at large gap sizes outside the limitations mentioned within of the Bohlin Geminini HR nano rheometer manual guide. Therefore, at high shear stress values where it proved a challenge to obtain results, an extrapolation was conducted to obtain missing information. This extrapolation was based on a power-law model where prior knowledge of flow index and consistency at every gap size was utilised.

4.4.2 APPLICATION OF THE MOONEY ANALYSIS METHOD

Having established that both coatings experienced AWS due to the systematic shift of the flow curves, the Mooney analysis was employed to quantify AWS characteristics such as slip velocity. However, the Mooney analysis was developed based on many assumptions, and some of them include: homogeneity of a material, isotropic conditions, the material is elastic and incompressible, amongst others. In the updated version of his theory, Mooney further assumed that Hooke's law is obeyed in simple shear (*i.e.* shear stress is proportional to shear strain). However, the coating samples under study are multiphase

complex systems with non - Newtonian behaviour which deviates from the Mooney analysis. Due to limited correlations that can be employed to model non - Newtonian and multiphase systems using a parallel plate, research work was conducted using the Mooney analysis.

Additionally, an assumption that the shear stress is constant throughout the gap sizes was made; however, the resultant apparent shear rate was not constant [61] The Mooney analysis further states that the total flowrate within the gap size is a summation of slip flow and bulk flow. Therefore, the Mooney analysis was re-arranged in the form of a linear regression fit, see Eqn. (4 – 1).

$$Y = Mx + C \qquad (4 - 1)$$

Where Y is a representative of apparent shear rate (measured shear rate), M is the gradient and a representative of slip velocity; x represents inverse gap -size and C is the intercept and a representative of the bulk shear rate.

Fig. 4 - 16 and Fig. 4 - 17 show the application of the Mooney analysis to the obtained data, for 109 – 510 Pa. A negative trend in apparent shear rate vs inverse gap size curve was credited to a negative slip velocity which indicates negative AWS or wall stick behaviour.

The Mooney analysis method was applied to all other shear stress values, but for illustration purposes, graphs of shear stress range of 109 – 510 Pa are presented. Two primary observations can be drawn from the attempt to model the behaviour of the coatings using the Mooney analysis.

Firstly, in all instances, the materials' behaviour deviates significantly from that predicted by the simple Mooney analysis, in that a linear relationship between the apparent shear rate and the inverse gap is a poor descriptor of the behaviour observed.

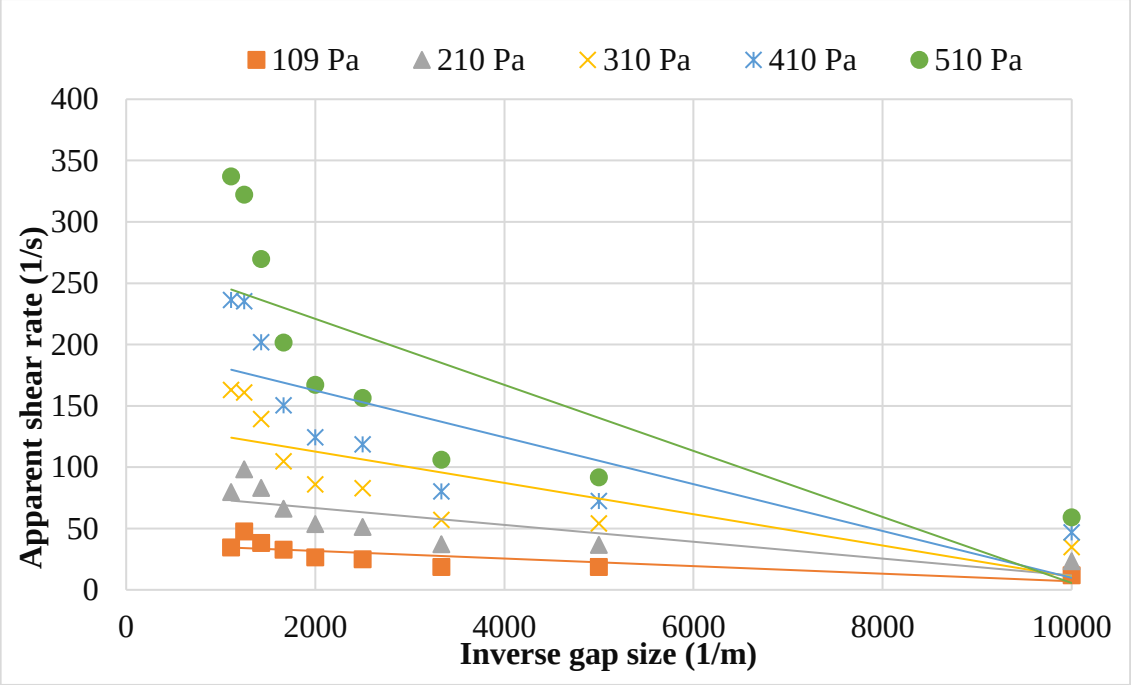

Fig. 4 - 16: Application of the Mooney analysis for Coating B

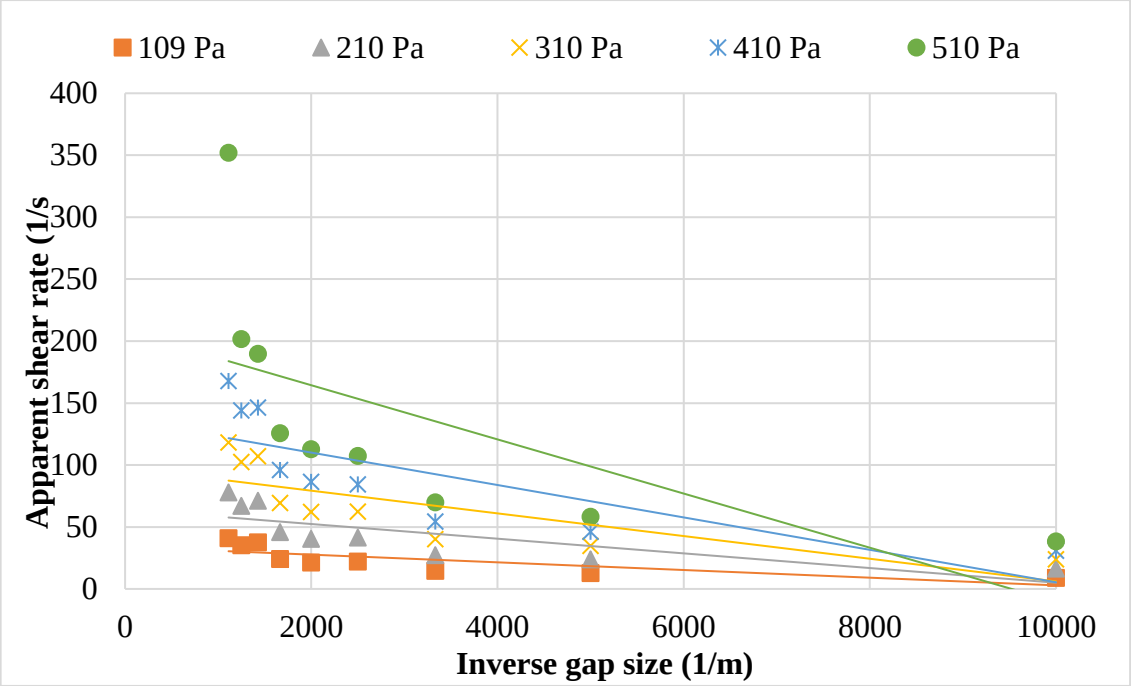

Fig. 4 - 17: Application of the Mooney analysis for Coating S

Secondly, it was seen that the Mooney analysis was more accurate at lower shear stresses and less accurate at high shear stresses. Notwithstanding, these misgivings was it believed that the model was most suitable for describing the flow in the coating trough. This statement is parallel to the findings presented in Fig. 4 -18, where R^2 values were lower than unity at all shear stress test ranges.

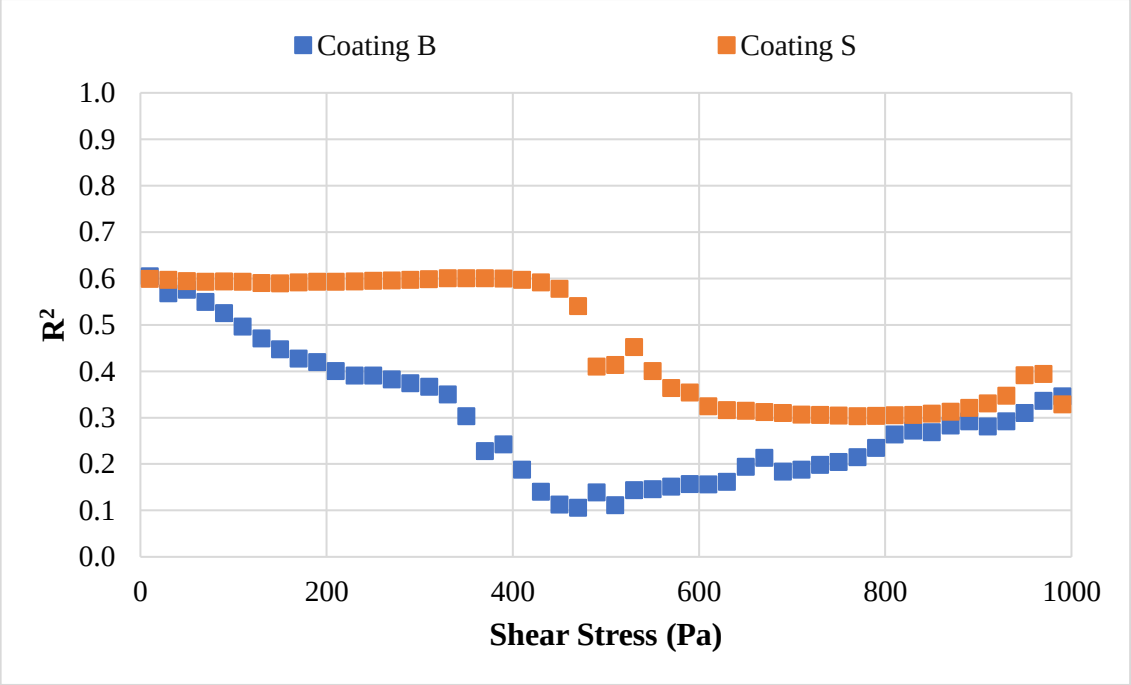

Fig. 4 - 18: Accuracy of Money correlation for Coating B and Coating S

AWS boundary condition employs slip velocity to quantify fluid-wall interactions for local shear stresses. Fig. 4 - 19 compares slip velocity of Coating B and Coating S as a function of shear stress.

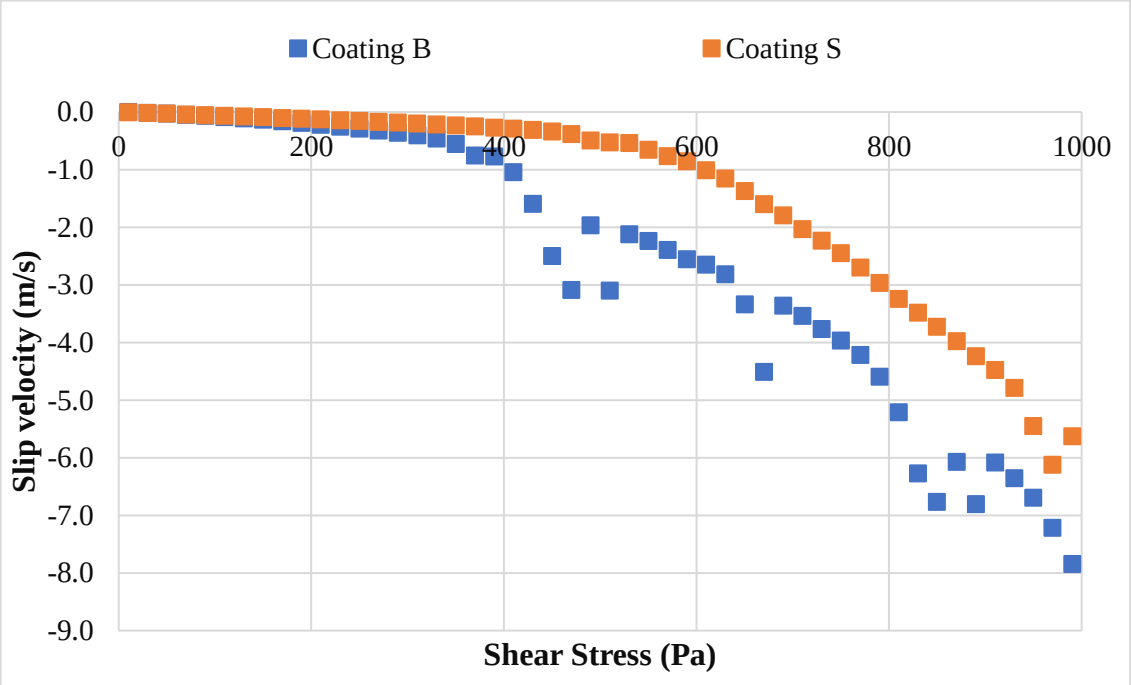

Fig. 4 - 19: Slip velocity against shear stress for both Coating B and Coating S

A slip velocity decreased non-linearly as shear stress increased. The concept of negative slip velocity seems nonsensical and thermodynamically ambiguous; however, a negative

and positive slip velocity is employed in rheology to describe the formation of a stagnant and a lubricating layer, respectively, near the wall. Slip velocity curves of Coating B and S overlapped at low shear stresses, depicting negligible slip contribution up to a critical shear stress of ~200 Pa.

Above the critical shear stress, an increase in slip velocity in a negative direction was observed. Negative AWS was credited to phase separation where a higher density layer adjacent to the moving plate creates a thick solid layer/ a sticky layer.

The particles - depleted layer, which is mainly solvent filled, migrates from the solid surfaces to the bulk. Rides [122] reports in the paper titled "Rheological characterisation of filled materials" that negative AWS is more pronounced at low flowrates due to insufficient stress to cause disentanglement of fibres/ fillers resulting in plug-like flow behaviour. The author's findings are contrary to the observed results in fig.4 – 20 because a higher magnitude of slip behaviour was more pronounced at high shear stresses than low shear stress.

4.4.3 SLIP LENGTH AGAINST SHEAR STRESS

Further characterisation of slip was conducted via slip length. Mathematically, slip length in eqn. (4 - 4), is the ratio of slip coefficient represented in eqn. (4 – 3) to fluidity coefficient represented in eqn. (4 - 2).

$$\varphi = \frac{\dot{\gamma}_{bulk}}{\sigma} \tag{4 - 2}$$

$$\chi = \frac{v_s}{\sigma} \tag{4 - 3}$$

$$\beta = \frac{\chi}{\varphi} \tag{4 - 4}$$

Whereφ, χ, β is the fluidity coefficient, slip coefficient and slip length (μm), respectively.

Fig. 4 – 20 compares slip length curves of Coating B and Coating S. Besides, slip length dependence on shear stress was strongest at medium shear stress values, especially for Coating B.

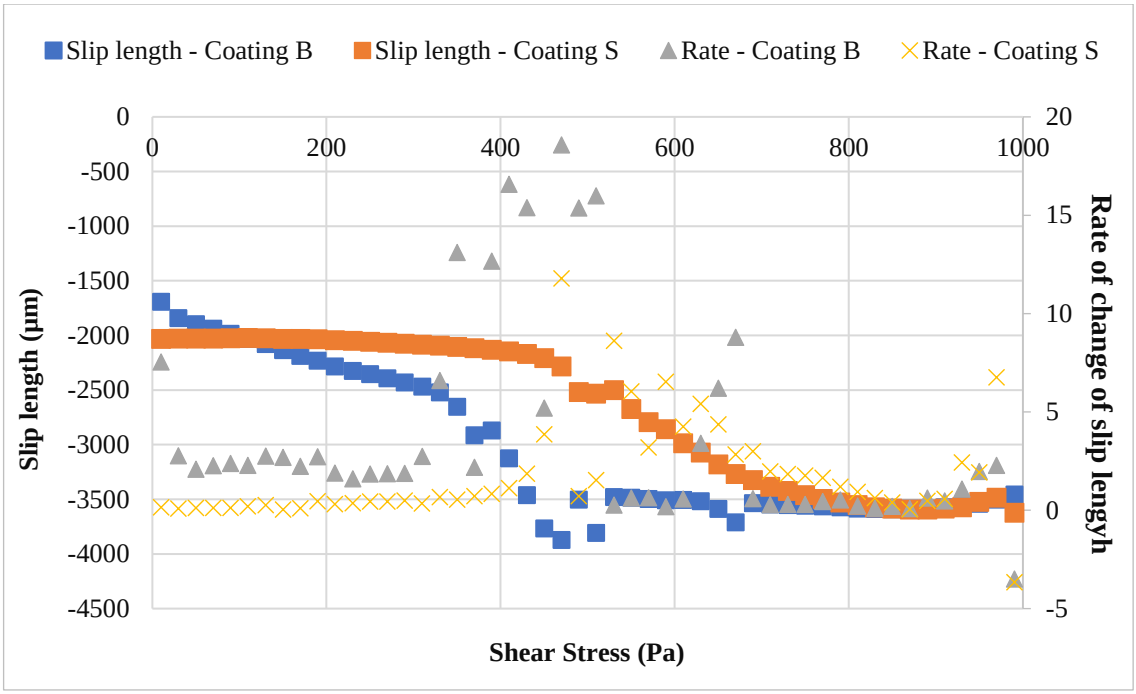

Fig. 4 - 20: Slip length (Primary axis) and Rate of decrease of slip length (secondary axis) with shear stress.

Upon success deformation and rupture of the coating system at low medium shear, particles have a higher affinity to moving surface. Coating B with higher pigment concentration showed a higher slip length that Coating S. The data scatter at medium shear stresses was attributed to the Mooney analysis break down; however, a recovery of the model was shear stresses increased.

Above 750 Pa, slip length curves completely overlapped and this was credited to the depleted particles from the bulk and the saturated attachment sites on the moving geometry. The rate of change of slip length plateaued.

4.4.4 RELATIVE SLIP CONTRIBUTION (A) AGAINST SLIDING SPEED

Apparent wall slip contribution to the total flow was determined using Eqn. (4 - 5) below, and the sliding speed was determined using Eqn. (4 – 6). It is noteworthy that slip contribution closer to zero signified a flow with negligible contribution from AWS, and large relative slip contribution described a flow with a high contribution by AWS.

$$A = \left(\frac{\dot{\gamma}_{meas} - \dot{\gamma}_{bulk}}{\dot{\gamma}_{bulk}}\right) \qquad (4 - 5)$$

$$V = \dot{\gamma}_{meas} * H \qquad (4 - 6)$$

Where V is the sliding speed/ geometry speed (m/min), A is the relative slip contribution, $\dot{\gamma}_{meas}$ is the measured shear rate (1/s), $\dot{\gamma}_{bulk}$ is the bulk flow, and H is the gap separation (μm). It is noteworthy that sliding speed in this context is used synonymously with moving plate speed.

It was possible to achieve very high sliding speeds at large gap sizes than small gap sizes although all gap sizes operated under the same shear stress. At large gap sizes, rotating geometries experienced less resistance to rotation due to negligible constriction effects that could otherwise reduce rotational speeds of the parallel plate geometry. This was reflected in the results obtained in fig. 4 – 21 and fig. 4 -22 where high sliding speeds were achieved at large separation gaps. Therefore, it was possible to determine the relative slip contribution at very high sliding speeds at large separation gaps but not possible at small separation gaps.

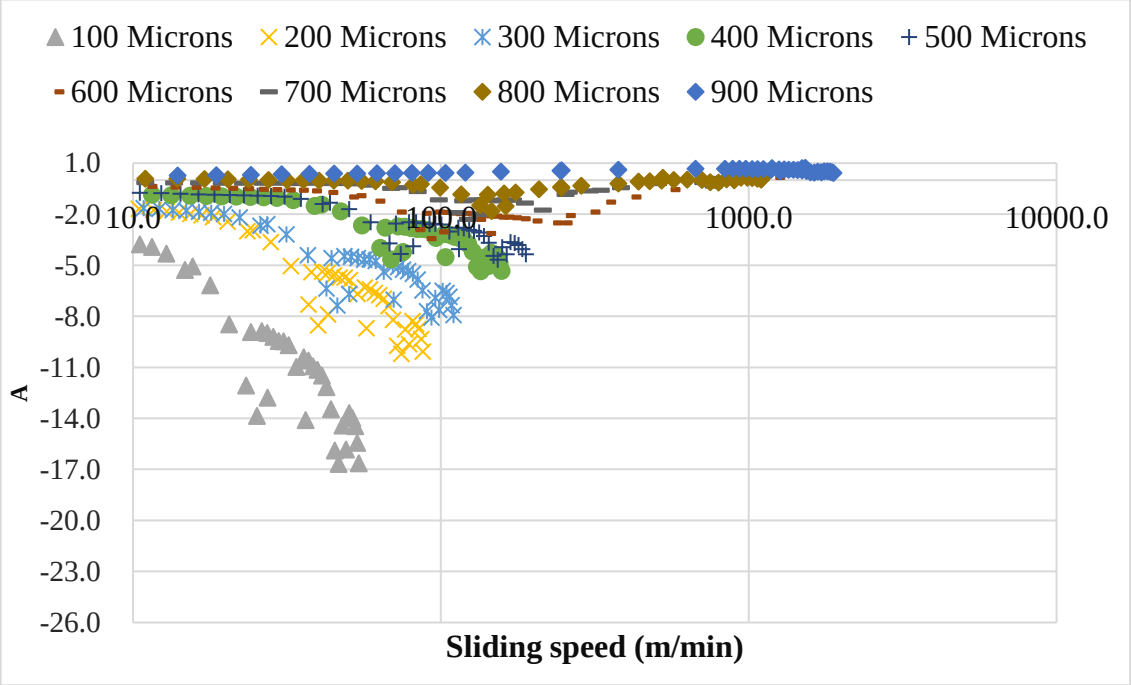

Fig. 4 - 21: Relative slip contribution against sliding speed for Coating B

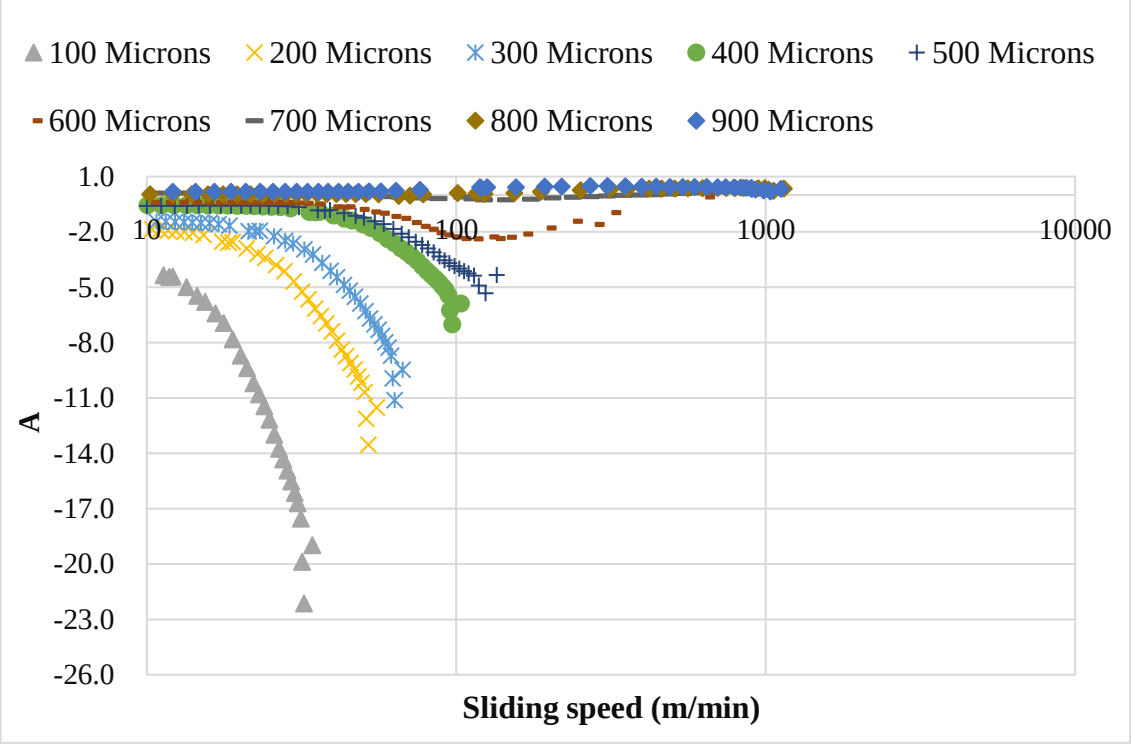

Fig. 4 - 22: Relative slip contribution against sliding speed for Coating S

There was three observation found in relative slip contribution results: firstly, absolute relative slip contribution decreased with increasing separation gap due to reduced constriction effect (Jamming phenomena) which were believed to contribute to the intermittent flow. At 700μm, a local maximum point at 165 m/min and 135 m/min for Coating B and Coatings, respectively was seen. This is a representative of a clog fragility point, where the flow constriction effects are overcome by application of high enough speed.

Secondly, absolute relative slip contribution increased with increasing sliding speeds, but this decreased at the clog fragility point, possibly due to high deformation rates that promoted structural breakdown.

Thirdly, absolute relative slip contribution was found to be more than unity for all gap sizes except for 800 and 900μm.

These results were seen for negative relative slip contribution, depicting a thicker stagnant anomalous layer than the gap size, which is nonsensical. The physical response of the curve gives logical meaning and can be explained; however, absolute relative slip contribution values higher than 1 are scientifically questionable. The possible reason for these values would explain the constriction effects which are investigated herein.

Nevertheless, further comparison of relative slip contribution of Coating S and Coating B was conducted in fig. 4 - 23, fig. 4 - 24 and fig. 4 – 25 at 100, 500 and 900 µm, respectively.

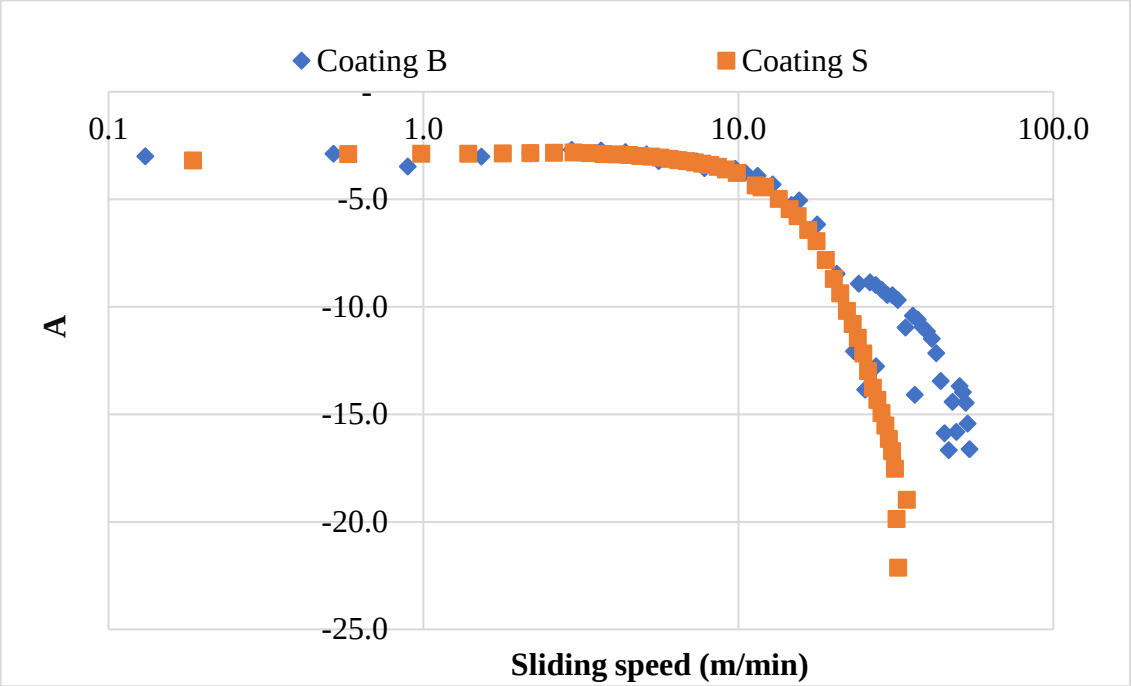

Fig. 4 - 23: A comparison of relative slip contribution (A) against sliding speed 100 µm gap for Coating B and Coating S

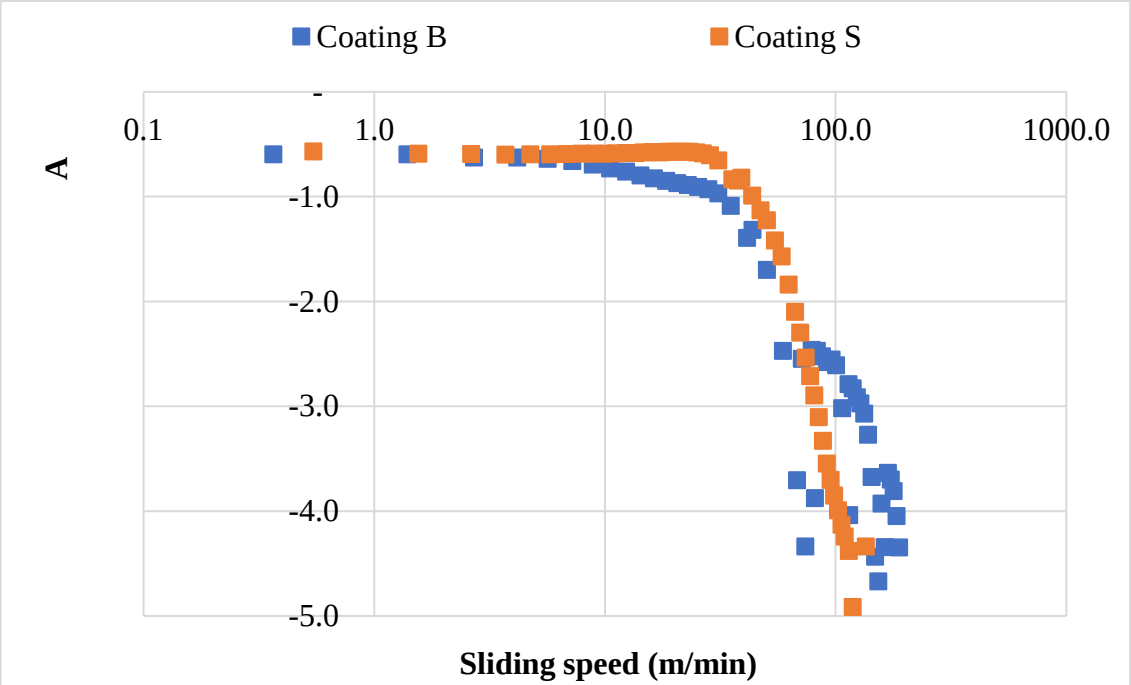

Fig. 4 - 24: A comparison of relative slip contribution (A) against sliding speed 500 µm gap for Coating B and Coating S

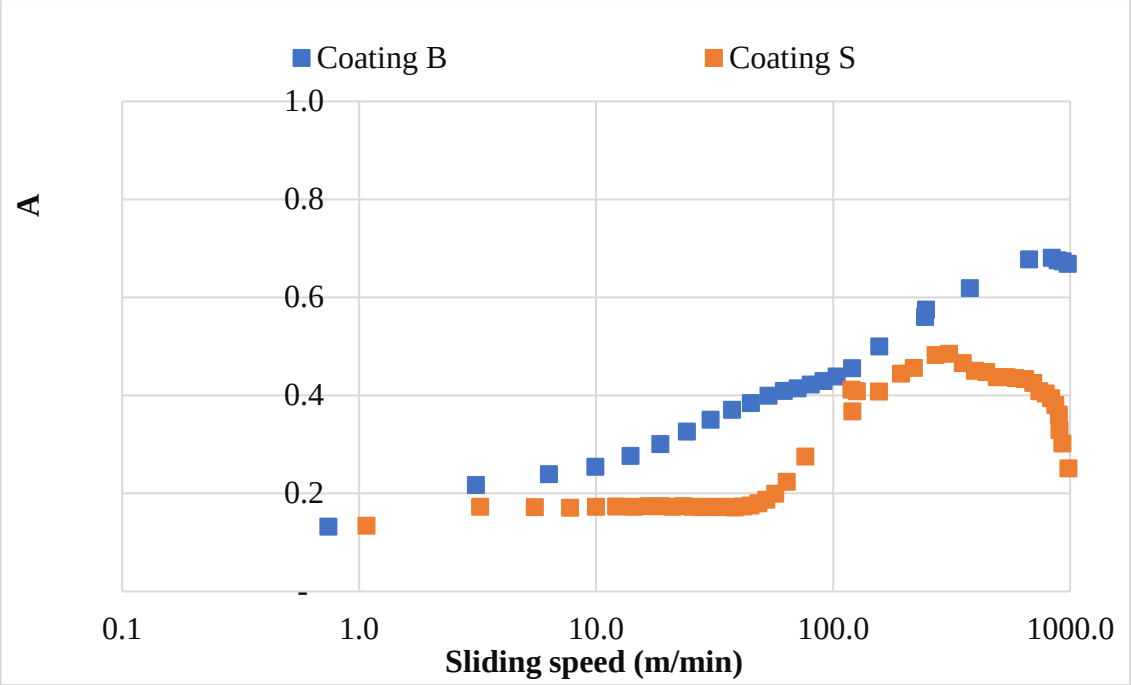

Fig. 4 - 25: A comparison of relative slip contribution (A) against sliding speed at 900 µm gap size for Coating B and Coating S

The above-mentioned sizes were chosen for comparison because they provide a better representation of small, medium and large gap sizes. Absolute slip contribution closer to zero signified a flow with negligible contribution from AWS.

A gap size of 100 and 500 μm, the negligible difference in relative slip contribution (negative relative slip contribution) at low sliding speeds was observed for Coating B and Coating S. However, at increased sliding speeds Coating S showed higher absolute relative (negative relative slip contribution) than Coating B depicting a thicker stagnation layer for Coating S.

At 900μm, both coatings showed positive relative slip contribution with the highest relative slip contribution noticed for Coating B. Positive relative slip contribution increased with increasing sliding speeds.

4.4.5 CONSTRICTION EFFECTS ON THE FLOW OF COATING B

Discrepancies observed in absolute relative slip contribution values of more than unity results in section 4.4.5 further inspired investigation in constriction effects, also known as jamming phenomena. Therefore, this section seeks to understand the contribution of jamming phenomena to the total flow. According to Penkavova *et al* [120], when the

measured kinetic flowrate is less than the bulk flow rate it is vital to determine stagnation ratio. Therefore, the stagnation ratio, N, was determined using Eqn. (4 -7) below;

$$N = \left(\frac{\dot{\gamma}_{bulk} - \dot{\gamma}_{meas}}{\dot{\gamma}_{bulk}}\right) \tag{4 - 7}$$

Stagnation ratio against sliding speed for Coating B and Coating S is presented in Fig. 4 – 26 and 4 – 27. At first glance, the stagnation ratio increased with increasing sliding speed for gap sizes of 100 – 700 μm. However, the increase was non – linear because stagnation ratio was independent of sliding speeds at low speeds. This trend was followed by a steady increase of stagnation ratio to a maximum point at high sliding speeds. It was likely that at low sliding speeds the flow was mainly liquid-like, but finally transformed from a liquid-like to a solid at elevated sliding speeds. The development of a solid-like behaviour was due to imposed unidirectional stress that leads to the development of force chains between particles hence the development of clogs. As a result, competition of particles for space in such a constricted space that leads to intermittent flow [123].

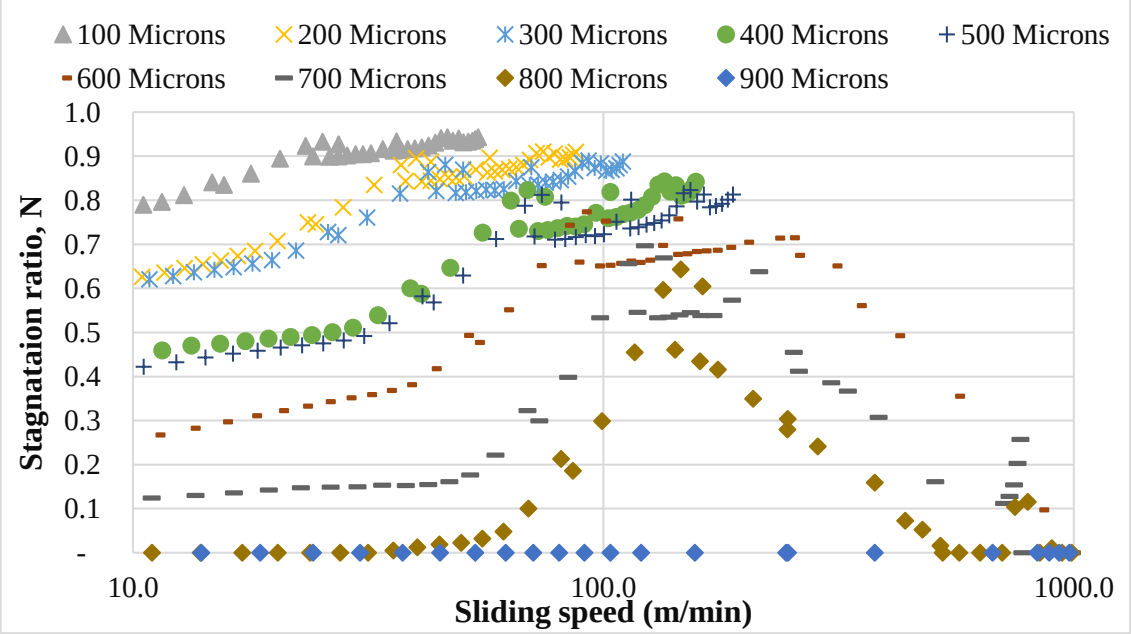

Fig. 4 - 26: Stagnation ration against Shear stress for Coating B at different gap sizes

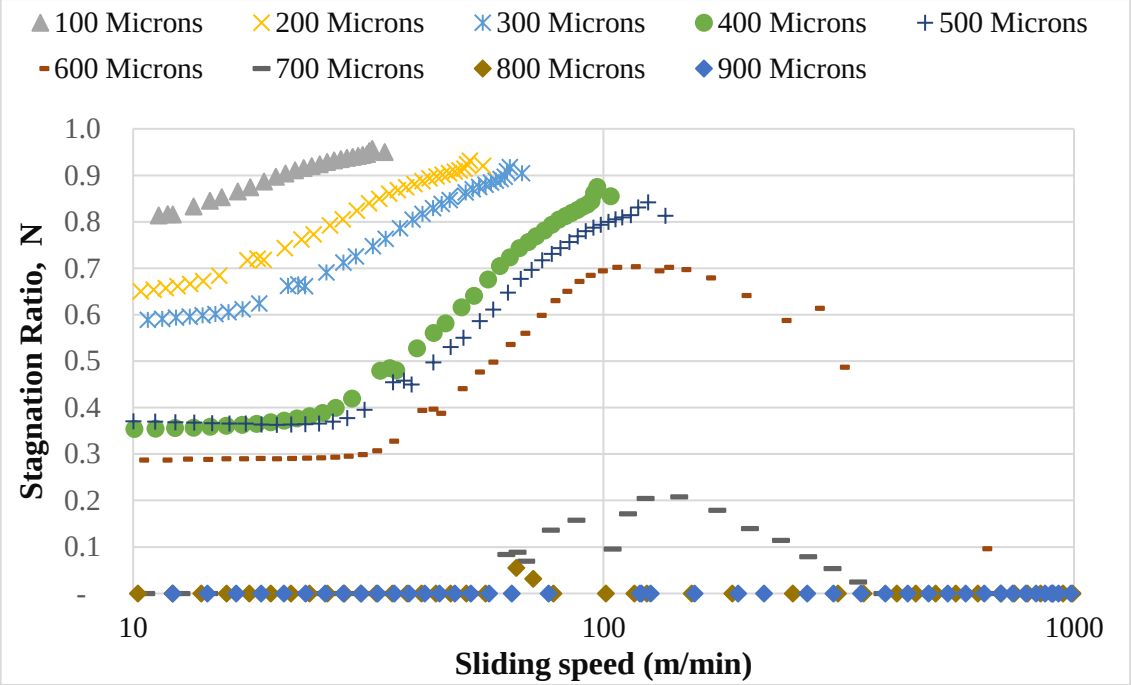

Fig. 4 - 27: Stagnation ratio against Shear stress for Coating B at different gap sizes

Gap sizes of 600, 700 and 800 μm exhibited a decrease in stagnation ratio as sliding speeds further increased. It was believed that the developed solid clogs at the gap sizes mentioned disintegrated. The sliding speed at which the clogs are broken is called a clog fragility point. Above the clog fragility point, the flow proceeds with negligible contribution from constriction effects. Coating flows at gap sizes below 600 μm did not achieve a clog fragility point because the flow regime was limited to the sliding speeds the gap sizes could achieve under the applied shear stress.

Both coatings displayed negligible stagnation ratio at 800 and 900 μm, and this was credited to the availability of free space within the separation gap to permit ease of flow. Therefore AWS, at large gap sizes, was linked to material/ electrochemical effects rather than constriction effect.

Fig. 4 - 28 schematically illustrates flow between large gap sizes and, flow with constriction effects at small gap sizes.

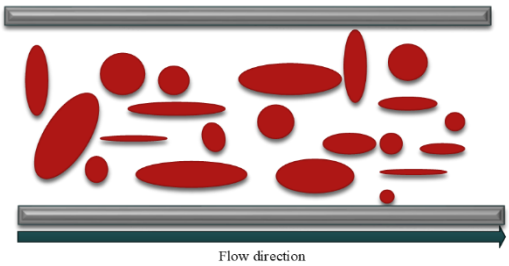

(a) Flow in large gap sizes

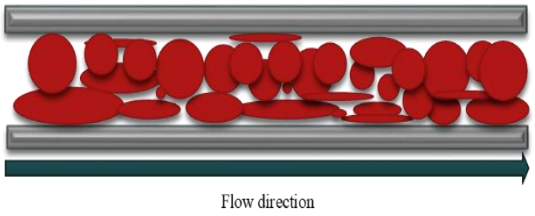

(b) Flow in small gap sizes

Fig. 4 - 28: Schematic of constriction effects during the flow-through plates

Fig. 4 - 29, fig. 4 – 30 and fig. 4 -31 compares stagnation ratio curves of Coating B and Coating S at gap sizes of 100, 500 and 900 µm, respectively. At 100 μm, stagnation ratio curves of Coating B and Coating S overlapped at low sliding speeds; however, Coating S showed higher stagnation ratio than Coating B as sliding speeds increased passed 25 m/min mark. The same trend was observed at a gap size of 200 μm. It was therefore deduced that Coating S has higher potential to stagnate than Coating B at high sliding speeds when flowing in small separation.

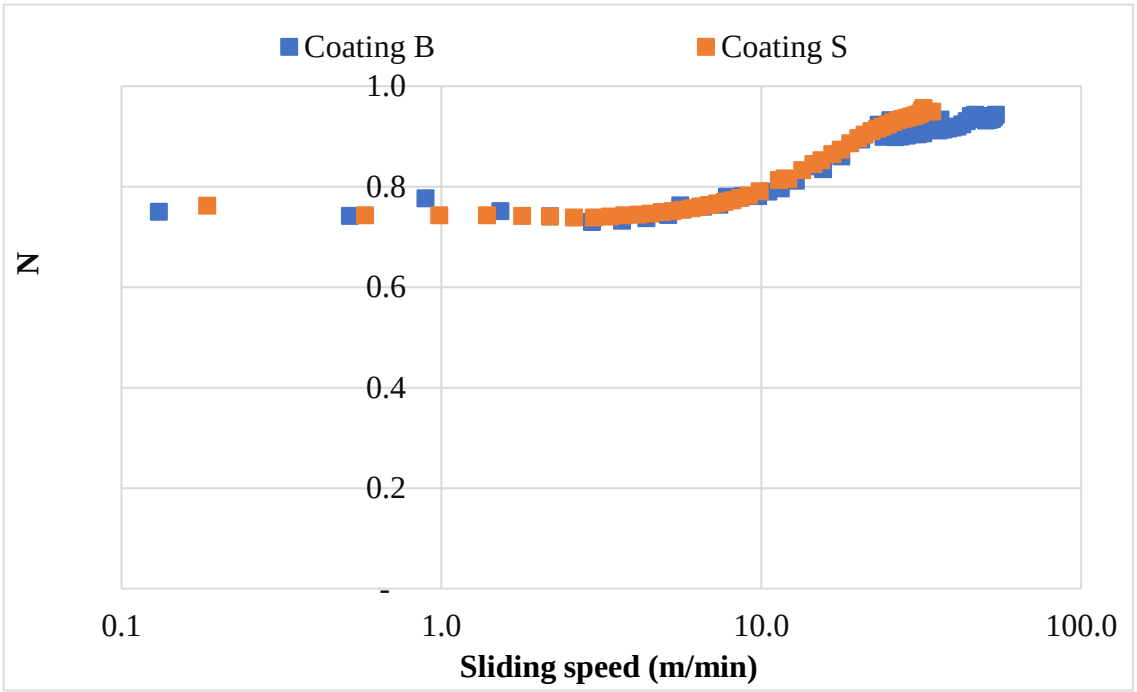

Fig. 4 - 29: A comparison of Stagnation ratio (N) against sliding speed at 100 µm gap size for Coating B and Coating S

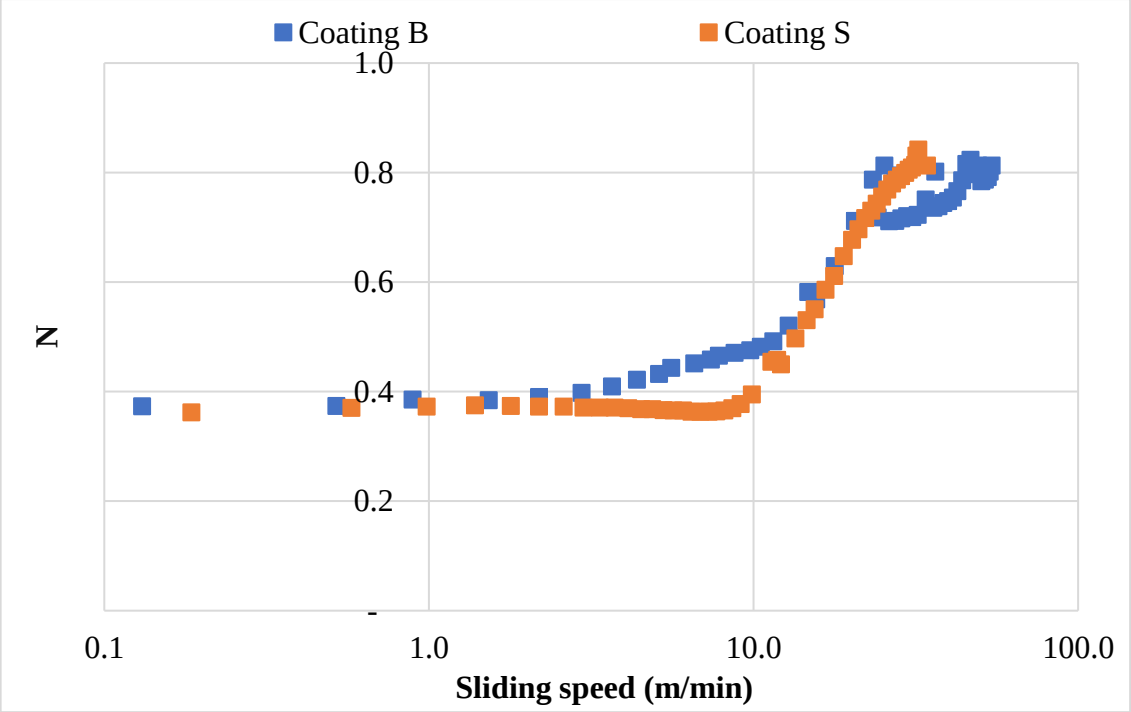

Fig. 4 - 30: A comparison of Stagnation ratio (N) against sliding speed at 500 µm gap size for Coating B and Coating S

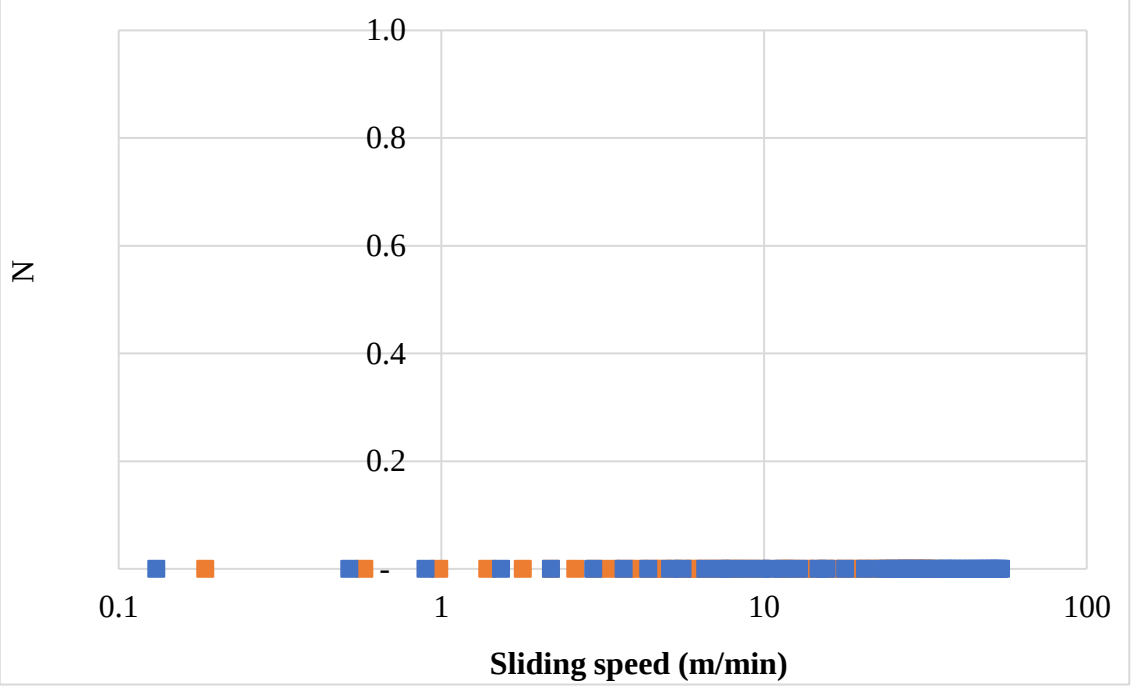

Fig. 4 - 31: A comparison of Stagnation ratio (N) against sliding speed at 900 µm gap size for Coating B and Coating S

A gap size of 900 μm, there was negligible stagnation ratio observed and therefore no contribution of constriction effect to the total flow at large gap size. Based on these findings, a comparison of anomalous layer thicknesses of Coating B and Coating S was conducted at 900µm gap separation. Additionally, the flow in the coating trough can only

be simulated using large gaps sizes hence 900µm gap size is a good candidate for this study.

4.4.6 DETERMINATION OF ANOMALOUS LAYER THICKNESS OF COATING B AT GAP SIZE OF 900 MICRONS.

Fig. 4 - 32 compares the anomalous layer thickness of Coating B and Coating S at 900 µm gap size. It is worth noting that a positive anomalous layer thickness represents a negative AWS and therefore a stagnant layer (sticky layer).

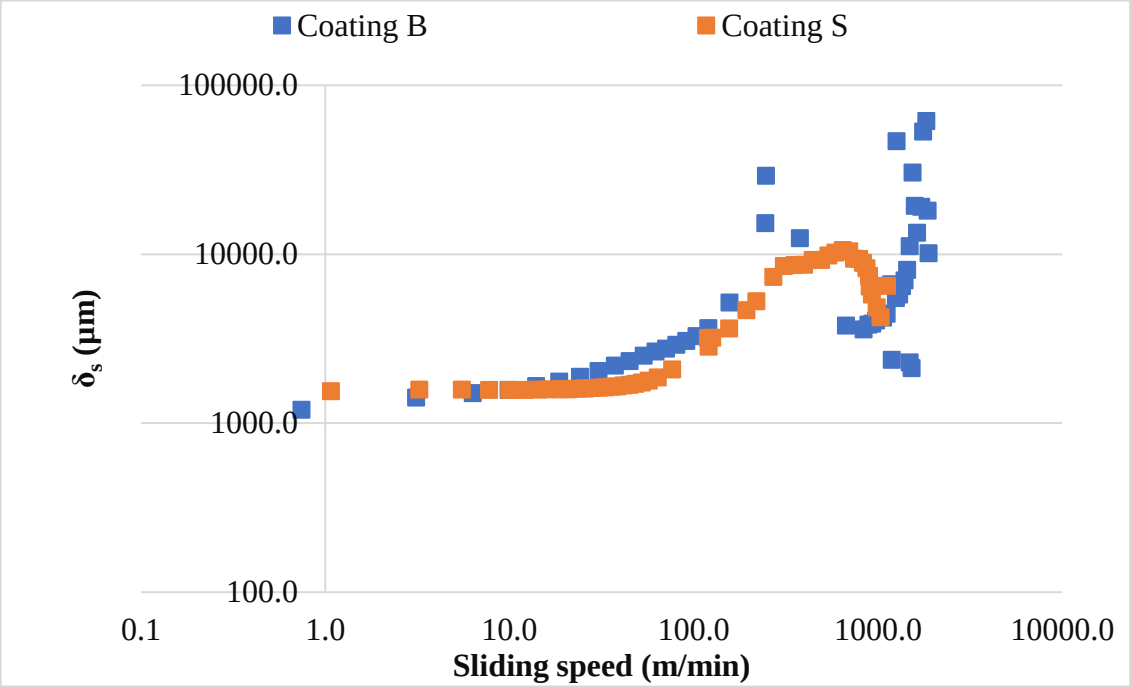

Fig. 4 - 32: A comparison of Stagnation ratio (N) against sliding speed at 900 µm gap size for Coating B and Coating S

A natural log-log plot of anomalous thicknesses and sliding speeds was utilised to focus on the pickup roll speeds between 10 – 100m/min as they represent an industrial pick up roll speed process.

Though constriction effects and negative relative slip contribution were negligible at large gap sizes for both coatings, fig. 4 – 32 shows the presence of stagnant (sticky) layer. For both coatings, it was noticed that the anomalous layer thickness was larger than the gap separation of 900 µm. This reflects a breakdown of the Mooney analysis when subjected to commercial coatings due to additives that might change the chemistry of the coatings. Therefore, a comparison between coatings was conducted based on relative slip

contribution as opposed to anomalous layer thicknesses and, any conclusions reached are more speculative than definite.

4.5 CONCLUSIONS

Numerous shear rheological tests have been conducted therein on Coating B and Coating S to gain an in-depth understanding of the contribution of shear rheology on PMD. Steady-state flow curves showed similarities between coatings, and any subtle differences between coatings were attributed to experimental errors, represented as error bars on the steady-state flow curves. It was therefore concluded that steady-state flow curves did not give us an insight into the origin of the PMD.

Coating B showed higher mechanical properties than Coating S, and therefore believed to award Coating B better ability to form a stable layer of film on the pick - up roll and substrate once deposited. However, high thixotropic behaviour, as a result, was likely to contribute to the formation of furrows and ridges (ribbing phenomena) in the coating film, which was transferred to subsequent units in the downstream end of the process. The effect of mechanical properties on ribbing is investigated in subsequent chapters.

And finally, AWS investigation provided a qualitative insight into the influence of phase separation on the onset of PMD based on relative slip contribution and stagnation ratio (constriction effects). Due to the poor fit of the Mooney analysis method on the rheological data obtained, subsequent results obtained were considered speculative as opposed to definitive. Constriction effects were observed to play a part in the manifestation of negative AWS at small gap sizes. These findings were correlated to flow through the nip gap. However, the scope of the research work was limited to the pick - up process, and therefore AWS at 900 µm was of interest. Large gaps sizes represented the flow in the coating trough because when the pick - up roll is immersed in a coating trough, the distance between the roll surface and the bottom of the trough and / or the sidewalls of the trough is more than $900\mu m$.

At large gap sizes, constriction effects and relative slip contribution were found negligible. However, the size of the anomalous layer for both coatings was thicker than the gap size they occupy. This showed discrepancies when employing the Mooney analysis method. Failure of the Mooney analysis method to accurately predict slip behaviour was likewise seen by the poor fit of the method to the primary data of coatings,

especially at high shear stresses. This was an initial indication of the model breakdown when applied to commercial coatings. Further research on the application of the Mooney analysis of simpler PVC coatings is conducted herein.

In conclusion, dynamic oscillatory tests have provided an insight into the manifestation of PMD. Gap size viscosity dependence, in the prediction of AWS, was found inconclusive in predicting the size of the anomalous layer because the method was developed on the assumption that doesn't fit complex fluids such as viscoelastic behaviour.

CHAPTER FIVE

ASSESSMENT OF THE "PAINT MISSES" DEFECT - PART 4 EXTENSIONAL RHEOLOGY

5.1.INTRODUCTION

Shear rheology in chapter five has provided an insight in the rheological differences between Better coating denoted as Coating B and Standard coating, denoted as Coating S; from steady sate flow curves right through to apparent wall slip. This chapter aims to establish differences in extensional rheology of Coating B from Coating S and thus supporting the third hypothesis. It is worth noting that extensional viscosity in this chapter and subsequent chapters refers to elongational (uniaxial) viscosity.

High extensional viscosity coupled with high speeds has been reported to produce undesired effects during the roll coating process. Undesired effects such as misting[40][41][42], ribbing, paint starvation, amongst others. In this study, we argue that high extensional viscosity at high pick up roll speeds counteracts PMD. To pick up a high quantity of coating from the coating trough especially when operating in a fully starved regime, a degree of extensional viscosity is necessary to allow a delayed film breakup time of the coating before film split.

Having found Coating B to possess higher elastic (solid-like) properties than Coating S from the dynamic oscillatory test, it was hypothesised that Coating B possessed high extensional viscosity than Coating S. Therefore, Coating B has a delayed film break up time than Coating S thus material properties enable high quantity of coating to be picked up from the trough to subsequent units. Fig. 5 - 1 schematically demonstrates the influence of extensional viscosity and mechanical properties on the quantity of the coating film picked up from the coating trough by the pick-up roll at Tata steel colors in Shotton. Scenario 1 shows a delayed break uptime of the coating film due to high extensional and mechanical properties, hence the high quantity of coating picked up from the coating trough. Scenario 2 demonstrates a quick film break up time of coating with low extensional viscosity and mechanical properties.

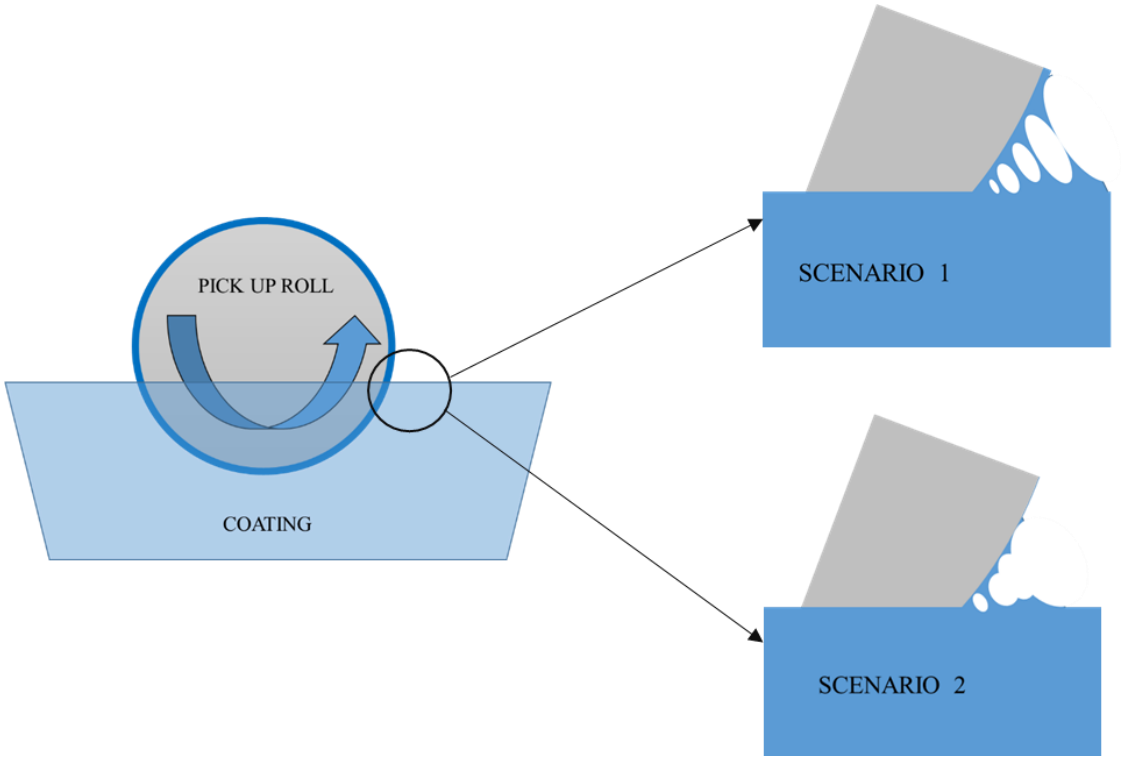

Fig. 5 - 1: Schematic of a pickup roll in the coating trough with high extensional flow (scenario 1) and low extensional flow (Scenario 2)

5.2.MATERIALS CHARACTERISATION

In addition to shear flow, extensional flow is encountered during the roll coating process over a short period [124]. Flow properties such as delayed film break-up time and flow index during extensional flow are believed to influence the onset of PMD. Extensional flow is therefore inevitable in this process.

A Capillary Break-Up Rheometer (CaBER), an in-house built experimental device at Swansea University under WCPC (Welsh Coating and Printing Centre) showed in fig. 5 - 2, was employed to study extensional viscosity of the coating samples.

A high-speed camera was employed to record a series of images of the progressive thinning of filament radius over a period time, at settings of 2000 frames per second. The experimental device consisted of 3 mm cylindrical diameter plates, a high-speed camera, computer device to control the separation of the plates, and the Lab view data acquisition program to record images or video of the progressive filament thinning of the coating sample.

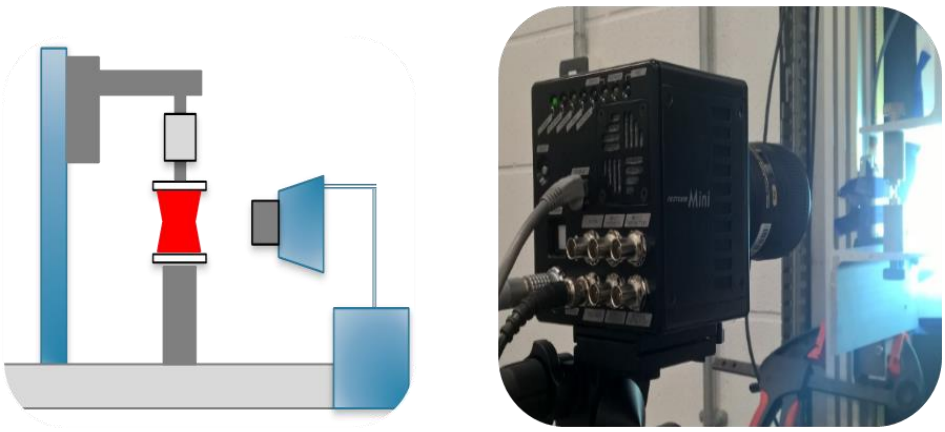

Fig. 5 - 2: CaBER employed in the study extensional flow properties of coating samples

The size of cylindrical plates is important as it dictates the influences of gravitational and surface tension forces on the obtained results. Gravitational forces are required to be lower than surface tension to avoid sagging effect.

Jürgen [7] studied the effect of cylindrical plate sizes on the gravitational effects using the Bond number (Bo) on cylindrical plate diameters of 4, 6 and 8 mm. The author concluded that the Bo number in Eqn. (5 -1) decreased with decreasing size of the cylindrical plate. This was possibly due to the increase in the mass of the test sample due to increased volume when a larger plate diameter was used. As a result, an increase in gravitational force is experienced thus increasing the bond number. Therefore, a 3 mm diameter plate was utilised in the experimental work.

$$B_0 = \frac{\Delta\rho g r_{mid}(t)^2}{\sigma} \qquad (5 - 1)$$

Where B_0 is the bond number, $\Delta\rho$ is the differential density (kg/m^3), $r_{mid}(t)$ is the radius at a specific time (m) and σ is the surface tension (N/m).

A sample of silicone oil sample was placed in the initial gap size of 1.3 mm between the two cylindrical plates using 1μm syringe and 1mm needle to form a cylindrical filament. Two coaxial plates were separated to a known final distance, *Lf*, by keeping the bottom plate stationery and moving the top plate. A series of images were collected and subsequently analysed to obtain strain rate, film break break-up time, strain and extensional viscosity of the coating samples.

5.2.1. EFFECT OF FINAL SEPARATION DISTANCE ON THE EXTENSIONAL RHEOLOGICAL PROPERTIES

The effect of the final gap size was investigated using silicone oil with 1mPas shear viscosity, 35mN/m surface tension and the specific gravity of 0.97 (970 kg/m^3). A sample of silicone oil was initially placed in the gap size of *Li* = 1.3 mm, between the two cylindrical plates using a pipette or syringe and 1mm needle, to form a cylindrical filament. Two coaxial plates were separated at a distance, *Lf*, = 3.4, 3.72 and, 5.2 mm. Fig. 5 – 3 shows the three separation distances of the cylindrical plates. The experiment was conducted at a room temperature of 20 ^{0}C.

The choice of using silicone oil was because e silicone oil is easier to load in small gap sizes employed in the CaBER equipment. Silicone oil is also low in viscosity and has a homogeneous phase, therefore less cumbersome to conduct experimental runs.

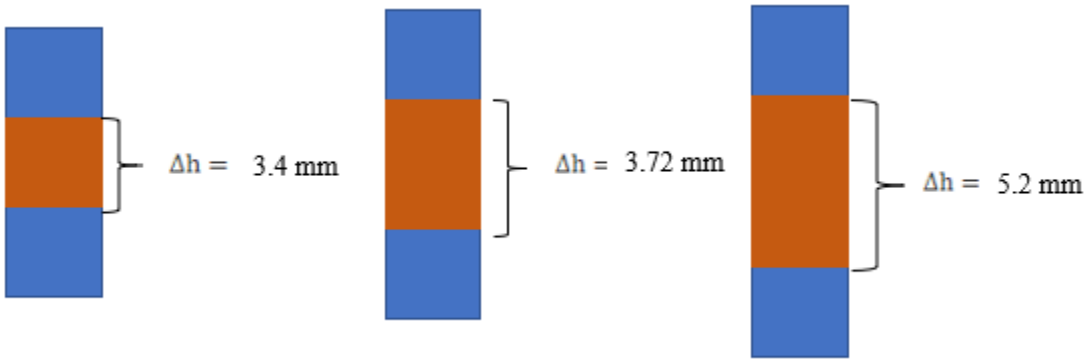

Fig. 5 - 3: Schematic of plate separation at different differential gap sizes. The initial separation gap of 1.3 mm is included in the total distance.

2.2. DETERMINATION OF EXTENSIONAL VISCOSITY OF COATING SAMPLES

Upon establishing the effect of gap size on extensional viscosity, experimental work was conducted on Coating B and Coating S using the same methodology in section 5.2.1. An initial and final separation distance of 1.3 mm and 5.2 mm, respectively, were employed. Data analysis was conducted using CaBER analyser tool, developed at WCPC.

5.3 RESULTS

5.3.1 EFFECT OF GAP SIZE DISTANCE ON THE EXTENSIONAL RHEOLOGICAL PROPERTIES

Effect of gap size (final gap size) on extensional rheology was conducted on three differential gap sizes, Δh = 2.08, 2.42 and 3.03 mm. Fig. 5 – 4 shows images of progressive filament thinning of silicone oil over a period, while fig. 5 – 5 compares progressive filament radius as a function of time for differential gap sizes.

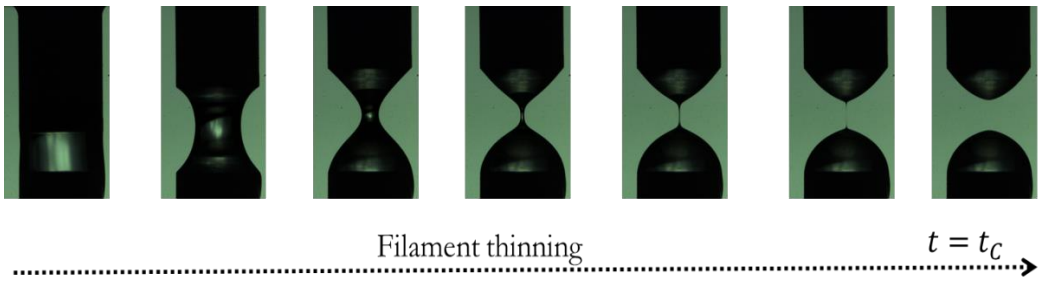

Fig. 5 - 4: Progressive filament thinning of Silicone oil

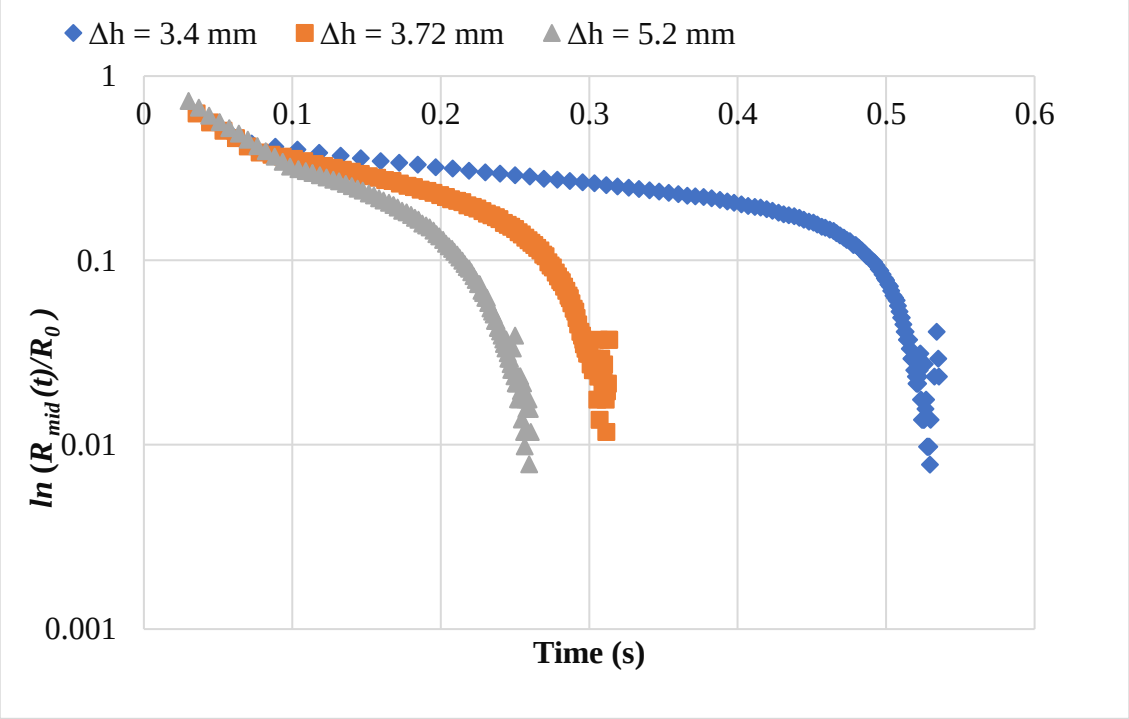

Fig. 5 - 5: Progressive filament thinning of silicone oil as a function time at different separation distances

The effect of gap size on coating flow properties – that is to say, flow index and consistency, were determined from the primary data collected. Silicone oil is a power-law model therefore; it obeys Eqn. (5 - 2). Eqn. (5 - 3) and (5 - 4). Employing the equations, rheological flow properties were determined.

$$\frac{R_{mid}(t)}{R_0} = \Phi \frac{\sigma}{k} (t_c - t)^n \quad (5 - 2)$$

Eqn. (5 – 3) can be rewritten into Eqn. (5 - 4) by applying natural logarithm to have the equation in the form of Y = mx+ c

$$ln \frac{R_{mid}(t)}{R_0} = \ln \left(\Phi \frac{\sigma}{k} \right) + nln(t_c - t) \quad (5 - 3)$$

$$\Phi = \frac{2^{-n}}{3} \quad (5 - 4)$$

Where $R_{mid}(t)$ the mid radius is at a specific time (m), t_c is the critical time (S) and Φ is the pre – factor (-) , n is the flow index (-), K is the consistency (Pas^n)

Fig. 5 – 6 shows a natural log-log plot of dimensionless radius against differential time, while Table 5 – 1summaries extensional flow properties of silicone oil obtained at different gap sizes.

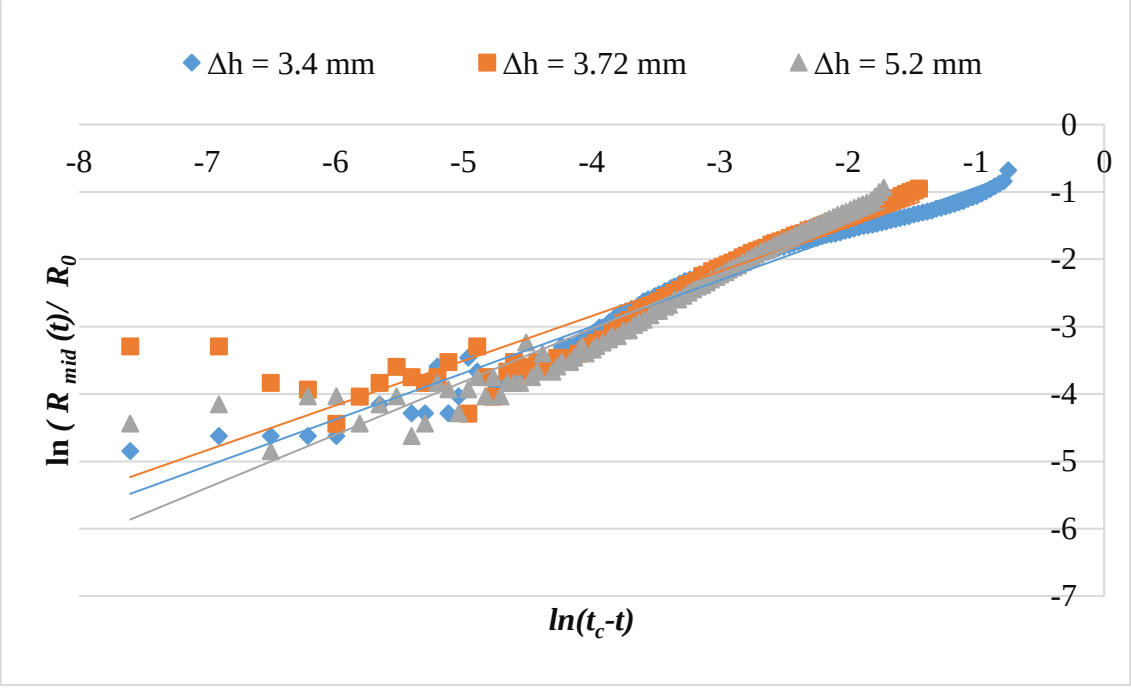

Fig. 5 - 6*:* Determination of flow properties of Silicon oil at different gap sizes

Table 5 - 1: A summary of extensional rheological properties of Silicone oil

ΔH [mm]	n [-]	K [Pas^n]	Break up time [s]	Ave. μ_E(Pas)
3.4	0.7	0.6	0.53	7.5
3.72	0.7	0.6	0.32	7.0
5.2	0.8	0.04	0.25	6.9

The curves exhibited two distinct regions; the first region was credited to the flow influenced by sagging and bulging, the second region was credited to the flow dictated by surface tension. Large gap sizes (Δh = 3.03 mm) were tremendously affected by gravitational forces which lead to sagging and bulging effects. This was reflected in the size of the first region in comparison to the second region.

Silicone oil showed stronger tension thinning properties at small gap sizes compared to a large gap size. The strength of a tension thinning material is quantitatively described by the flow index, n. when n > 1 the material is tension thickening. At n < 1, the material is tension thinning, while n = 1, the material is known to be a Newtonian fluid. The closer the n value to 0, the stronger the tension thinning properties, and the vice versa is true for tension thickening properties. In this context, silicone oil showed weak tension properties at all gap sizes while critical breakup times varied at all gap size.

Additionally, the critical filament breakup time of silicone oil at gap separations of 3.4, 3.72 and 5.2 mm were determined at 0.25, 0.31and 0.54 seconds, respectively. This inferred that there is a strong dependence of critical film break up time on gap size. It is worth noting that the film break - uptime is a function of both material properties and operating parameters, and therefore cannot be solely attributed to material properties.

However, the difference in the average extensional viscosity due to gap size was found to be negligible, with acceptable error tolerance ± 0.3 Pas. It was therefore deduced that gap size influences the flow properties of the silicone oil, but the negligible difference on average extensional viscosity. A high degree of confidence in the CaBER experimental equipment is therefore guaranteed to test tensile properties on the coating samples.

For the subsequent investigation of tensile properties on coating samples, a separation distance of 3.03 mm was employed to enable better loading of coating sample into the separation gap.

3.2. CABER FILAMENT RADIUS PROFILE AS A FUNCTION OF TIME

A comparison of Caber filament radius profile of Coating S and Coating B was conducted, and the results are presented in fig. 5 – 7. A faster rate of filament radius reduction with time was observed for Coating B compared to Coating S. Also, a critical filament breaks up time was determined at 0.45 and 0.57 seconds for coating S and B, respectively

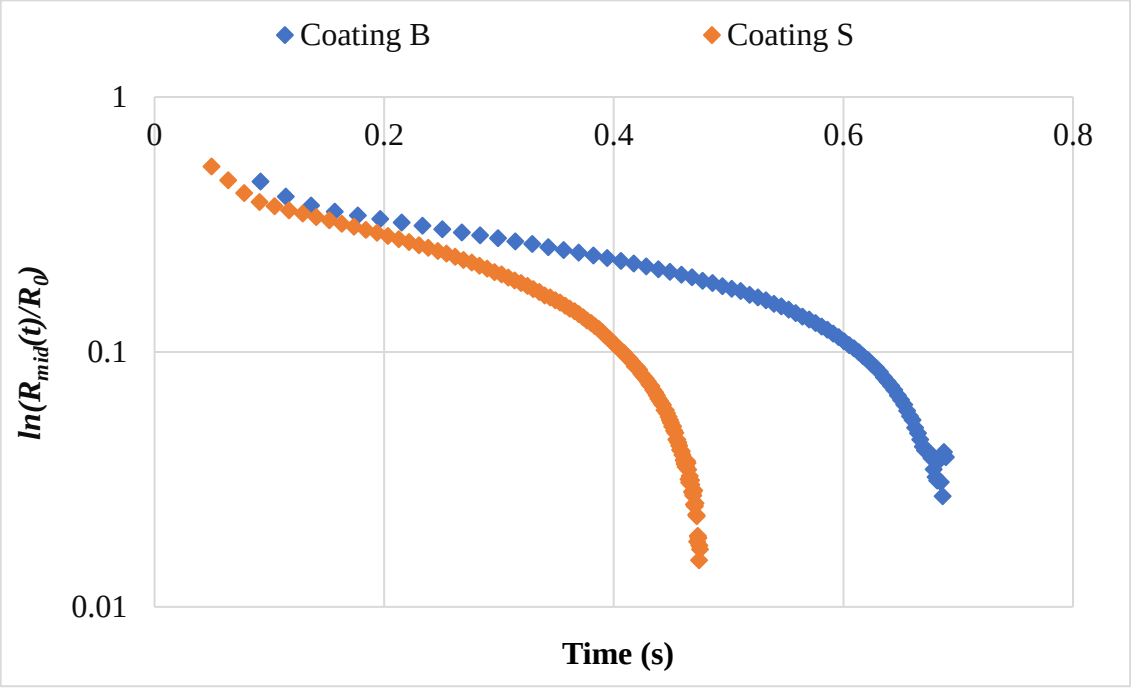

Fig. 5 - 7: Progressive filament thinning radius of Coating samples against time.

Flow index of 0.49 and 0.56 for Coating B and Coating S, respectively, were determined in fig. 5 – 8 when the power-law model was fitted on the primary data. The data scatter at the low experimental times was credited to the sagging and bulging effect. The flow properties suggested that Coating B is a stronger tension thinning fluid compared to Coating S.

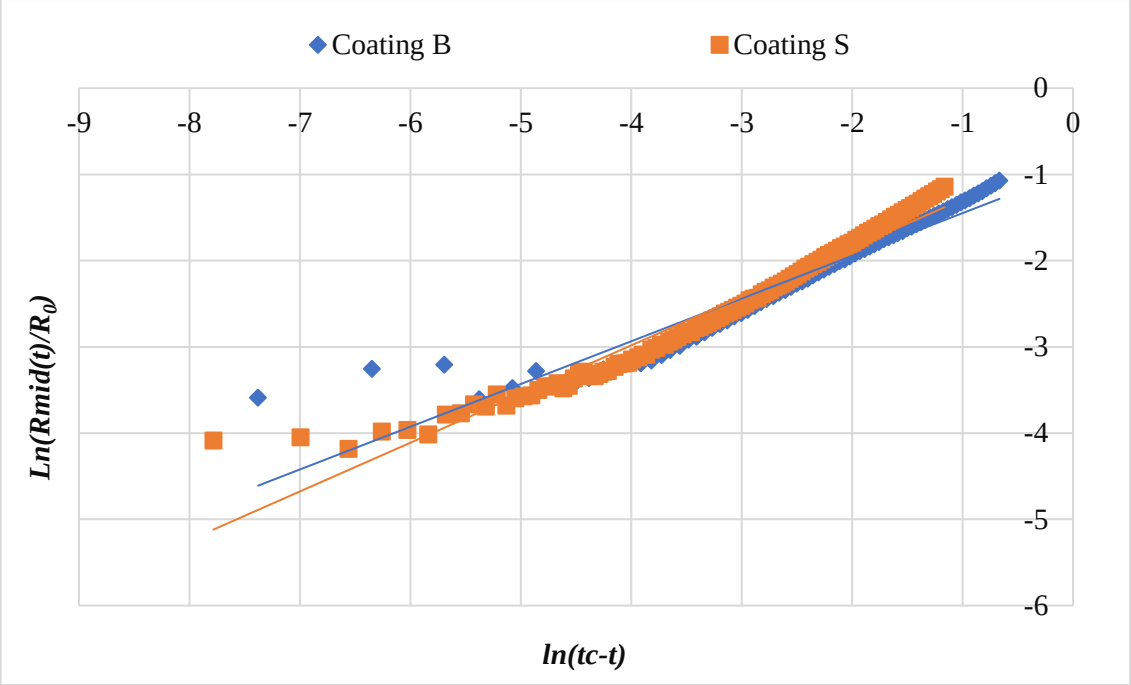

Fig. 5 - 8: Progressive filament thinning radius of Coating samples against time.

5.3.2 EXTENSIONAL VISCOSITY AGAINST HENCKY STRAIN

Fig. 5 – 9 compares extensional flow curves of Coating B and Coating S. Coating B not only showed stronger tension thinning behaviour but also exhibited higher zero and plastic viscosity compared to Coating S.

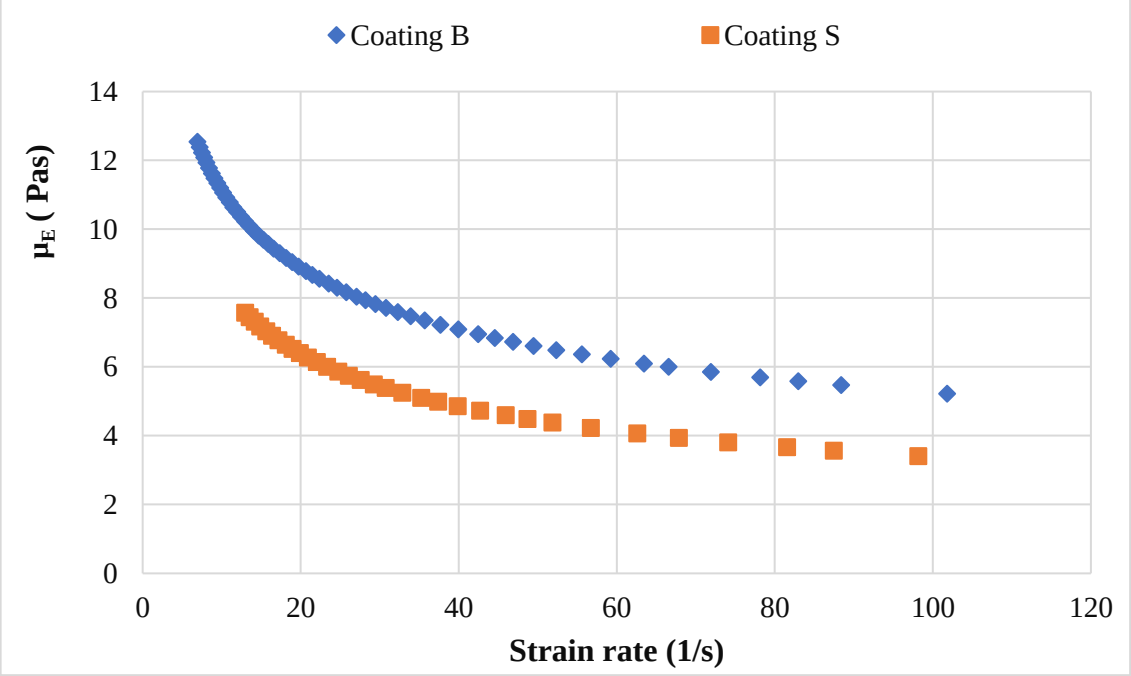

Fig. 5 - 9: Extensional viscosity against strain

It was therefore believed that higher extensional viscosity leads to a delayed critical film break up time which aids a high quantity of coating to be picked up from the coating trough onto the pick-up roll. Coating S with low extensional viscosity and a faster break up time is limited to the quantity of coating picked up from the coating trough by the pick-up roll

5.4 CONCLUSION

The measurement of shear and extensional behaviour of the coatings have highlighted that small deviations in the initial formulation and manufacturing can be measured using rheological techniques and these can be used to identify a material which is liable to suffer PMD. Rheological techniques can more clearly identify deviations from ideal behaviour than chemical and wetting techniques and also provide evidence for the principle mechanisms of process failure.

The current QC method is inadequate for the measurement of incoming coatings as it is insensitive to the small changes in coating characteristics, which dictate performance. Therefore, an improved QC method that can identify differences in batches before coating deposition is given herein. PVC coatings that meet the criteria of rheological properties below should be deemed appropriate for the roll coating process during the manufacturing of PVC plastisol pre-coated steels for architectural steels.

Ideally, during steady-state viscosity measurements coatings should be characterized using controlled stress employing a small sample cone and plate/parallel plate rheometer.

Under dynamic oscillatory rheometry, phase angle values in the frequency range of 0.1 to 20 Hz, conducted within the LVR, should lie in the range of $55 – 70^0$. Additionally, Coating B and Coating S showed an overlap of viscous modulus but the difference in elastic modulus curve was seen. Therefore, the elastic modulus is more influential than the viscous modulus. This is because materials with high solid-like behaviour are more versatile in a high-speed roll coating process.

And finally, extensional/ elongational viscosity with flow index equal to or less than 0.5, accompanied by plastic viscosity of ~ 7 Pas is enough to control the critical filament break up time at a given pick up roll speeds.

To test the validity of the QC system developed in this chapter, an initial test procedure is given in chapter six for another set of PVC coatings.

CHAPTER SIX

ASSESSMENT OF THE "PAINT MISSES" DEFECT - PART 6 METHOD VALIDATION

6.1 INTRODUCTION

Considering characterisation work conducted on Plasticeram black coatings, a blind test was conducted on two coating samples. The aim was to test the hypothesis that the rheological methodologies developed in previous chapters could be employed to identify materials which were likely to PMD. Two batches of a grey paint (Plasticeram sun Merlin), one of which had exhibited PMD on the coating line but had passed the QC system were tested. In this instance, the sample which had experienced the operational defect was not known at the outset. A successful outcome would be the identification of sample which had exhibited PMD, purely from characterization.

6.2 METHODOLOGY

The methodology of the experimental work conducted in this chapter was identical to that detailed in Chapter three to chapter five. However, contact angle and surface energy measurements were excluded from the list of characterization techniques because negligible differences in wettability were observed. Additionally, FT - IR analysis was also excluded from the list of experiments conducted. The samples were labelled Coating X and Coating Y and each was put through the same rigorous testing.

6.3 RESULTS AND DISCUSSIONS

6.3.1 MICROSTRUCTURAL ANALYSIS AND ELEMENTAL ANALYSIS

In this section of chapter six, microstructure and elemental analysis were studied on Coating X and Coating Y. Particle size and distribution contributions did not also appear to be significantly different, represented in Fig. 6 – 1, and the elemental analysis in Fig. 6 – 2 did not indicate any detectable differences in chemical constituents.

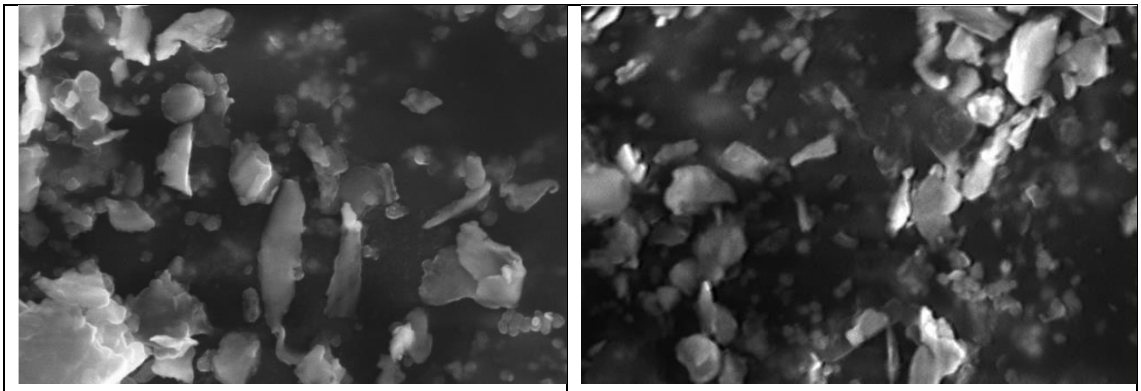

(a) Coating X | (b) Coating Y

Fig. 6 - 1: Micrograph of Coating (a) X and (b) Y showing particle size and distribution at 1 µm scale and 8.42K resolution.

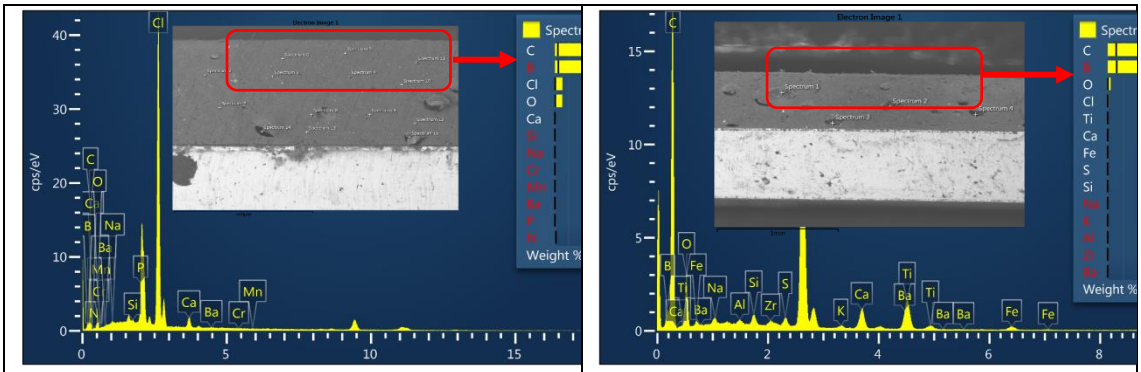

(a) Coating X | (b) Coating Y

Fig. 6 - 2: Elemental analysis of Coating (a) X and (b) Y

6.3.2 THERMAL GRAVIMETRIC ANALYSIS

Coating X and Coating Y were thermally analysed using TGA – DTG. Fig. 6 – 3 compares thermograms of Coating X and Coating Y. The mass loss stages observed for Plasticeram Black coating samples in chapter three-show similarities with mass loss stages for Coating B and Coating S. Therefore, in-depth analysis of thermal degradation of Coating B and Coating S was employed for Coating X and Coating Y.

The comparison of TGA-DTG thermographs showed negligible differences in compositions of the coatings understudy, though the subtle difference in the first mass loss stage within a temperature range of 236 – 263 ^{0}C was observed. The first mass loss stage was ascribed to the loss of the solvent mix of BDA and Petrosol. The flashpoint of BDA and Petrosol is 94 and 116 ^{0}C, respectively. Therefore, Coating X showed ~ 2%

more Petrosol than Coating Y. Otherwise, there was a negligible difference seen under thermal analysis. Table 6 - 1 and Table 6 -2 summarise the composition analysis and thermal properties, respectively.

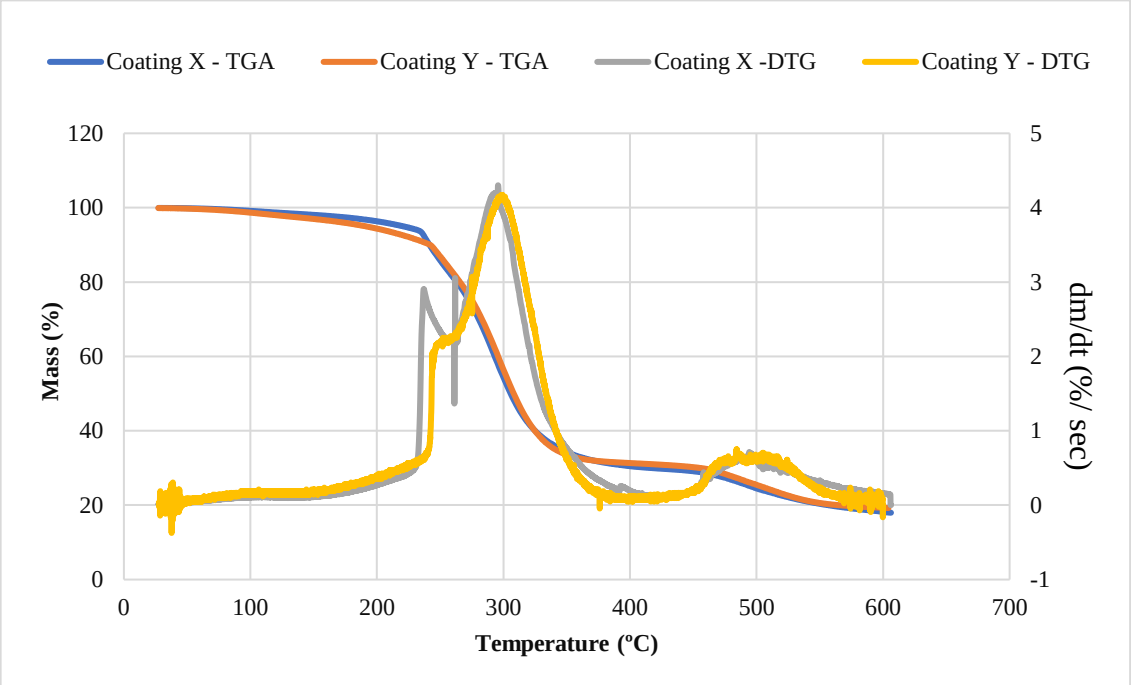

Fig. 6 - 3: Comparison of thermal degradation (primary axis) and rate of degradation (secondary axis) as a function of temperature for Sample X and Y

Table 6 - 1: Summary of TGA results

	Coating X		**Coating Y**	
	Temperature range (^{0}C)	Mass (%)	Temperature range (^{0}C)	Mass (%)
Solvent (First Peak)	28 - 237	~10	28 – 245	~11
(De - chlorination) Second peak	237 - 300	~59	245 - 300	~58
(Decomposition of Polyene) (Third Peak)	300 - 552	~19	300- 552	~16
Final residual Mass (Char, Pigment and fillers)	552 - 600	~19	552-600	~19

Table 6 - 2: Thermal properties obtained from (TGA- DTG) results

	Coating X	**Coating Y**
Initial decomposition Temperature (IDT)	~ 28 ^{0}C	~ 50 ^{0}C
$D_{1/2}$ (50% mass decomposition) temperature	~ 276 ^{0}C	~ 276 ^{0}C
Maximum rate of decomposition temperature (MRDT)	~ 267 ^{0}C	~ 267 ^{0}C

6.3.3 SHEAR RATE DEPENDENT VISCOSITY

A comparison of steady-state viscosity flow curves of Coating X and Y is carried in fig. 6 – 4. Coating X and Y are non – Newtonian shear-thinning fluids with both a power law and Newtonian plateau. However, Coating X presented a higher zero shear viscosity and a plastic viscosity than Coating Y at the Newtonian plateau.

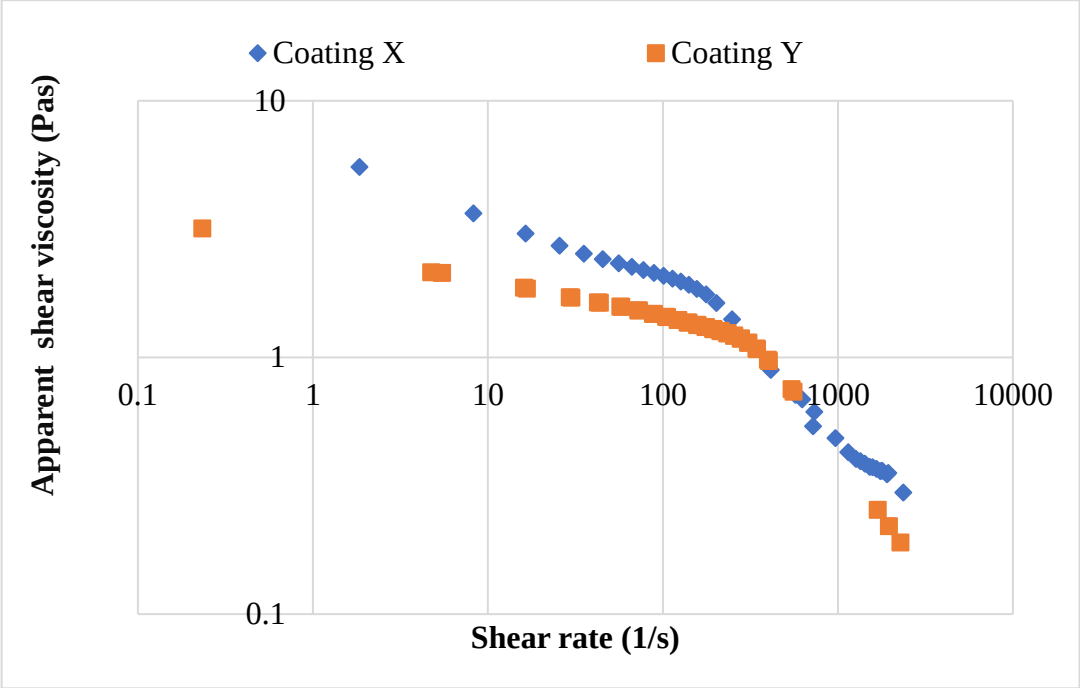

Fig. 6 - 4*:* A comparison of the steady-state viscosity flow curves of Coating X and Coating Y

6.3.5 DYNAMIC OSCILLATORY RHEOMETRY

6.3.5.1 DYNAMIC AMPLITUDE SWEEP

Fig. 6 – 5 and fig. 6 – 6 show amplitude sweeps of Coating X and Coating Y, respectively, conducted at a frequency value of 1 Hz in strain range of 0.01 to 20.

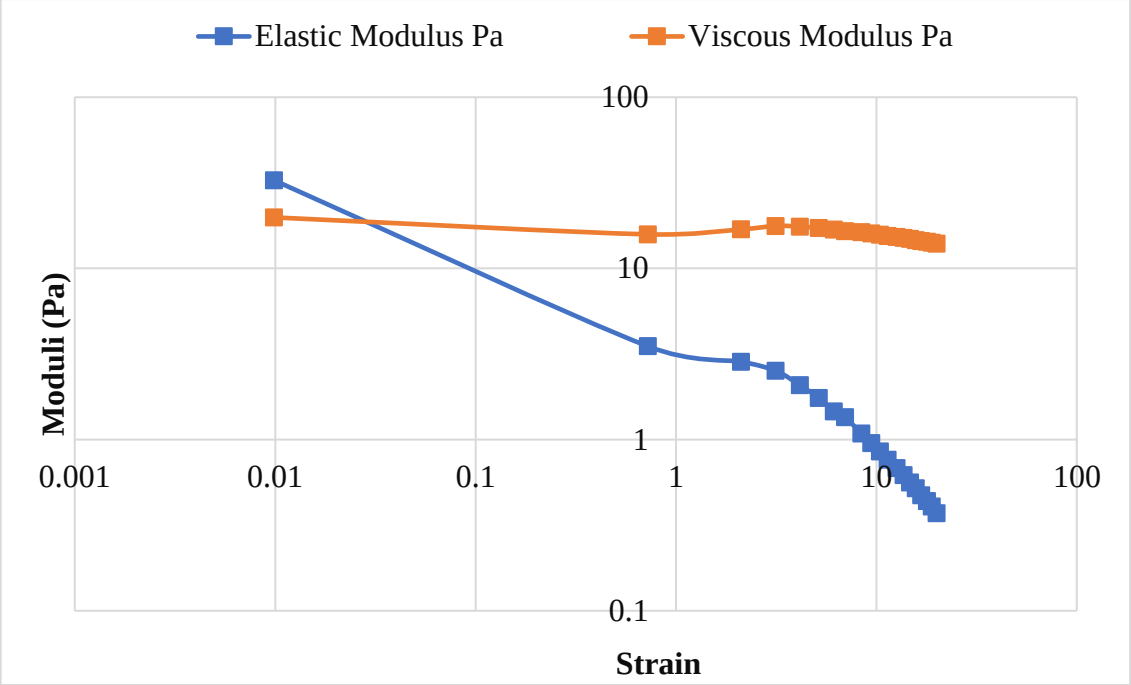

Fig. 6 - 5: Amplitude sweep for Coating X

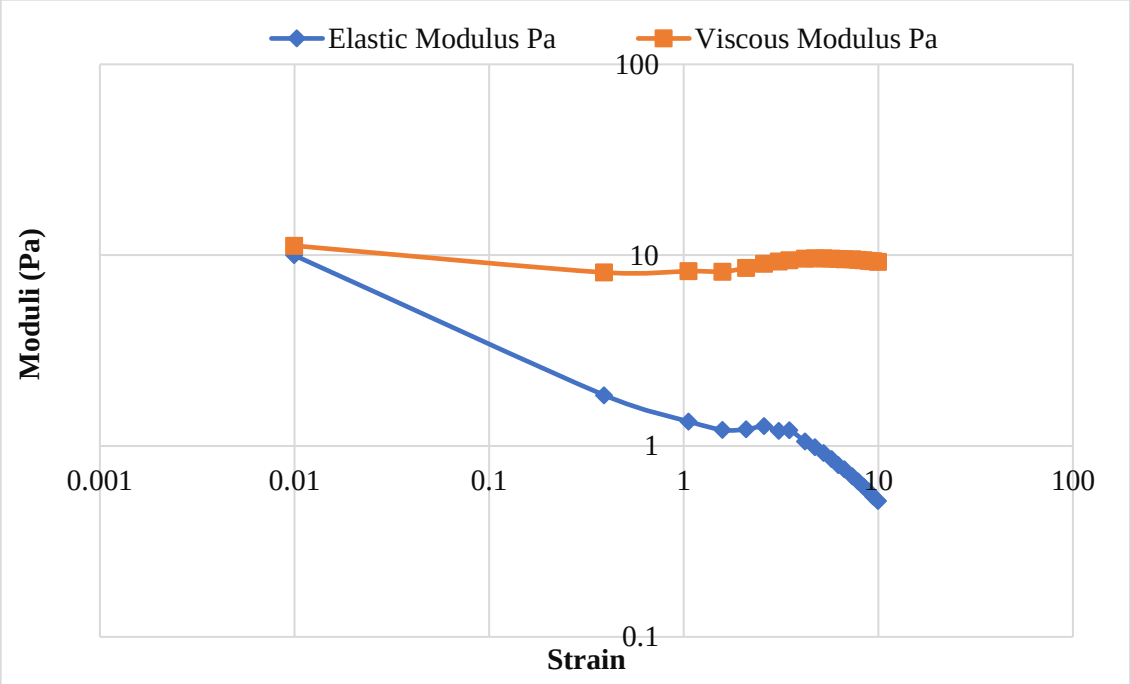

Fig. 6 - 6: Amplitude sweep for Coating Y

6.3.5.2 DYNAMIC FREQUENCY SWEEP

A strain value of 0.7 and 0.4 for Coating X and Coating Y respectively were employed for in frequency sweeps. The strain values mentioned above lay within the LVR region and therefore suitable for characterising materials within the SAOS region. Fig. 6 - 7 and

6 - 8 show frequency dependence of both elastic and viscous modulus for Coating X and Coating Y, respectively.

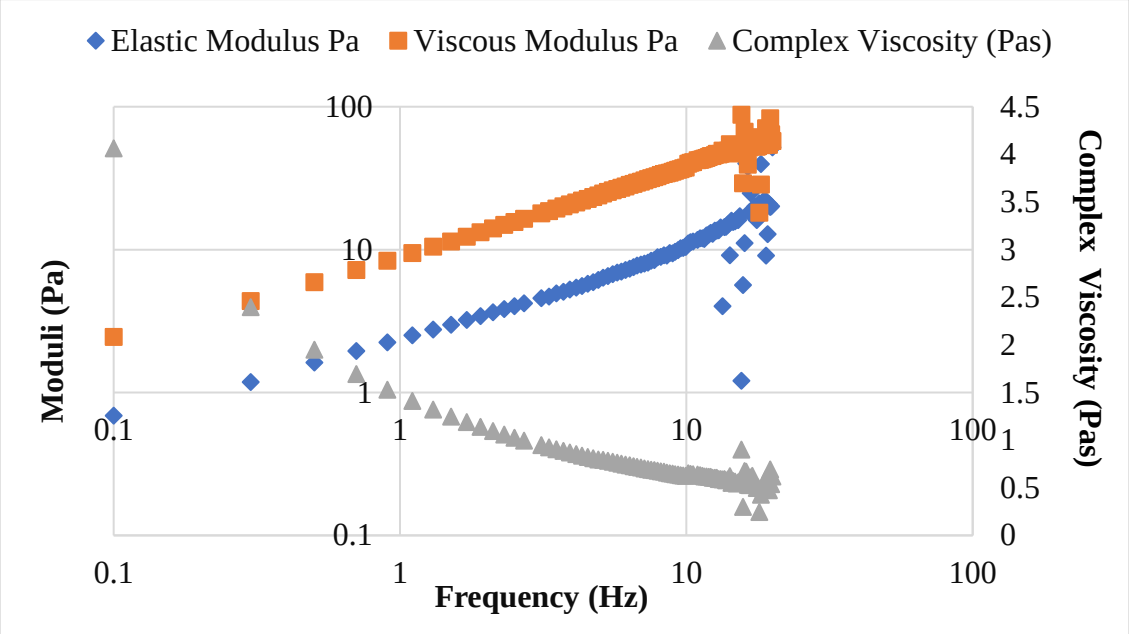

Fig. 6 - 7: Frequency sweep for Coating X at strain value of 0.7

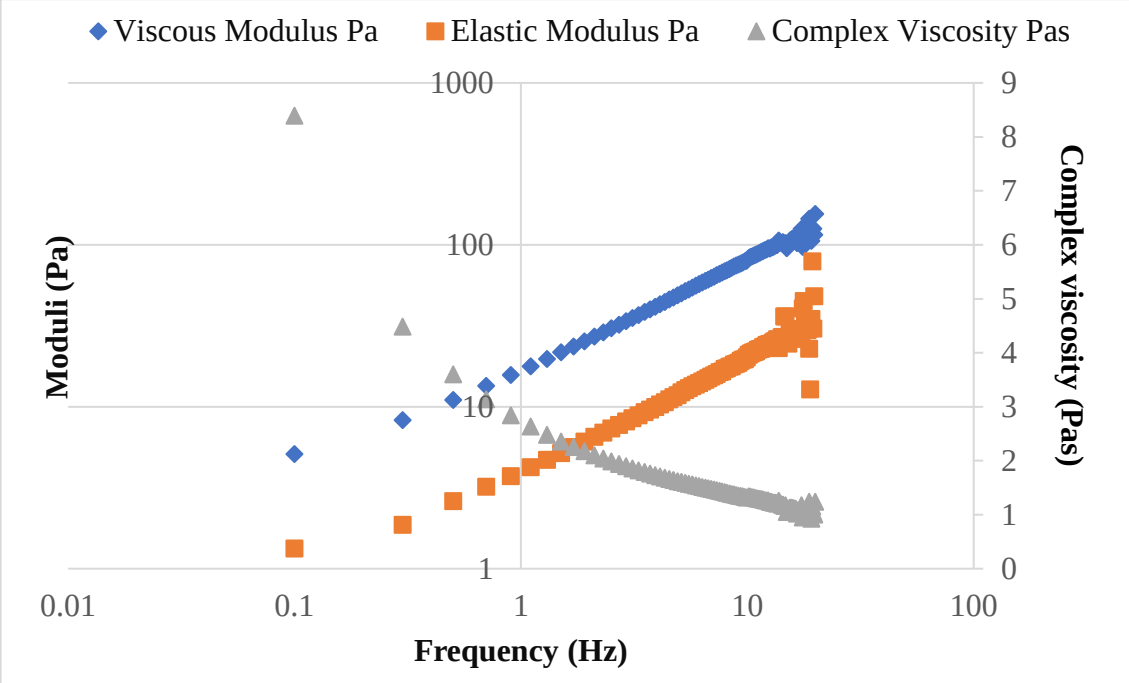

Fig. 6 - 8: Frequency sweep for Coating Y at strain value of 0.4

Two observations found from the frequency sweeps of Coating X and Coating Y. Firstly, both the elastic and viscous moduli increased with increasing frequency denoting an increase in solid-like and liquid-like behaviour when the time was reduced during the deformation of the material. Secondly, viscous moduli were higher than the elastic moduli

on both coatings. This signified that both coatings behave more liquid-like than solid-like and therefore they are viscoelastic liquids throughout the frequency test range. And finally, the complex viscosity decreased with increased frequency due to the non-Newtonian behaviour of coating materials when the deformation rate increased.

A comparison of elastic and viscous moduli and complex fluids, for Coating X and Coating Y are presented in fig.6 – 9, 6 – 10 and 6 – 11, respectively.

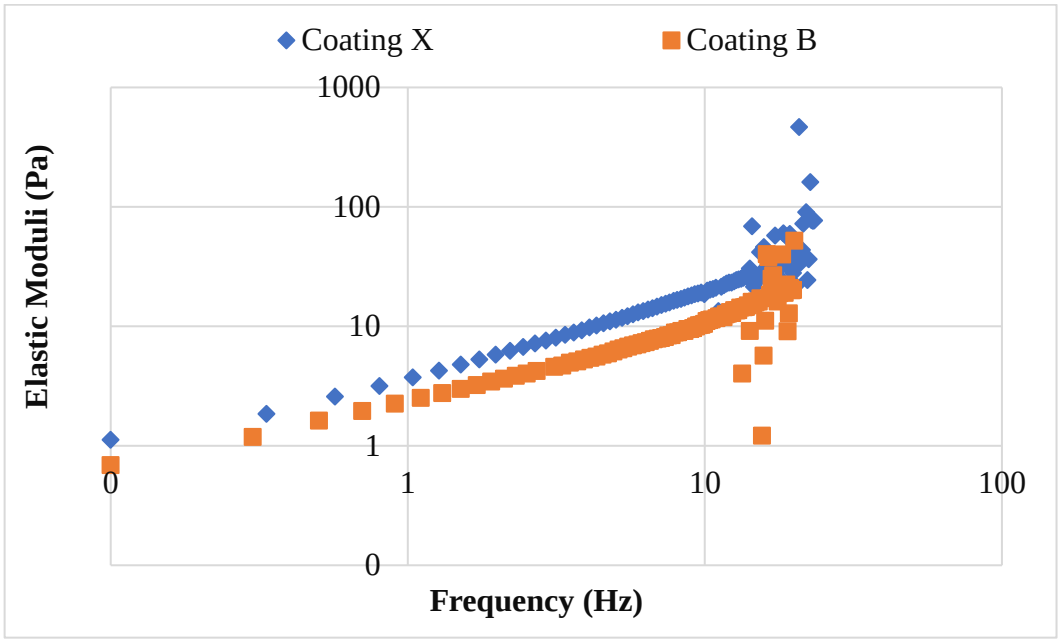

Fig. 6 - 9: Comparison of elastic moduli for Coating X and Coating Y

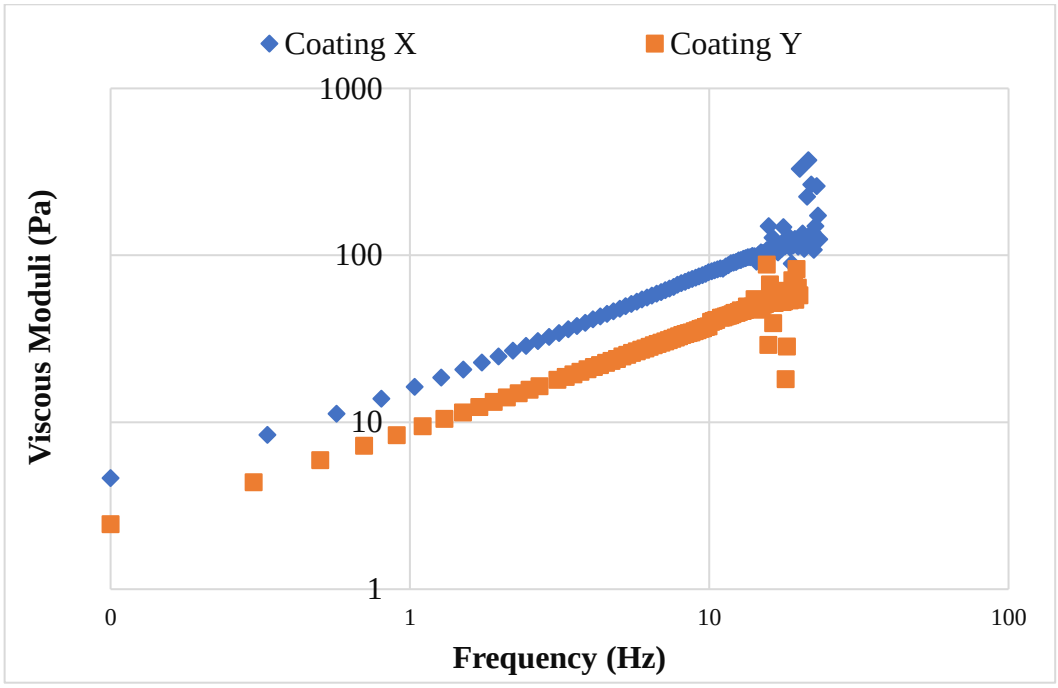

Fig. 6 - 10: Comparison of Viscous moduli for Coating X and Coating Y

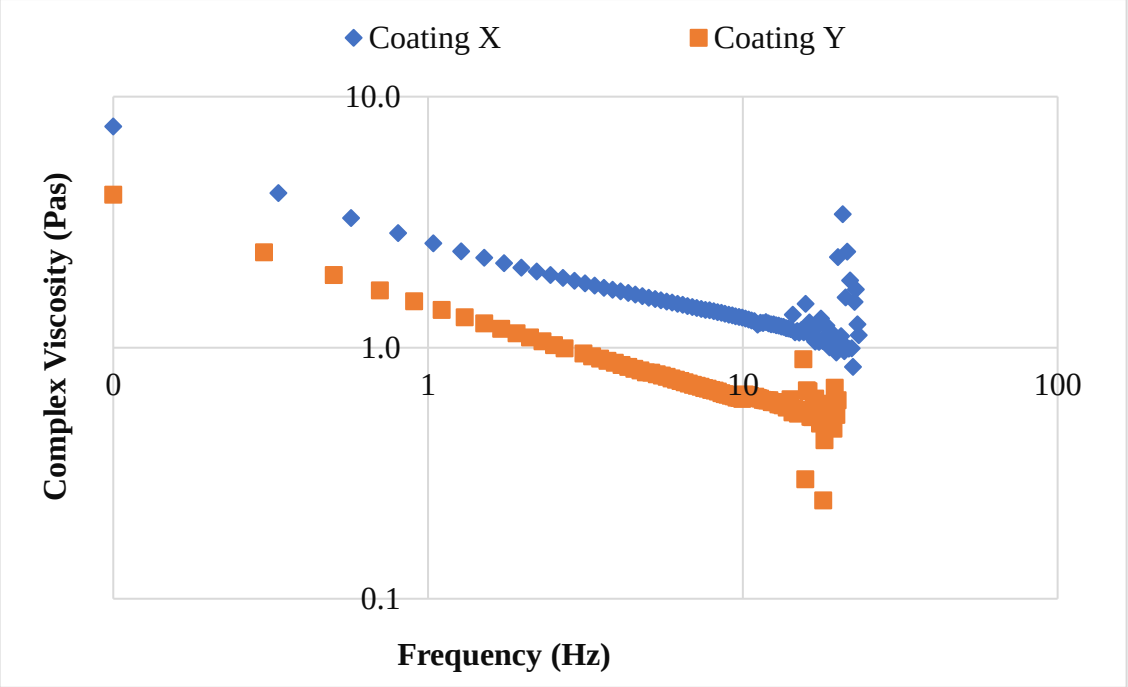

Fig. 6 - 11: Comparison of complex viscosity for Coating X and Coating Y

The elastic and viscous moduli of Coating X were noticeably higher than Coating Y, depicting higher solid-like and liquid-like behaviour of Coating X. Similarly, complex viscosity was higher for Coating X than Coating Y despite the results obtained from the composition and elemental analysis for both coatings that inferred the same elements and composition within the coating systems.

6.3.6. APPARENT WALL SLIP INVESTIGATION

6.3.6.1. APPARENT SHEAR RATE AGAINST SHEAR STRESS

It has been shown that shear and viscoelastic behaviour of the two blind samples are appreciably different, although both were able to pass the current QC system. Previously, in chapter four, it was postulated that the mechanism by which PMD occurred could be attributed to AWS near the rotating roll in the coating trough. To investigate whether such differences could also be seen in the blind sample, these were put through the same characterization process.

Fig. 6 - 12 and 6 – 13 show gap size apparent shear rate dependence of Coating X and Coating Y from 100 to 900 µm. The apparent shear rate increased with increasing shear stress linearly at small gap sizes. However, a non- linear relationship between apparent shear rate and shear stress was observed at large gap sizes; apparent shear stress increased nonlinearly with increased shear rate.

Also, the apparent shear rate increased with increasing separation gap and, therefore viscosity decreased with increasing gap size for both coatings. This depicted the presence of AWS in the coating flows. At 610 - 1000 Pa, Coating X exhibited a noticeable shift in flow curves. This indicated the presence of AWS in Coating X than Coating Y.

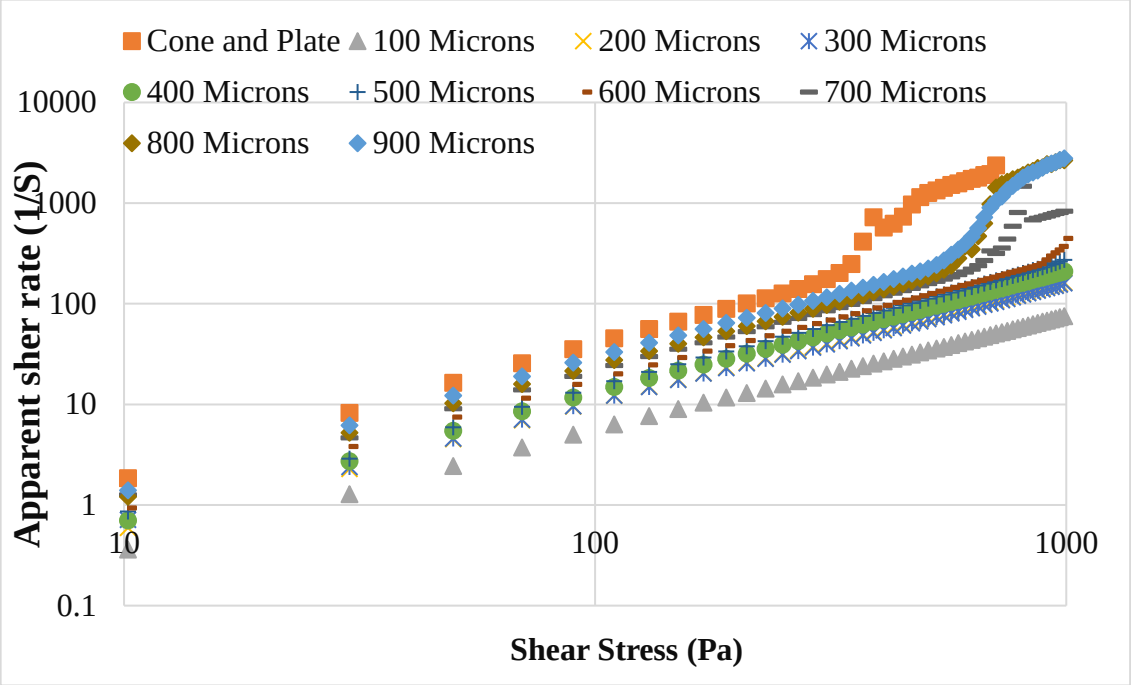

Fig. 6 - 12: Apparent shear rate against shear stress for Coating X

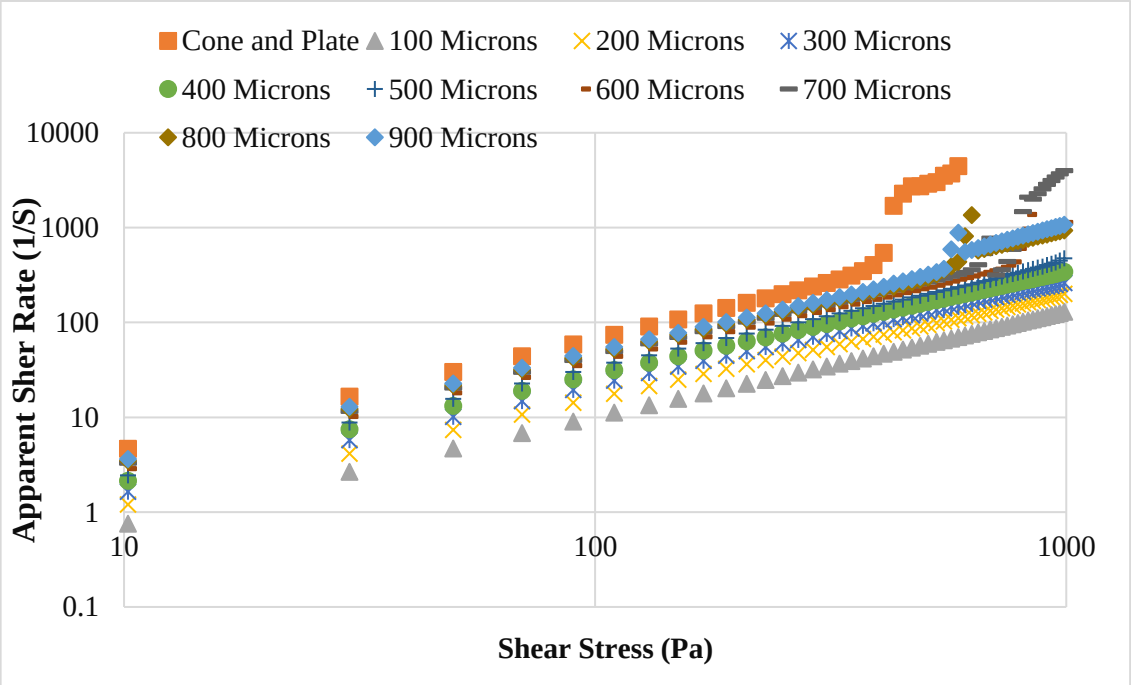

Fig. 6 - 13: Apparent shear rate against shear stress for Coating Y

AWS characteristics were determined using the Mooney method as that employed for Plasticeram Black coatings. Fig. 6 – 14 and Fig. 6 – 15 show apparent shear rate against

inverse gap for Coating X and Coating Y, respectively. And fig. 6 – 16 compares the accuracy of the Mooney method on the primary data obtained for both coatings.

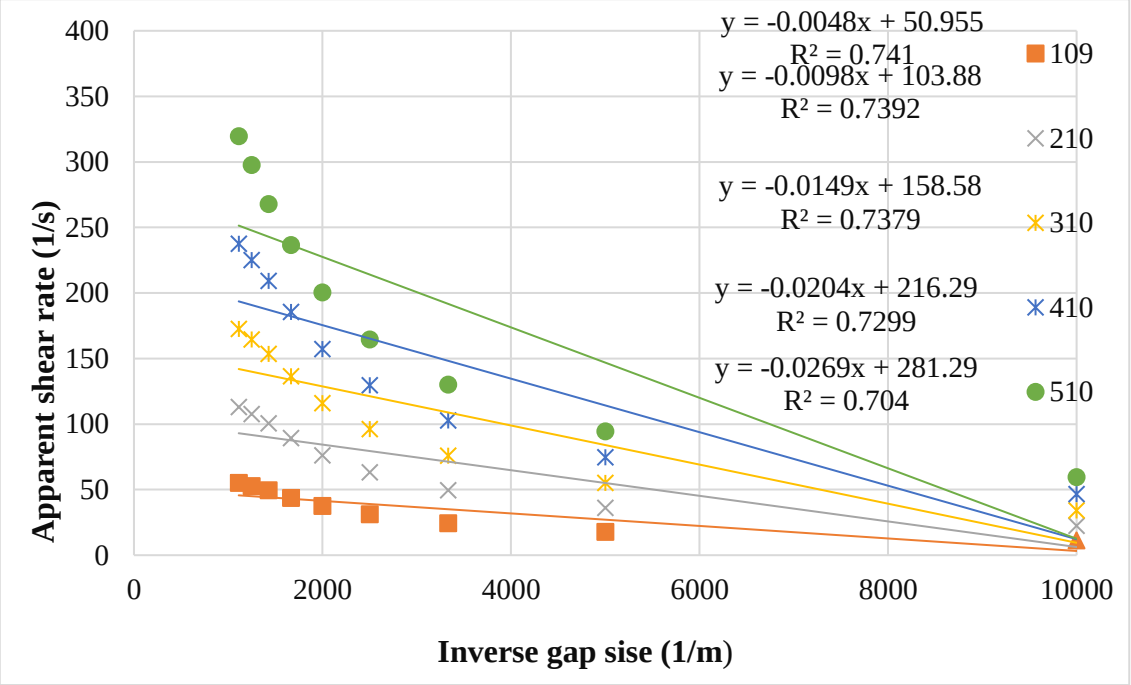

Fig. 6 - 14: Apparent shear rate against inverse gap between from 109 – 510 Pa for Coating X

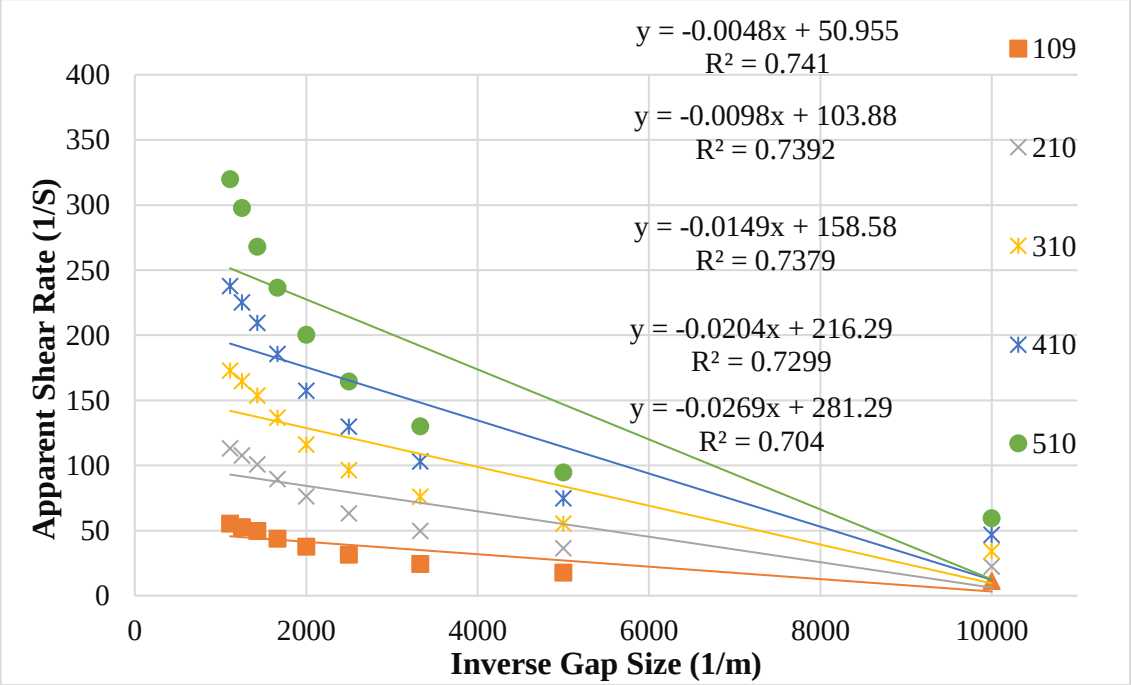

Fig. 6 - 15: Apparent shear rate against inverse gap between from 109 – 510 Pa for Coating Y

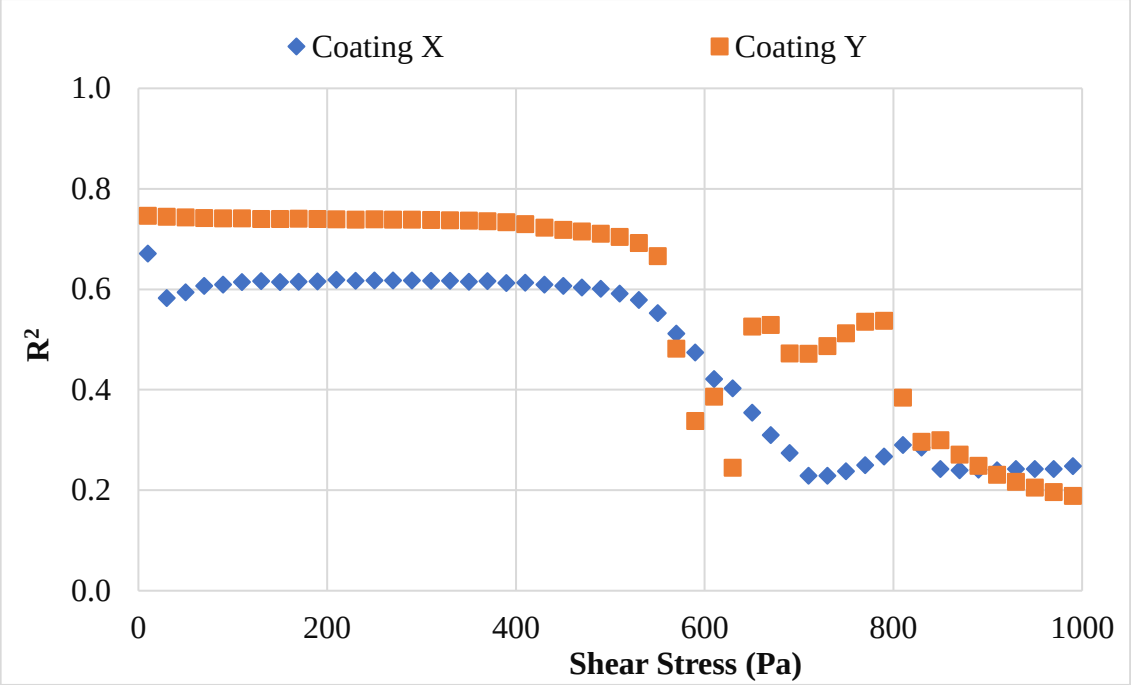

Fig. 6 - 16: Accuracy of Money correlation for Sample X and Y

The results show the out outcome of the limitations of the model and do not reflect the quality of the measurements. The predictions made by the Mooney analysis were poor and its relevance decreased with increasing shear stress. Notwithstanding the reservations made by the model, it was possible to calculate relative slip contribution to illustrate that each coating exhibits AWS behaviour differently. Large gap sizes represent the flow in the coating trough thus the flow at 900 μm gap size was chosen to represent the flow in the coating trough. Fig. 6 – 17 presents relative slip contribution of coatings at 900 μm gap size at sliding speeds between 1 to 1000 m/min.

It was seen that relative slip contribution was positive, depicting the formation of a lubricating layer throughout the sliding speed test range. However, relative slip contribution was ~ 0.2 and 0.1 for Coating X and Coating Y, respectively at 70 and 90 m/min. However, Coating X showed higher relative slip contribution than Coating Y.

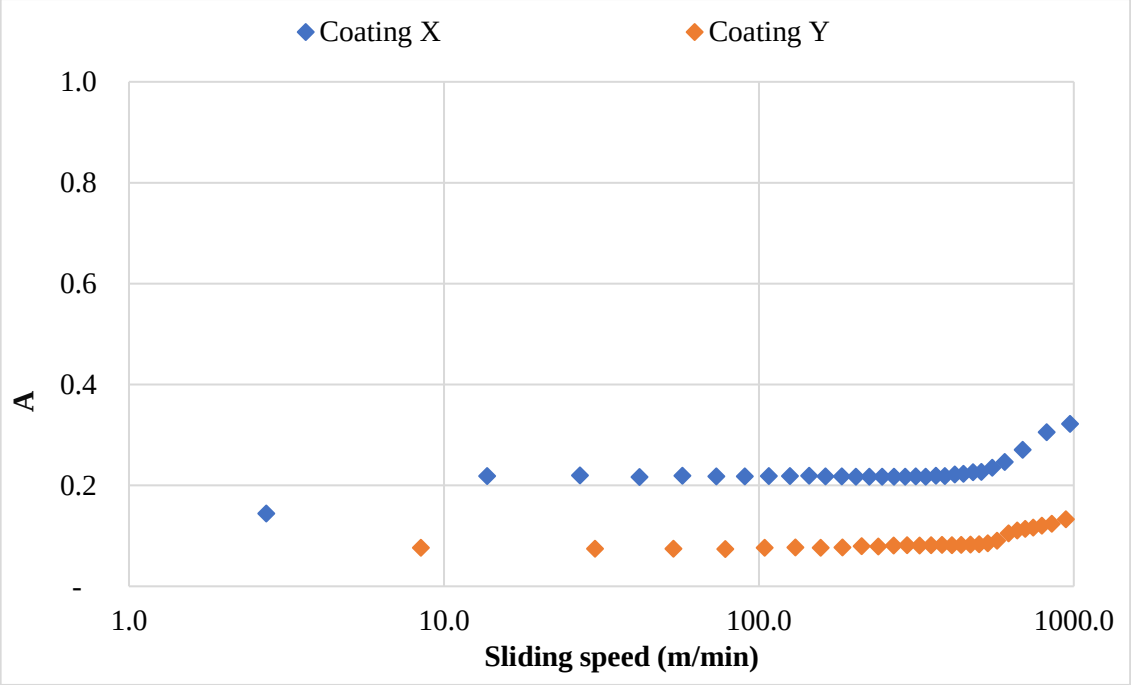

Fig. 6 - 17: Relative slip contribution against sliding speed against shear stress for both Coating X and Coating Y

6.3.7. EXTENSIONAL VISCOSITY

The rheological differences between the coatings were also observed in their extensional properties. Fig. 6 - 19 compares extensional viscosity of Coating X and Y. Coating X exhibited stronger tension thinning properties and higher extensional viscosity than Coating Y. The consequence of high extensional viscosity is the delayed film break up time which is beneficial during the pick-up process in the coating trough. From the rheological tests conducted above, ranging from steady-state flow curve, oscillatory rheology, AWS contribution and extensional viscosity, Coating X has exhibited similar behaviour to Coating B in chapter three to chapter five. It was therefore believed that Coating X was more versatile at a high-speed coating line that Coating Y to strong shear thinning and high viscosity; stronger gel system based on high solid-like behaviour.

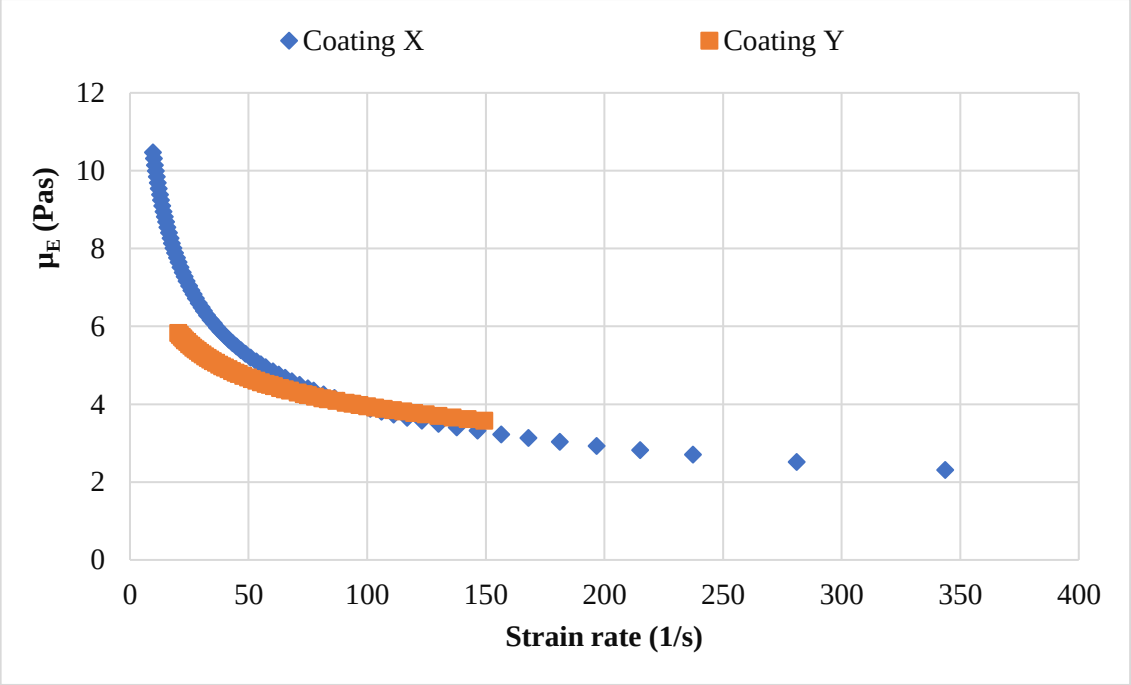

Fig.6 - 18: Extensional viscosity against strain rate

6.3.8. ANALYSIS AND VALIDATION

Having carried out a full characterization on the Plasticeram sun Merlin grey, the results were analysed to validate the hypothesis that it is possible to identify coatings which would have a greater tendency to exhibit PMD. A simplistic of analysis of those properties are identified in the known Plasticeram black coatings can be used to identify those measurable characteristics which are beneficial to operate at higher speeds. This baseline known knowledge was used to examine the behaviour of Plasticeram sun Merlin under a blind test.

From this simplistic analysis, the coating which suffered from PMD was deemed to be Coating Y, since it exhibited many rheological characteristics which were in common with the standard (S) black coating. Similarly, the grey Coating X performance most resembled that of the better coating, Coating B, in the pair of Plasticeram Black. The validity of methodology is clear in Fig 6 – 19 to fig. 6 - 21, which compares three key characteristics of the materials.

The three material characteristics are based on dynamic oscillatory rheometry, relative slip contribution, right through to extensional viscosity. All four commercial coating materials when subjected to the characterization methods which best identified coatings which could be prone to PMD

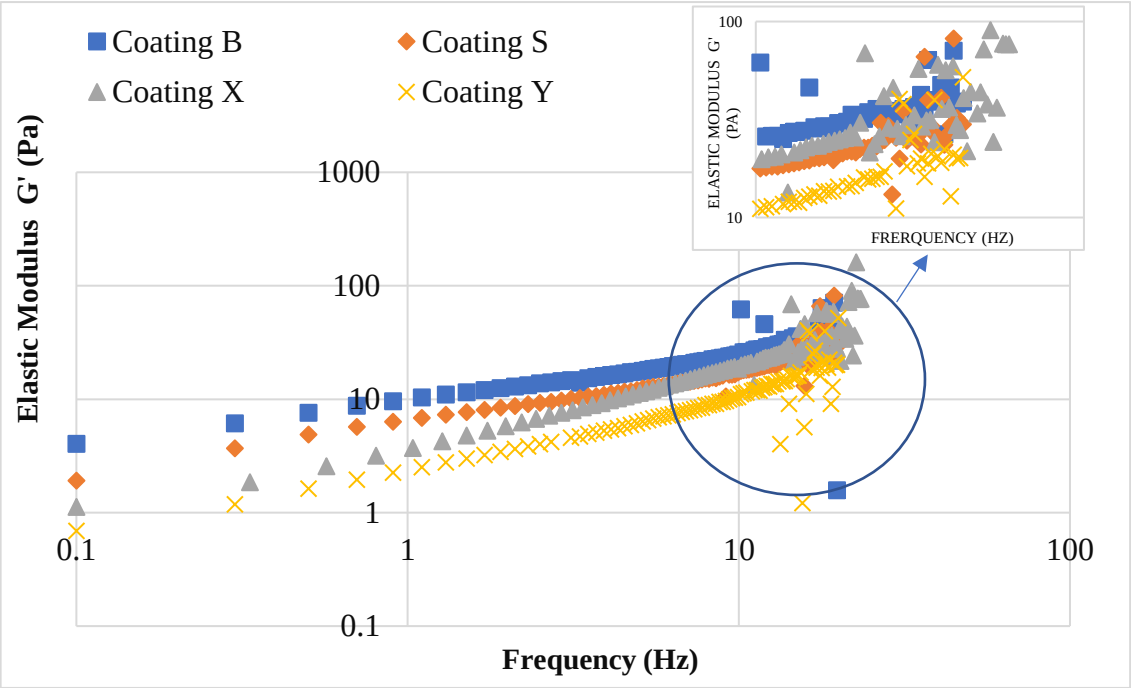

Fig. 6 - 19: Compares elastic moduli of Coating S, B, X and S with Coating S at the datum point. Insert: Elastic moduli in frequency range of 5 to 25 Hz

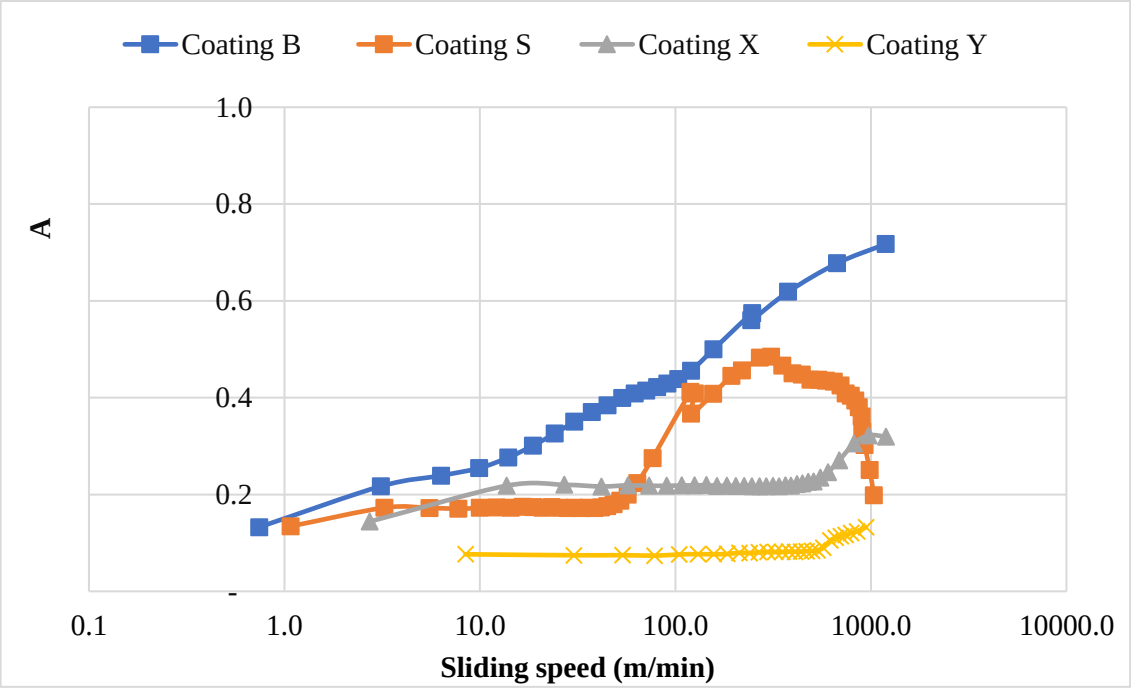

Fig. 6 - 20: Compares relative slip contribution of Coating S, B, X, Y and S with Coating S at the datum point

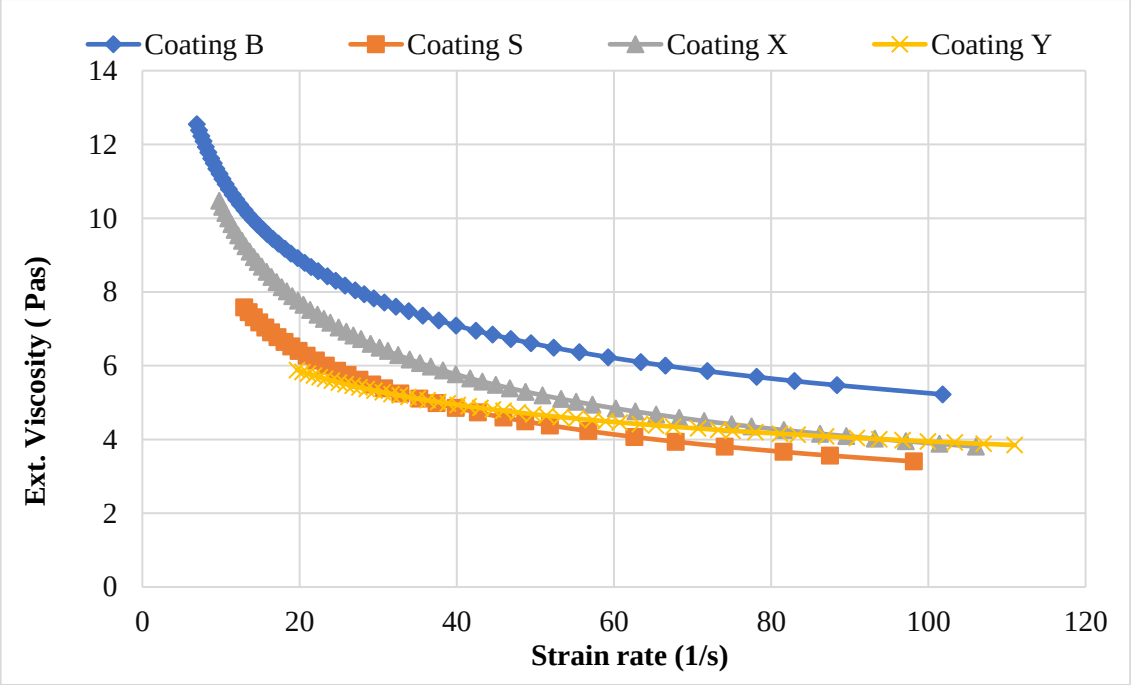

Fig. 6 - 21: Compares extensional viscosity of Coating S, B, X, Y and S with Coating S at the datum point

A comparison of elastic modulus shows higher solid-like properties for Plasticeram Black coatings than Plasticeram grey sun Merlin coatings at low frequencies. However; at elevated frequencies, Coating X and Coating B showed higher solid-like behaviour. Note: the graph is a log-log plot, therefore values at low frequencies are exaggerated. It can, therefore, be deduced that Coating B and Coating X exhibit higher solid-like properties than Coating S and Coating Y, as was expected. Data scatter was seen for all coatings at 15 Hz and above. Possibly a lower strain value with the LVR region could eradicate this behaviour. A comparison of relative slip contribution of commercial coatings was also conducted at a gap size of 900 μm as a representative of coating flow in the coating trough. Considering sliding speeds of 70 and 90 m/min, Coating B and Coating X showed higher slipping tendencies than Coating S and Coating Y. This contradicted with what was expected because the formation of a lubricating layer will lead to PMD.

Extensional viscosity flow curves showed higher values for Coating X and Coating B than Coating S and Coating Y, with Coating Y showing the lowest value of extensional viscosity.

6.3. CONCLUSIONS

A suite of characterization tests has been carried out to test the hypothesis that it is possible to identify materials which exhibit PMD utilising rheological test methods. It has been proven that materials with a high level of extensional viscosity, shear viscosity and elasticity are more versatile in a high-speed roll coating process. The properties mentioned are believed to award a higher quantity of coating pick up from the trough due to high extensional viscosity and viscoelasticity.

A comparison of elastic moduli shows higher solid-like properties for Coating B than Coating X. At high frequencies, Coating X and Coating B showed the highest elastic moduli. Therefore, an elastic modulus as part of the QC system should be operated at high-frequency value, and a lower strain value to avoid data scatter.

There are discrepancies noticed when employing the Mooney analysis to predict AWS characteristics. The low values of R^2show limitations of the model. However, the model shows prospects to characterise coating flow when extra terms have been included such as elasticity, surface tension and surface energy. Therefore, the Mooney analysis is tested in subsequent chapters on model fluids to test the model limitations when less coating additives are employed within the coating system.

Distinct differences are seen when employing extensional viscosity against strain rate. Therefore, extensional viscosity is the most important test out of the QC system because it draws visible differences between coatings.

CHAPTER SEVEN

EFFECT OF PIGMENT CONCENTRATION ON RHEOLOGICAL PROPERTIES OF PVC- CLEAR BASE

7.1. INTRODUCTION

Having established that there exists a relationship between commercial coatings (PVC coatings) rheology and its performance, further study of PVC systems was carried out to understand the relationship between the coatings components, rheology and their effect of mechanism by which PMD occurs. This would give a unique insight into how characteristics such as positive AWS and extensional rheometry are related to the constituents within a complex pigmented system. This would also serve to provide a suite of well characterized model coatings with known constituents which could be used to examine the fluid dynamics of the roll coating pick up process. This chapter describes the approach used to meet these aims.

7.2. METHODOLOGY

It was initially hoped that the test formulations could be provided by the industrial supporter of the work, but commercial formulation sensitivity, the number of additives used in the formulation and small quantities required made this approach impossible. Instead, a generic PVC based coating (PVC clear base) was obtained from BASF (the business has since transferred to AkzoNobel). The constituents of a custom formulation could then be manipulated in a strategic and controlled manner. Thus, the coatings tested represent a scientifically controlled set of simulated materials whose performance is likely to deviate from commercial paint systems.

To this basic PVC clear base, pigment and solvent controlled quantities of materials were added (Table 7 – 1) and mixed together. To simulate the particle/ liquid interactions, carbon black pigment was added to PVC clear base and this was mixed by a Speed mixer DAC 150.1.FVZ.K in fig.7 – 1 at room temperature for 10 minutes (5 minutes x 2, with 5 minutes interval) at 500 RPM.

Fig. 7 - 1: Image of a Speed mixer DAC150.1 FVZ.K employed during pigmented model fluids preparations

Table 7 - 1: Pigment additions to the basic PVC clear base coating

PVC clear base concentration [wt. %]	**Pigment concentration [wt. %]**
99.3	0.7
99	1
98.3	1.7
98	2
97.3	2.7
97	3
96.48	3.52

To examine the impact of pigment concentration on rheological properties, carbon black pigment applicable in paint systems, purchased from Sigma- Aldrich, was used as pigment additives. The choice of carbon black was to create model fluids with properties like Plasticeram Black coatings employed in chapter four to five. Approximately150 g of each pigmented model fluids were made, which allowed enough material for testing and allowed accurate determination of masses, even at low concentrations. All model coatings were stored in airtight containers in a thermally controlled laboratory. Each material was subjected to the same comprehensive suite of rheological testing as was described in chapter four and five.

7.3. RESULTS: PIGMENTED MODEL FLUIDS

7.3.1. STEADY STATE FLOW CURVES: PIGMENTED MODEL FLUIDS

Effect of pigment concentration on apparent viscosity was investigated and the results are shown in fig. 7 - 2.

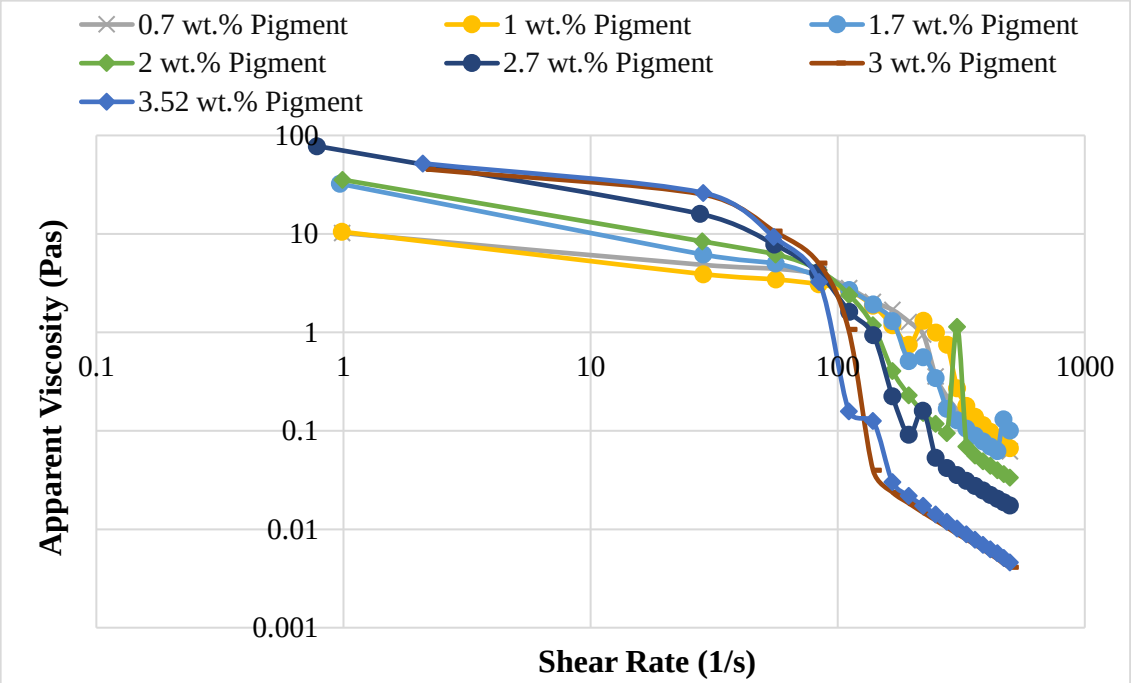

Fig. 7 - 2: Apparent viscosity against shear rate for pigmented model fluids of 0.7 – 3.52 wt.% pigment concentration.

All apparent viscosity - shear rate curves of pigmented model fluids showed a non-Newtonian pseudoplastic behaviour with the strongest shear-thinning tendencies observed at high pigment concentrations. All pigmented model fluids displayed a power-law region at low shear rates where the apparent viscosity was shear rate dependent, followed by a Newtonian region where apparent viscosity was shear rate independent.

At low shear rates, the polymer chains are believed to be in an entanglement state, and therefore the rate of recovery supersedes the rate of deformation. However, as the shear rate increases, the rate of recovery equilibrates with the rate of deformation, and consequently, a Newtonian plateau is exhibited.

Within the power-law region, high pigment concentrations such as 3.52 and 3wt.% displayed higher apparent viscosity than low pigment concentrations. However, low pigment concentrated model fluids showed higher apparent viscosity than high pigment concentrated model fluids at the Newtonian plateau. The strong dependence on the shear

rate for high pigment concentration was attributed to strong shear thinning behaviour. It was postulated that the strong tension thinning behaviour was due to strong particle-particle interactions due to the close packing of pigments and polymers which was believed to have caused “clogs”. Consequently, high values of apparent shear viscosity at low shear rates were seen. This was contrary to the apparent shear viscosity at high shear rates, where the apparent shear viscosity was very low and shear rate independent. The reduction in viscosity was credited to the destruction of particle-particle interaction and the alignment of polymer chains.

Zero shear viscosity against pigment concentration was investigated and the results are presented in Fig. 7 - 3. Zero shear viscosity is vital during the picking up process from the coating trough because it dictates the quantity of coating picked by the pick-up roll.

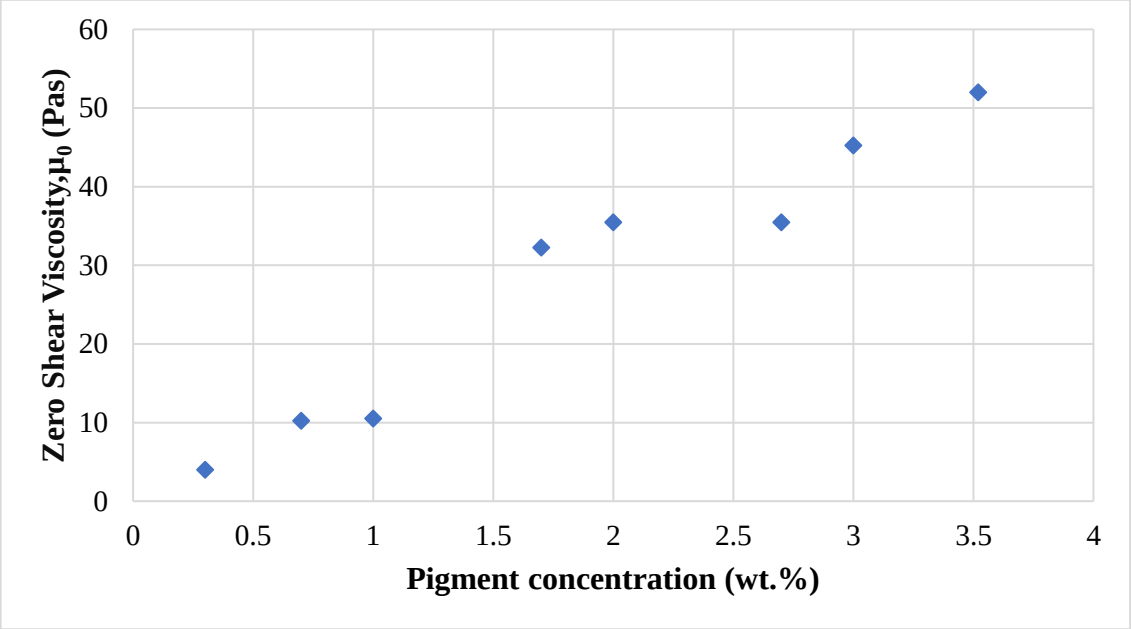

Fig. 7 - 3: Zero shear viscosity against pigment concentration

The higher the zero-shear viscosity, the higher the quantity of coating on the pick roll. It is worth noting that zero – shear viscosity values were determined at a shear stress of 10 Pa. A strong dependence of zero-shear viscosity on pigment concentration is evident.

In summary, polymer entanglement coupled with particle-particle interactions award high pigmented model fluids strong tension thinning properties and high zero-shear viscosity, in comparison to low pigment concentrations.

7.3.2. OSCILLATORY RHEOLOGY: PIGMENTED MODEL COATINGS

7.3.2.1. AMPLITUDE SWEEP

The effect of pigment concentration on mechanical (viscous and elastic) properties of model fluids was conducted via oscillatory rheology, which was divided into two parts: amplitude and frequency sweep. The amplitude sweep was initially conducted to determine the LVR region to enable subsequent frequency sweep studies to be carried out without structural break down of the pigmented model fluids. Fig.7 - 4 shows elastic modulus against strain at a frequency of 1 Hz within a strain range of 0.01 to 20.

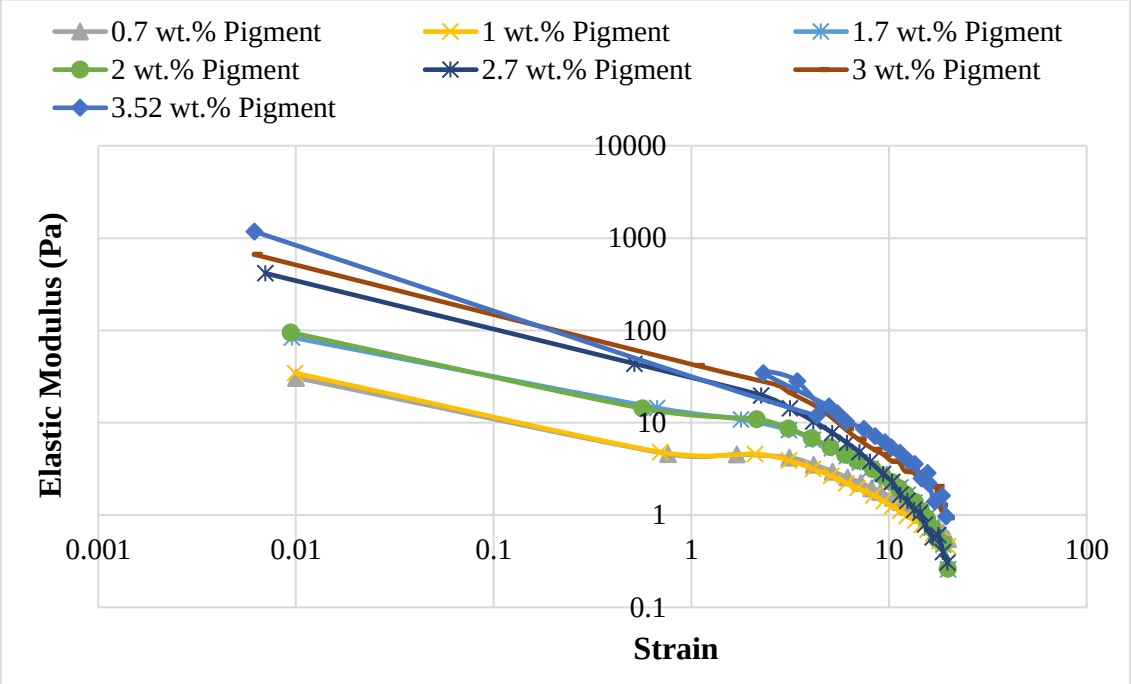

Fig. 7 - 4: Elastic modulus against strain sweep for pigmented model fluids of 0.7 – 3.52 wt.% pigment concentration.

It was observed that the elastic modulus increased with pigment concentration throughout the test range, except for the highest pigment concentration of 3.52 wt. % at strain value of 4.32 where the data appeared to be erroneous. The data erroneousness was likely to be material rigidness (almost crystalline) at low strain values, and therefore sudden particle deformation was felt as “a snap” as opposed to smooth deformation from higher degree to the next when external forces were applied.

Also, all model fluids were identified as strain- thinning due to the decrease of elastic modulus at an increased strain. The strain thinning phenomena was due to the deformation and destruction of the intrinsic structure of the model fluids as external forces were exerted on the model fluid [125].

The change in the elastic modulus was observed in three stages. Firstly, a faster rate of decline was observed at low strains. This was followed by a slow rate of decline in the modulus. And finally, a gradual decrease in the elastic modulus.

This was contrary to what was expected at low strain values, as a linear region was expected to appear before the non-linear region. The non-linear response was attributed to the linear settings in the rheometer, as previously seen in chapter four with Plasticeram Black coating samples.

A strain value of 0.7 was employed for all pigmented model fluids in subsequent testing of the frequency sweeps. The effect of pigment concentration on viscous modulus was also studied and the results are presented in fig. 7 – 5. The 3.52 wt. % pigment concentration model fluid exhibited the highest viscous modulus while 0.7 and 1 wt. % pigment concentration showed the least viscous modulus dependence.

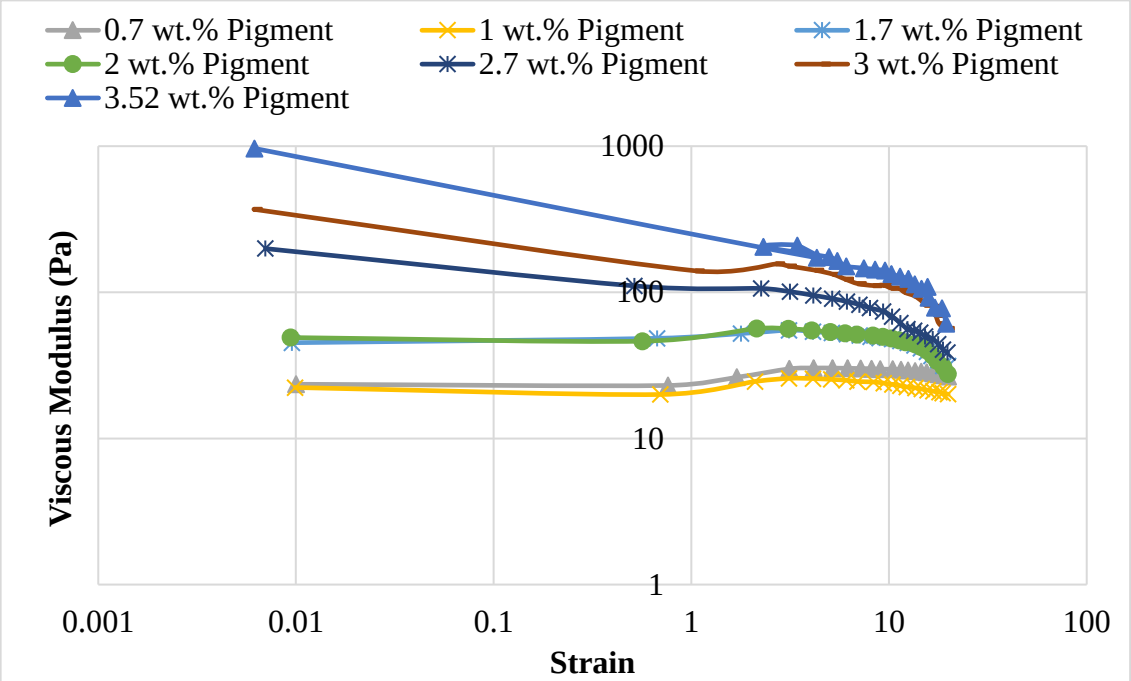

Fig. 7 - 5: Viscous modulus against strain sweep for pigmented model fluids of 0.7 – 3.52 wt.% pigment concentration.

At low pigment concentrations such as 0.7, 1.7 and 2 wt. %, viscous modulus curves initially showed a linear response, followed by a sudden increase in viscous modulus between 0.7 – 3 strain values, and finally a gradual decrease.

Wilhelm *et al* [126]conducted an in-depth investigation of various non-linear viscoelastic behaviour of complex liquids, and states that there are at least four types of LAOS flow behaviour, namely;

(1) Type 1 involves a strain thinning flow behaviour where both storage and viscous modulus decrease at increased deformation.
(2) Type II involves strain hardening flow behaviour where both viscous and elastic moduli increase at increased deformation.
(3) Type III involves weak strain – overshoot, where the elastic modulus is observed to decrease whilst viscous modulus slightly increased, followed by the gradual decrease
(4) Type IV involves strong strain – overshoot, where both elastic and viscous curves are observed to slightly increase followed by a gradual decrease upon the application of strain.

From this explanation, pigmented model fluids of 0.7 - 3 wt.% exhibited a weak strain-overshoot behaviour while 3.5 wt.% revealed a strong overshoot. The presence of both a weak and strong strain overshoot was due to intermolecular interactions between polymers and pigments, through covalent bonding and electrostatic interactions, which yield a weak and extended (backbone) structure in the side chains. Upon application of an external strain, a complex side-chain structure resists deformation and hence the moduli finitely increase but is overcome at elevated strain values.

It can, therefore, be deduced that PVC based resin coatings yield a weak strain - overshoot but increasing pigment concentration leads to strong or hard gel systems and a strong strain-overshoot.

7.3.2.2. FREQUENCY SWEEP

Elastic and viscous modulus curves of pigment concentrations presented in fig. 7 – 6 and fig. 7 – 7 respectively increased at an increased frequency.

However, a stronger elastic moduli dependence on the frequency at lower pigment concentration compared to higher pigment concentration was ascribed to a weak gel structure of low pigmented model fluids. Also, viscous modulus increased with high pigment concentrations. Therefore, a phase angle was employed to compare the solid-like properties of pigmented model fluids because it provides a better understanding of viscoelastic materials. The phase angle is the ratio of viscous moduli to elastic moduli. Phase angle less than 45^0 depicts a viscoelastic liquid where solid-like properties dominate over liquid-like properties in viscoelastic material. Conversely, phase angle

values of more than 45^0 depict a viscoelastic liquid where liquid-like properties dictate over solid-like properties.

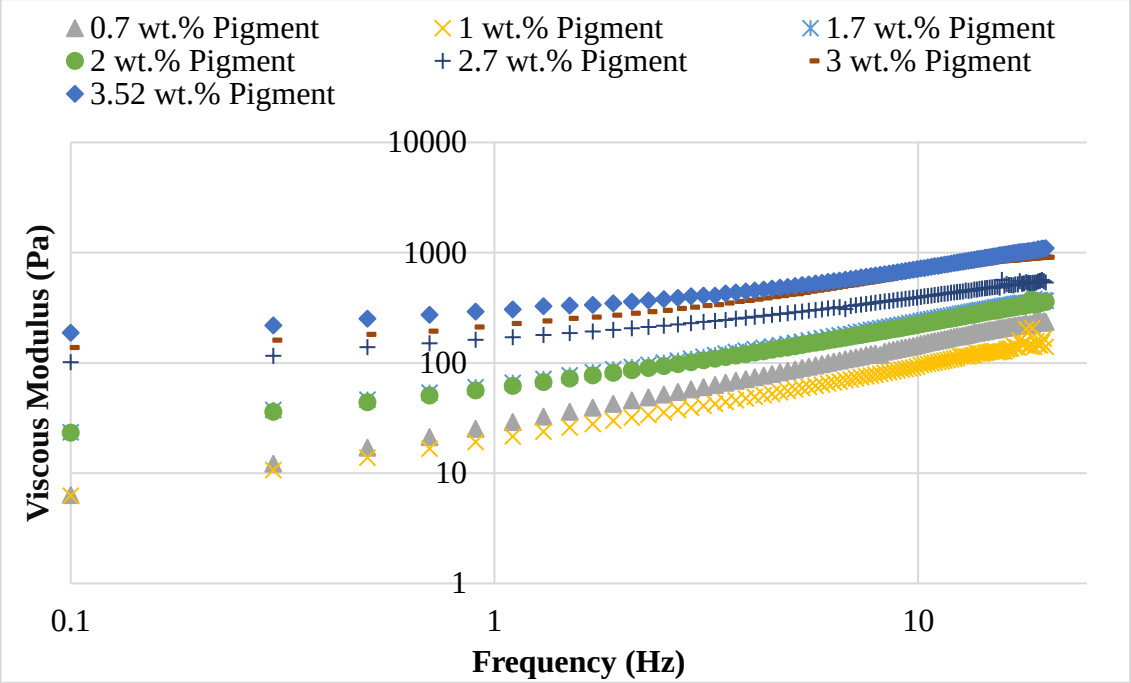

Fig. 7 - 6: Viscous modulus Frequency sweep for pigmented model fluids of 0.7 – 3.52 wt.% pigment concentration.

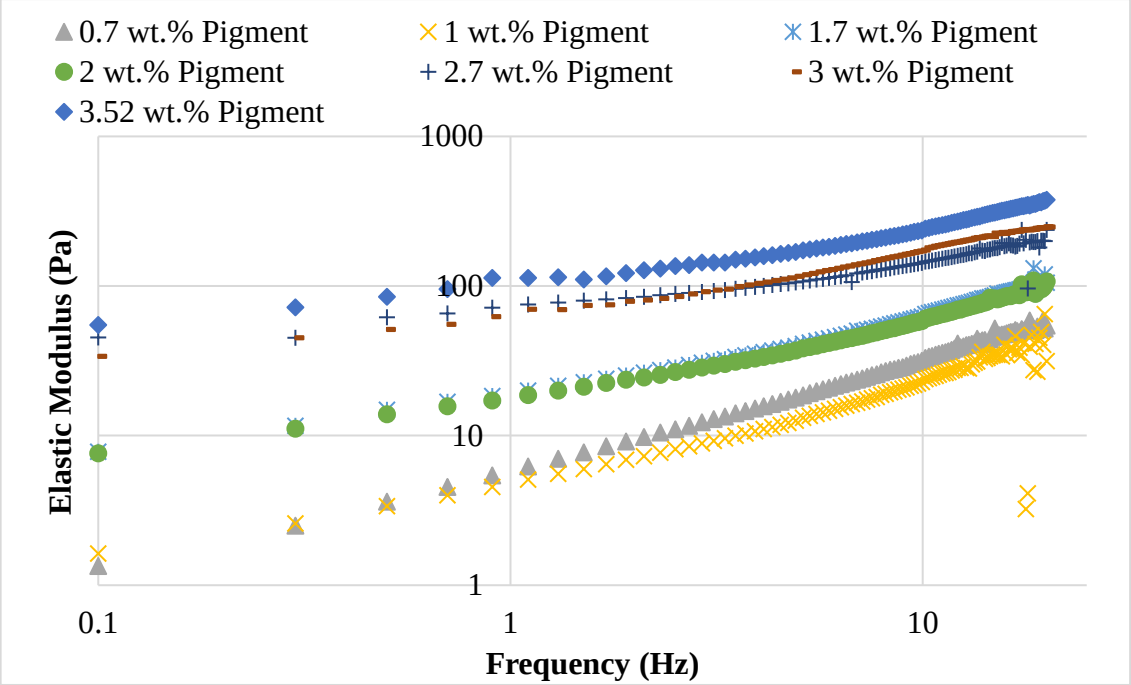

Fig. 7 - 7: Elastic modulus Frequency sweep for pigmented model fluids of 0.7 – 3.52 wt.% pigment concentration.

Fig. 7 – 8 shows the phase angle as a function of frequency at different pigment concentration.

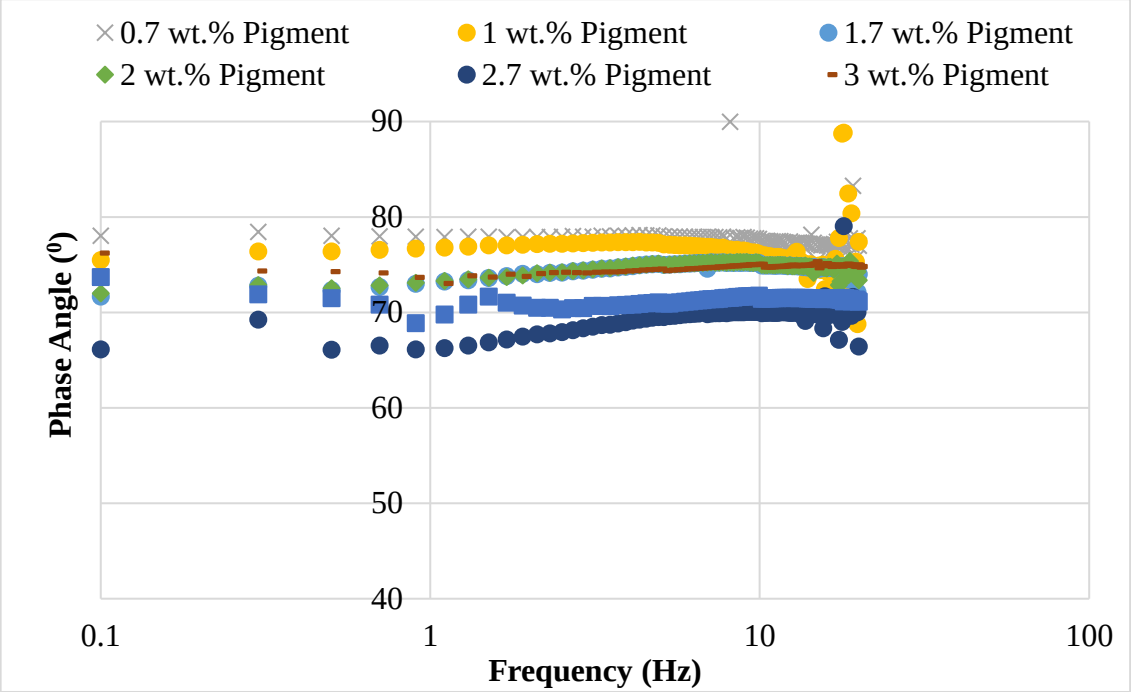

Fig. 7 - 8: Phase angle against frequency for pigmented model fluids of 0.7 – 3.52 wt.% pigment concentration.

There were two observations found: phase angle curves for all pigment concentrations were more than 45^0, depicting a dominance of viscous modulus over elastic modulus for all pigment concentration. Secondly, low pigmented model fluids showed a higher phase angle than high pigmented model fluids denoting stronger gel system for high pigment concentrations. Effect of pigment concentration on mechanical flow properties is summarised in Table 7 – 2 (elastic modulus).

$$G' = K'\omega^n \qquad (7\text{- }1)$$

Table 7 - 2: Parameters for elastic modulus as a function of frequency

Pigment Concentration	K' [Pa]	n'	R^2
0.7 wt.%	5.75	0.75	0.99
1 wt.%	4.79	0.68	0.97
1.7 wt.%	18.34	0.55	0.97
2.0 wt.%	17.2	0.6	0.97
2.7 wt.%	67.86	0.34	0.91
3.0 wt.%	62.63	0.45	0.96
3.52 wt.%	98.30	0.41	0.95

The effect of pigment concentration on complex viscosity was investigated and the results are presented in fig. 7 – 9. Highly pigmented model fluids exhibited higher complex viscosity, and this was credited to the strong particle-particle interactions brought about by the close compactness of the pigments within the model fluid system. Upon application of an external force, a clogged system resists deformation thus exhibiting high complex viscosity at high pigment concentration and low deformation rates.

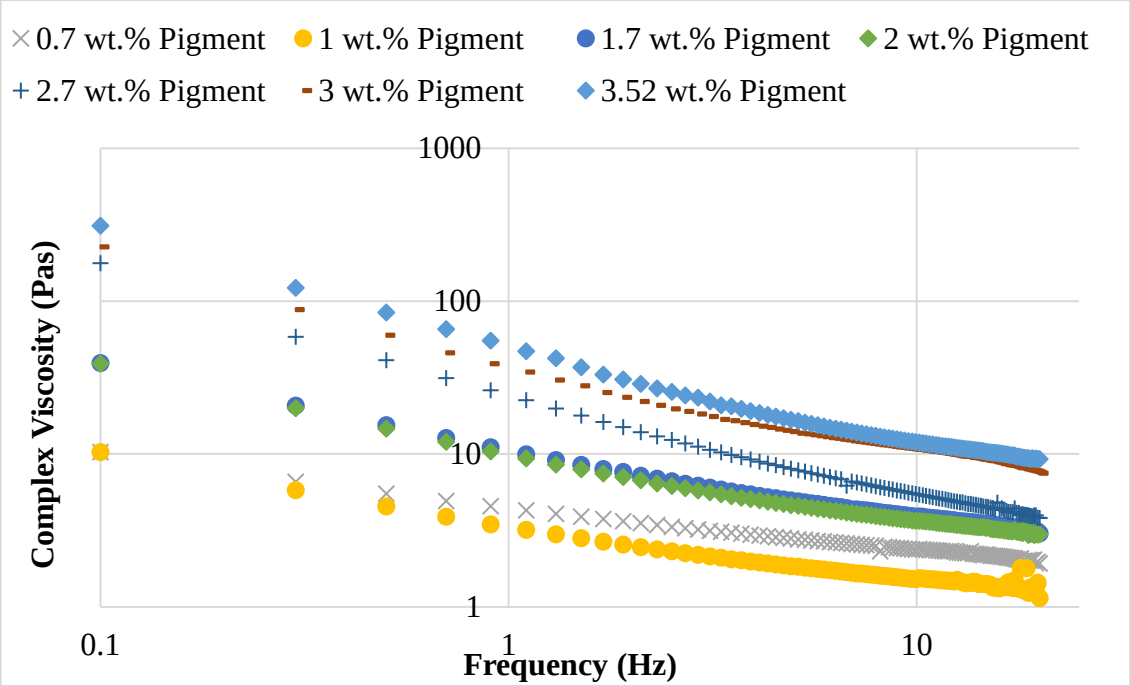

Fig. 7 - 9: Complex viscosity against angular frequency for pigmented model fluids (0.7 – 3.52 wt.%)

Generally, the strength of shear thinning behaviour (pseudoplasticity) increased with high pigment concentration than at low pigment concertation. The findings were in line with steady-state flow curve results in section 7.3.1. Additionally, low-frequency viscosity increased with pigment concentration due to higher solids content. It was concluded that pigment concentration affects the mechanical properties by creating stronger gel systems. Solid-like properties increased with increased pigment concentration and therefore complex viscosity increased.

7.3.3 GAP SIZE DEPENDENT VISCOSITY

Commercial coatings exhibited AWS behaviour; it was decided that the impact of pigment on the AWS behaviour would establish key physical mechanisms of flow within the coating system. Therefore, the effect of pigment concentration on AWS was investigated in this section of the report.

7.3.3.1. EFFECT OF PIGMENT CONCENTRATION ON CRITICAL SHEAR STRESS

Fig.7 - 10 shows apparent shear rate flow curves against shear stress for pigment concentrations of 0.7, 1, 1.7, 2, 2.7, 3 and 3.52 wt. %.

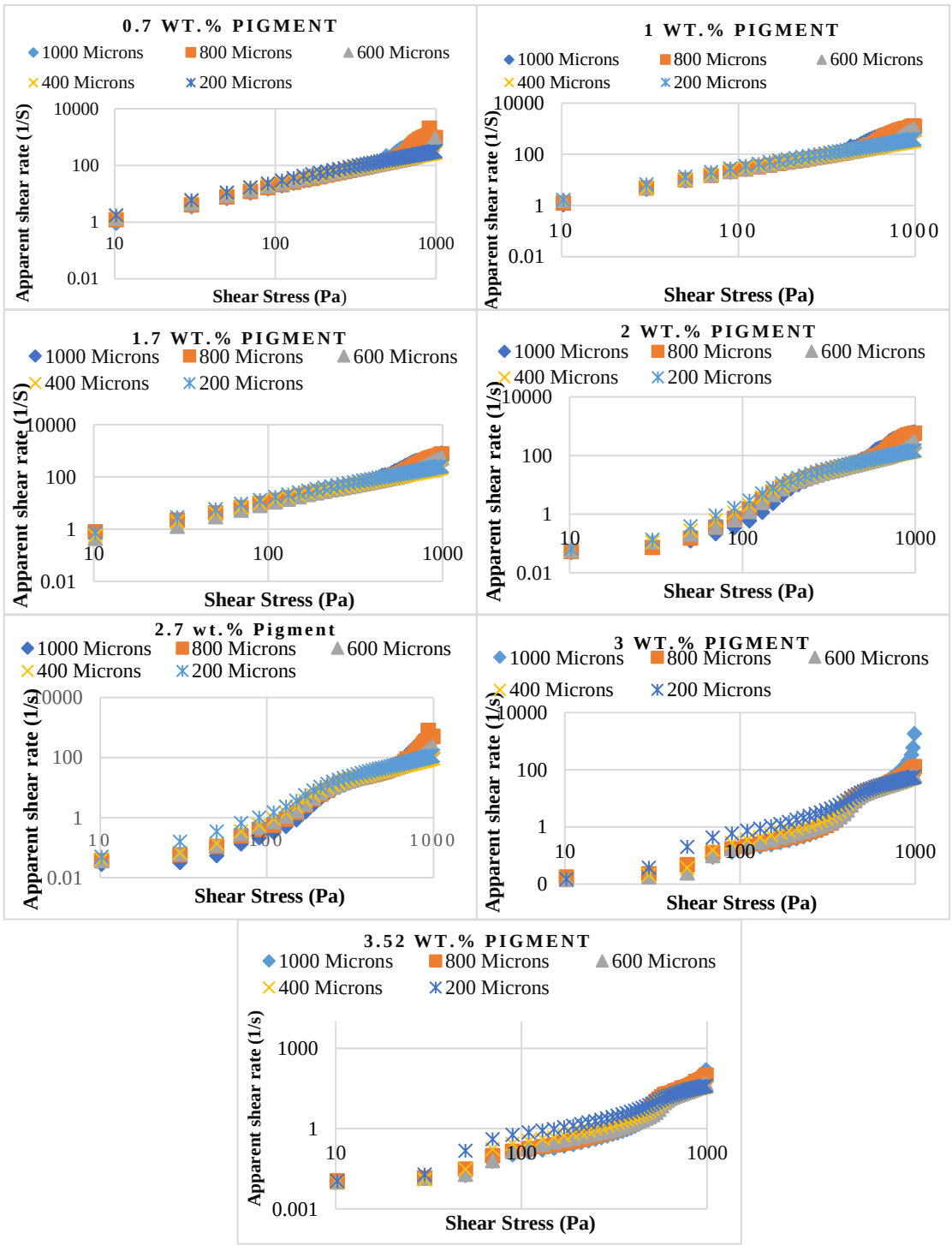

Fig. 7 - 10: Apparent shear rate against shear stress for pigmented model fluids of 0.7 – 3.52 wt.% pigment concentration.

AWS was seen through a systematic shift of flow curves at gap sizes of 200, 400, 600, 800 and 1000 µm. For all pigmented model fluids, the apparent shear rate increased with increasing shear stress. At low shear stresses of 10 – 409 Pa, pigment concentrations of 1 to 1.7 wt. % exhibited an overlap of flow curves depicting negligible AWS. This was observed up to a critical shear stress. And above the critical shear stress, flow curves at large gap sizes dominated over small gap sizes; flow curves at 1000 µm dominated other gap sizes.

Pigment concentrations above 1.7 wt. % displayed a visible shift in flow curves at all shear stresses. However, a swap of flow curve governance from a small gap to large gap size at a critical shear stress was evidenced. Flow curves at 200 µm gap size were higher than those at lows shear stress values. However, at high shear stresses flow curves at large gap size of1000 µm gap were higher than small gap sizes. The dominance swap occurred at a critical shear stress for all model fluids tested.

The swap of flow curve dominance by the gap sizes at different shear stresses was an indication of the presence of more than one type of AWS; a transition from a positive to a negative AWS. The critical shear stress was a point at which the flow curves transitioned from one slip regime to another. It was therefore believed that at the critical shear stress, an absence of both positive and negative AWS was achieved; it was the "safe operating" point at which phase homogeneity in the fluid was achieved.

Critical shear stress was dependent on both pigment concentrations and gap size. For example; the critical shear stress at 0.7, 1.7, 2, 2.7, 3 and 3.52 wt. %. Pigment concentration was determined at ~ 470, 410, 490, 470, 610, 650 and 570 Pa respectively.

7.3.3.2. APPLICATION OF THE MOONEY ANALYSIS

The Mooney analysis was employed to obtain slip characteristics of the pigmented model fluids. The assumption of the Mooney analysis is explained in chapter four (4.4.2). Fig. 7 – 11and Fig. 7 - 12 represent apparent shear rate against inverse gap for 0.7 wt.% pigment concentration.

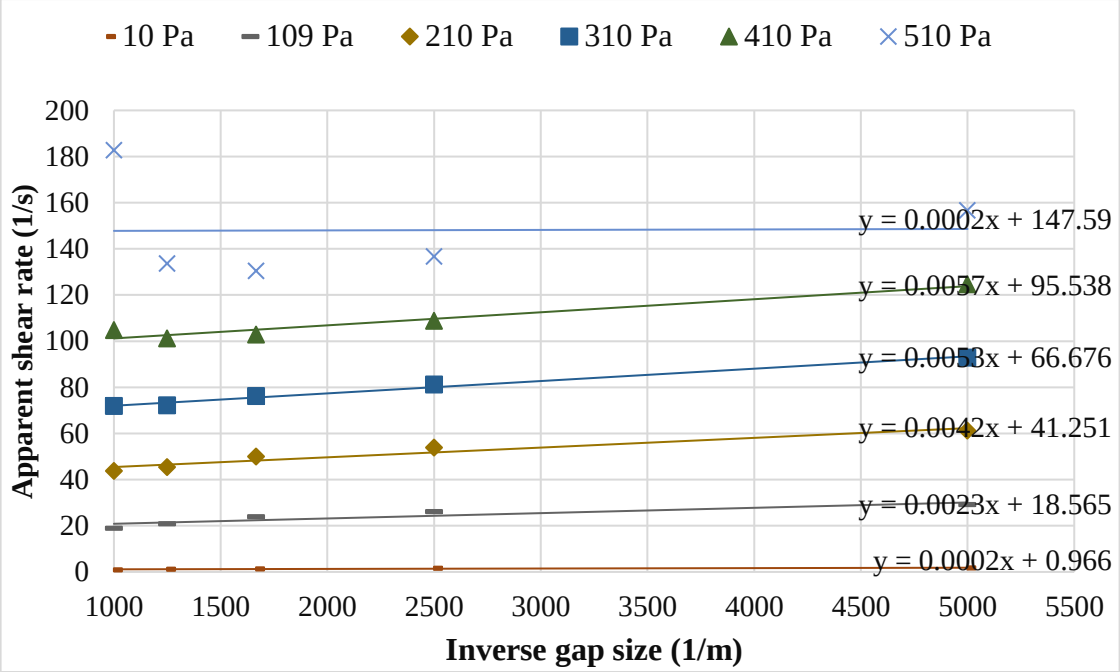

Fig. 7 - 11: Apparent shear rate against inverse gap size for 0.7 wt. % Pigment for 10 to 510 Pa

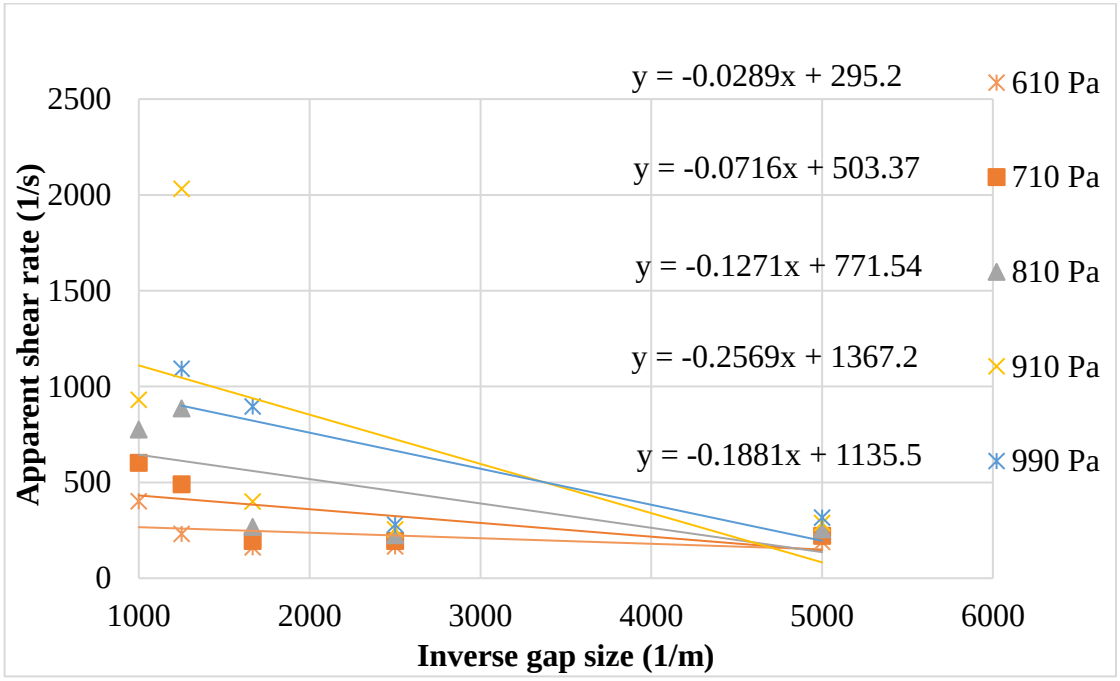

Fig. 7 - 12: Apparent shear rate against inverse gap size for 0.7 wt. % Pigment for 10 to 510 Pa

The same response when the Mooney analysis was applied to the primary data, was seen for pigment concentrations of 1, 1.7, 2. 2.7, 3 and 3.52 wt.%. The observations made from the Mooney analysis application on the model fluids are; a change in the gradient sign from positive to negative gradient denotes a dichotomy of slip velocity from positive to

negative. This observation deviated from that presented by the commercial coatings, as model fluids showed two distinct regimes.

The transition signified a transition from positive AWS (depleted layer) to negative AWS (stagnant layer). Positive AWS was exhibited between 10 to 410 Pa, while and negative AWS was observed between 510 to 990 Pa. Therefore, critical shear stress for 07 wt. % pigment concentration was observed at 510 Pa, this was also observed in the primary data. The response was seen for all pigment concentration.

7.3.3.3. ACCURACY OF THE MOONEY ANALYSIS

The accuracy of the Mooney analysis on pigmented model fluids was investigated and the results are presented in fig. 7 – 13.

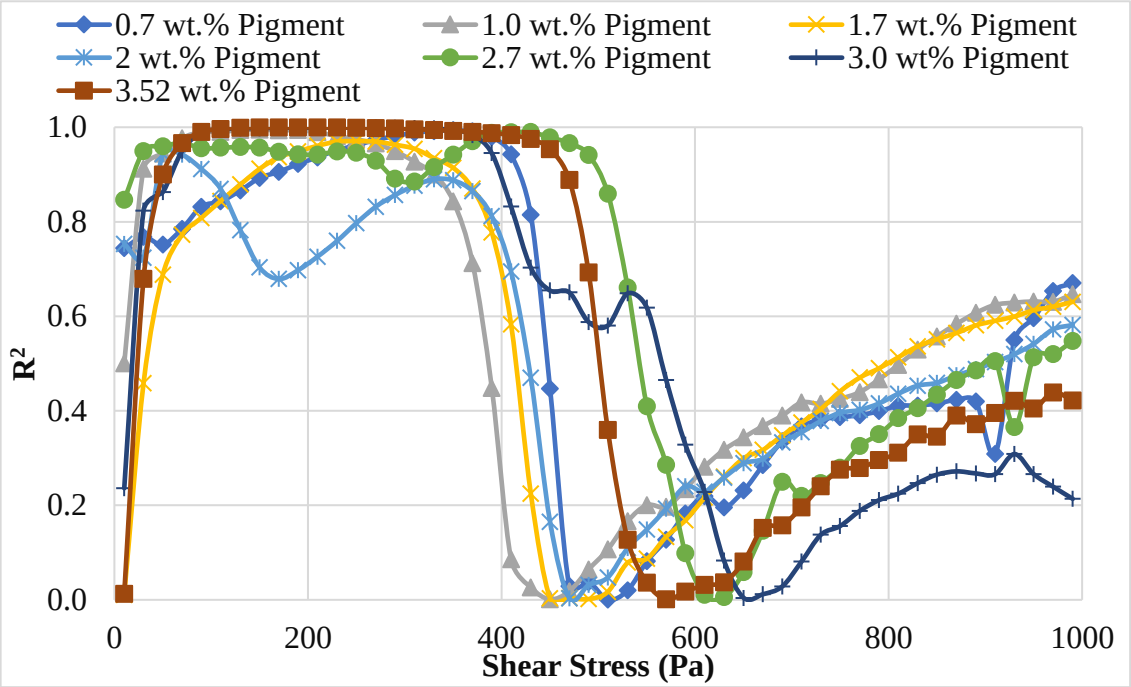

Fig. 7 - 13: Determination of the Mooney analysis against Shear stress

High accuracy was observed at low shear stresses; in the region of positive AWS, and less accurate at high shear stresses in the region of negative AWS. However, the failure of the Mooney analysis at the critical shear stress was due to the absence of AWS where bulk flow dominated over slip flow.

Apart from the pigment concentration of 2 wt. %, all model fluids generally achieved R^2 closer to 1 at low shear stress; followed by a gradual decrease within the transition region Above the transition region, a gradual increase in R^2 for all model fluids was seen;

however, low pigment concentrations showed higher accuracy than high pigment concentration. It was thus deduced that the Mooney analysis starts to break down at high shear stress and this was considered during data analysis at high sliding speeds.

7.3.3.4. SLIP LENGTH AGAINST SHEAR STRESS

Fig. 7 – 14 shows slip length against shear stress for all pigment concentrations. All pigment concentrations exhibited both positive and negative values.

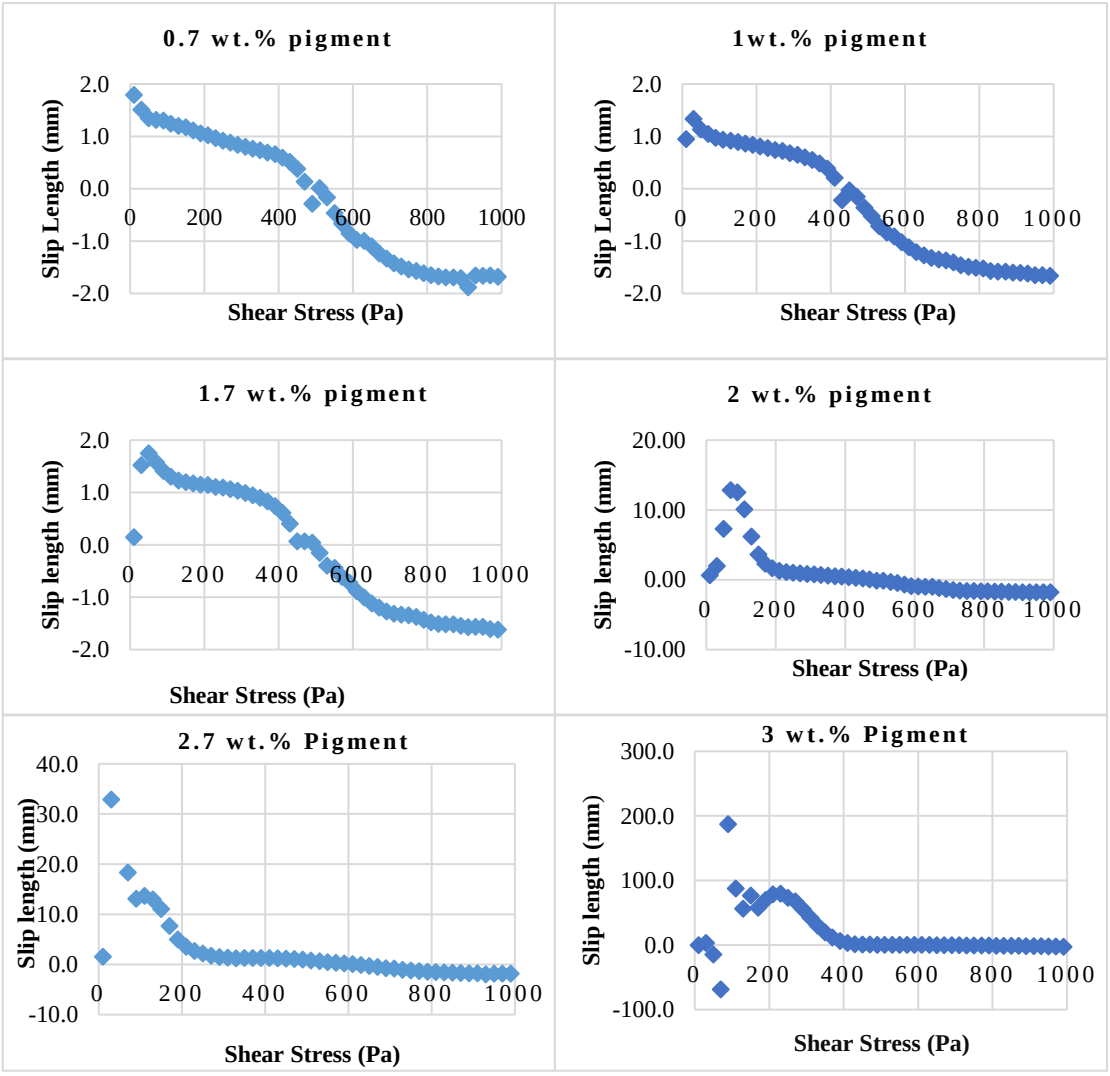

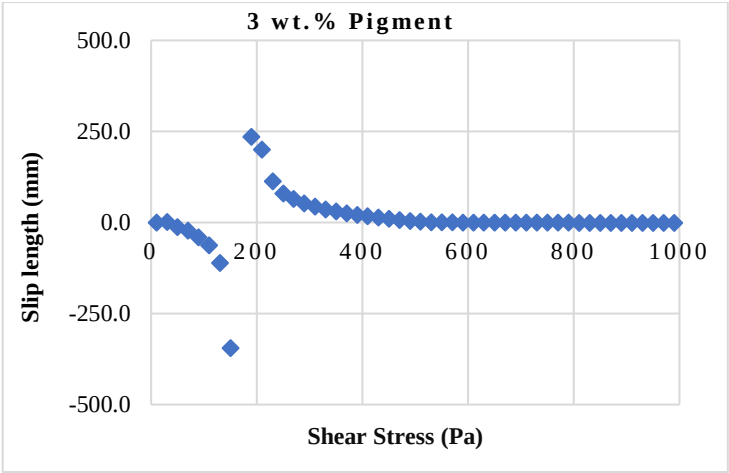

Fig. 7 - 14: Slip length against shear stress for pigment PVC coatings

Positive slip length estimates the distance from the plate (datum point) where the velocity profile of the flow, extrapolated from the bulk velocity, achieves the velocity equivalent to that of the plate into the wall [72]. And negative slip length estimates the distance from the plate where the velocity profile of the flow, extrapolated from the bulk velocity, achieves the velocity equivalent to that of the plate in the fluid.

Generally, positive slip length decreased with increasing shear stress, while negative slip length increased with shear stress for all pigmented model fluid. However, the magnitude of the anomalous layer is proportional to slip length. Therefore, slip length can be employed to estimate the thickness of the anomalous layer.

Interestingly, the critical transitional shear stress from positive to negative slip length varied with pigment concentration and was highest for 3 and 3.52 wt. % pigment concentration and lowest for 0.7 and 1 wt. % pigment concentration. For pigment concentrations of 0.7, 1 and 1.7 wt. %, a “sigmoid” fit of slip length against shear stress, with a perfect fit at 0.7 wt. % was observed

There were four stages identified in the sigmoid curve for pigment concentration of 0.7, 1 and 1.7 wt. %: Region I, in the shear stress range of 10 – 130 Pa, was attributed to the random orientation of polymeric and pigment particles moving at a low sliding speed. Due to low tangential stress and speed, the particles and polymer molecules are greatly affected by cohesive forces. Therefore, low external forces or shear stress within this region is insufficient to promote mixing/ homogeneous phase within the gap size. It was within this region that the size of the lubricating layer was highest due to positive AWS.

Region II, within shear stress range of 130 - 430 Pa, with relatively higher sliding speeds than region I was seen. This region still experienced positive AWS; however, a slower rate of change of slip length was evident due to the "nearly" achieved homogeneous phase.

Region III was observed within a shear stress range of 430 – 800 Pa, with positive and negative slip length.

Region III showed the highest rate of change with positive AWS and thus a lubricating layer at relatively low shear stress and a stagnation/ sticky layer above the critical shear stress.

Within region III, a critical shear stress/ critical sliding speed was observed where a transition from positive to negative AWS (wall stick) was observed. Fig. 7 – 15 schematically describes the four regions identified in a sigmoid curve of pigment concentration 0.7, 1 and 1.wt.%. It is noteworthy that the critical shear stress is a function of gap size and pigment concentration.

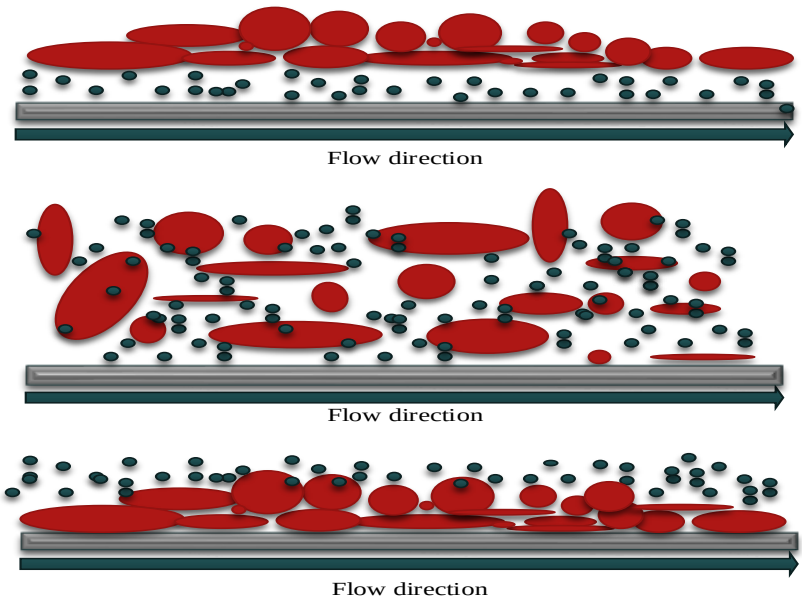

Fig. 7 - 15: Region II at medium shear stress (mid image), and Region III and IV at high shear stress (bottom image).

And finally, region IV, above shear stress of 800 Pa, exhibited the slowest rate of change of slip length. The slowest rate of change could be credited to the saturation of the attachment sites on the moving plate and less free particles available in the bulk to migrate to the solid surface.

Pigmented model fluids of concentration 2, 2.7 and 3 wt. % behaved differently from lower concentrations mentioned previously a sigmoid curve disappeared. Firstly, the response at low shear stress was possibly due to low torque values exerted by the rotational geometry that struggles to move the pigmented model fluid in the gap separation. Hence the scattered data at low shear stress is an experimental artefact as opposed to the material response.

Secondly, an increase in slip length to a local maximum was seen at low shear stress, followed by a gradual decrease to a plateau at medium shear stress. A decrease of slip length to a plateau signified the dominance of bulk fluidity flow over slip flow, which is the desired flow to avoid AWS.

At pigment concentration of 3.52 wt. %, slip length response deviated from the sigmoid fit; an asymptotic response at both low and high shear stresses was observed.

7.3.3.5. RELATIVE SLIP CONTRIBUTION AGAINST SLIDING SPEED

Relative slip contribution (A) against sliding speed for all pigmented fluids was studied at gap sizes of 200 -1000 µm and, the results are presented in Fig. 7 - 16.

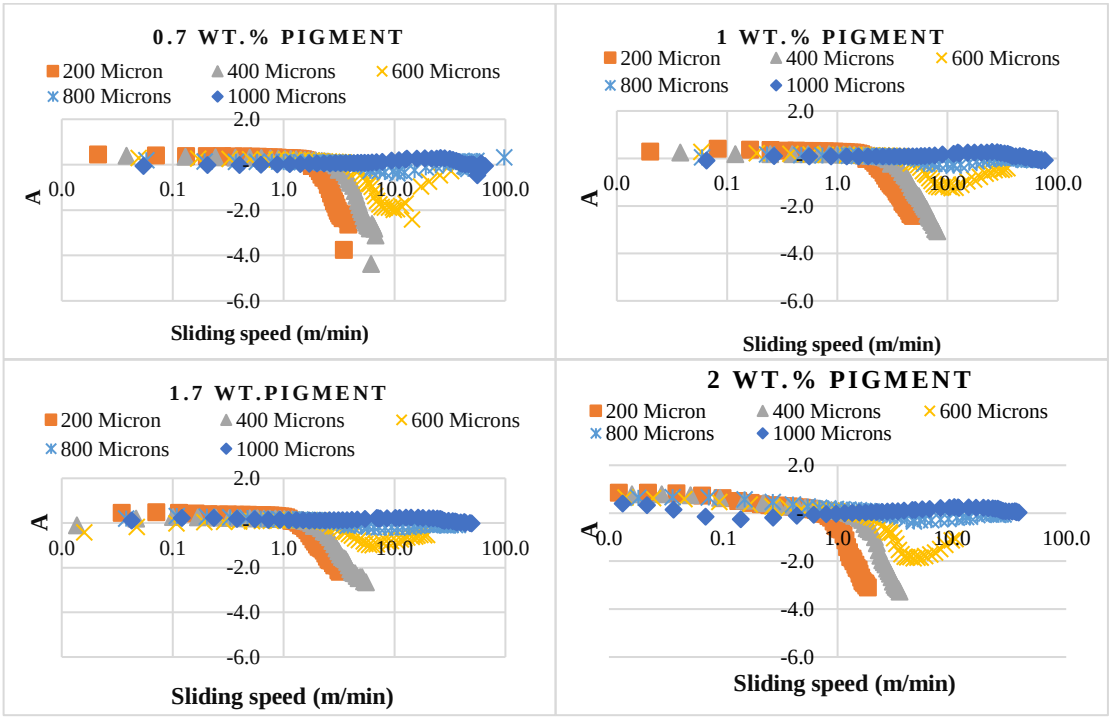

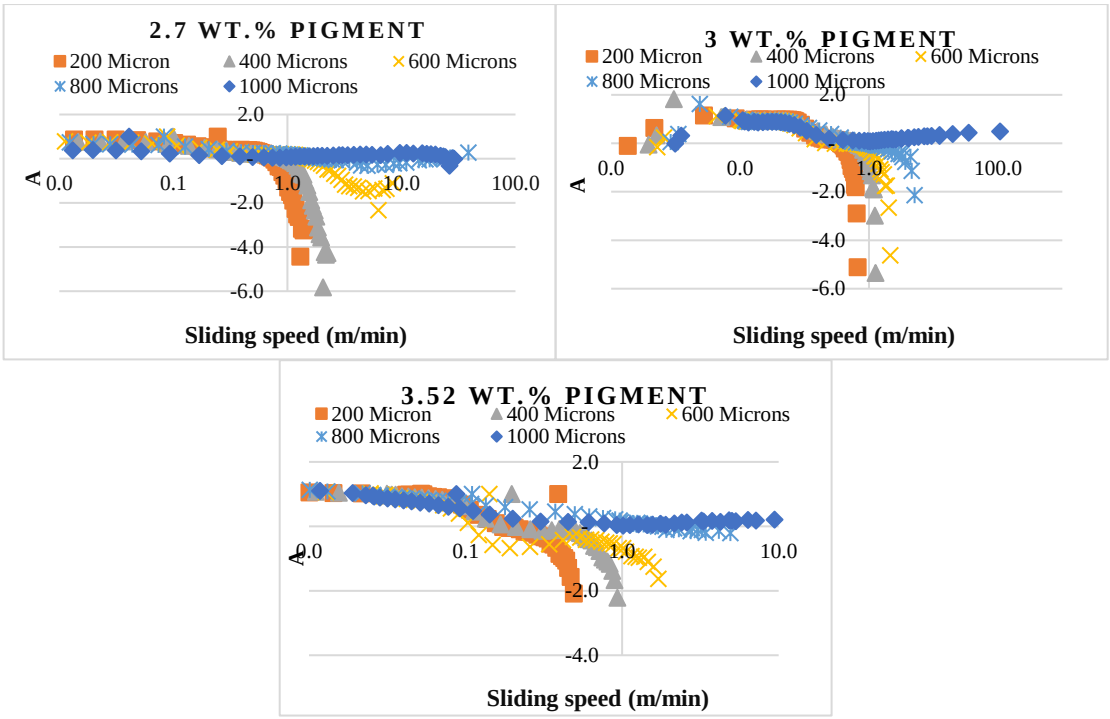

Fig. 7 - 16: Relative slip contribution against sliding speeds for model fluids with varying Pigment concentrations.

The gap size of 200 µm showed the highest relative slip contribution while 1000 µm showed the least relative slip contribution for all pigment concentration. This response was observed in commercial coatings (see chapter four) and was attributed to constriction effects experienced at small gap sizes.

The local minimum points were seen at gap sizes above 600 µm, followed by a recovery of negative relative slip contribution; the curve shifting towards a zero value depicted a flow recovery from slip dominated flow to the bulk dominated flow. A local minimum was possibly due to clogging development, and the flow shift was ascribed to the clog breakage at a clog fragility point. Clog fragility points were observed at sliding speeds of ~ 10 m/min for 0.7 – 2.7 wt. % pigment; and ~ 0.2 m/min for 3 and 3.52 wt. % pigment concentration.

Additionally, a transition from positive to negative relative slip contribution was noticed at elevated sliding speeds. It is worth noting that at the transition point, relative slip contribution closer to zero denotes a flow dominated by bulk flow and therefore negligible influence of slip. All pigment concentrations showed a transitional point where they transition from one AWS regime to another.

A comparison of relative slip contribution of pigment concentrations at each gap size is presented in fig. 7 – 17. At low sliding speeds, all pigment concentrations exhibited a weak dependence of relative slip contribution to the total flow, and this was more pronounced at small gap sizes. However, as gap sizes increased, a dependence of absolute relative slip contribution on sliding speed, more so at low sliding speeds, was seen. It was believed that the dependence of relative slip contribution at large gap sizes was due to less hindrance of movement, and therefore, geometry rotation

At high sliding speeds, all pigment concentrations showed a strong dependence of relative slip contribution on sliding speed, with the strongest dependence observed at 3.52 wt.% pigment concentration. Interestingly, all pigment concentrations showed an overlap at large gap sizes (800 and 1000μm), signifying that constriction effects are more influential than pigment concentration in causing slip behaviour.

At small gap sizes, negative relative slip contribution of more than -1 was recognised. This was considered miss leading because it suggested an anomalous layer thicker than the gap size. It was likely that the Mooney analysis breaks down when constriction effects dominate the flow, and therefore, can give an accurate physical response but the misleading quantity of anomalous layer thickness. 200 and 400 μm gap size show a flow that continuously increasing in negative relative slip contribution, while the flow at 600 μm shows a recovery past the clog fragility point.

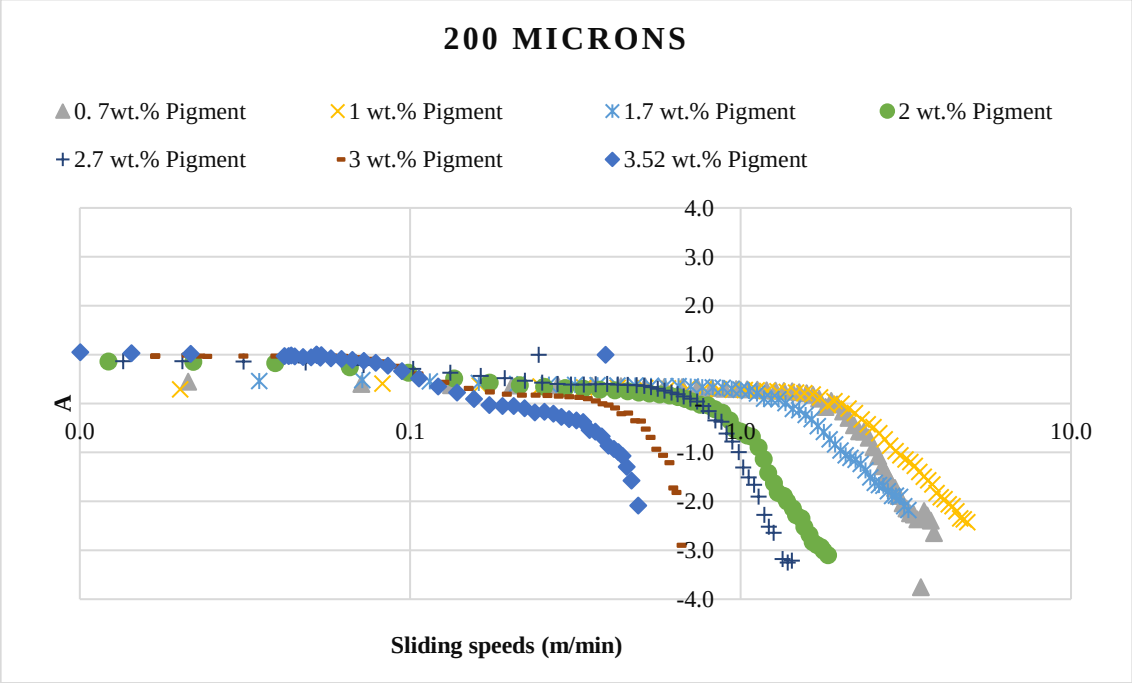

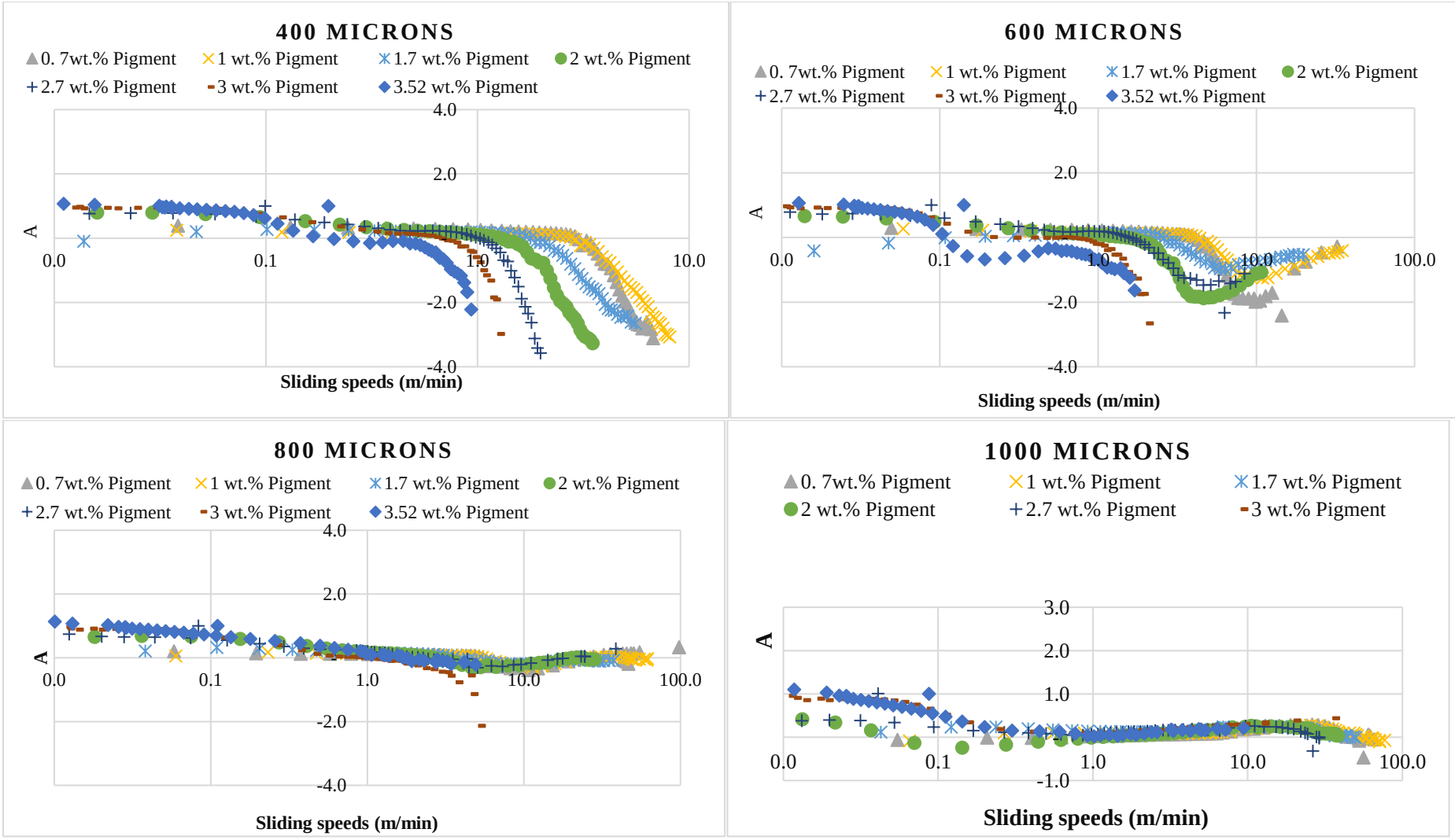

Fig. 7 - 17*:* Relative slip contribution against sliding speed for all pigmented model fluids

7.3.3.6. CONSTRICTION EFFECTS ON THE FLOW OF PVC OACTINGS WITH VARYING PIGMENT CONCENTRATION

It was stipulated in the previous section, section 7.3.3.5, that constriction effects to the flow-through small gap sizes is of high magnitude, it was followed up in this section by investigating the number of constriction effects for all pigment concentrations. Fig 7 - 18 explores constriction effects/ jamming phenomena (N) of pigmented model fluids against sliding speeds.

There were three observations made; firstly, at 200 and 400 µm all pigmented model fluids showed the highest constriction of more than 80%. Constriction effects were seen to steadily increase with increasing speed with no point of recovery, clog fragility point

Secondly, at medium gap sizes, 600 and 800 µm showed an increase of stagnation ratio up to a local maximum known as a clog fragility point. Above the clog fragility point, stagnation ratio sharply decreased. Flow at pigment concentration of 3.52 wt. % showed a clog fragility point but also showed the reform of the clogs at elevated shear stresses. It was believed that the re-formation of clogs was due to the close "compactness" of the coating system where cohesive forces were more effective due to the pigment particle – particles interactions.

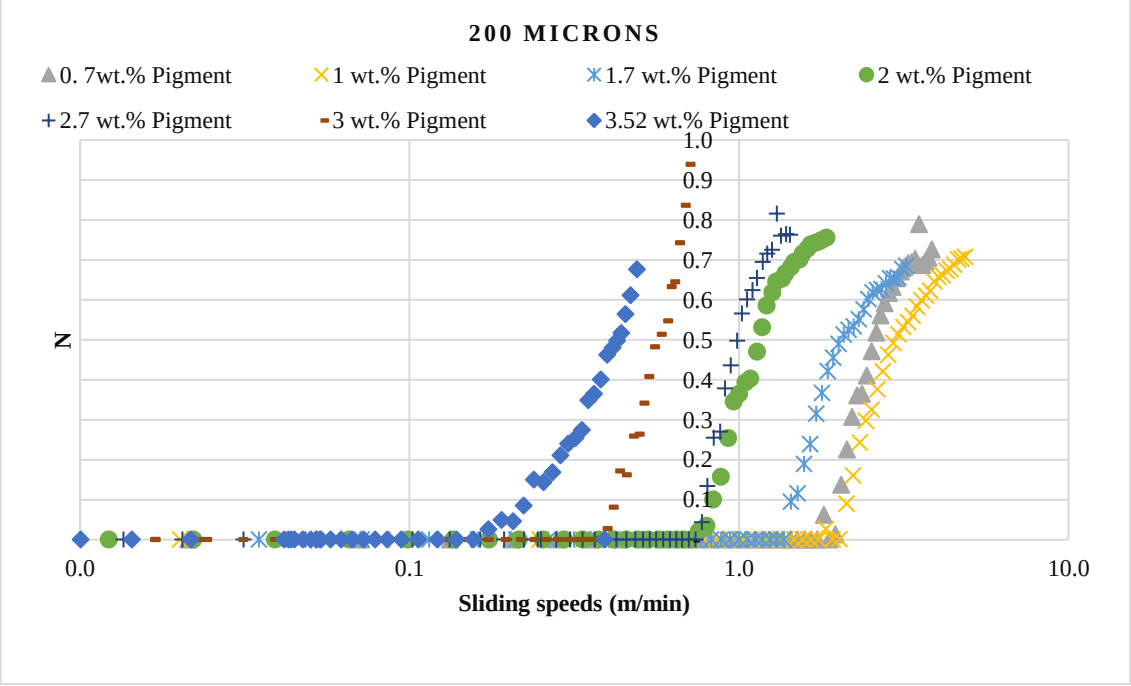

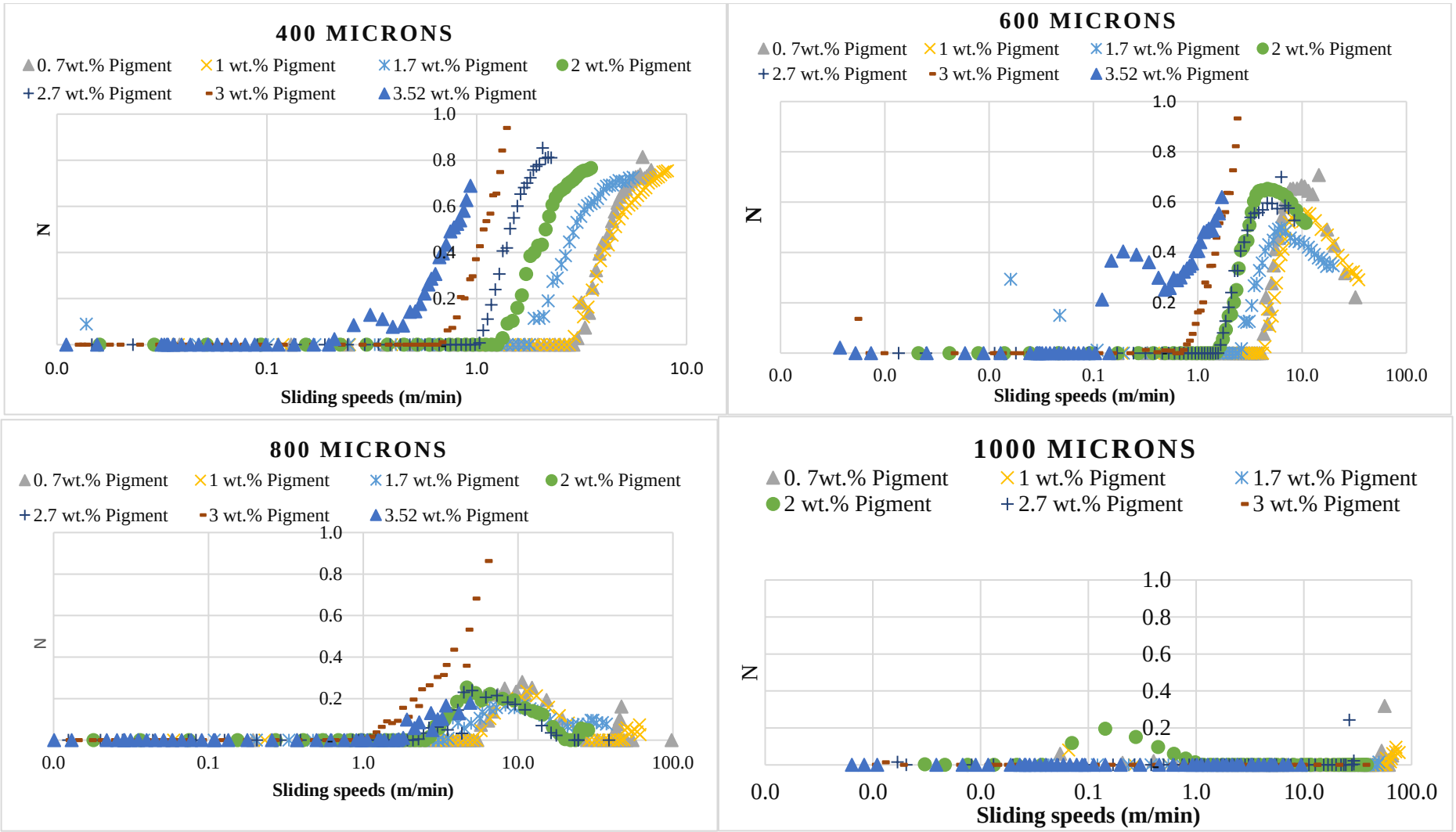

Fig. 7 - 18: Percentage stagnation ration against sliding speed for all pigmented model fluids

7.3.3.7. ANOMALOUS LAYER THICKNESS AGAINST SLIDING SPEED

A comparison of anomalous layer thickness at gap sizes of 200, 400, 600, 800 and 1000 µm is presented in fig. 7 -19. The anomalous layer thickness was calculated using Eqn. (2 – 20) in chapter two. At all gap sizes, all pigmented model fluids displayed both a negative and positive anomalous layer. A positive anomalous layer denotes a development of a stagnant/ sticky layer, while a negative thickness denotes a lubricating layer. The signs should not be confused with slip length, slip velocity and relative contribution signs.

Unlike gap size of 1000 µm, anomalous layer thicknesses – both positive and negative – were thicker than the gap size. These results were also seen in relative slip contribution values. It was therefore deduced that the Mooney analysis is limited in predicting the size of the anomalous layer thicknesses where characterising slip behaviour of complex, no linear materials. Also, the high degree of constriction effects in gap sizes between 200 - 600 µm further suggested that the Mooney analysis breaks down in the presence of constriction; and therefore, fails to quantify slip characteristics. However, the physical response of the curves makes scientific sense.

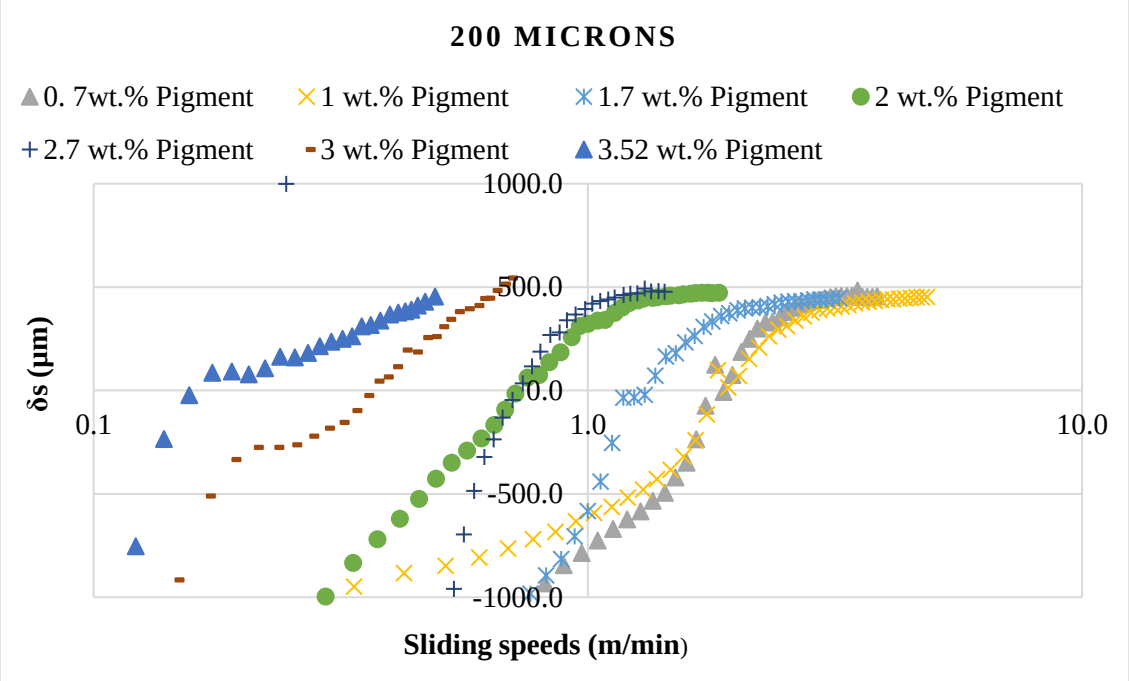

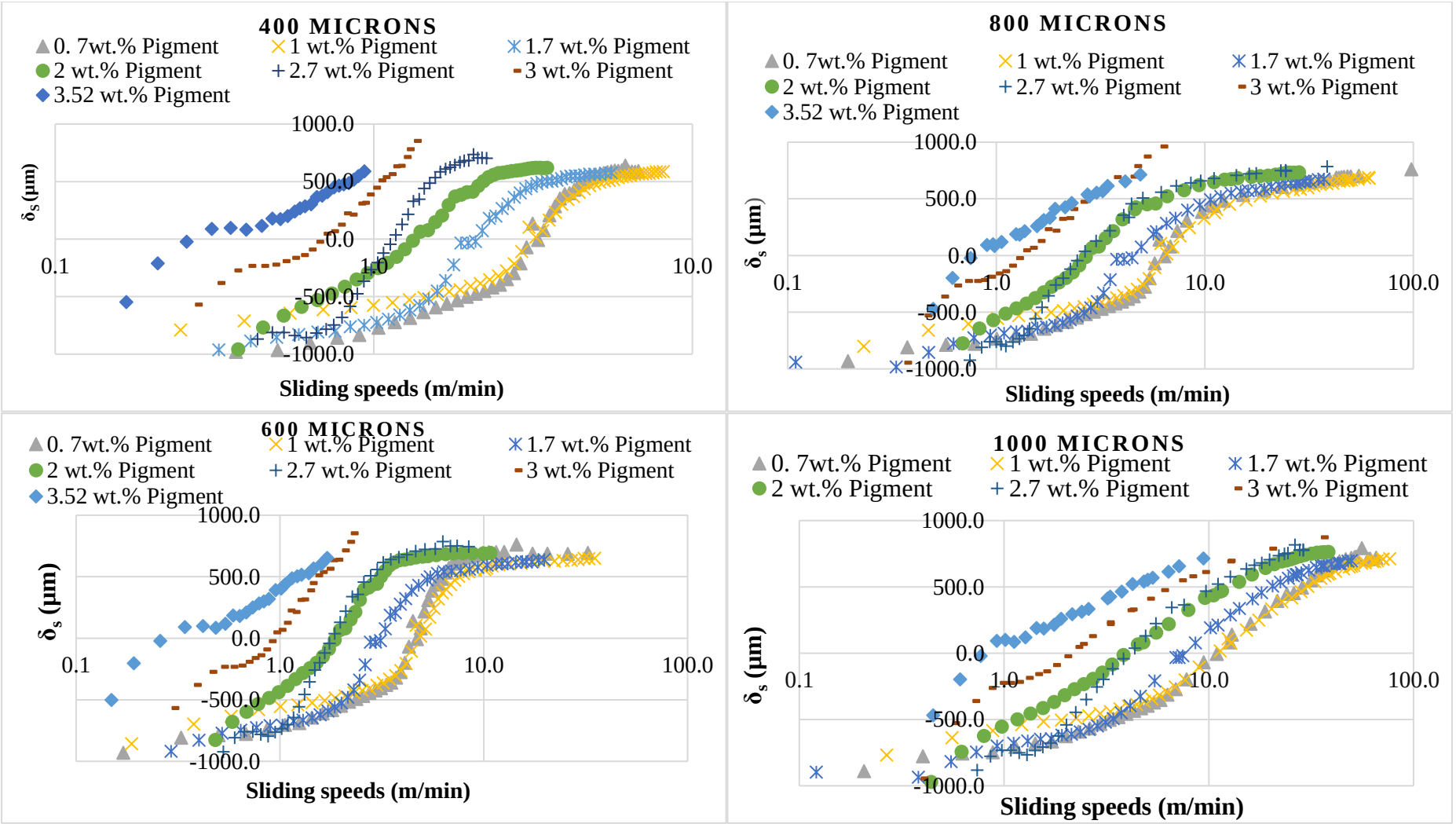

Fig. 7 - 19: A comparison of **a**nomalous layer thickness against sliding speed for all pigmented model fluids at different gap sizes

At gap size of 1000 µm, the anomalous layer thickness was well within the gap size of 1000 µm. There were negligible constriction effects observed at gap size of 1000 µm and therefore slip characteristics in this gap size were due to material characteristics as opposed to clogging formation.

The flow at 1000μm was employed to describe the flow in the coating trough during the pick-up process. The distance of the pick- up roll surface from walls and the base of the coating trough is more than 1000 μm. Thus, the conclusions made from 1000 μm are transferable to the coating trough. 3.52 wt. % pigment concentration showed the thickest stagnant layer and a faster transition from positive to negative wall slip. Both 0.7 and 1 wt. % pigment concentration showed the thickest lubricating layer and the delayed transition from positive to negative apparent wall slip. At sliding speeds of 70 and 90 minutes, all pigment concentration achieved ~ 730 µm thickness of the stagnant layer.

A transition from a lubricating to a stagnant layer was investigated and the results are presented in fig. 7 – 20. Transitional speed against pigment concentration at gap sizes showed a power-law relationship though. Overall, the transitional speed was higher for low pigment concentration thus a delayed shift from a positive apparent wall slip to a negative apparent wall slip.

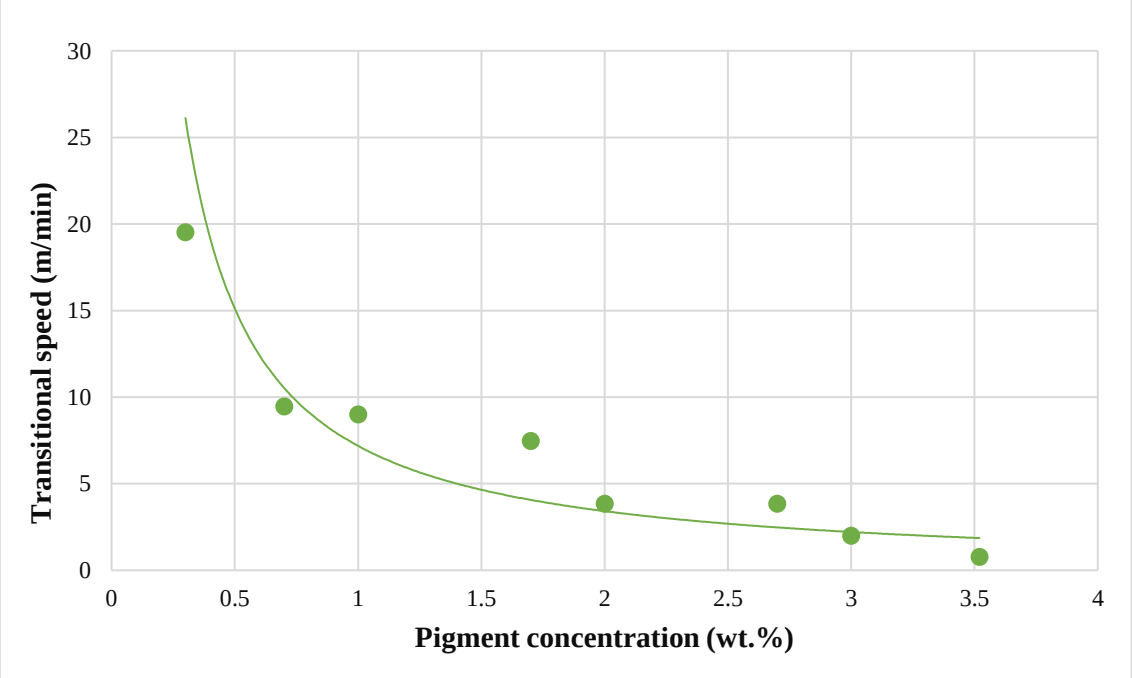

Fig. 7 - 20: Transitional speed against pigment concentration at 1000 μm

7.3.4. EXTENSIONAL VISCOSITY

So far, pigment concentration has shown an influence on shear rheology of PVC coatings. High pigment concentration increases solid-like properties of a coating due to change of the intrinsic structure. This was believed to also impact the film split process during pick up roll separation from the bulk coating in the coating trough. Therefore, this section investigates the influence of pigment concentration extensional rheology of the coating such as film break-up time. The experimental procedure employed during the extensional rheological characterisation of commercial paints was the same for this study and therefore presented in chapter five.

Pigmented model fluids with a concentration of 0.7 and 1.7 wt. % were employed for this study. Above 1.7 wt. % pigment concentration, it proved a challenge for the CaBER rheometer to induce film separation split. Additionally, prior knowledge of surface tension and density is vital for determining extensional viscosity but also gravitational effects the results. However, surface tension measurement was also a challenge to obtain at higher concentrations of over 1.7wt. %. An optical tensiometer FTA relies on the formation of a pendant drop of the test fluid from the needle to obtain surface tension measurement. However, high concentration pigmented fluids models failed to freely form pendant drop. For the two reasons discussed, 0.7 and 1.7 wt. % pigment concentration was employed.

Fig. 7 – 21 and Fig. 7 – 22 show a sequence of images of progressive filament thinning for 0.7 and 1.7 wt.% pigment concentration respectively. While Fig. 7 - 23 shows a natural log-log plot of thinning filament radius against time.

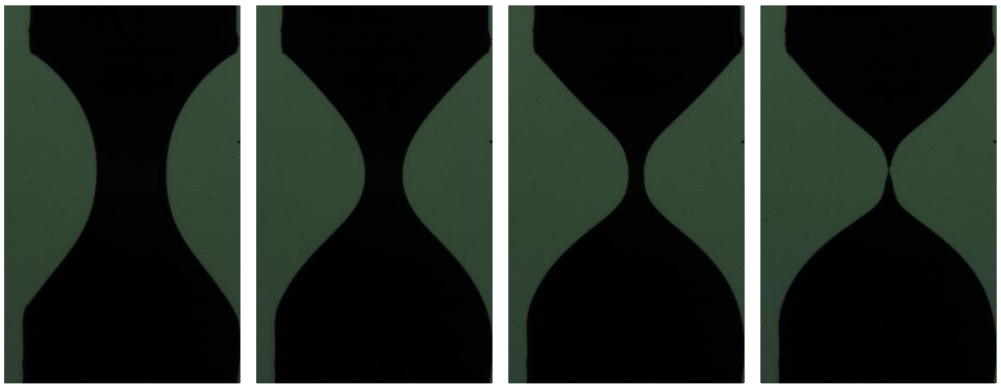

Fig. 7 - 21**:** Sequence of images progressive filament radius at 0.001, 1.135, 1.519, and 1.81 seconds, respectively.

A. 1.7 wt. % Pigment concentration

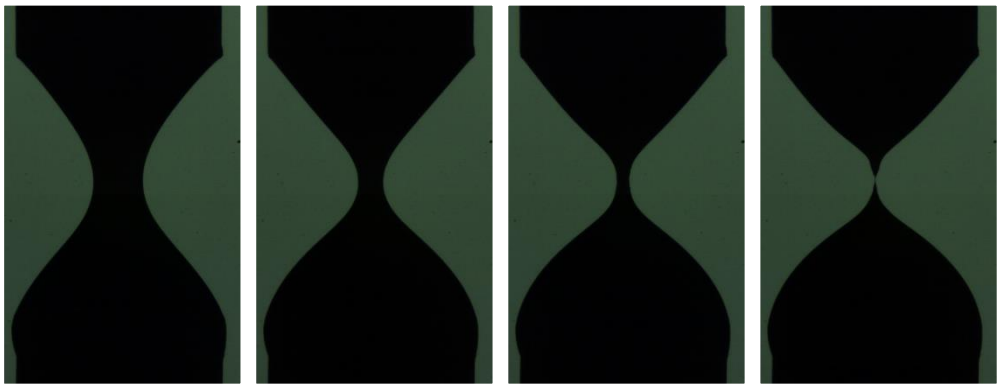

Fig. 7 - 22: Sequence of images progressive filament radius at 0.001, 2.26, 2.71 and 2.733 seconds, respectively.

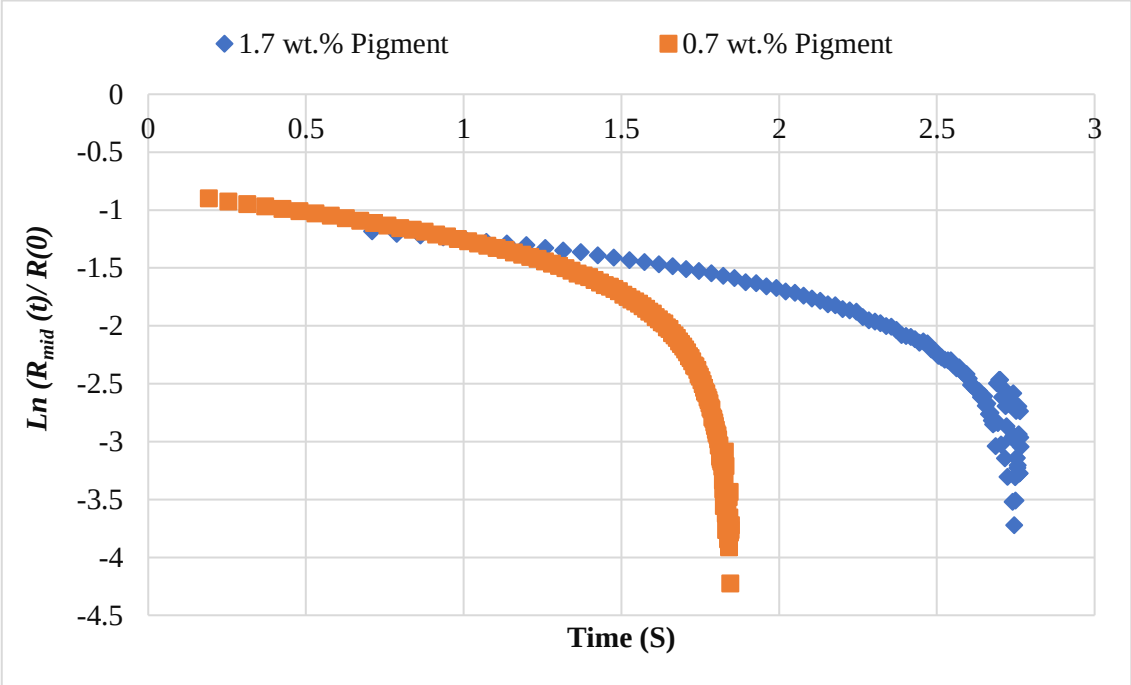

Fig. 7 - 23: Progressive filament radius against time.

The result of pigment addition to PVC -clear base at the varying concentration on extensional rheology is drastic. Firstly, the rate of filament thinning was slower at 1.7 wt. % concentration than at 0.7wt. % in concentration. This was evident in the sequence images of the two pigment concentrations in Fig. 7 – 21 and Fig. 7 – 22. 0.7 wt. % pigment concentration. This was also reflected in Fig. 7 -23 as the film bridge was thinned slower for high pigment concentration. t time was higher for 1.7wt.% than its counterpart, 0.7wt.%.

The pigmented model fluids displayed power law -tension thinning behaviour based on the “non - slender” visco-capillary forced balanced filament bridge. The tension thinning behaviour was also seen in Fig. 7 – 24. A power law region at low strain values credited to the heavily entangled state of polymers and pigments. And a Newtonian plateau where particles and polymers are fully aligned.

The rate of deformation and recovery are in equilibrium at the Newtonian plateau. Higher pigmentation showed stronger tension thinning behaviour than low pigment concentration; though the low-pigmented concentration showed higher viscosity at the Newtonian plateau.

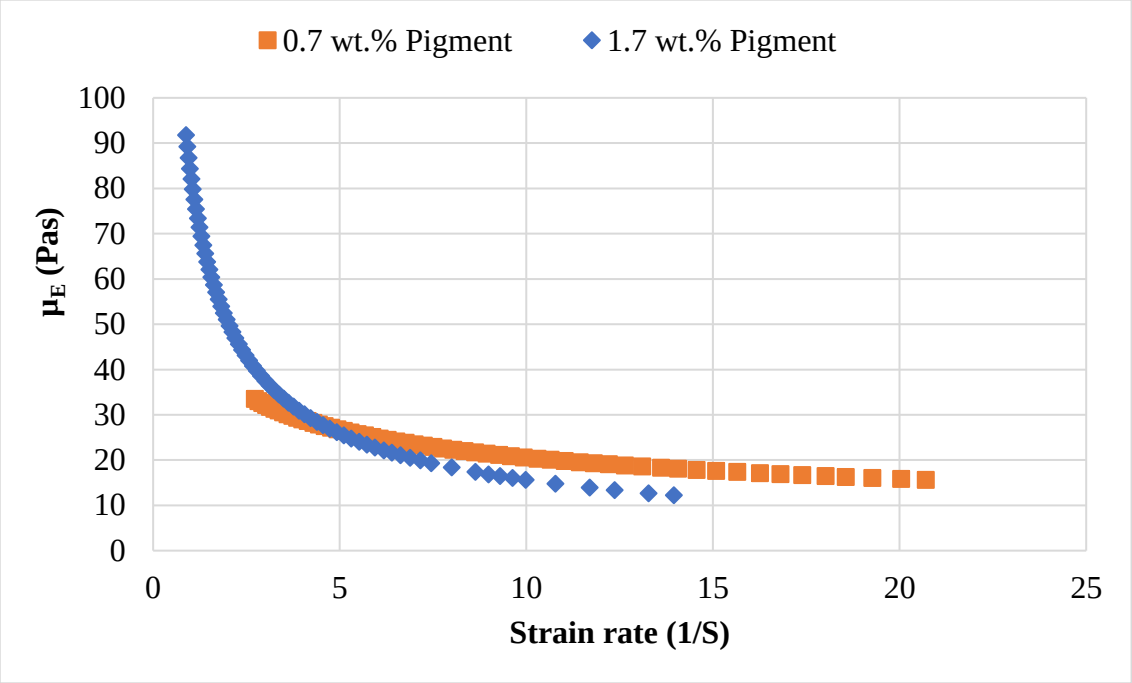

Fig. 7 - 24: Extensional viscosity against strain rate

7.4. CONCLUSIONS

This chapter has determined the impact of pigment t concentration on the rheological behaviour of PVC coatings. This has highlighted that the pigment concentration not only increases shear viscosity but also shear thinning properties of PVC coatings.

Furthermore, the mechanical properties of PVC coatings drastically increased which subsequently increased the tensile properties such as film break up time and extensional viscosity increased. The strength of tension- thinning properties also increased with increasing pigment concentration.

Flow indices under shear flow and extensional flow decreased with pigment concentration depicting stronger extension and shear thinning behaviour with higher pigment concentration. Zero shear viscosity also increased were believed to enable high quantity pick - up from the coating trough, but also enable easier flowability through the nip gap during the flow through the nip gap.

Unlike commercial coatings, all pigmented model fluids displayed both a lubricating and a stagnant layer at gap size of 200 – 1000 µm. The gap size of 200, 400 and 1000 µm represented a nip gap between applicator and pickup roll, nip gap between metering and pick-up roll, and between pick - up roll and the bottom of the trough and/ or sides of the coating trough, respectively. However, the scope of this study is limited to the pick - up roll. Therefore, the focus of this study was limited to 1000µm gap size.

In the absence of constriction effects at large gap sizes, relative slip contribution was the same for all pigmented model fluids. However, the anomalous layer thickness varied greatly. Though all pigment concentrations showed both a lubricating and a stagnant layer, high pigment concentration favour a thicker stagnant layer, whilst low pigment concentration favoured the formation of a lubricating layer. Both cases are undesirable as they are credited to phase separation, thus a compromise lies with a concentration that provides the least anomalous layer thickness of the lubricating and stagnant layer.

Hence the information obtained provides a well-characterized set of materials which can be used to further examine the pickup process in the roll coating process.

CHAPTER EIGHT

EFFECT OF SOLVENT CONCENTRATION ON RHEOLOGICAL PROPERTIES OF PVC CLEAR BASE

8.1. INTRODUCTION

Having established that there exists a relationship between pigment fraction in the last chapter, further study of PVC systems was carried out to understand the relationship whereby the PVC was reduced in viscosity with a solvent. This would give a unique insight into how characteristics such as positive and negative AWS and extensional rheometry are related to the constituents within a complex pigmented system. This would also serve to provide a suite of well-characterized model coatings with known constituents which could be used to examine the fluid dynamics of the roll coating pick up process (Chapter nine). This chapter describes the approach used to meet these aims.

8.2. METHODOLOGY

As with the previous chapter, a generic PVC based coating (PVC clear base) was obtained from AkzoNobel, formerly known as BASF. To this basic PVC clear base, solvent controlled quantities of materials were added and mixed (Table 8 - 1). To simulate the particle/ liquid interactions, a solvent blend of Butyl Carbdol Acetate (BDA) and Petrosol, in the ratio of 2:1 was to the PVC base coating was mixed by a Speed mixer DAC 150.1.FVZ.K. (Fig. 7 - 1) at room temperature and 10 minutes (5 minutes x 2, with 5 minutes interval). Around 150 g of each model material was made per batch, which allowed enough material for testing and allowed accurate determination of masses.

Table 8 - 1: Solvent additions to the basic PVC clear base material

PVC clear base concentration [wt.%]	**Pigment concentration [wt.%]**
100	0 (PVC Clear base)
96	4
92	8
88	12

All model coatings were stored in airtight containers in a thermally controlled laboratory. Each material was subjected to the same comprehensive suite of rheological testing as

was described in Chapter four to chapter five, with exception of thixotropy and shear rate dependent curve.

8.3. RESULTS AND DISCUSSION

A range of rheological tests; dynamic tests, gap size viscosity dependence and extensional rheology are presented and discussed herein. The experimental procedures that were undertaken during commercial paints were also adopted to solvated model fluids. Access to the laboratory with rheometers was limited; and therefore, proved a challenge to carry out shear rate dependent viscosity curves.

8.3.1. DYNAMIC OSCILLATORY RHEOLOGY

8.3.1.1. AMPLITUDE SWEEP

The amplitude sweeps on PVC coating with the solvent concentration of 0 – 12 wt.% was conducted in the strain range of 0.01 to 20 at a constant frequency of 1 Hz and at temperatures of 20 ^{0}C. The program settings were set in a linear mode. Fig. 8 – 1 and Fig. 8 - 2 compares elastic and viscous modulus, respectively, of PVC coatings. A decrease in the LVR region in the elastic modulus curve was credited to the linear setting as opposed to the logarithmic setting within the Bohlin software.

Despite the decrease of moduli in LVR region, a strain value of 0.7 was employed in the frequency sweep because it was assumed to lay within the linear region. The elastic and viscous modulus curves lessened with increasing solvent concentration, due to weakened binding powers by high solvent concentrations in the PVC coating system. As a result, solid-like behaviour decreased with increasing concentration.

Also, PVC coatings at all concentrations showed a double strain overshoot in the elastic and viscous modulus. According to Hyun *et al* [16]and [126] this behaviour is often associated with associative polymers, but rarely studied in the literature

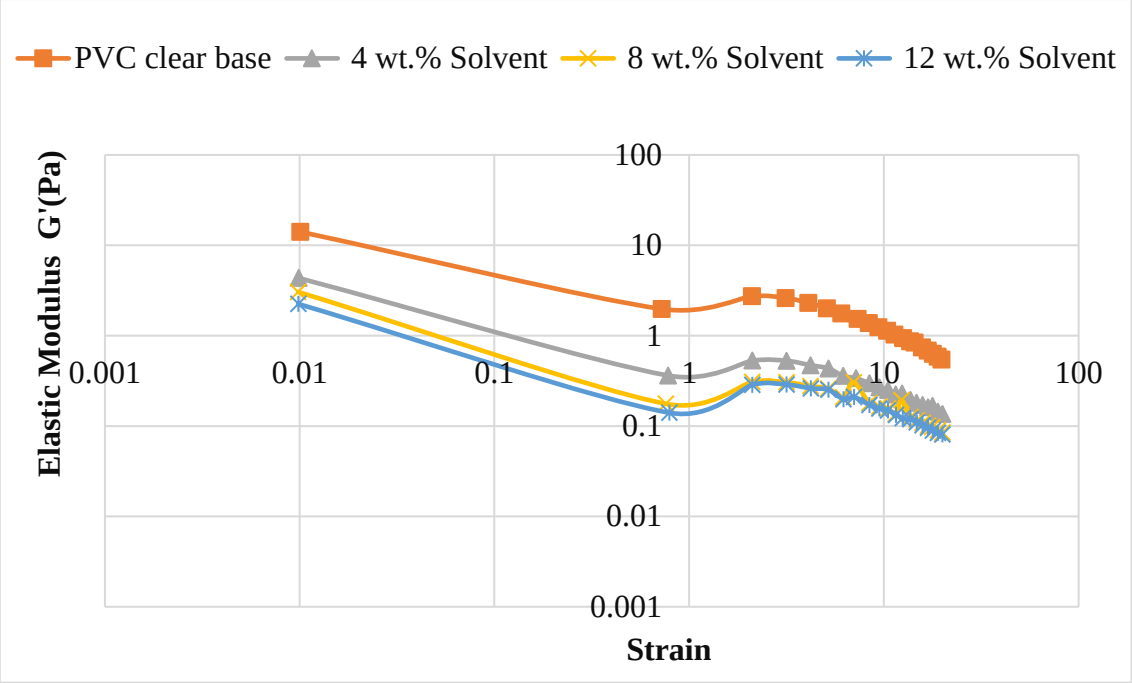

Fig. 8 - 1: A comparison of elastic modulus curves of solvent concentration of 0 (PVC clear base), 4, 8 and 12 wt. %

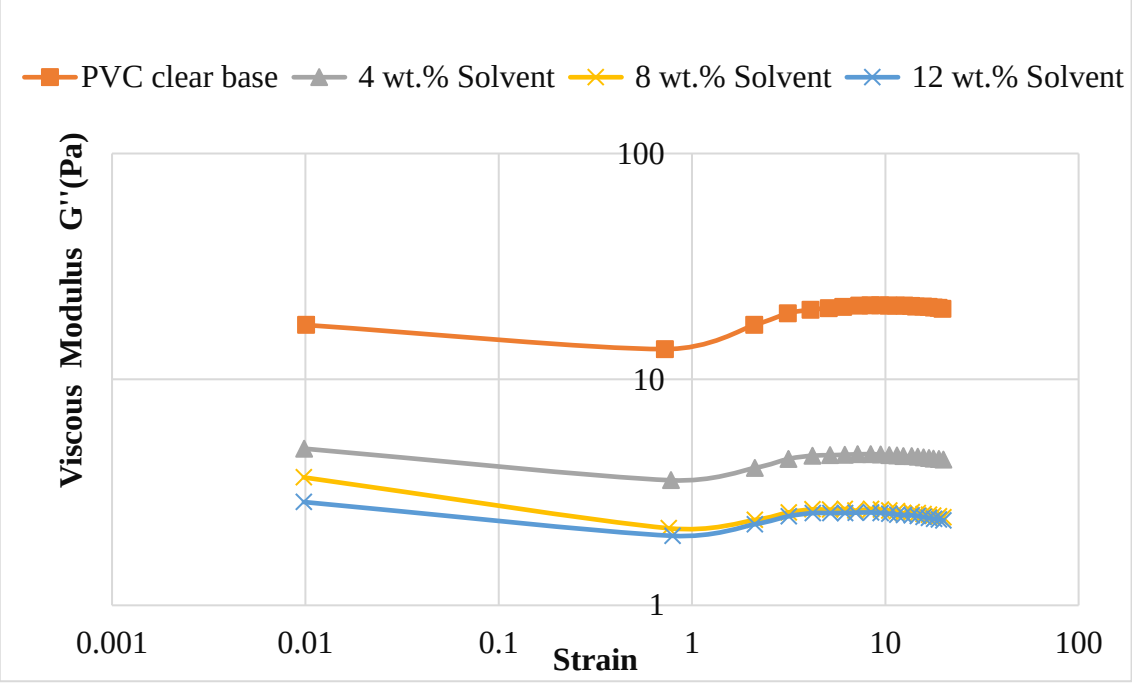

Fig. 8 - 2: A comparison of viscous modulus curves of solvent concentration of 0 (PVC clear base), 4, 8 and 12 wt. %

The double strain overshoot was credited to the polymer side chains of the backbone of the PVC polymer chain. At low strain value, the chain aligns to a certain degree due to the electrostatic charge between neighbouring polymer groups. However, at medium strains, the side chains of the long polymer backbone resist deformation due to the entanglement of the side chains with the nearest side chains on the neighbouring polymer

group. Thus, the entangled and entwined side polymer side chains exhibit a weakly complex structure in the form of a strain overshoot in the amplitude sweep. At high enough strain values above the critical strain, the weak structure is deformed, and the material initiates flow as expected. A strong strain overshoot was also exhibited by commercial paints.

8.3.1.2. FREQUENCY SWEEP

A frequency sweep was conducted at a strain value of 0.7 in the frequency range of 20 Hz. Fig. 8 – 3 and Fig. 8 - 4 compare elastic and viscous modulus of PVC coatings with different concentrations. It witnessed that at both moduli, PVC clear base showed the highest value than the other solvent concentrations, as expected, due to a higher polymer density in the PVC clear base.

A dependence of elastic and viscous moduli on frequency was seen at all frequency test range, except for frequency values of 10 Hz and above where erroneous data was. Elastic modulus dependence on frequency is an indication of a weak gel system of the model fluids.

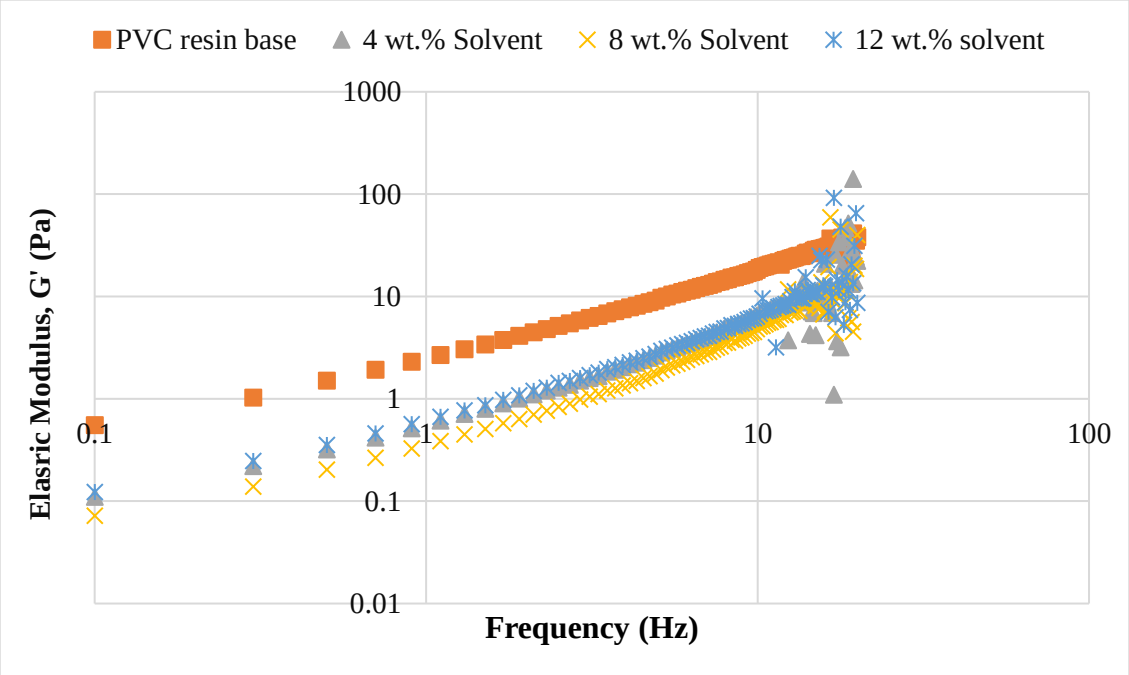

Fig. 8 - 3: A comparison of elastic modulus curves of solvent concentration of 0 (PVC clear base), 4, 8 and 12 wt. %

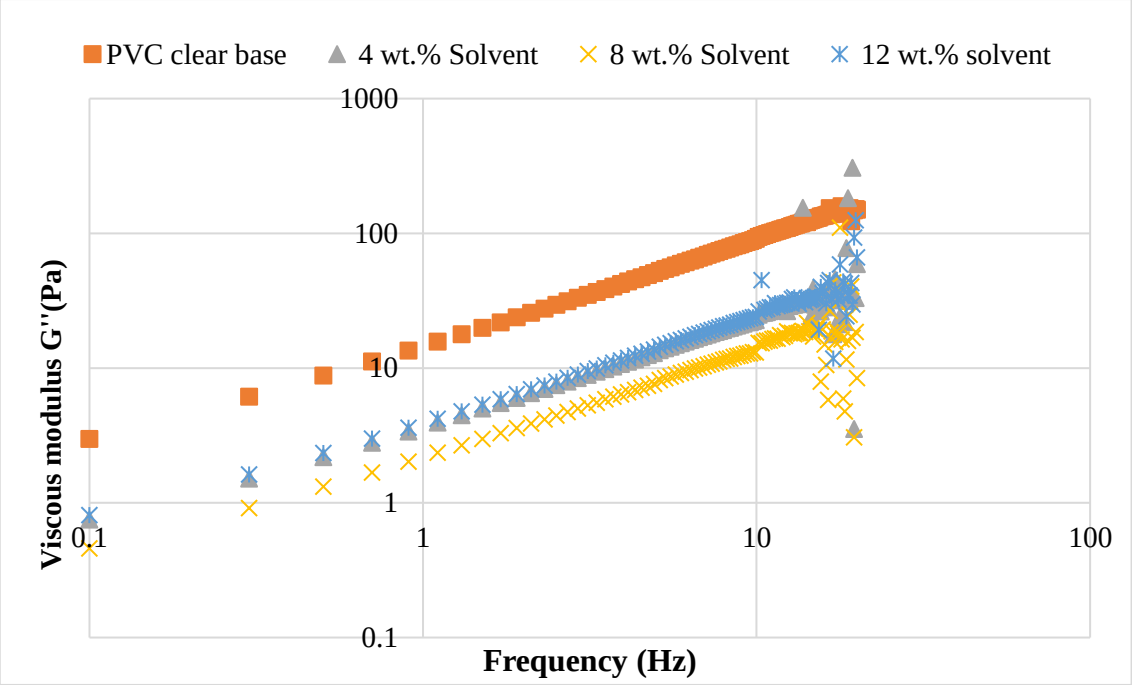

Fig. 8 - 4: A comparison of viscous modulus curves of solvent concentration of 0 (PVC clear base), 4, 8 and 12 wt. %

A comparison of the phase angle of solvated model fluids is represented in fig. 8 – 5. Phase angles of solvated PVC coatings responded differently from pigmented PVC coating. Firstly, almost a complete overlap of phase angles was seen between frequency ranges of 0.1 – 3 Hz, and above the mentioned frequencies, differences in the curves were seen.

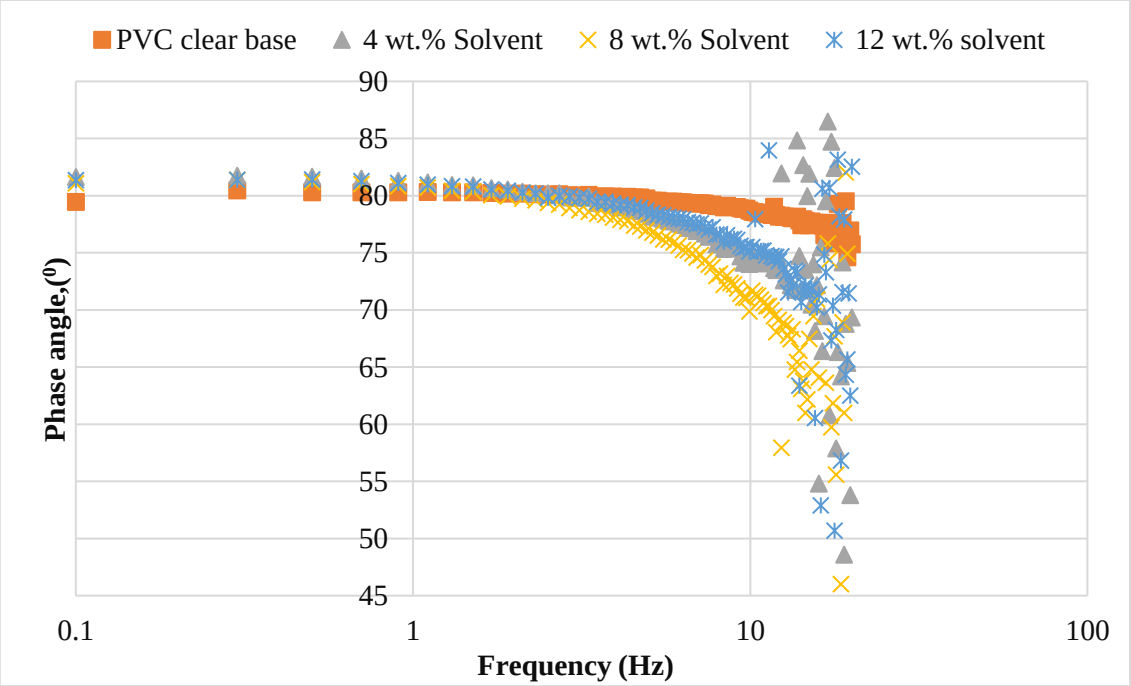

Fig. 8 - 5: A comparison of phase angle curves of solvent concentration of 0 (PVC clear base), 4, 8 and 12 wt. %

Secondly, the phase angle of higher solvent concentration was lower than those seen for low solvent concentration portrayed that solvent concentration increased elastic properties, though individually elastic modulus was higher for low solvated model fluids.

Thirdly, the increased frequency decreased the phase and thus increased solid-like properties due to reduced time. These results showed time dependence of solvated PVC coatings than pigmented model fluids that showed negligible change with frequency.

8.3.2. APPARENT WALL SLIP (AWS)

Effect of solvent concentration on AWS behaviour of PVC coatings was investigated by conducting a gap-size shear rate dependence of model fluids with solvent concentrations of 0 wt. % (PVC clean base), 4, 8,12 and 36 wt. %. The experimental plan is presented in chapter four.

8.3.2.1. GAP SIZE VISCOSITY DEPENDENCE

Fig. 8 – 6 shows the gap size shear rate dependence of model fluids of solvent concentration 0 – 36 wt. %. The primary data shows a shift in steady-state flow curves, more so for low solvent concentrations, when gap sizes were varied, denoting the presence of apparent wall slip behaviour. All PVC coatings exhibited a swap of dominance; though may not be that obvious from the primary data; flow curves of small gap sizes showed the higher apparent shear rate at low shear stress, while flow curves of large gap size showed the highest apparent shear rate at high shear stress.

It was witnessed that at large gap sizes, reported apparent shear rates were very high and often out of the capabilities of the Bohlin Geminin rheometer. Consequently, the rotating geometry often ceased rotation. PVC coatings with high solvent concentrations such as 36 wt. % and tested at large gap sizes were prone to this issue. Therefore, extrapolation of flow curves for shear stress values that could not provide the resultant apparent shear rates, using the power-law model, was carried out to proceed with the investigation of AWS. The extrapolated apparent shear rates highlighted with different colours on the flow curves in Fig. 8 - 6.

Minimal extrapolation was required for low solvent concentrations in comparison to high solvent concentration. As a result of a high degree of extrapolation carried out at 36 wt. % solvent concentration, PVC coating with a solvent concentration of 36 wt. % was eliminated from test materials

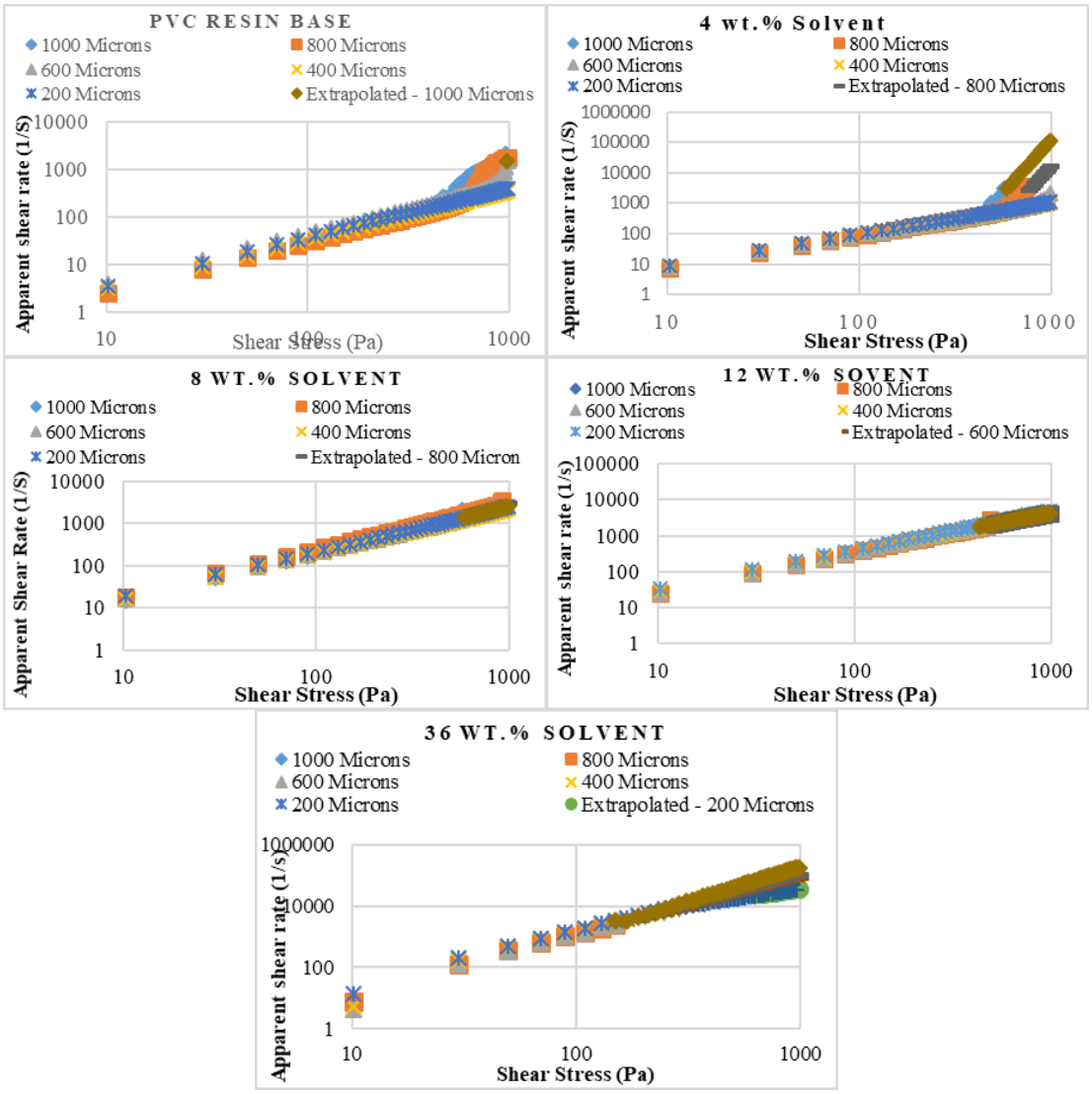

Fig. 8 - 6: Accuracy of the Mooney analysis for model fluids with 0 wt.% (PVC clear base), 4 wt.% , 8 wt.%, 12 wt.% and 36.wt.% solvent concentration.

8.3.2. EXTENSIONAL RHEOLOGY

Commercial coatings that are more versatile under industrial condition displayed higher extensional viscosity with strong tension thinning properties. Thus, the effect of solvent concentration on PVC coatings was investigated using a PVC clear base and PVC clear coatings with solvent concentration of 4, 8 and 12 wt.%. A detailed experimental procedure employed in chapter five was employed in this work.

8.3.2.1 PROGRESSIVE FILAMENT RADIUS

A sequence of images (Fig. 8 – 7 to fig 8 – 10), denoted as A, B, and D for PVC clear base, 4 wt.%, 8 wt.%, and 12 wt.% solvent concentration, show progressive filament radius of solvated PVC coatings as a function time.

(A) PVC clear base

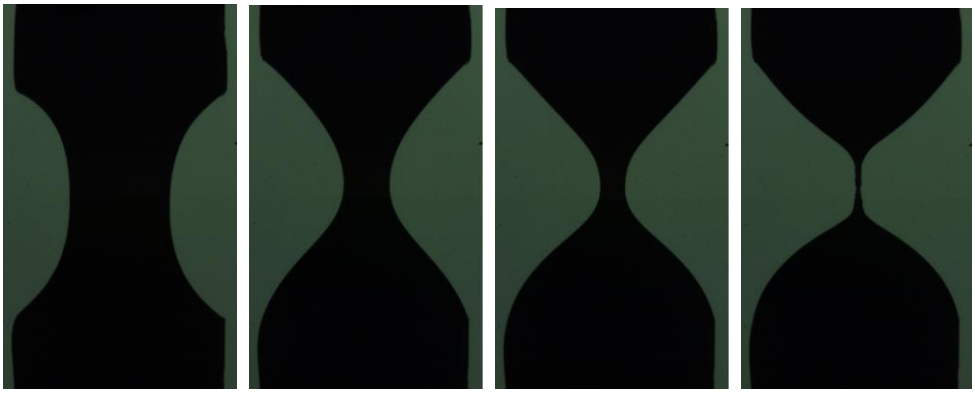

Fig. 8 - 7: Sequence of images showing progressive filament radius at 0.15, 1.04, 1.43 and 1.62 seconds, respectively.

(B) 4 wt.% Solvent concentration

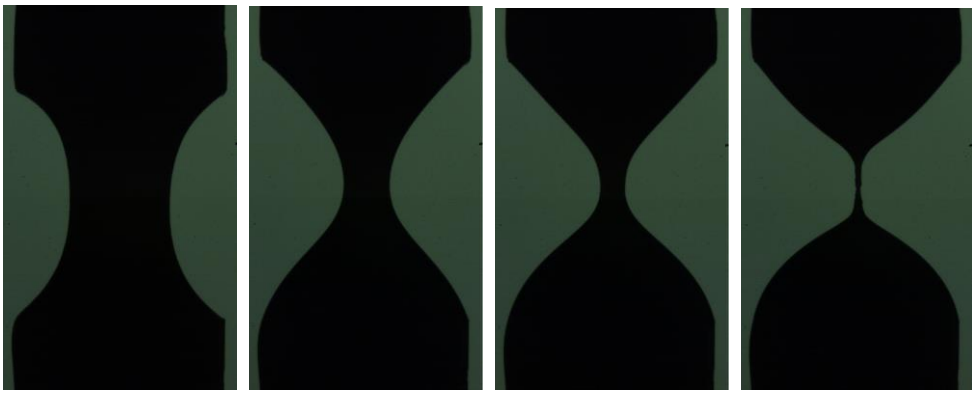

Fig. 8 - 8: Sequence of images progressive filament radius at 0.028, 0.239, 0.46 and 0.5 seconds, respectively.

(C) 8 wt.% Solvent concentration

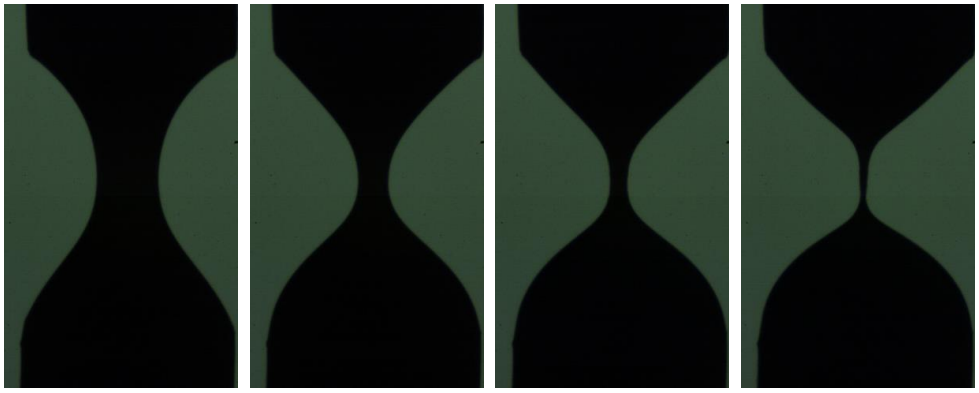

Fig. 8 - 9: *Sequence* of images progressive filament radius at 0.028, 0.052, 0.59and 0.63 seconds, respectively.

(D) 12 wt.% Solvent concentration

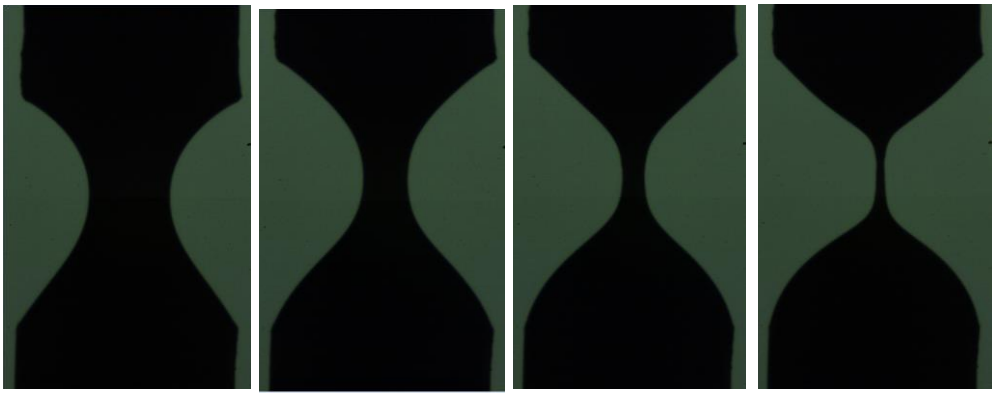

Fig. 8 - 10: Sequence of images progressive filament radius at 0.05, 0.18, 0.21 and 0.23 seconds, respectively.

Filament radius of the same size for each solvated coating was compared to monitor the effect of solvent concentration on the rate of filament radius.

PVC clear base exhibited a slower rate of filament thinning in comparison to solvated PVC coatings. Conversely, 12 wt. % solvated PVC coating showed a faster rate of filament thinning. However, images are qualitative, and a human eye is prone to error. Therefore, using a CaBER analyser tool, a series of obtained images were quantified to provide information about the progressive filament radius as a function of time. Fig 8 - 11 shows a semi-log plot of progressive filament radius with time.

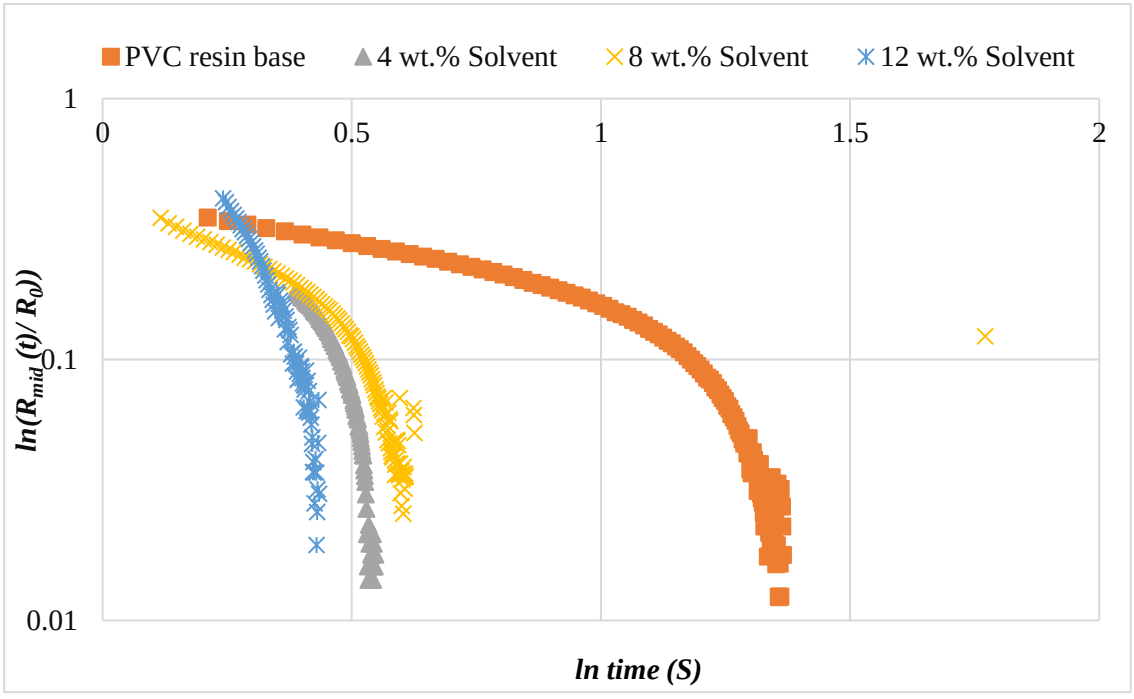

Fig. 8 - 11: Semi-log plot of progressive filament radius with time for different solvent concentrations

All PVC coatings showed a visco-capillary regime at all tested time test range denoting non-Newtonian, tension-thinning tendencies. The absence of the elasto-capillary regime depicted predominately viscous materials. There were instabilities observed at the critical filament break up radius due film break up and recombination. High surface tension materials are often prone to film split and recombination; however, the initial film break was considered as the film break up point and thus critical-up time.

The power law tension-thinning model shows great accuracy, with R^2 ranging between 0.97 - 1.00; R^2 is highest at PVC clear base (0 wt. % solvent). Flow indices, prefactor and critical filament radius increased with solvent concentration, denoting weak tension thinning behaviour that film splits at thicker filament thickness. The opposite is true for low solvent or no solvent PVC coatings; generally, the critical radius and flow indices reduced with reduced solvent concentration, indicating stronger tension thinning tendencies at low solvent concentration.

8.3.2.1 EXTENSIONAL VISCOSITY AGAINST HENCKY STRAIN

Fig. 8 – 12 represents extensional viscosity of solvated PVC coatings and PVC clear base as a function of strain rate.

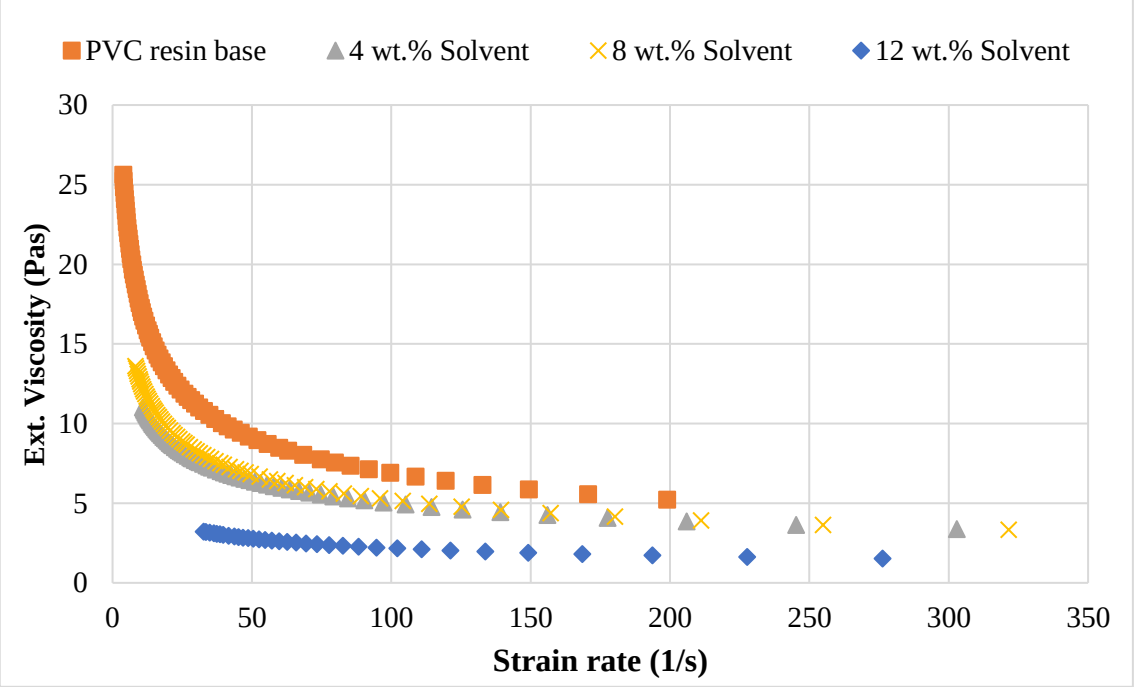

Fig. 8 - 12: extensional viscosity against strain rate for different solvent concentrations

Tension thinning strength increased with decreased solvent concentration; for example, PVC clear base showed two regions in the flow curve; a distinct power-law region and a

Newtonian plateau. While a 12 wt. % solvated PVC coating showed a strain rate-independent extensional viscosity.

Low solvent concentrations not only possess strong tension thinning, properties but also show high zero-viscosity and high effective viscosity at the Newtonian plateau; zero-viscosity is observed at 25.3, 13.45,10.68 and 3.21 Pas for PVC clear base, 4 wt.%, 8 wt.% and 12 wt.%. The same trend is observed for the Newtonian plateau viscosity, except that the 4 wt. % and 8 wt. % curves overlap with a viscosity value of 3.9 Pa. High extensional viscosity was credited to stronger binding powers between polymer molecule thus higher extensional viscosities. At high solvent concentration, solvent weakens the bonds holding polymeric molecules thus low viscosity reported.

8.4. CONCLUSIONS

Chapter eight has addressed the effect of solvent concentration on the rheological behaviour of PVC coatings were studied. Rheological studies from dynamic oscillatory rheometry, to apparent wall slip characterisation and extensional rheometry, showed an influence off solvent concentration on PVC coating behaviour.

Dynamic oscillatory rheometry showed a decrease in elastic modulus curves; however, phase angle results exhibited a decrease with increasing solvent concentration. This depicted a decrease in both the elastic and viscous modulus when solvent concentration increased.

Gap size viscosity dependence of low solvent concentration (PVC clear base and 4 wt.% solvent concentration) showed the development of both a lubricating and stagnant layer. Additionally, the Mooney analysis broke down at small gap sizes when tested at low solvent concentrations, and apparent wall slip characteristics varied with gap sizes.

High solvent concentrations (8 wt. % and 12 wt. % solvent concentration), interestingly, showed the development of one of each AWS behaviour. 8 wt.% solvent concentration showed the development of a thin stagnant layer (almost negligible) to be formed; while 12 wt.% exhibited the development of a thin lubricating layer at predominantly all sliding speeds. Therefore, the optimal solvent concentration with negligible AWS lies between 8 – 12 wt. %.

Additionally, the sizes of the anomalous layer thicknesses and relative slip contribution did not change with gaps sizes when high solvent concentration PVC coatings were tested. This was the opposite behaviour of the PVC clear base and 4 wt. % solvent concentration. The findings, therefore, confirmed the accuracy of the Mooney analysis to simpler liquids such as highly solvated PVC coatings.

Finally, high extensional rheology of low solvent PVC coatings revealed an increase of tension thinning properties (lower flow index) coupled with higher extensional viscosity. Additionally, a delayed coating film break for low solvent PVC coatings was parallel to the filament behaviour of Coating B (chapter five) and Coating X (chapter six), and thus denoted a better performance at the coating line.

Therefore, this chapter has highlighted the rheological impact of varying solvent concentration and provided a well-characterized set of materials which can be employed to further examine the pickup process in the roll coating process.

CHAPTER NINE:

PARAMETRIC STUDIES ON ROLL COATING RIG – PART 1; COMMERCIAL PAINTS

9.1. INTRODUCTION

Rheological studies conducted on commercial coatings revealed a difference between Coating S and Coating B, and Coating X and Coating Y. Similarly, Model fluids of pigmented and solvated PVC coatings exhibited a difference in rheological performance because of variation of pigment and solvent concentration. However, the failure of the Mooney analysis to predict sensible slip layer thicknesses and relative slip contribution results of multiphase systems inspired further research of coating film thickness on the pick-up roll, $H_{pick-up}$ from the coating trough. Therefore, Chapter nine focuses on parametric studies, a variation of pick up roll speeds, on the film thickness. This information, in addition to theological studies, provides information about PMD encountered at the coating line. The investigation aimed to investigate the steady-state relationship between the pickup roll rotation, coating rheology and the quantity of material picked up from the trough to the roll.

9.2. MATERIALS AND METHODS

9.2.1. MATERIALS

9.2.1.1. COMMERCIAL COATINGS

Under rheological characterisation, Coating B and Coating X met the criteria of a coating that was deemed successful, following the QC system developed. The two coatings tested on the roll coating rig to monitor their performance under controlled conditions.

9.2.2 DESCRIPTION OF EXPERIMENTAL SET - UP

The effect of pick-up roll speed and rheological properties on pickup process was investigated using a benchtop roll - coater rig showed in fig. 9 – 1. The rig consisted of

various components, namely: 40 mm Pickup roll, laser gauge thickness, coating trough, data logger, DC motor drive and a PC.

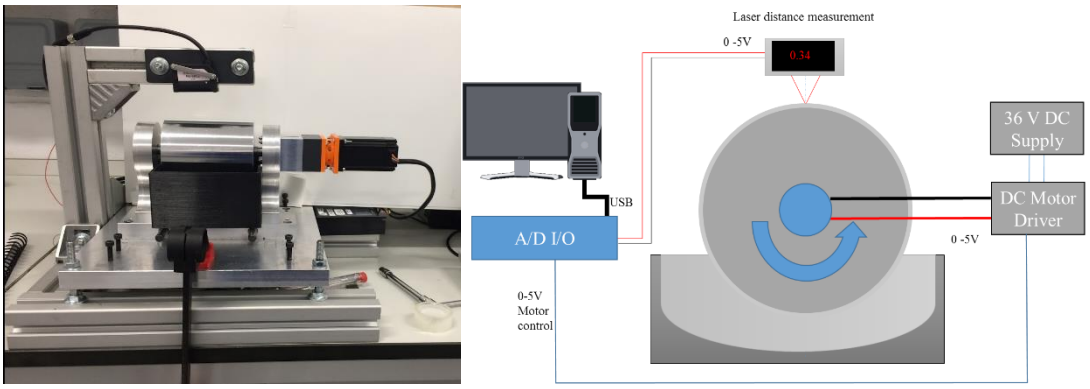

Fig. 9 - 1: Schematic of a benchtop roll coater rig

The coating film thickness on the pick-up roll was measured using a ILD1750-2 Laser optical displacement measuring system with an integrated digital signal processor, purchased from Keyence Limited, which operated by shining a laser at the surface of the roll with a layer of coating and measuring the distance by the location of the reflected light on a linear CCD array. The measurement system was operated in a voltage output mode with a distance range of 25 - 40 mm and a quoted measurement accuracy of 0.002 mm. The voltage signal was subsequently captured by a LabJack 3 A/D I/O module linked to the PC using a USB interface. The Labjack unit was set to operate in a 0 - 5 V input mode with 4096-bit resolution meaning a nominal accuracy of 0.25 mV. Custom software was written which allowed for direct setting of the motor speed (following an acceleration phase of around 120 seconds) and direct data collection of the laser distance measurement (voltage) at 7.5 kHz for a specified period of up to 30 minutes

The experimental rig was constructed from rigid Rexroth aluminium section clamped securely to a fixed steel laboratory such that vibrations were minimized. The roll was constructed from solid aluminium and finished with a ground surface. The motor was joined to the roll via direct coupling to the roll shaft. A BL060 –H03 –G brushless DC drive motor was used to drive the roll and the current limit of 7.2 A dictated the 120 seconds acceleration time to limit the sudden inertial load on the motor.

The coating was held in a coating trough which was 3D printed in 3 parts to facilitate installation and cleaning. These parts were bolted together using a threaded bar to provide the necessary mechanical integrity. The porous nature of the 3D printed coating trough

structure necessitated the covering of the inner surface of the trough using waxed adhesive tape. This was replaced each time the fluid was changed in the trough.

The pickup process was comprised of two processes: the immersion of the pick-up roll with 40 mm diameter and 110 mm roll length, in a coating trough with ~ 200 ml volume of test liquid. This was followed by coating deposition onto the pickup roll, followed by the roll withdrawal from the coating trough. Immersion (residence) time of the pickup roll in the coating trough was governed by the pickup-roll speed, and the concept of the dip-coating process at an angle was considered under this study.

The pickup roll speed was varied from 0 – 5V (34 – 56 m/min) to enable investigation of roll speed effect on the coating thickness picked up. The Laser optical displacement measuring system was positioned at the centre of the pick-up roll length, equidistant from the edge of the roll length. Note: an eye was kept a flash LED red light on the roll/ coating surface as an indicator of a "soiled lens" and ensuring that the laser source was cleaned.

The assumption that the width and depth of the coating trough were large enough not to influence free surface flow was made. Before data collection, a preconditioning time of ~2 minutes was considered to factor in rotation start-up issues and uniform conditions throughput the coating troughs. The pickup roll at a given speed was set to run for ~ 10 minutes whilst collecting data on coating thickness over that time.

9.2.3. MEASUREMENT CALIBRATION

Prior to parametric studies, machine calibration was conducted to understand roll cylindricity, background noise, the relationship between a substrate thickness and output voltage and error approximation on the obtained. Polyester sheets of 175 μm thickness were employed in the calibration process which resulted in the film thickness/ voltage output presented in fig. 9 – 2.

The relationship between voltage output and substrate thickness is linear (see Eqn. (9 – 2) derived from Eqn. (9 – 1)) with an accuracy of $R^2 = 0.9961$. Thus, coating thicknesses calculated from voltage output from the data logger was determined from the relationship mentioned.

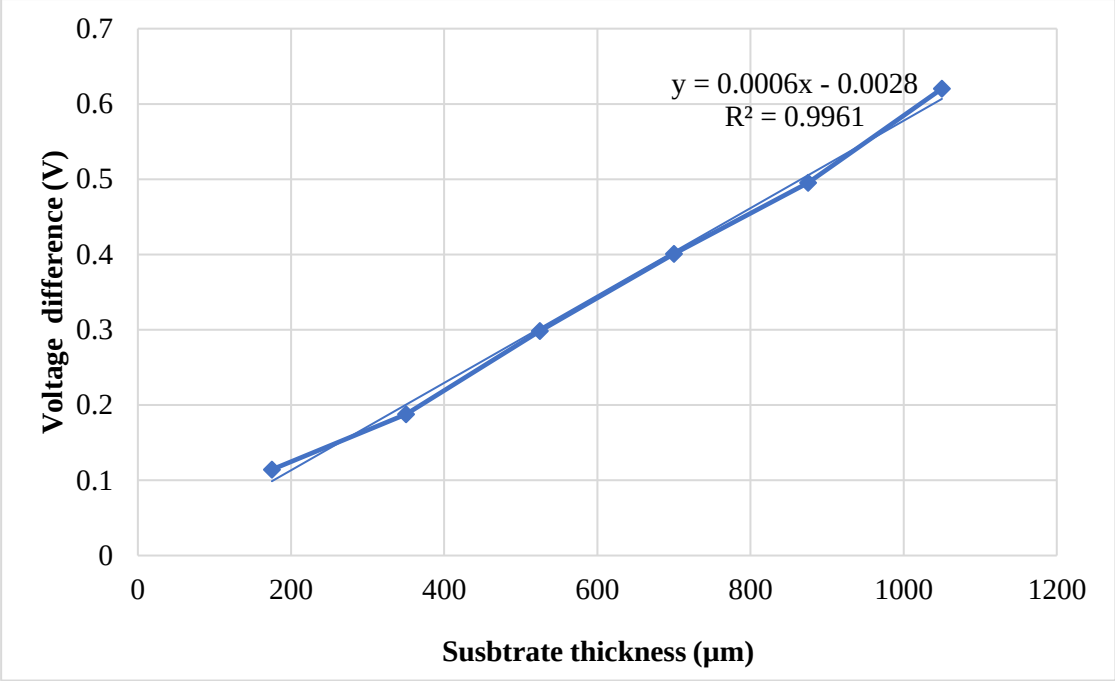

Fig. 9 - 2: Relationship between the position of the laser gauge and Voltage differences

$$V = 0.0006\,\delta - 0.0028 \qquad (9 - 1)$$

$$H_{app} = 1716\,V + 7.2336 \qquad (9 - 2)$$

Where H_{app} coating thickness (µm) and V is voltage output from the data logger (V). Having calibrated the system, initial trials identified interesting phenomena, which is occasionally observed on the full-scale production line; the ribbing phenomena.

9.2.4. RIBBING CONTRIBUTION TO THE TOTAL COATING THICKNESS OF COMMERCIAL COATING

The initial experimental trials found that the coating exhibited variation in coating thicknesses along the roll length, also known as ribbing, over a period at the same speed. This can be seen in Fig. 9 - 3(a), visually observed as high points in the measured thickness, Fig 9 - 3(b). Occasionally following a high amplitude in the rib, a zero-film thickness was measured.

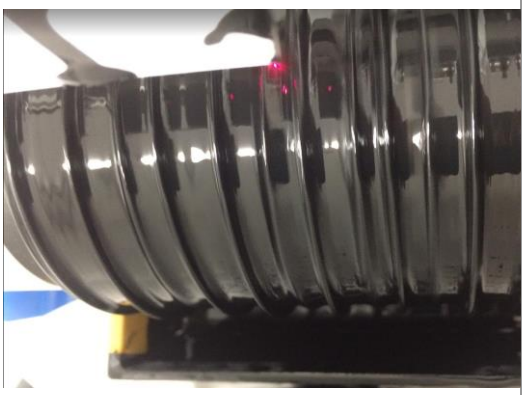

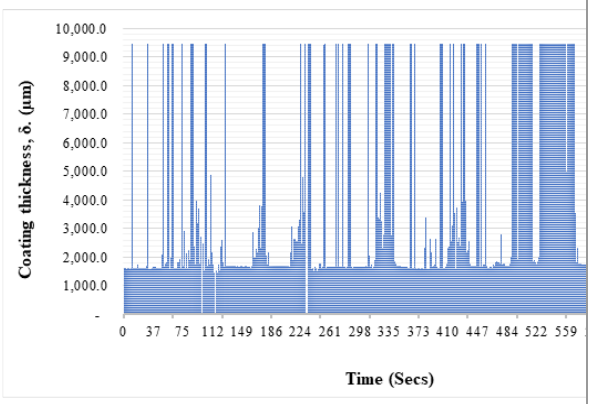

(a) (b)

Fig. 9 - 3: (a) Example Coating ribbing and (b) Measured thickness (with ribbing contribution) against rotation time for Coating B at 34 m/min (13 RPM)

These could be attributed to the edge of passing rib causing an optical barrier between the laser and detector. These ribs were not present with all operating conditions and materials and would tend to oscillate laterally across the roll such that a measurement of film thickness at a fixed position on the roll surface tended to fluctuate with the passing of a rib. The presence of the ribs provided a challenge when attempting to calculate the film thickness that has been picked up, in that coating picked up is highly discontinuous, and thus a consistent method of calculating a mean value needed to be developed. To calculate the mean film thickness, sudden peaks in height above a mean baseline were removed from the signal. The resultant film thickness measured without ribbing is presented in fig. 9 – 4. This also allowed an estimation of percentage ribbing contribution, through the counting of null values within the measurement period.

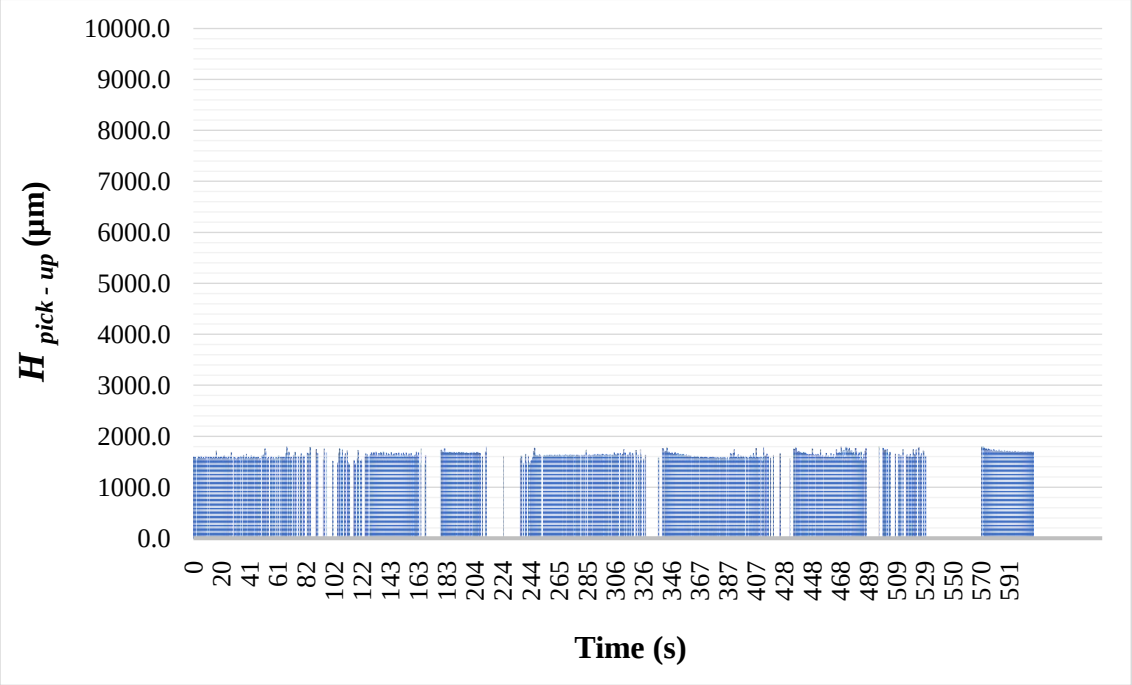

Fig. 9 - 4: Coating thickness (without ribbing contribution) against rotation time (0.15 V or 13 RPM)

9.3. RESULTS AND DISCUSSION

The quantity of material which was required for each test meant that a full analysis of the all commercial coatings could not be carried out due to limited quantity of material available. The coatings that were under study were Coating B (Better coating for Plasticeram black coating) and Coating X (Coating X for Plasticeram Sun Merlin)

A series of images of the coating layer on rotating pickup roll over some time were randomly taken during the experiment to visualise the uniformity of the coating layer being picked up.

9.3.1 COMMERCIAL COATINGS

Fig. 9 – 5 and fig. 9 - 6 show coating layer uniformity of Coating B and Coating X on the pickup roll during geometry rotation depicting that PVC coating systems possess a high tendency to rib; the image on the left shows the presence of ribbing phenomena while the image on the right shows the absence of ribbing phenomena. The ribbing phenomena prevailed during rotation, and the ribs often shifted across the roll length and therefore intermittently picked up by the Laser optical displacement measuring system.

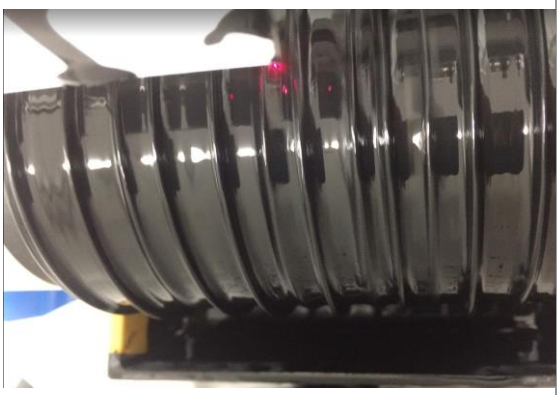

(a) **(b)**

Fig. 9 - 5: Image of coating thickness of Coating B on the pickup roll surface during rotation (a) and pickup roll surface without roll rotation (b)

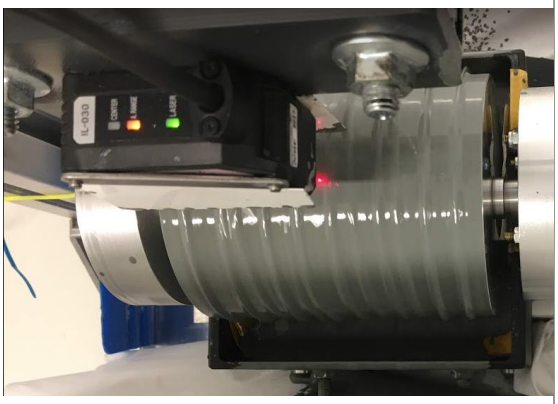

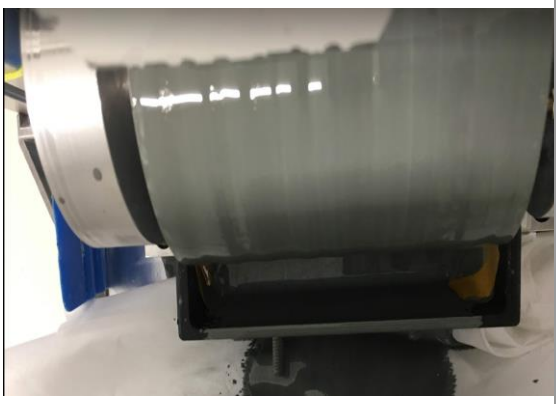

(a) **(b)**

Fig. 9 - 6**:** Image of coating thickness of Coating B on the pickup roll surface during rotation (a) and pickup roll surface without roll rotation (b)

Coating B and Coating X displayed ribbing phenomena during the pickup roll rotation; however, the ribbings disappeared upon cessation of roll rotation. The ribs showed the same wavelength throughout the experimental test time for both coatings though Coating B showed prominent ribs than Coating X. Furthermore, pigment separation was observed on the pickup layer of Coating X upon roll rotation cessation; white lines were seen on the picked - up coating layer. The pigment separation was not exhibited by Coating B denoting a possible colour/ pigment separation in Coating X due to possible pigment blend of Plasticeram sun Merlin – Titanium dioxide and carbon black pigment. Coating B did not display colour separation as one coloured pigment (possibly carbon black) was employed in its formulation.

Also, ribs disappeared upon cessation of roll rotation for all coatings was observed. It is worth noting that the recovery from ribbing to a uniform layer was a gradual process that took place over time. This recovery of coating layer thickness was attributed to the thixotropic tendencies of coating and was believed to play a crucial part during the levelling process (rectification of defects) at the upstream end of the roll coating process. Cohu and Magnin [55] write that levelling and structural rebuilding due to thixotropy are always in competition with each; therefore, sufficient structural rebuilding time should be given for better levelling.

Fig. 9 – 7 compares coating thickness with ribbing contribution against sliding speed for Coating B and Coating X. The solid line represents a polynomial fit through the points. It was observed that coating thickness increased with sliding speeds for coating B. on a further look, the highest film thickness for Coating B was observed in sliding speed range of 46 – 51 m/min whilst the lowest coating thickness was detected at very low sliding speeds.

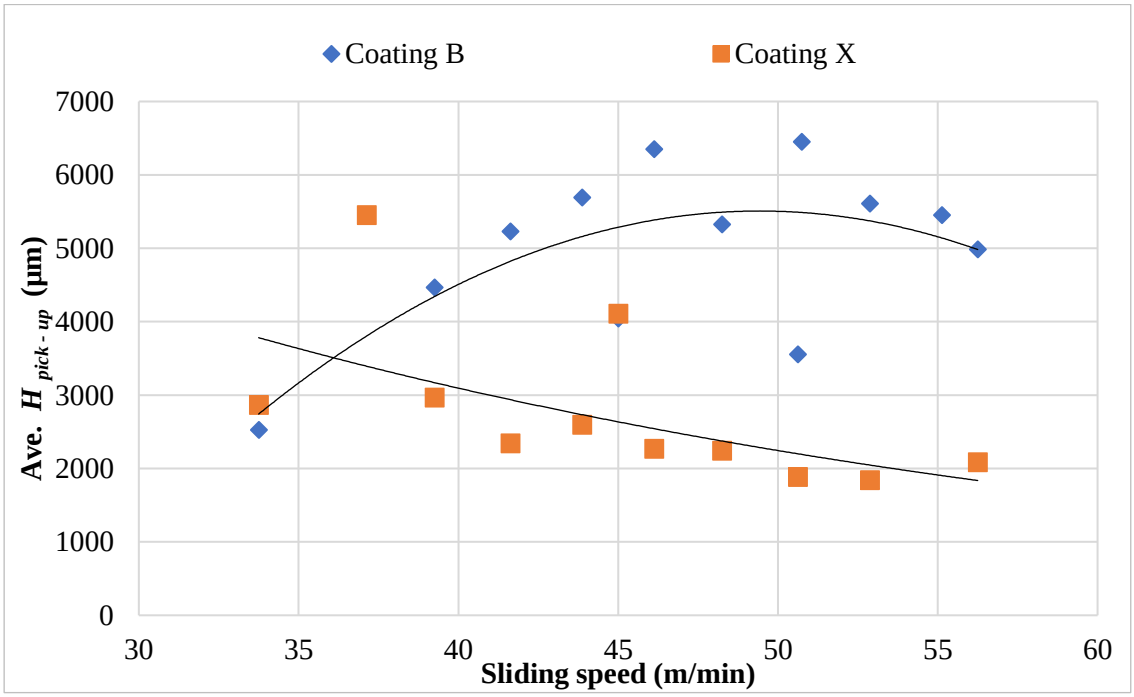

Fig. 9 - 7**:** Average coating thickness (with rib contribution) against sliding speeds

Conversely, Coating X displayed the opposite trend to that of Coating B; coating layer thickness decreased as sliding speeds increased, with optimal coating thicknesses at low speeds. Based on the information provided from the operators and process engineers at the coating line, slow line speeds to aid the pickup of a thicker coating layer. Therefore, this information was parallel to typical industrial observation.

The difference in trends of Coating B and Coating X at elevated sliding speeds was attributed to the in the degree of ribbing phenomena (see fig. 9 – 8) that coating B suffers when sliding speeds increase. The Percentage rib contribution for both coatings followed a polynomial trend; the same trend was observed in fig. 9 – 7, depicting that ribbing phenomenon had a significant contribution to the total thickness of coating being picked up from the coating trough.

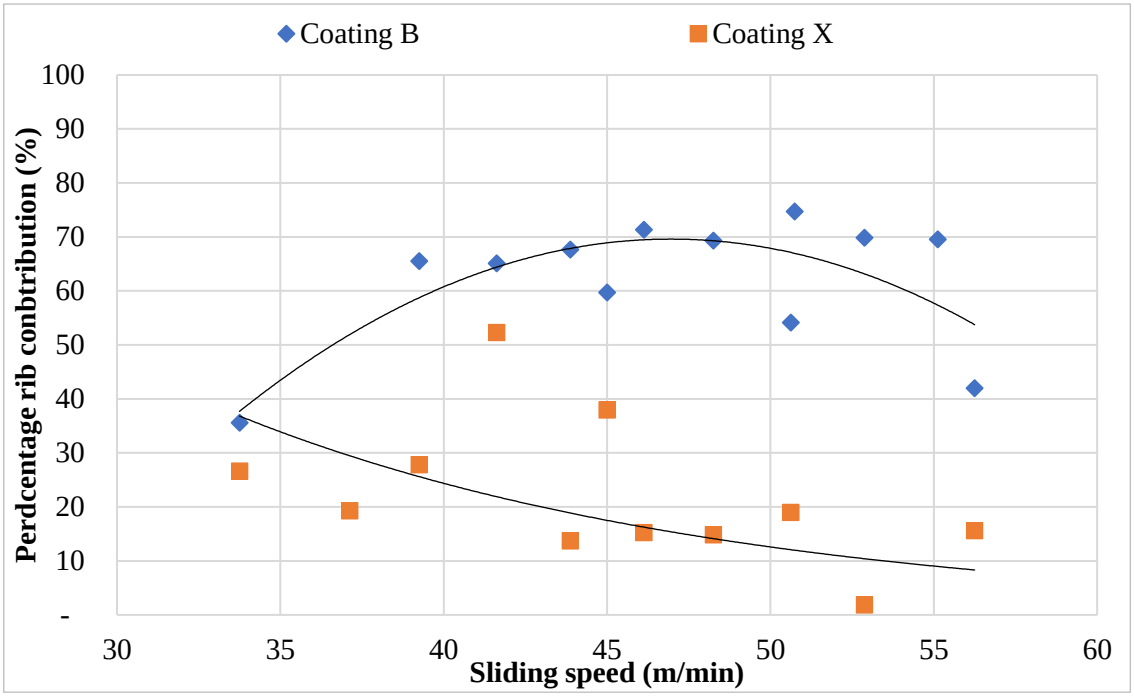

Fig. 9 - 8**:** Coating thickness (without ribbing contribution) against Surface speeds

Coating B showed a higher percentage of ribbing due to higher extensional viscosity and viscoelasticity. The latter properties coupled with high sliding speeds yield ribbing as reported by [29] because surface tension fails to stabilise the flow hence the manifestation of the inertial 3 –D instability, ribbing. Coating layer thickness with ribbing is undesirable because uneven layer thickness is carried to upstream units and subsequently causing the defect. Therefore, ribbing contribution was eliminated and the effect of coating thickness against surface speed was investigated.

Fig. 9 – 9 compares coating thickness without ribbing contribution against surface speed for coating B and Coating X. Coating layer thickness for Coating B increased with surface speeds while Coating X showed the opposite response. Also, less dependence on coating thickness on surface speed was observed. The average coating thickness for Coating B and Coating X was 1790 and 1,878 µm.

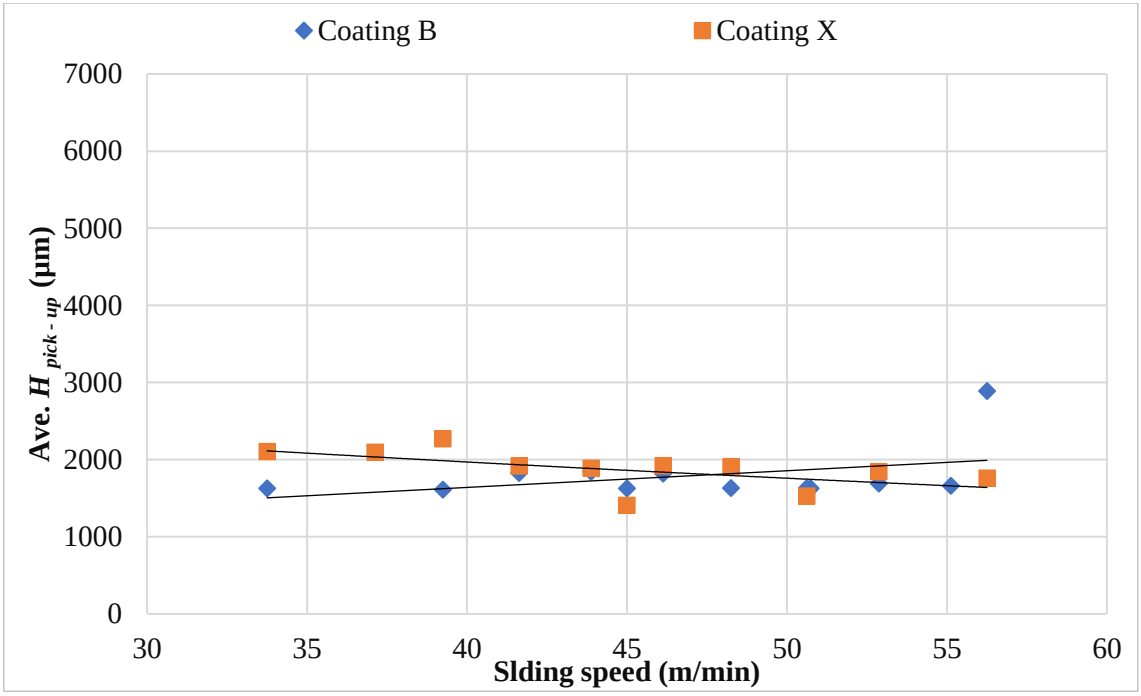

Fig. 9 - 9**:** Coating thickness (without ribbing contribution) against sliding speeds

9.4. CONCLUSIONS

The picking up process of commercial coatings as a function of sliding speeds from the coating trough has been investigated in chapter nine. Although the experimental work was set to investigate the effect of operating parameters and liquid coating rheology on the quantity of coating pick up from the trough, ribbing instabilities were manifested, and it was an interesting phenomenon.

The impact of viscoelasticity on the appearance of the coating layer on the pick-up roller is undesirable. The manifestation of ribbing phenomena was seen to be prominent at higher degrees of viscoelasticity and sliding speeds. This was evidenced when Coating B, a Plasticeram Black coating, showed a higher percentage of ribbing in comparison to Coating X, a Plasticeram grey sun Merlin coatings. Therefore, Coating B showed a thicker coating layer with ribbing than Coating X throughout the sliding speed test range.

Under industrial conditions, the impact of ribbing on the pick - up roll does not affect the quality of coating deposited on the substrate because the coating knife is positioned in the metering nip gap to deduct excess coating thickness from the deposited layer.

To compare both coatings with consideration of the coating knife, coating ribs were excluded from the data. Having excluded ribbing contribution, Coating B showed a lower coating thickness than Coating X, though the difference between the two coatings was

not significant. The methodology of deducting ribs from the collected data, however, introduced inaccuracy in results because a high quantity of coating picked was contained within each rib.

Due to the inability of the experimental rig to provide data without the influence of ribs, it was therefore deemed impossible to determine a correlation between pick up sliding speeds and coating pick up. Nonetheless, the impact of ribbing phenomena and rheological properties was of interest and subsequently studied in the next chapters.

CHAPTER TEN:

PARAMETRIC STUDIES ON ROLL COATING RIG – PART 2; MODEL PVC COATINGS

10.1. INTRODUCTION

It has been established in chapter nine that commercial PVC coatings with different rheological properties experience fluid flow and coating pick up from the coating trough differently; Plasticeram Black coatings experience higher percentage contribution of ribbing to the coating; however, Coating X shows exhibited thicker coating layer a when ribbing was excluded from the obtained results.

Therefore, this section of the thesis focuses on the investigation of the effect of pigment and solvent concentration (characterized in chapter eight and nine) on coating pickup, coating layer thickness and coating layer uniformity, from the trough to the subsequent units, in light of apparent wall slip effects during coating pickup from the trough.

10.2. MATERIALS AND METHODS

10.2.1.MODEL PVC COATINGS

(a). Pigment concentration

In order to investigate the effect of the interaction of operating parameters and pigment concentration on the thickness of coating picked up from the coating trough, PVC coating with pigment concentrations of 0.3wt. %, 0.7wt. %and 1 wt. % were prepared. Due to the high degree of pigment concentrations above 1.0 wt. %, it proved a challenge to the run the model PVC coatings with pigment concentrations higher than 1.0wt%, through the rig and therefore the test was limited to concentrations mentioned above.

(b). Solvent concentration

To investigate the effect of the interaction of operating parameters and solvent concentration on the thickness of the coating layer being picked up from the coating trough, PVC coatings with solvent concentration of 0 wt.% (PVC clear base), 4 wt.%, 36 wt.% and 57.7 wt.% were prepared. The preparation procedure in chapter nine was followed in this chapter.

10.3. RESULTS

10.3.1 RIBBING CONTRIBUTION TO THE TOTAL COATING THICKNESS OF COMMERCIAL COATING

Fig. 10 - 1 shows the physical appearance of the coating picked up when pigment concentration is varied for PVC clear base (a) & (b) and 0.7 wt. % Pigment concentration in PVC (c) & (d).

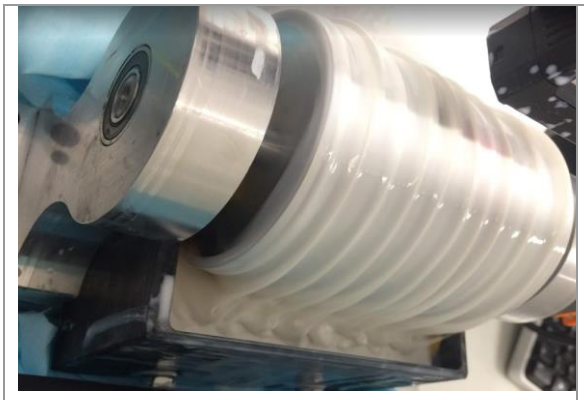

(a) No pigment coating, motion

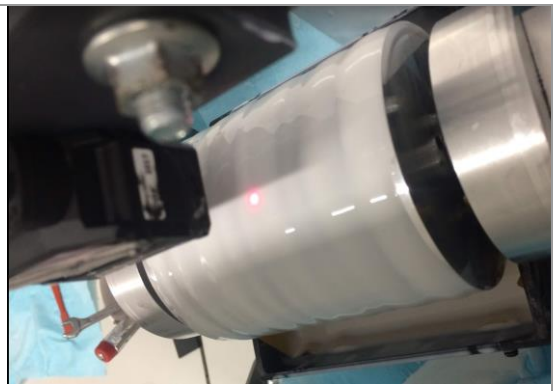

(b) No pigment coating, no motion

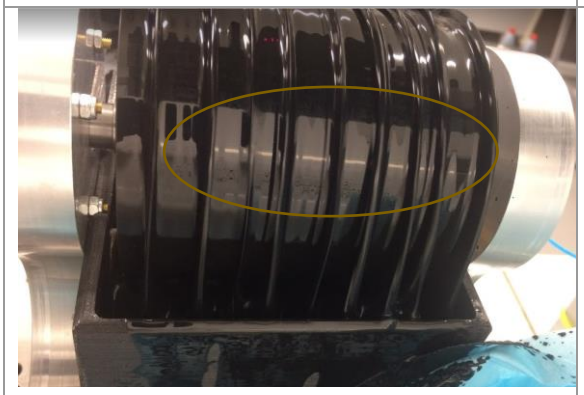

(c) Pigmented coating, motion

(d) Pigmented coating, no motion

Fig. 10 - 1: Images of PVC coating thickness on the pickup roll surface; ribbing phenomena (a) & (c) and typical coating thickness without roll rotation (b) & (d)); PVC clear base at the top and 07 wt. % Pigment at the bottom

Both model fluids experience flow instabilities during geometry rotation (a) & (c), but also shows a coating recovery upon cessation of rotating geometry (b) & (d). The ribbed coating layer of PVC clear base showed tighter wavelength (higher frequency) and smaller amplitude of the ribs, while 0.7 wt. % pigment concentration showed a shorter wavelength (higher frequency) and a larger amplitude.

Based on the results obtained from the dynamic oscillatory rheometry tests, increased pigment concentration increases the elastic modulus, but also affects the frequency and the amplitude of the ribs. The higher amplitude of the ribs was attributed to the Weissenberg effect or rod clubbing effect as reported by Johnson, M.A.[29] and Alonso *et al* [127].The consequence of the Weissenberg effect is beyond the scope of the research project and therefore not looked into.

It is worth noting, that the circled region on the ribbed coating layer of 0.7 wt. % pigment is not a coating defect but light reflection off the coating-guard which was white and also had coating sputter off the roll.

Furthermore, the relaxed coating layer upon cessation of geometry rotation, for PVC clear base showed a recovery from ribbing; however, a complete recovery was not achieved. For 0.7 wt. % Pigment concentration, a complete recovery from ribbing was achieved though white lines in areas where ribs were once positioned, could be seen, and was attributed to phase separation of particles from the bulk during shearing. Besides, the layer of coating thickness picked up from the coating trough appeared to be thicker than that of PVC clear base depicting an influence of pigment concentration on the quantity of coating picked up from the trough.

10.3.2 EFFECT OF PIGMENT CONCENTRATION ON COATING THICKNESS

Fig. 10 – 2 shows coating thickness against sliding speed with ribs (blue) and without ribs (orange), for PVC clear base (a), 0.3 wt. % Pigment (b), 0.7 wt. % Pigment (c) and 1 wt. % Pigment concentration (d).

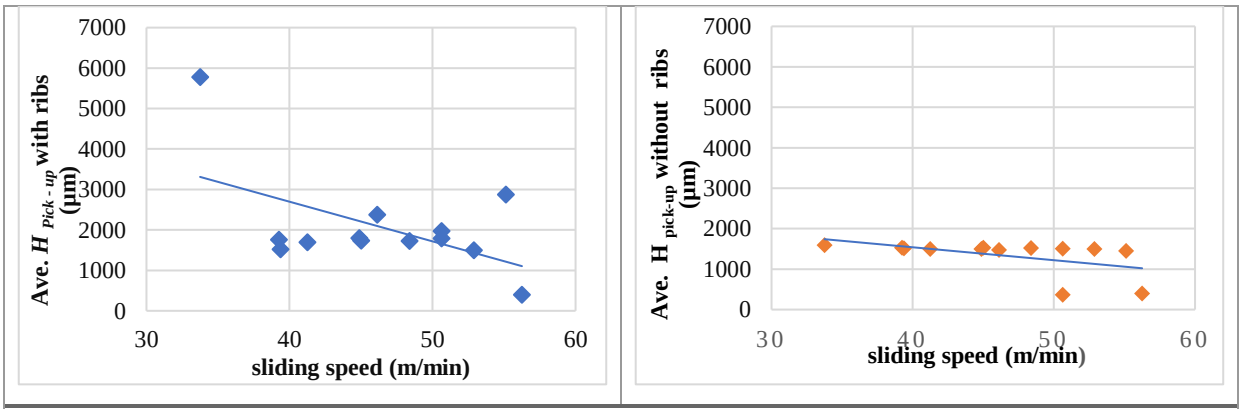

(a) 0 wt.% PVC Clear base

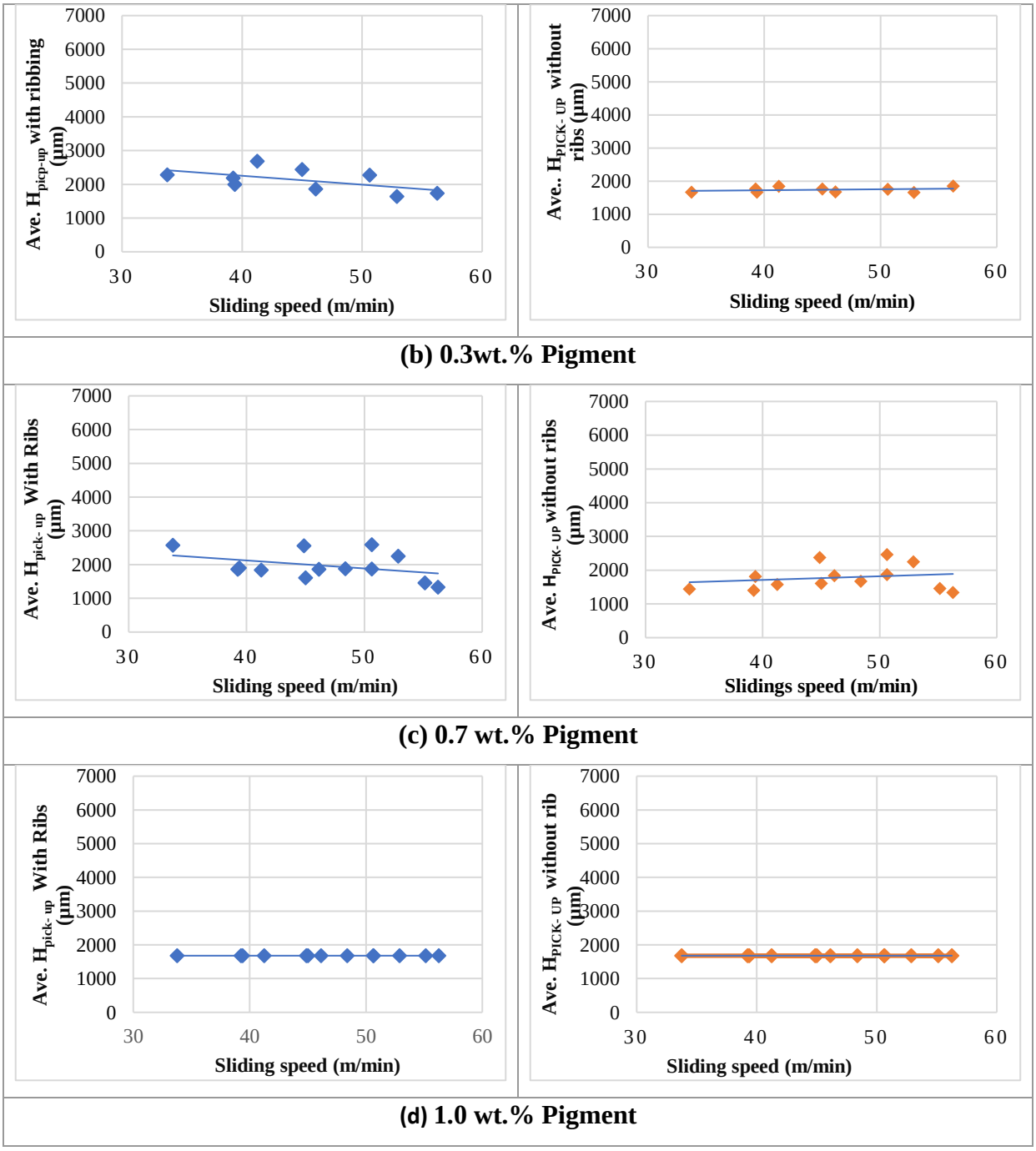

Fig. 10 - 2: Coating thickness with ribs (blue) and without ribs (orange) against geometry speeds for PVC clear base (Top row), 0.3 wt. % Pigment (second Top row), 0.7 wt. % Pigment (second Bottom row) and 1 wt. % Pigment (Bottom row).

The lower the pigment concentration the less stable the coating layer picked up depicted as ribs. For example, PVC clear base exhibited a range of $H_{pick-up}$ values from ~ 6000 µm at 34 m/min to ~396 µm at 56 m/min. However, 1 wt. % pigment concentration exhibited ~1679 µm throughout the test range speeds. This was credited to the higher elasticity of PVC clear base than other solvated PVC models that make PVC clear base more susceptible to flow instabilities at varying speeds.

The lower pigment concentration produced the highest coating thickness. The effect of sliding speed was more pronounced for PVC clear base; coating thickness decreased with increased sliding speed for PVC clear base while the negligible effect of speed was seen for other concentration.

Fig. 10 - 3 and Fig. 10 - 4 compares coating thickness with pigment concentration at different sliding speeds, with ribbing and with no ribs, respectively.

The coating thickness with ribs showed higher thickness at low sliding speeds, more so for low pigment concentration and this is likely due to the strong shear-thinning nature of the model fluids – high viscosity at low sliding speeds and low viscosity at high sliding speeds. However, as sliding speeds increased, coating thickness decreased. Coating thickness was seen to be dependent on pigment concentration at low sliding speed but became independent of sliding speed at elevated speeds. The high coating thickness for low pigment concentration was credited to the ease of movement of the rib across the roll surface, thus the laser constantly picked up the rib thickness. Contrary to high pigment concentration, the ease of movement of the rib across the surface was limited and hence was not constantly picked up by the laser.

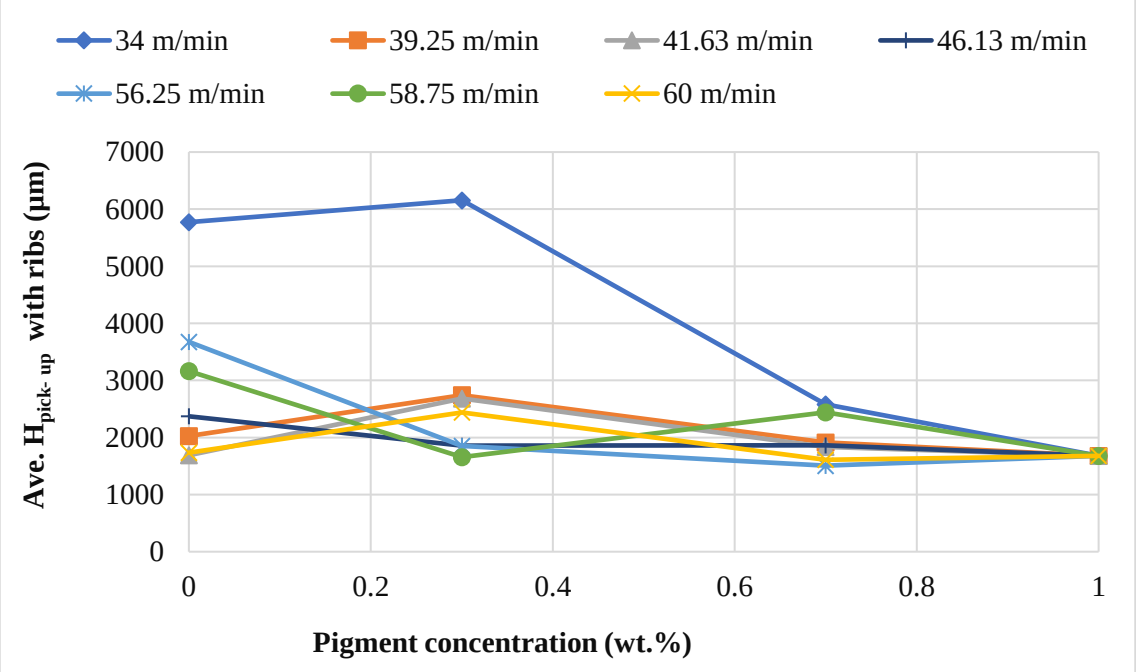

Fig. 10 - 3: Coating thickness (without ribbing contribution) against geometry speeds note: PVC clear base 0 wt. % pigment concentration)

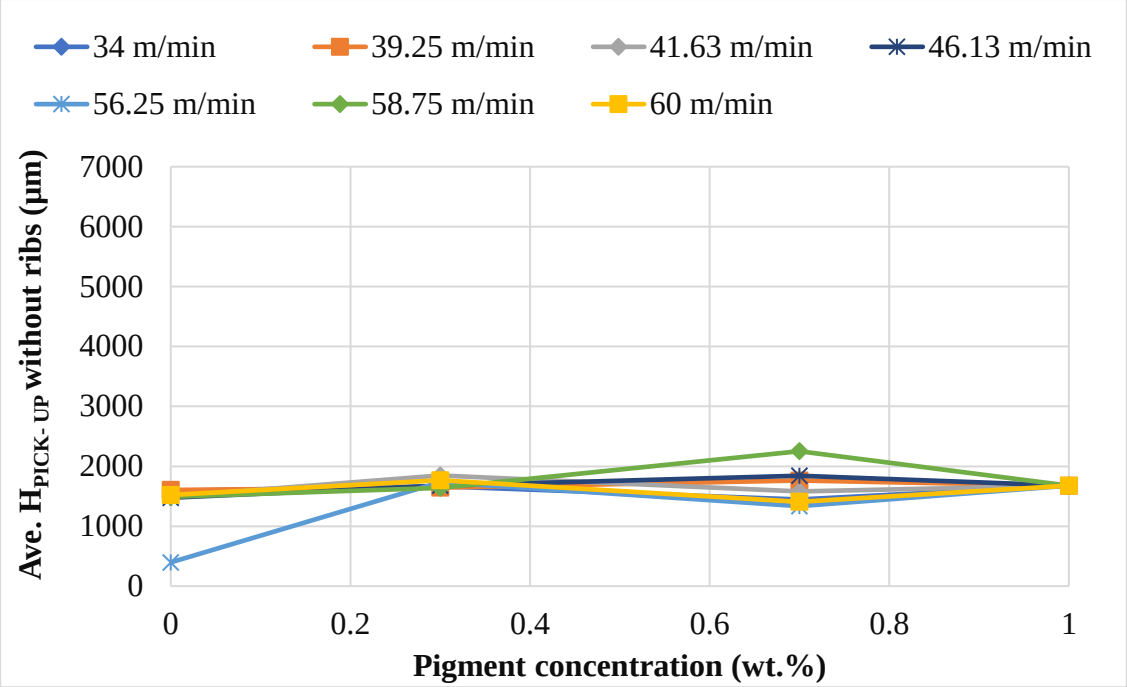

Fig. 10 - 4: Coating thickness (with ribbing contribution) against geometry speeds note: PVC clear base 0 wt. % pigment concentration)

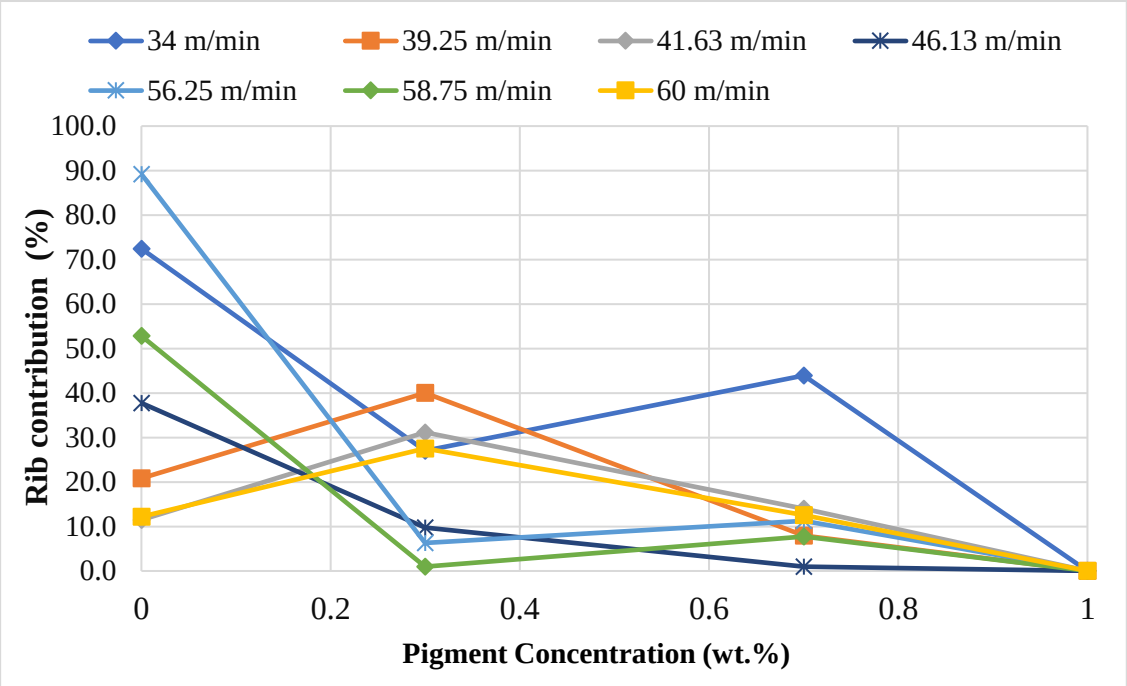

Fig. 10 - 5: Rib contribution to coating thickness against pigment concentration (note: PVC clear base 0 wt. % pigment concentration)

Except for PVC clear base at 56.25 m/min and 0.7 wt. % pigment concentration at 58.75 m/min, the coating thickness without ribs showed negligible variation as a function of sliding speeds. A linear relation between coating thickness and pigment concentration was observed.

Percentage contribution of ribs to the total coating thickness picked up from trough is represented in fig. 10 - 5. The highest rib contribution was observed for low pigment concentration, in particular PVC clear base. There was no correlation drawn between rib contribution and sliding speeds.

10.3.3 EFFECT OF SOLVENT CONCENTRATION ON COATING THICKNESS

In light of the investigation of coating constituents such as pigment concentration on the quality and quantity coating pick up from the trough in section 10.3.2 has inspired the need to further understand the impact of solvent concentration on coating pick up from the trough. It was seen in fig. 10 - 6 that PVC clear base with no solvent addition experienced high ribbing phenomena on the picking up roll in comparison to 57.7 wt.% solvent concentration.

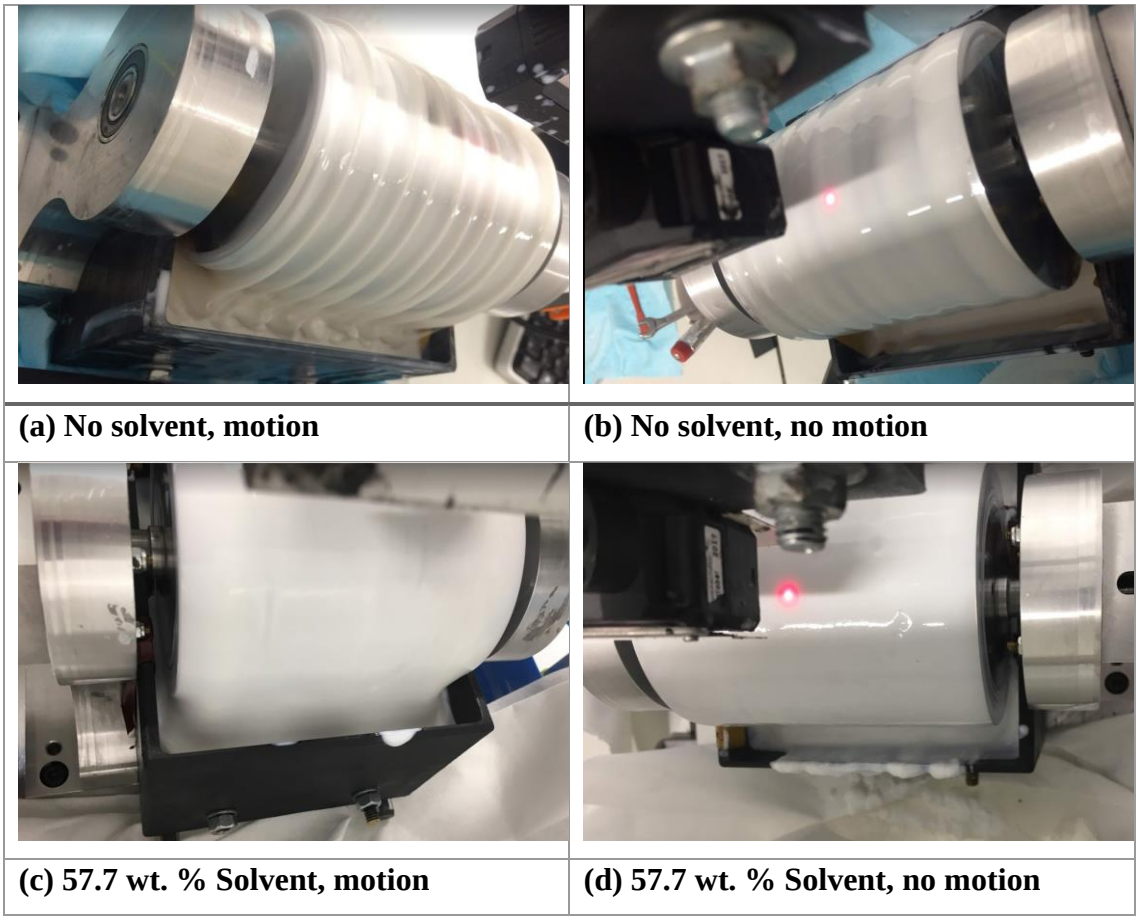

(a) No solvent, motion	(b) No solvent, no motion
(c) 57.7 wt. % Solvent, motion	**(d) 57.7 wt. % Solvent, no motion**

Fig. 10 - 6: Photographs of PVC coating thickness on the pickup roll surface; during roll rotation with ribbing phenomena (a) and typical coating thickness without ribs when there isn't roll rotation (b); PVC clear base at the top and 57.7 wt. % solvent at the bottom.

Furthermore, turbulence effects at the liquid-air interface were observed for PVC clear base during roll rotation and it was believed that these instabilities were carried onto the roll surface thus the development of ribs on the roll surface. Upon cessation of roll rotation, PVC clear base did not fully level out from the appearing ribs despite longer period the layer coating was left to settle.

57.7 wt. % solvated PVC coating showed a uniform coating thickness during roll rotation and after roll rotation. The air and liquid interface showed a smoother curtain. This implied that simpler liquids (Newtonian – like behaviour fluids and low elasticity) experience fewer instabilities in comparison to complex liquids.

Fig. 10 - 7 shows the effect of solvent concentration on coating thickness with ribs (blue) and without ribs (orange), picked up by the pickup roll when sliding speed is varied.

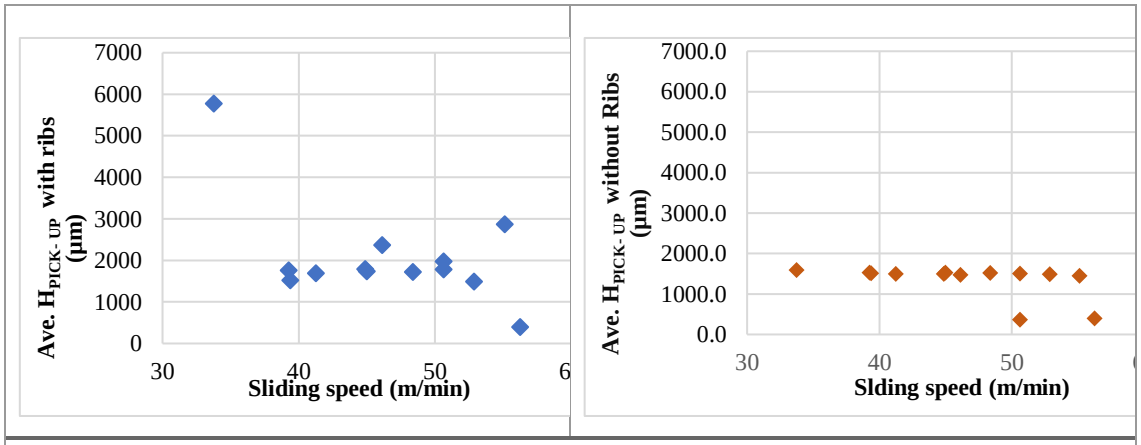

(a) 0 wt. % PVC Clear base

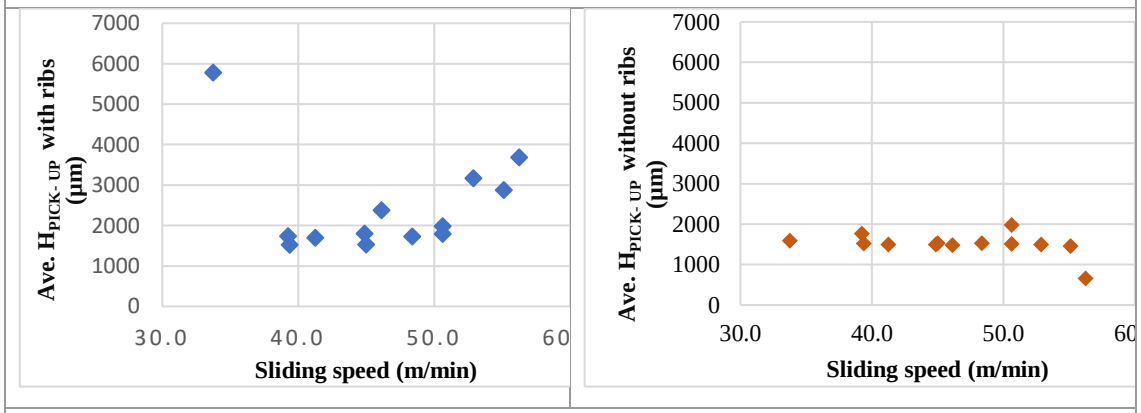

(b) 4 wt.% solvent t

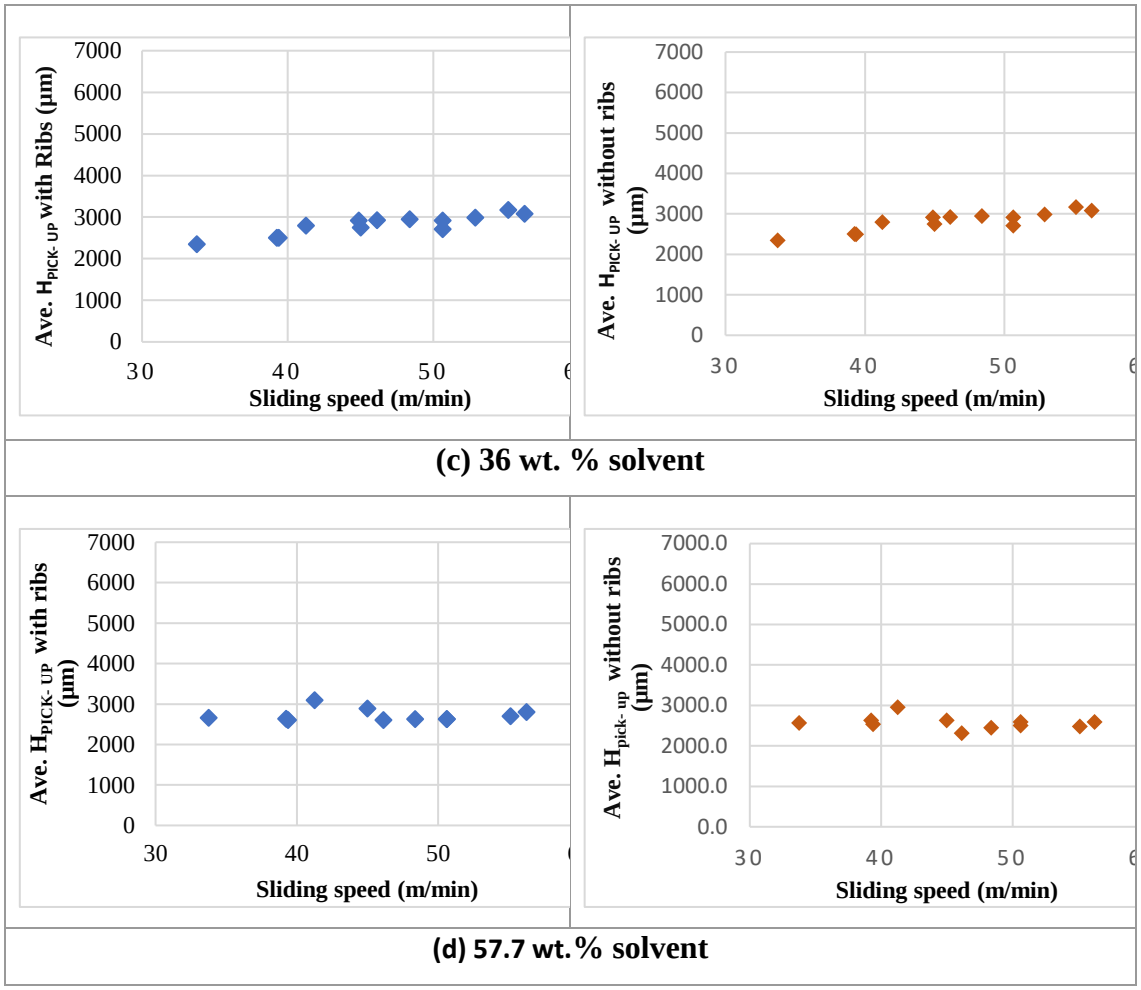

Fig. 10 - 7: Coating thickness with ribs (blue) and without ribs (orange) against geometry speeds for PVC clear base (Top row), 4 wt. % solvent (second Top row), 36 wt. % Pigment (second Bottom row) and 57.7 wt. % Pigment (Bottom row).

Low solvent concentration (such as 0 and 4 wt. %) exhibited data scatter whilst high solvent concentrations (such as 36 and 57.7 wt. %) exhibited a more stable/ uniform response, and this was attributed to the ribbing phenomena that shifted along the roll length and thus detected by the laser gauge sensor. Interestingly, as ribbing contribution was excluded from the data, the thickness of the coating layer being picked up increased with increased solvent concentration, and the vice versa was true for low solvent concentration.

Fig. 10 – 8 summaries the effect of solvent concentration on coating layer thickness with ribbing. Unlike coating thickness at a sliding speed of 34 and 56. 25 m/min, the average coating thickness picked up from the trough increased with solvent concentration. In the absence of ribs, fig.10 – 9, coating thickness increased with increased solvent concentration at all sliding speeds.

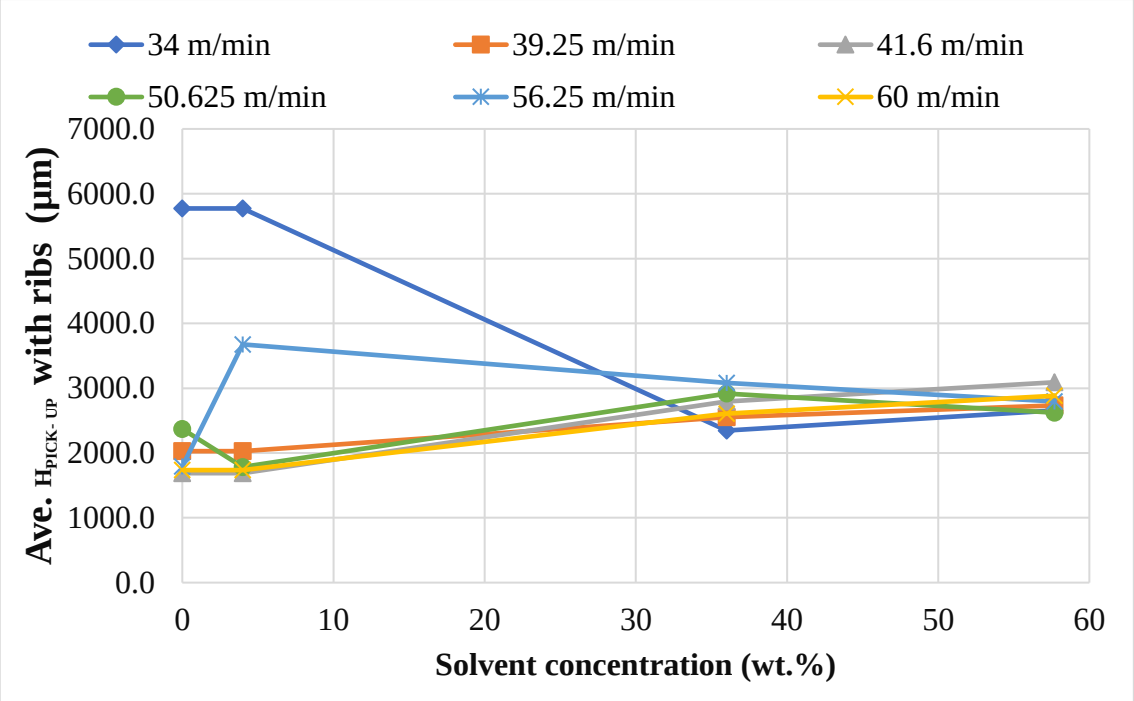

Fig. 10 - 8: Solvent concentration thickness (with ribbing contribution) against sliding speeds.

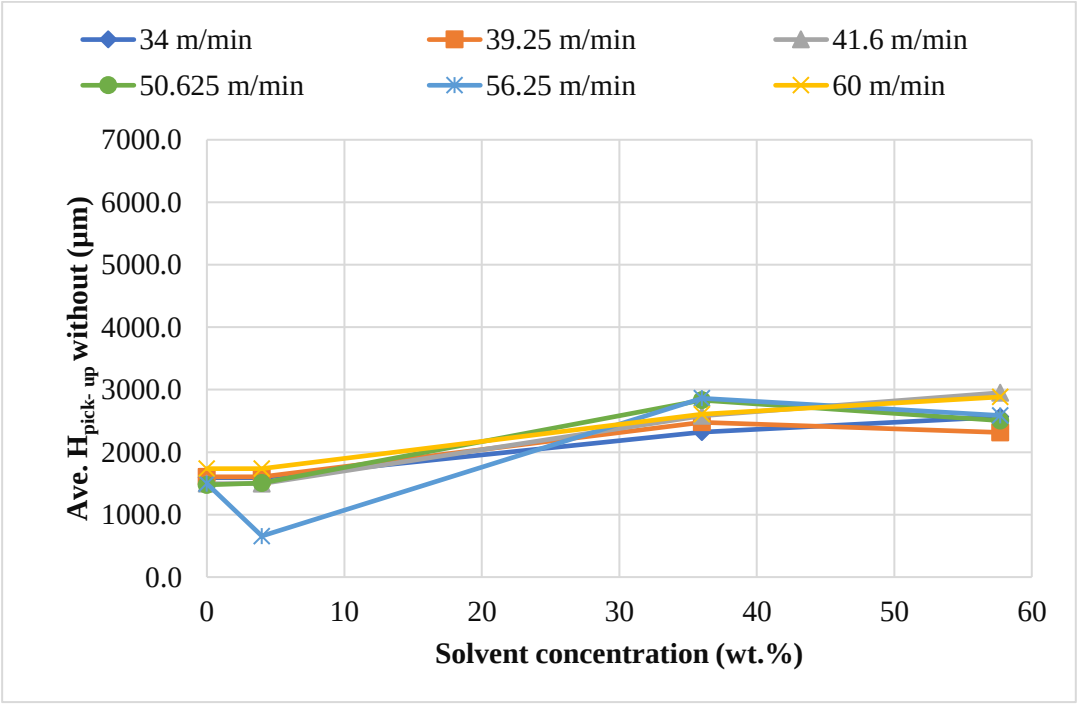

Fig. 10 - 9: Solvated PVC coatings thickness (without ribbing contribution) against sliding speeds

Fig. 10 – 10 shows the effect of solvent concentration on ribbing phenomena during the pick-up process of materials from the coating trough. It was seen that at low solvent concentration, ribbing phenomena prevailed at less sliding speeds. However, ribbing drastically reduced as sliding speeds decreased.

It was possible that most of coating picked was accumulated within the ribs for low solvent concentrations; therefore, excluding the ribs from the data during data analysis would the final thickness calculated for low solvent PVC coatings. While negligible ribs are seen for high solvent concentration, all the coating thickness on the roll is accounted for during coating thickness calculation. This was more to do with experimental artefact than material properties. Sliding speeds showed negligible effect on coating thickness picked up. It was therefore deduced that material properties dictate over operating parameters in determining coating layer thickness.

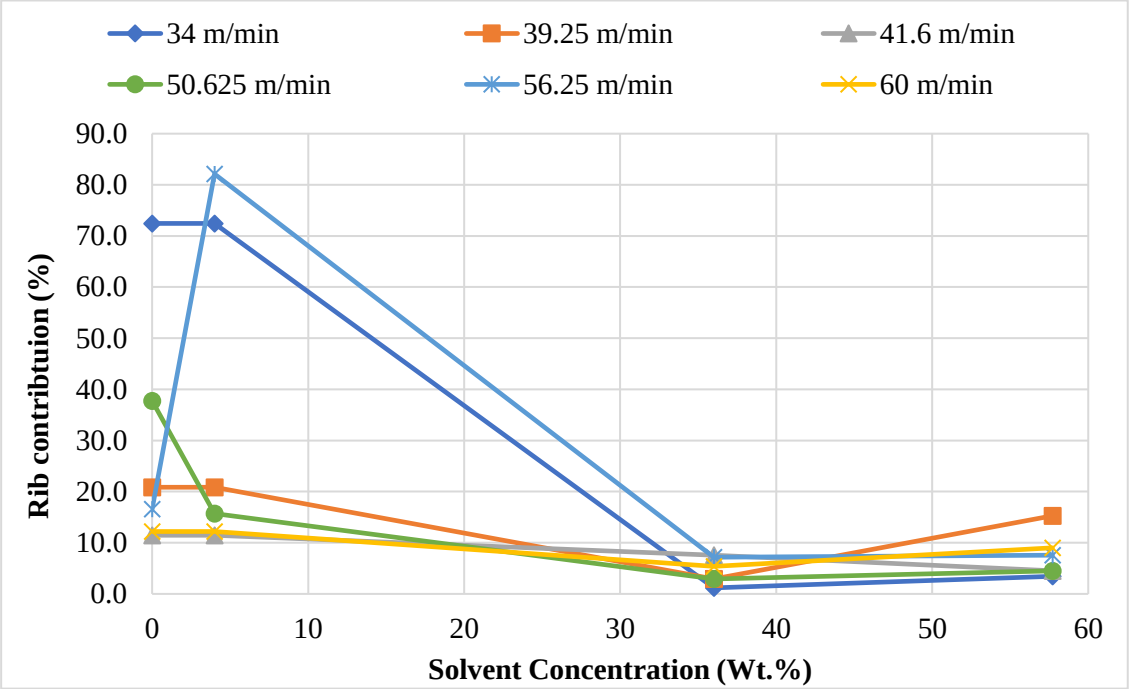

Fig. 10 - 10: Rib contribution to coating thickness against solvent concentration.

The prevalence of ribbing at low solvent concentration was attributed to the contribution of elasticity, high extensional rheology of PVC coatings and zero shear viscosity. At low sliding speeds, shear and strain rates were believed to be unable to cause rearrangement and restructuring of the polymer chains thus resistance to the flowing motion, viscosity, which then contributes to ribbing contribution. Yang *et al* [35] studied the influence of polymer additives on operating windows of slot die, and they found that polymer additives will have ribbing instability at a lower coating speed. The technique used is different, but the concept is the same as that employed in this work. Their results are in line with the results in fig. 10 – 10 where low solvent concentration (high polymer concentration) showed a higher percentage of ribbing contribution.

At high sliding speeds, all solvent concentration exhibits the same ribbing contribution and seen to be lower, and this was ascribed to high enough strain rates that consequently reduce both shear and extensional properties to the acceptable degree.

10.4. CONCLUSIONS

The effect of Pigment and solvent concentration on the pick-up process of PVC coatings from the trough has been thoroughly investigated in chapter ten.

Unlike commercial coatings, ribbing contribution to the total flow for the solvated PVC was highest at low speeds and high polymer concentration (low solvent concentration) possibly due to higher viscous force and viscoelasticity at low sliding speeds.

In the presence of ribbing, pigment concentration influenced the quantity of coating picks up from the trough; higher pigment concentrations exhibited a thicker coating layer on the pick-up roll. However; the exclusion of the ribs from the data suggested the negligible effect of pigment concentration on the coating layer thickness. This was credited to the fact that a larger percentage of the coating is contained within the ribs, therefore the exclusion of ribs reduces the accuracy of the data collected of coating thickness. The same observation was made with a variation of solvent concentration on PVC coating behaviour where ribbing contribution was higher for low solvent materials.

Though the concept of the Weissenberg effect (climbing rod effect) manifested by high amplitudes of ribs on the pick-up roll and accompanied by the low frequency of the ribs is out of the scope of this project, the manifestation of this phenomena was an interesting phenomenon to observe. Its direct correlation to high pigment concentration and thus viscoelasticity presents an opportunity to further study its effect in the pick-up process of the roll coating process.

It was noticed that when ribs were excluded, sliding speeds of the pick-up roll had negligible influence on the coating picked. This was expected as a great data is excluded when the ribs are excluded from the data collected. None the less, material properties were believed to influence coating to pick up from the trough than roll speeds.

CHAPTER ELEVEN

DISCUSSIONS

As a result of the research work carried out in this thesis, there are several technical and scientific points of discussion. These cover the practical implications of the work and the fundamental aspects of the flow of non-Newtonian particulate laden polymeric fluids. This chapter summarizes, below, these findings and identifies further work which is worthy of investigation.

1. QC Methods
2. PMD mechanism
3. Limitation of the Mooney analysis with real paint systems
4. Ribbing phenomena
5. The roll rig as a model
6. Recommendations and future work

11.1. QC METHODS

The causes of change in rheology cannot be readily attributed to any ingredient in the paint or the method by which it has been manufactured, thus rheology provides an efficient method characterization. Both the QC methods at the supplier (as goods despatched) and the customer (as goods in) are inadequate for identifying paints which will cause problems in production. The single viscosity measurement can result in a false positive pass for paints with significantly different shear thinning, thixotropic, viscoelastic and extensional properties. Cleary any recommendations on the QC methods which should be adopted need to take into account the time taken for each test, the human resources level required to complete the test, the capital cost of the equipment and balance these needs against the confidence with which coating batches are refused/ accepted accurately.

The minimum requirement for QC is a viscosity profile across a wide shear rate range which would not have identified the differences in behaviour of Plasticeram black samples. However, a rheometer which allows some investigation of thixotropy would have identified differences between the paints. This could be further validated using a controlled stress rheometer where the elastic modulus gives a further means of material

differentiation. While costs of such devices have dropped significantly over the last 20 years, capital costs would likely be in excess of £10K with testing being of the order of 30 minutes per sample. Further validation could be obtained through measurement of slip behaviour, but this would likely require 2 – 3 hours per sample and its interpretation would require significant post processing (which could be automated) and whose interpretation is also reliant on theories which should not readily be applied to the coating materials. Measurement of extensional viscosity remains a research laboratory methodology and is impractical in an industrial environment.

The exact values required, and tolerances required may depend on the organic coating being measured and the creation of reliable test which covers all pigments and coating polymers is no trivial task. In the first instance, incoming coatings could be run against a sample of a given paint which has successfully operated at the maximum production speed and judgements made according to the deviation from this accepted behaviour. Using multiple samples, a learning system could be used which where the relevant coating samples were characterized and learn deviations from an ideal which could be accepted without risk of failure.

11.2. PMD MECHANISM

Several mechanisms have been postulated which explains the PMD. From the measurements and analysis carried out during the investigation, it has been concluded that the pickup process is the primary cause of this, either by a slip or extension mechanism at the point of pickup. There is direct experimental evidence for both mechanisms and it is difficult to identify which mechanism dominates. The lack of a definitive answer can be attributed to the difficulty in formulating a material where these characteristics can be independently controlled.

This work has focussed on PMD, but other defects may arise due to rheological properties of the coating that may not be compatible with operating parameters. For example, a case study of streaks was briefly studied; a sample of a batch of coating susceptible to streaks and the one that was versatile in industrial setting was studied. Note: the coatings were metallic coatings. The two batches named Standard and Better coatings exhibited the same shear flow properties (see Table 11 – 1); however, extensional viscosity (Fig. 11 – 1) varied greatly. The difference in extensional viscosity was ~ 23%. It was believed that

higher extensional viscosity is compatible in high line speeds and therefore higher quantities of coatings can be picked despite of fast-moving process.

Table 11 - 1: summary physical properties and shear flow properties of Metallic coatings

Metallic coatings	σ (mN/m)	ρ (Kg/m3)	Steady state shear viscosity, μ_s, (Pas)	Complex viscosity, μ*, (Pas)
Standard coating	19.93	1042	0.48	0.50
Better coating	18.3	1000.4	0.50	0.50

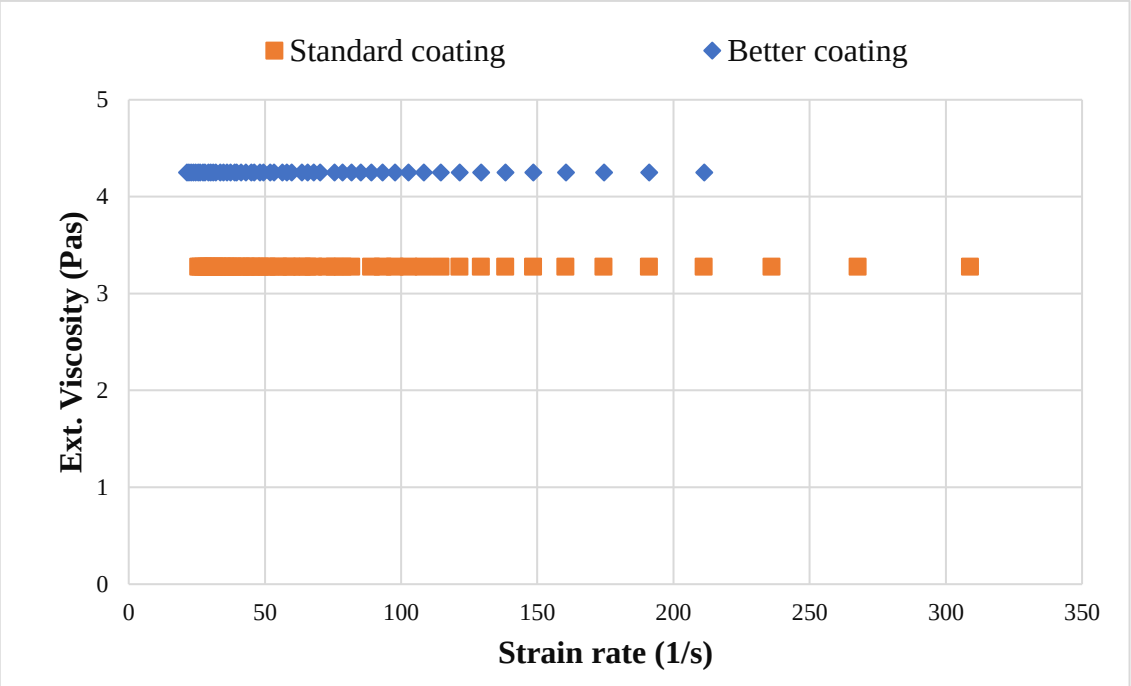

Fig. 11 - 1: Extensional viscosity against strain rate

11.3. LIMITATION OF THE MOONEY ANALYSIS WITH REAL PAINT SYSTEMS

The Mooney analysis has been established based on relatively simple fluids using dilute polymeric solutions. This work has clearly illustrated that this correlation breaks down rapidly if the polymer fraction is increased or any particulates are included in the material. The applicability of the model cannot therefore be considered for these fluids. The research work conducted on commercial coatings employing the Mooney analysis showed a physical response accurately described the occurrence to apparent wall slip; however, the number of slip characteristics such as relative slip contribution and

anomalous layer thickness were significantly higher than what was expected and therefore nonsensical. The Mooney analysis to apply to commercial coatings employed in the roll coating process may require a "fudge" factor to put into consideration of paint elasticity; effect of surface tension of the coatings and surface energy of the pick-up roll, amongst other parameters.

Other potential methods of determining slip effects such as Nuclear Magnetic Resonance (NMR) could provide a more accurate means of determining slip behaviour and ultimately determine anomalous layer thickness on the pick – up roll. A class example of using NMR was published by Gibbs *et al* [128] in their study titled "Rheometry and detection of apparent wall slip for Poiseuille flow of polymer solutions and particulate dispersions be nuclear magnetic resonance velocimetry" to identify velocity of within the capillary.

11.4. RIBBING PHENOMENA

The ribbing phenomena experienced in the experimental trials on the roll coating rig is fundamentally interesting from a fluid mechanics and rheological perspective. On a laboratory scale, it had a significant impact on the pickup phenomena and its measurement. There is a clear correlation between material rheology and the degree of ribbing with more pigmented systems, and higher solvent fractions experiencing less ribbing. It is postulated that the mechanisms behind these relationships are different. The effect of increasing pigment fractions is to increase the number of nucleation points which reduce the extensional viscosity during the extension flow. High pigment fraction in PVC coatings was observed to reduce the rate of filament radius change and subsequent delay in the film break uptime.

On the full-scale line, some ribbing is evident, but this has the tendency to disappear before the contact nips (metering nip gap) and is not observed as film thickness variations on the final coated product. Therefore, ribbing appearance observed in the laboratory environment is significantly more visible than that experienced on an industrial coating line.

Further investigation of the ribbing phenomena using the current laboratory equipment could be carried out using an increased number of laser displacement gauges but would more reliably be examined through high-speed video image. Individual images could be taken from the video stream and analysed using automatic image processing, e.g. in a MATLAB environment. This could more accurately determine appropriate metrics to examine the relationship between ribbing phenomena and material properties/ operational parameters. Such a study will have an impact in other areas as well as steel roll coating.

CHAPTER TWELVE

CONCLUSIONS AND RECOMMENDATIONS

12.1THESIS CONCLUSIONS

The thesis has investigated the impact of the interaction between the material properties and the operation for a coil roll coating of steel substrates. As a direct result of the work, the following can be concluded:

(1). Physical characterisation methods such rheological techniques can more clearly identify deviations from ideal behaviour than chemical analysis and wetting techniques. Thus, physical characterisation methods provide evidence for the principle mechanisms of process failure.

(2). The current QC system of rheological testing of organic coatings at Tata steel colors is not fit for purpose. It allows materials which will exhibit paint misses to pass into production. A more suitable QC system for PVC coatings has been discussed and its limitations with regards to capital investments and skilled workforce have been highlighted. When done correctly, rheological testing provides a reliable method to identify the materials which may be prone to paint misses.

(3) The two mechanisms of PMD have also been addressed and the difficulty involved in controlled one mechanism over the other is impractical, namely; film break-up from the coating trough and AWS phenomena. The mechanism of PMD is dominated by the extension and film break-up of the coating as the roll leaves the coating trough. Those materials which exhibit a low extensional viscosity are more prone to PMD. Extensional rheometry provides an ideal method for characterizing coating materials and their tendency to exhibit PMD. However, this is difficult in practice as commercial systems are not widely available. Additionally, skilled staff members with rheological knowledge will have to be employed to analyse data which adds to the cost of operating costs.

(4). Mooney analysis does not completely represent coating flow through the roll coating process and therefore further improvements to the model could be

necessary to use it as a tool of representing material behaviour in the coating trough and nip gaps.

(5). AWS investigation showed discrepancies in the quantifiable results of relative slip contribution and anomalous layer thicknesses. These discrepancies showed limitations of the Mooney analysis method during the flow of highly pigmented materials and viscoelastic coatings in small constrictions. However, the model showed the great potential of applying to liquid coatings provided additional terms that account for elasticity, surface tension, packing density and pressure effects are included.

(6) Additionally, the potential of employing rheology to predict the on-set of paint streaks has been addressed. The initial work that was conducted on metallic coatings shows the potential of expanding the rheological study of streaks which will also enable the development of an inward QC system of materials that are prone to streak manifestation.

12.2 RECOMMENDATIONS FOR FURTHER WORK

Great knowledge of the rheological impact of material behaviour on the coil roll coating process has been obtained in this research. However, interesting further research activities are expected to come from this research utilising the knowledge obtained. The activities with the potential to push this project further include: -

(1) The QC system employed in Tata steel color at Shotton should be redefined using controlled stress rheometer. The economic case for this should be developed in terms of the loss of production due to incorrect diagnosis causes.

(2) The relationship between AWS slip behaviour of other pigmented PVC systems such $Ti0_2$ pigmented systems should be investigated, as the interaction between the rigid pigment and the elastic liquid is likely to be the key role in the slip phenomena

(3) A refined model of the Mooney analysis should be adopted for elastic liquids and this should also be refined for pigmented systems. This will need to include a term for surface tension, surface energy, pressure effects, elastic modulus, temperature effects, amongst others

(4) Numerical models of the pick - up roll should be developed to investigate the role of parametric material properties (which cannot be carried out experimentally) on the pick-up due to ribbing phenomena, using a different software other than Ansys fluent.

(5) Similar studies should be carried out on polyurethane, Polyvinylidene difluoride (PVDF) and polyester coatings which are currently used at Tata steel colors in Shotton. Although initial measurements and literature indicate that they are rheologically simpler liquids, there would be a benefit in understanding the interaction between the material and process.

(6) A methodology for accurate measurement of coating film thickness which is picked up by the roll should be investigated. High-speed image capture and processing would provide the necessary information.

(7) Preliminary work on utilising rheology to investigate paint streaks was conducted in briefly mentioned in the discussion chapter. There is potential to push this activity further because metallic coatings pose a challenge under industrial setting due to aluminium flake orientation during coating deposition on the substrate.

BIBLIOGRAPHY

[1] P. Additives, “Structural Aspects of Decreasing the Corrosion Resistance of Zinc Coating Obtained in Baths with Al ,” 2020.

[2] D. J. Penney, J. H. Sullivan, and D. A. Worsley, “Investigation into the effects of metallic coating thickness on the corrosion properties of Zn-Al alloy galvanising coatings,” *Corros. Sci.*, vol. 49, no. 3, pp. 1321–1339, 2007.

[3] W. Gao, “Corrosion behaviour of Zincalume ® and galvanised coatings in a sulphur-containing atmosphere,” no. December, 2015.

[4] EU, “Commision delegated directive (EU) 2015/863 of 31 March 2015 amending Annex II to Directive 2011/65/EU of the European Parliament and of the Council as regards the list of restricted substances,” 2015.

[5] Ria Louise Woffinden, “Development and characterisation of powder slurry for domestic appliance coil coating,” University of Swansea, 2010.

[6] T. Dirking, N. Willenbacher, and Lori Bloggs, “Elongational flow behaviour of automotive coating and its relation to atomization and mottling,” *Prog. Org. Coatingsorganic Coat.*, vol. 42, pp. 59–64, 2001.

[7] J. Eckermann, “Optimising High Speed Coating Processes,” University of Swanesa, 2012.

[8] Direttiva 2004/42/CE del Parlamento Europeo e del Consiglio del 21 aprile 2004, “Direttiva 2004/42/CE del Parlamento Europeo e del Consiglio del 21 aprile 2004 relativa alla limitazione delle emissioni di composti organici volatili dovute all’uso di solventi organici in talune pitture e vernici e in taluni prodotti per carrozzeria e r,” no. 10, 2004.

[9] BASF, “Coil Coatings.” BASF coatings AG, Shotton.

[10] ARCELOR FCS COMMERCIAL, “Organic coated steel Organic coated steel.”

[11] Arcelormittal Europe and Products, “Organic coated steel User manual.”

[12] H. Benkreira and O. Cohu, “Direct forward gravure coating on unsupported web,” *Chem. Eng. Sci.*, vol. 53, no. 6, pp. 1223–1231, 1998.

[13] J. Ashmore, a. Q. Shen, H. P. Kavehpour, H. a. Stone, and G. H. McKinley, "Coating flows of non-Newtonian fluids: Weakly and strongly elastic limits," *J. Eng. Math.*, vol. 60, no. 1, pp. 17–41, 2008.

[14] G. A. Æ. P. J. C. Æ. P. A. Tanguy, "High-speed roll coating with complex rheology fluids," no. January 2006, 2015.

[15] B. Willinger and A. Delgado, "Analytical prediction of roll coating with counter-rotating deformable rolls," *J. Coatings Technol. Res.*, vol. 11, no. 1, pp. 31–37, 2014.

[16] I. J. Lee, S. Park, S. M. Noh, H. W. Jung, and J. M. Park, "Rheology and roll coating dynamics of metallic basecoats for automotive pre-coated metal sheet," *Prog. Org. Coatings*, vol. 76, no. 5, pp. 917–923, 2013.

[17] G. a. Zevallos, M. S. Carvalho, and M. Pasquali, "Forward roll coating flows of viscoelastic liquids," *J. Nonnewton. Fluid Mech.*, vol. 130, pp. 96–109, 2005.

[18] Y. H. Chong, P. H. Gaskell, and N. Kapur, "Coating with deformable rolls: An experimental investigation of the ribbing instability," *Chem. Eng. Sci.*, vol. 62, pp. 4138–4145, 2007.

[19] D. J. Coyle, C. W. Macosko, and L. E. Scriven, "A Simple Model of Reverse Roll Coating," pp. 1416–1419, 1990.

[20] M savage, "Meniscus Roll coating: Steady Flows and Instabilities," in *Free boundary problems: theory and applications*, Florida: Chapman & Hall/ CRC, 1999.

[21] S. J. Abbott, N. Kapur, P. A. Sleigh, J. L. Summers, and H. M. Thompson, "A review of the fluid mechanics of rigid roll coating systems," *Convert. e-Print*, vol. 1, no. 2(March/April), pp. 47–51, 2011.

[22] P. H. Gaskell, G. E. Innes, and M. D. Savage, "An experimental investigation of meniscus roll coating," 1998.

[23] S. J. Abbot, N. Kapur, P. A. Sleigh, J. L. Summers, and H. M. Thompson, "A review of the fluid mechanics of Rigid Roll coating systems," *Fundam. Coat. Res.*, vol. 2, no. 1, pp. 47–51, 2011.

[24] P. H. Gaskell, M. D. Savage, J. L. Summers, and H. M. Thompson, “Modelling and analysis of meniscus roll coating,” *J. Fluid Mech.*, vol. 298, p. 113, 1995.

[25] “The Fluid Dynamics of Reverse Roll Coating,” vol. 36, no. 2, pp. 161–176, 1990.

[26] J. Greener and S. Middleman, “Reverse roll coating of viscous and viscoelastic liquids,” *Ind. Eng. Chem. Fundam.*, vol. 20, no. 1, pp. 63–66, 1981.

[27] M. S. Carvalho and L. E. Scriven, “Deformable roll coating flows: steady state and linear perturbation analysis,” *J. Fluid Mech.*, vol. 339, pp. 143–172, 1997.

[28] O. Cohu and A. Magnin, “Forward roll coating of Newtonian fluids with deformable rolls: An experimental investigation,” *Chem. Eng. Sci.*, vol. 52, no. 8, pp. 1339–1347, 1997.

[29] M. A. Johnson, “Viscoelastic Roll Coating Flows,” *Chem. Eng.*, p. 131, 2003.

[30] M. D. S. Carvalho and L. E. Scriven, “Flows in forward deformable roll coating gaps : Comparison between spring and plane-strain models of roll cover,” *J. Comput. Phys.*, vol. 138, no. 2, pp. 449–479, 1997.

[31] D J Coyle, “Forward roll coating with deformable rolls: A simple one-dimensional elastohydrodynamiuc model,” *Chem. Eng. Sci.*, vol. 43, no. 10, pp. 2673–2684, 1988.

[32] M. J. Gostling, “Stability of rigid and deformable roll coating flows,” no. September, 2001.

[33] M. S. Carvalho, “Viscoelatsic Effects of Deformable Roll cover.”

[34] M. J. Gostling, M. D. Savage, A. E. Young, and P. H. Gaskell, “A model for deformable roll coating with negative gaps and incompressible compliant layers,” *J. Fluid Mech. starvation/Wall slip.pdf*, vol. 489, pp. 155–184, 2003.

[35] C. K. Yang, D. S. H. Wong, and T. J. Liu, “The effects of polymer additives on the operating windows of slot coating,” *Polym. Eng. Sci.*, vol. 44, no. 10, pp. 1970–1976, 2004.

[36] J. H. Lee, S. K. Han, J. S. Lee, H. W. Jung, and J. C. Hyun, “Ribbing instability

in rigid and deformable forward roll coating flows," *Korea Aust. Rheol. J.*, vol. 22, no. 1, pp. 75–80, 2010.

[37] F. V. Lopez, L. Pauchard, M. Rosen, and M. Rabaud, "Threshold of ribbing instability with Non-Newtonian fluids," no. Ap 45, pp. 1–6, 1999.

[38] Y. Shibata, "HIGH SPEED VERY THIN FILMS WITH REVERSE ROLL COATING SUBTITLE : An experimental investigation of reverse roll coating of fluids using rigid and deformable rolls at high speeds Yusuke SHIBATA (BEng , MEng) Submitted as a PhD thesis for the School of Engi," 2012.

[39] Dennis J. Coyle, *Liquid Film Coating*, First. Dordrecht: Springer Netherlands, 1997.

[40] M. S. Owens, M. Vinjamur, L. E. Scriven, and C. W. Macosko, "Misting of Newtonian liquids in forward roll coating," *J. Nonnewton. Fluid Mech.*, vol. 166, no. 19–20, pp. 1123–1128, 2011.

[41] S. Sarma, P. H. Benkreira, E. Van Vliet^{o}, M. Klaassen^{o}, and S. Bohm, "The misting phenomena in Roll Coating : Experiments and CFD simulations Presented at the 16 th International Coating Science and Technology Symposium , Unpublished . ISCST shall not be responsible for statements or opinions contained in papers or printed ," pp. 1–4, 2012.

[42] M. S. Owens, M. Vinjamur, L. E. Scriven, and C. W. Macosko, "Misting of Newtonian Liquids in forward roll coating," *Ind. Eng. Chem. Res.*, vol. 50, pp. 3212–3219, 2011.

[43] R. H. Fernando, L. L. Xing, and J. E. Glass, "Rheology parameters controlling spray atomization and roll misting behavior of waterborne coatings," *Prog. Org. Coatings*, vol. 40, pp. 35–38, 2000.

[44] G. Ascanio, P. J. Carreau, E. Brito-de la Fuente, and P. a. Tanguy, "Forward deformable roll coating at high speed with newtonian fluids," *Trans. Inst. Chem. Eng. Part A, Chem. Eng. Res. Des.*, vol. 82, no. A3, pp. 390–397, 2004.

[45] Ferdinand R. Pranckh; Dennis J. Coyle, "ELASTOHYDRODYNAMIC COATING SYSTEMS," in *Liquid film coating*, FIRST., S.F Kistler; P.M

Scheizer, Ed. London: Chapman and Hall, 1997, p. 643.

[46] C. K. Schoff, “Surface defects: Diagnosis and cure,” *J. Coatings Technol.*, vol. 71, no. 888, pp. 56–73, 1999.

[47] J. Hajas and John Du, “Application of of surface addtives,” in *Handbook of coating additives*, Second., J. J. Florio and D. J. Miller, Eds. New York: Marcel Dekker, 2004, p. 329.

[48] Haroon S Kheshgi, “The fate of thin liquids films after coating,” in *Liquid film coating*, Stephan F Kistler and Peter M sheizer, Eds. Glasgow: Springer science+Business Media, 1997, p. 183.

[49] Yves-M. Tricot, “SURFACTANTS: STATIC AND DYNAMIC SURFACE TENSION,” in *Liquid Film coating*, 1st ed., S.F. Kristler; P. M Scheizer, Ed. London: Chapman and Hall, 1997, pp. 104–105.

[50] P. R. Letters, “Dewetting of thin polymer films,” no. January 1992, 2013.

[51] O. Al-khayat, “DEWETTING POLYMER BILAYERS BY SOLVENT VAPOUR ANNEALING : A PATHWAY TO MANUFACTURING BIOMIMETIC WATER HARVESTING SURFACE COATINGS Omar Al-Khayat School of Chemical and Biomolecular Engineering and School of Chemistry The University of Sydney,” THE UNIVERSITY OF SYDNEY, 2016.

[52] D. Peschka, S. Haefner, L. Marquant, K. Jacobs, and B. Wagner, “Signatures of slip in dewetting polymer films,” vol. 116, no. 19, 2019.

[53] S. Ankur, Verma; and Ashutosh, “Self-organized Nano-lens Arrays by Intensified Dewetting of Electron Beam Modified Polymer Thin-filmse,” vol. 7, no. 23, pp. 1–16, 2011.

[54] H. A. Barnes, *Handbook of elementry rheology.pdf*. Wales: The University of Wales Institute of Non-Newtonian Fluid, 2000.

[55] O. Cohu and A. Magnin, “Rheology and flow of paints in roll coating processes,” *Surf. coatings internantional*, vol. 3, pp. 102–107, 1997.

[56] S. Kazemian, A. Prasad, and B. B. K. Huat, “Review of newtonian and non-

Newtonian fluids behaviour in the context of grouts," *Geotech. Asp. Undergr. Constr. Soft Gr. - Proc. 7th Int. Symp. Geotech. Asp. Undergr. Constr. Soft Gr.*, pp. 321–326, 2012.

[57] F. Varela López and M. Rosen, "Rheological effects in roll coating of paints," *Lat. Am. Appl. Res.*, vol. 32, pp. 247–252, 2002.

[58] M. Hojjat, S. G. Etemad, R. Bagheri, and J. Thibault, "Rheological characteristics of non-Newtonian nanofluids: Experimental investigation," *Int. Commun. Heat Mass Transf.*, vol. 38, no. 2, pp. 144–148, 2011.

[59] R. K. Thakur, C. Vial, G. Djelveh, and M. Labbafi, "Mixing of complex fluids with flat-bladed impellers: Effect of impeller geometry and highly shear-thinning behavior," *Chem. Eng. Process. Process Intensif.*, vol. 43, no. 10, pp. 1211–1222, 2004.

[60] E. Armelin, M. Martí, E. Rudé, J. Labanda, J. Llorens, and C. Alemán, "A simple model to describe the thixotropic behavior of paints," *Prog. Org. Coatings*, vol. 57, pp. 229–235, 2006.

[61] K. Sadeghy and D. F. James, "Elasticity of associative polymer solutions and slip at high shear stress," *J. Nonnewton. Fluid Mech.*, vol. 90, no. 2–3, pp. 127–158, 2000.

[62] R. Durairaj, S. Mallik, A. Seman, and N. N. Ekere, "Investigation of wall-slip effect on lead-free solder paste and isotropic conductive adhesives," *Sadhana - Acad. Proc. Eng. Sci.*, vol. 34, no. 5, pp. 799–810, 2009.

[63] T. Sochi, "Slip at fluid-solid interface," *Polym. Rev.*, vol. 51, no. 4, pp. 309–340, 2011.

[64] G. A. Davies and J. R. Stokes, "Thin film and high shear rheology of multiphase complex fluids," *J. Nonnewton. Fluid Mech.*, vol. 148, no. 1–3, pp. 73–87, 2008.

[65] H. A. Barnes and Q. D. Nguyen, "Rotating vane rheometry — a review," *J. Nonnewton. Fluid Mech.*, vol. 98, no. 1, pp. 1–14, 2001.

[66] A. Barnes, "Thixotropy," vol. 0257, no. 97, pp. 4–9, 1997.

[67] B. Cross, C. Barraud, C. Picard, L. Léger, F. Restagno, and É. Charlaix, “Wall slip of complex fluids: Interfacial friction versus slip length,” *Phys. Rev. Fluids*, vol. 3, no. 6, 2018.

[68] A. Y. Malkin and S. A. Patlazhan, “Wall slip for complex liquids – Phenomenon and its causes,” *Adv. Colloid Interface Sci.*, vol. 257, pp. 42–57, 2018.

[69] S. G. Hatzikiriakos and J. M. Dealy, “Wall slip of molten high density polyethylenes. II. Capillary rheometer studies,” *J. Rheol. (N. Y. N. Y).*, vol. 36, no. 4, pp. 703–741, May 1992.

[70] D. M. Kalyon, “Apparent slip and viscoplasticity of concentrated suspensions,” *J. Rheol. (N. Y. N. Y).*, vol. 49, no. 3, pp. 621–640, 2005.

[71] A. G. Chryss, S. N. Bhattacharya, and L. Pullum, “Rheology of shear thickening suspensions and the effects of wall slip in torsional flow,” *Rheol. Acta*, vol. 45, no. 2, pp. 124–131, 2005.

[72] N. V. Priezjev, “Shear rate threshold for the boundary slip in dense polymer films,” *Phys. Rev. E - Stat. Nonlinear, Soft Matter Phys.*, vol. 80, no. 3, pp. 1–37, 2009.

[73] G. A. Davies and J. R. Stokes, “Thin film and high shear rheology of multiphase complex fluids,” *J. Nonnewton. Fluid Mech.*, vol. 148, no. 1–3, pp. 73–87, 2008.

[74] M. Rides, “NPL REPORT Rheological characterisation Of filled materials : a review,” 2005.

[75] M. Ansari, Y. W. Inn, A. M. Sukhadia, P. J. Deslauriers, and S. G. Hatzikirikos, “Wall slip of HDPEs Molecular weight and molecular weight distribution effects,” *J. Rheol. (N. Y. N. Y).*, vol. 57, no. 3, pp. 927–948, 2013.

[76] J.-F. Agassant *et al.*, “Polymer Processing Extrusion Instabilities and Methods for their Elimination or Minimisation,” 2006.

[77] P. J. Cullen, a P. Duffy, and D. J. O. Callaghan, “In situ rheological monitoring of viscous non-Newtonian fluids using a helical ribbon agitator,” 2005.

[78] M. da S. Carvalho and L. E. Scriven, “Flows in forward deformable roll coating

gaps : Comparison between spring and plane-strain models of roll cover," *J. Comput. Phys.*, vol. 138, no. 2, pp. 449–479, 1997.

[79] M. Tassieri *et al.*, "i-Rheo: Measuring the materials' linear viscoelastic properties 'in a step ' !," *J. Rheol. (N. Y. N. Y).*, vol. 60, no. 4, pp. 649–660, 2016.

[80] J. Nam, K. Hyun, K. Ahn, and S. Lee, "Phase angle of the first normal stress difference in oscillatory shear flow," *Korea-Australia Rheol. …*, vol. 22, no. 4, pp. 247–257, 2010.

[81] B. J. Dobraszczyk and M. P. Morgenstern, "Rheology and the breadmaking process," *J. Cereal Sci.*, vol. 38, no. 3, pp. 229–245, 2003.

[82] John M Dealy and J. Wang, *Melt Rheology and its Applications in the plastics Industry*, Second. New York: Springer science+Business Media, 2013.

[83] P. Van Puyvelde, A. Vananroye, A. S. Hanot, M. Dees, M. Mangnus, and N. Hermans, "On the pressure dependency of the bagley correction," *Int. Polym. Process.*, vol. 28, no. 5, pp. 558–564, 2013.

[84] J. E. Glass and Robert K Prud'homme, "Coating Rheology: Component influence on the rheological response and perfomance of water-borne coatings in roll applications," in *Liquid Film coating*, First., S. F. Kristler and P. M. Scheize, Eds. London: Chapman and Hall, 1997, pp. 139–140.

[85] J. M. R. M. Rousseau, "Coil roller coating," 2006.

[86] J. Jader, N. Willenbacher, G. Engstrom, and L. Jarnstrom, "The influence of Extensional properties on the Dewatering of Coating Colours," *J. Pulp Pap. Sci.*, vol. 31, no. 4, pp. 181–187, 2005.

[87] R. R. Eley, "Rgheology and Viscometry," in *Paint and coating testing manual*, Fourth., American Society For testing and Materials, 1995, p. 350.

[88] Stephen Cordy, "EXTENSIONAL FLOW OF COMPLEX FLUIDS," University of Wales, SwAnsea, 2004.

[89] M. Nyström, H. R. T. Jahromi, M. Stading, and M. F. Webster, "Numerical

simulations of Boger fluids through different contraction configurations for the development of a measuring system for extensional viscosity," *Rheol. Acta*, vol. 51, no. 8, pp. 713–727, 2012.

[90] E. Submitted, "Optimising High Speed Coating Processes," 2012.

[91] M. Chellamuthu, "A Comprehensive Study Of The Extensional Rheology Of Complex Fluids," 2010.

[92] T. A. Osswald, "Mechanical Behaviour of Polymers," *Underst. Polym. Process. Process. Gov. Equations*, p. 310, 2010.

[93] S. Rózańska, "Extensional viscosity of w/o emulsions," *Procedia Eng.*, vol. 42, no. August, pp. 742–752, 2012.

[94] D. F, James, Y. N, and R. J. A, "Fluid Elasticity in Extension, Measured by a New Technique, Correlates with Misting," in *Advanced Coating Fundamentals Symposium Proceedings*, 2003.

[95] R. Lima, T. Ishikawa, and I. Nano-biomechanics, "Learn more about Extensional Flow Microfluidic Devices Based on Biome- chanics," 2018.

[96] G. H. Mckinley, O. Brauner, and M. Yao, "Filament stretching rheometry and the extensional viscosity of dilute and concentrated polymer solution, Massachusetts Institute of Technology , Cambridge , MA 02139 Goodyear Technical Research Center , Akron , Ohio , USA," in *1st International Symposium on Applied Rheology*, 2001, no. 1990, pp. 65–75.

[97] S. L. Anna *et al.*, "An interlaboratory comparison of measurements from filament-stretching rheometers using common test fluids," *J. Rheol. (N. Y. N. Y).*, vol. 45, no. 1, pp. 83–114, 2001.

[98] S. J. Haward, V. Sharma, C. P. Butts, G. H. McKinley, and S. S. Rahatekar, "Shear and extensional rheology of cellulose/ionic liquid solutions," *Biomacromolecules*, vol. 13, no. 5, pp. 1688–1699, 2012.

[99] L. E. Rodd, T. P. Scott, J. J. Cooper-white, and G. H. Mckinley, "Capillary Break-up Rheometry of Low-Viscosity Elastic Fluids Abstract :," vol. 15, no. 1, pp. 12–27, 2005.

[100] T. D. Blake and Y. D. Shikhmurzaev, “Dynamic wetting by liquids of different viscosity.,” *J. Colloid Interface Sci.*, vol. 253, no. 1, pp. 196–202, 2002.

[101] T. For *et al.*, “TABLES FOR THE DETERMINATION OF THE SURFACE TENSIONS.” .

[102] D. E. Weidner, L. W. Schwartz, and R. R. Eley, “Role of surface tension gradients in correcting coating defects in corners,” *J. Colloid Interface Sci.*, vol. 179, no. 179, pp. 66–75, 1996.

[103] P. Doye, T. Mena, and N. Das, “Formulation and Bio-Availability Parameters of Pharmaceutical Suspension,” *Int. J. Curr. Pharm. Res.*, vol. 9, no. 3, p. 8, 2017.

[104] T. Blake and K. Ruschak, *Liquid Film Coating*. Glasgow: Glagow, 1997.

[105] Dr. Enrico Gnecco, “Surface Diffusion,” *Presentation*, no. 6, pp. 3099–3109, 2008.

[106] Artur Goldschmidt and Hans-Joachim Streitberger, *BASF Handbook on Basics of coating Technology*. Hannover: BASF coatings AG, 2003.

[107] Rudy Berndlmaier, “Rheology additives for solvent and solventless coating,” in *Handbook of coating additives*, Second., J. J. Florio and D. J. Miller, Eds. New York: Marcel Dekker, 2004, pp. 363–364.

[108] Joel Swartz, “Surfactants and surface tension,” in *Rheology additives for solvent and solventless coating*, Second., J. J. Florio and Daniel J Miller, Eds. New York: Marcel Dekker, 2014, p. 319.

[109] A. A. Balakit, A. Ahmed, G. A. El-Hiti, K. Smith, and E. Yousif, “Synthesis of new thiophene derivatives and their use as photostabilizers for rigid poly(vinyl chloride),” *Int. J. Polym. Sci.*, vol. 2015, 2015.

[110] A. Marcilla and M. Beltrán, “Kinetic models for the thermal decomposition of commercial PVC resins and plasticizers studied by thermogravimetric analysis,” *Polym. Degrad. Stab.*, vol. 53, no. 2, pp. 251–260, 1996.

[111] M. Altenhofen Da Silva, M. G. Adeodato Vieira, A. C. Gomes Maumoto, and M. M. Beppu, “Polyvinylchloride (PVC) and natural rubber films plasticized with a

natural polymeric plasticizer obtained through polyesterification of rice fatty acid," *Polym. Test.*, vol. 30, no. 5, pp. 478–484, 2011.

[112] C. Babeela, T. C. Sabari Girisun, and G. Vinitha, "Optical limiting behavior of β-BaB2O4 nanoparticles in pulsed and continuous wave regime," *J. Phys. D. Appl. Phys.*, vol. 48, no. 6, p. 65102, 2015.

[113] E. Yousif and A. Hasan, "Photostabilization of poly(vinyl chloride) – Still on the run," *J. Taibah Univ. Sci.*, vol. 9, no. 4, pp. 421–448, 2014.

[114] C. Paper, J. Komasatitaya, and K. Mongkut, "Comparison of Black-Pigment-Particle Dispersing and Particle Size Using Surfactants for Water Based Inkjet Ink Comparison of Dispersing and Particle Size of Black-," no. August, 2016.

[115] J. Yu, L. Sun, C. Ma, Y. Qiao, and H. Yao, "Thermal degradation of PVC: A review," *Waste Manag.*, vol. 48, pp. 300–314, 2016.

[116] A. Castro, D. Soares, C. Vilarinho, and F. Castro, "Kinetics of thermal de-chlorination of PVC under pyrolytic conditions," *Waste Manag.*, vol. 32, no. 5, pp. 847–851, 2012.

[117] W. H. Starnes, "Structural Defects in Poly(vinyl chloride) and the Mechanism of Vinyl Chloride Polymerization: Comments on Recent Studies," *Procedia Chem.*, 2012.

[118] J. R. a. Pearson and P. M. J. Tardy, "Models for flow of non-Newtonian and complex fluids through porous media," *J. Nonnewton. Fluid Mech.*, vol. 102, pp. 447–473, 2002.

[119] S. X. Huang and C. J. Lu, "Thixotropy-loop behaviors of an LDPE melt: Experiment and simple analysis," *J. Hydrodyn.*, 2006.

[120] V. Pěnkavová, J. Tihon, and O. Wein, "Bulk fluidity and apparent wall slip of aqueous kaolin suspensions studied using the cone-cone (KK) sensor: The effect of concentration and temperature," *Colloids Surfaces A Physicochem. Eng. Asp.*, 2016.

[121] W. E. Buy, U. Equipment, L. For, M. Information, and R. Inspection, "Bohlin Gemini & CVO Rheometer user manual."

[122] M. Rides, “NPL REPORT Rheological characterisation Of filled materials : a review,” no. February, pp. 1–39, 2005.

[123] Z. B. Sendekie and P. Bacchin, “Colloidal Jamming Dynamics in Microchannel Bottlenecks,” *Langmuir*, vol. 32, no. 6, pp. 1478–1488, 2016.

[124] S. Alonso, O. Réglat, F. Bertrand, L. Choplin, and P. A. Tanguy, “Process Viscosity in Reverse Roll Coating,” *Chem. Eng. Res. Des.*, vol. 79, no. 2, pp. 128–136, 2001.

[125] X. Fan, H. Xu, Q. Zhang, D. Xiao, Y. Song, and Q. Zheng, “Insight into the weak strain overshoot of carbon black filled natural rubber,” *Polymer (Guildf).*, vol. 167, no. March, pp. 109–117, 2019.

[126] M. Wilhelm *et al.*, “Accessed A Review of Nonlinear Oscillatory Shear Tests : Analysis and Application of Large Amplitude Oscillatory Shear (LAOS),” 2019.

[127] S. Alonso, F. Bertrand, and P. A. Tanguy, “A torque-based analysis of the reverse roll coating process,” *Chem. Eng. Sci.*, vol. 58, no. 9, pp. 1831–1837, 2003.

[128] S. J. K. L. H. L. D. H. Gibbs, “Rheometry and detection of apparent wall slip for Poiseuille flow of polymer solutions and particulate dispersions be nuclear magnetic resonance valecimetry,” *J. Rheol. (N. Y. N. Y).*, vol. 40, p. 425, 1998.

APPENDINCES

APPENDIX A: MATERIALS SAFETY DATA SHEETS (MSDS)

MSDS FOR PLASTICERAM BLACK

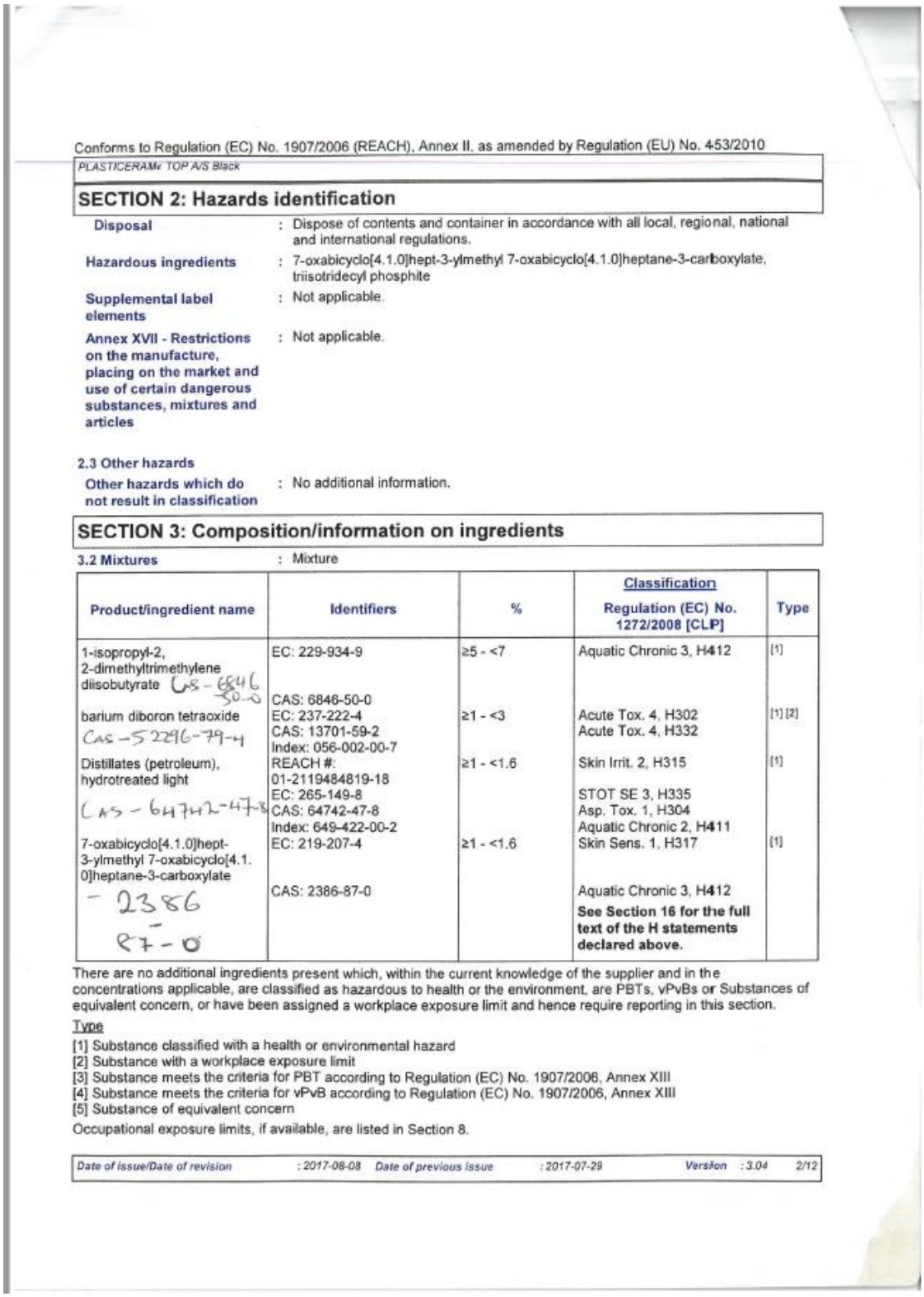

Conforms to Regulation (EC) No. 1907/2006 (REACH), Annex II, as amended by Regulation (EU) No. 453/2010

PLASTICERAM® TOP A/S Black

SECTION 2: Hazards identification

Disposal	:	Dispose of contents and container in accordance with all local, regional, national and international regulations.
Hazardous ingredients	:	7-oxabicyclo[4.1.0]hept-3-ylmethyl 7-oxabicyclo[4.1.0]heptane-3-carboxylate, triisotridecyl phosphite
Supplemental label elements	:	Not applicable.
Annex XVII - Restrictions on the manufacture, placing on the market and use of certain dangerous substances, mixtures and articles	:	Not applicable.

2.3 Other hazards

Other hazards which do not result in classification	:	No additional information.

SECTION 3: Composition/information on ingredients

3.2 Mixtures : Mixture

Product/ingredient name	Identifiers	%	Classification Regulation (EC) No. 1272/2008 [CLP]	Type
1-isopropyl-2, 2-dimethyltrimethylene diisobutyrate CAS - 6846 50-0	EC: 229-934-9 CAS: 6846-50-0	≥5 - <7	Aquatic Chronic 3, H412	[1]
barium diboron tetraoxide CAS - 52296-79-4	EC: 237-222-4 CAS: 13701-59-2 Index: 056-002-00-7	≥1 - <3	Acute Tox. 4, H302 Acute Tox. 4, H332	[1] [2]
Distillates (petroleum), hydrotreated light CAS - 64742-47-8	REACH #: 01-2119484819-18 EC: 265-149-8 CAS: 64742-47-8 Index: 649-422-00-2	≥1 - <1.6	Skin Irrit. 2, H315 STOT SE 3, H335 Asp. Tox. 1, H304 Aquatic Chronic 2, H411	[1]
7-oxabicyclo[4.1.0]hept-3-ylmethyl 7-oxabicyclo[4.1.0]heptane-3-carboxylate - 2386 87-0	EC: 219-207-4 CAS: 2386-87-0	≥1 - <1.6	Skin Sens. 1, H317 Aquatic Chronic 3, H412 **See Section 16 for the full text of the H statements declared above.**	[1]

There are no additional ingredients present which, within the current knowledge of the supplier and in the concentrations applicable, are classified as hazardous to health or the environment, are PBTs, vPvBs or Substances of equivalent concern, or have been assigned a workplace exposure limit and hence require reporting in this section.

Type

[1] Substance classified with a health or environmental hazard
[2] Substance with a workplace exposure limit
[3] Substance meets the criteria for PBT according to Regulation (EC) No. 1907/2006, Annex XIII
[4] Substance meets the criteria for vPvB according to Regulation (EC) No. 1907/2006, Annex XIII
[5] Substance of equivalent concern

Occupational exposure limits, if available, are listed in Section 8.

Date of issue/Date of revision : 2017-08-08 Date of previous issue : 2017-07-29 Version : 3.04 2/12

Fig.13 - 1: MSDS of Plasticeram Top Black showing coating constituents

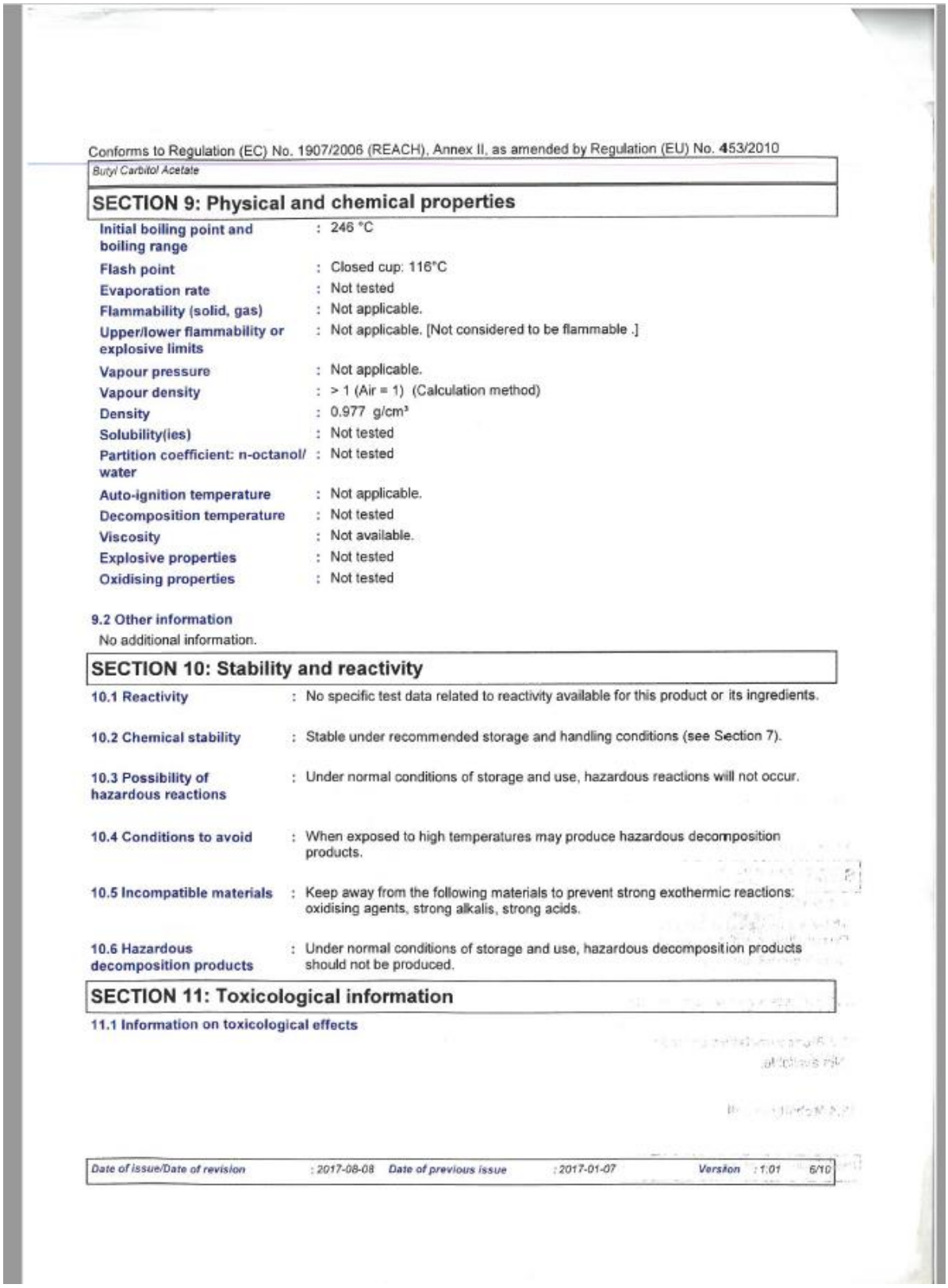

Conforms to Regulation (EC) No. 1907/2006 (REACH), Annex II, as amended by Regulation (EU) No. 453/2010

Butyl Carbitol Acetate

SECTION 9: Physical and chemical properties

Initial boiling point and boiling range	: 246 °C
Flash point	: Closed cup: 116°C
Evaporation rate	: Not tested
Flammability (solid, gas)	: Not applicable.
Upper/lower flammability or explosive limits	: Not applicable. [Not considered to be flammable .]
Vapour pressure	: Not applicable.
Vapour density	: > 1 (Air = 1) (Calculation method)
Density	: 0.977 g/cm³
Solubility(ies)	: Not tested
Partition coefficient: n-octanol/ water	: Not tested
Auto-ignition temperature	: Not applicable.
Decomposition temperature	: Not tested
Viscosity	: Not available.
Explosive properties	: Not tested
Oxidising properties	: Not tested

9.2 Other information

No additional information.

SECTION 10: Stability and reactivity

10.1 Reactivity	: No specific test data related to reactivity available for this product or its ingredients.
10.2 Chemical stability	: Stable under recommended storage and handling conditions (see Section 7).
10.3 Possibility of hazardous reactions	: Under normal conditions of storage and use, hazardous reactions will not occur.
10.4 Conditions to avoid	: When exposed to high temperatures may produce hazardous decomposition products.
10.5 Incompatible materials	: Keep away from the following materials to prevent strong exothermic reactions: oxidising agents, strong alkalis, strong acids.
10.6 Hazardous decomposition products	: Under normal conditions of storage and use, hazardous decomposition products should not be produced.

SECTION 11: Toxicological information

11.1 Information on toxicological effects

Date of issue/Date of revision : 2017-08-08 *Date of previous issue* : 2017-01-07 *Version* : 1.01 6/10

Fig.13 - 2: MSDS of BDA showing chemical and physical properties of solvent

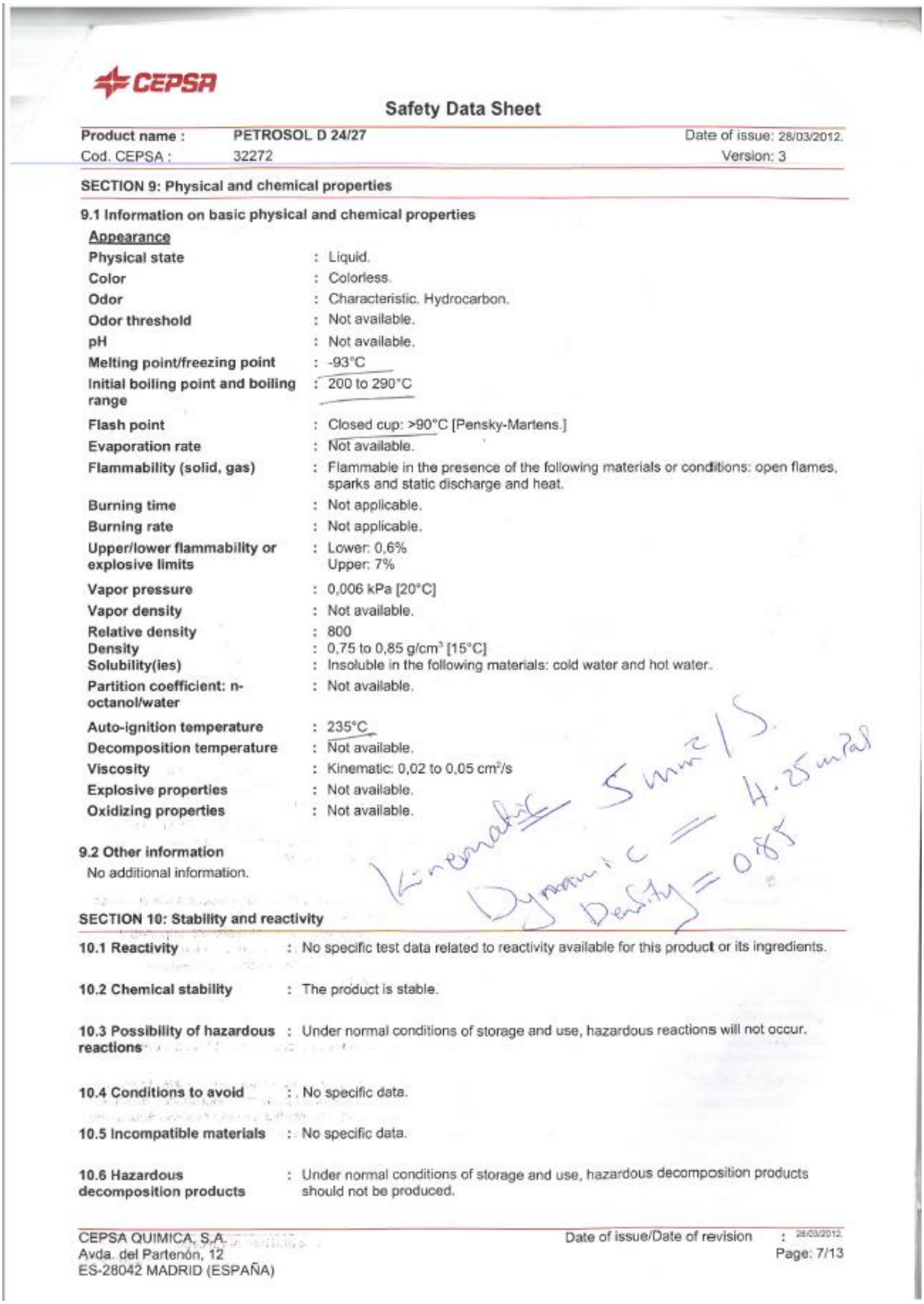

CEPSA

Safety Data Sheet

Product name :	**PETROSOL D 24/27**	Date of issue: 28/03/2012.
Cod. CEPSA :	32272	Version: 3

SECTION 9: Physical and chemical properties

9.1 Information on basic physical and chemical properties

Appearance

Physical state	: Liquid.
Color	: Colorless.
Odor	: Characteristic. Hydrocarbon.
Odor threshold	: Not available.
pH	: Not available.
Melting point/freezing point	: -93°C
Initial boiling point and boiling range	: 200 to 290°C
Flash point	: Closed cup: >90°C [Pensky-Martens.]
Evaporation rate	: Not available.
Flammability (solid, gas)	: Flammable in the presence of the following materials or conditions: open flames, sparks and static discharge and heat.
Burning time	: Not applicable.
Burning rate	: Not applicable.
Upper/lower flammability or explosive limits	: Lower: 0,6% Upper: 7%
Vapor pressure	: 0,006 kPa [20°C]
Vapor density	: Not available.
Relative density	: 800
Density	: 0,75 to 0,85 g/cm^3 [15°C]
Solubility(ies)	: Insoluble in the following materials: cold water and hot water.
Partition coefficient: n-octanol/water	: Not available.
Auto-ignition temperature	: 235°C
Decomposition temperature	: Not available.
Viscosity	: Kinematic: 0,02 to 0,05 cm^2/s
Explosive properties	: Not available.
Oxidizing properties	: Not available.

Kinematic 5 mm²/s.
Dynamic — 4.25 mPas
Density = 0.85

9.2 Other information

No additional information.

SECTION 10: Stability and reactivity

10.1 Reactivity	: No specific test data related to reactivity available for this product or its ingredients.
10.2 Chemical stability	: The product is stable.
10.3 Possibility of hazardous reactions	: Under normal conditions of storage and use, hazardous reactions will not occur.
10.4 Conditions to avoid	: No specific data.
10.5 Incompatible materials	: No specific data.
10.6 Hazardous decomposition products	: Under normal conditions of storage and use, hazardous decomposition products should not be produced.

Fig.13 - 3: MSDS of Petrosol showing chemical and physical properties of solvent

APPENDIX B: REPEATABILITY AND RELIABILITY STUDIES FOR TGA-DTG STUDIES.

To determine the accuracy of the thermal gravimetric analysis (TGA) experiments, thermal analysis tests were repeated three times for both coatings, and the results are presented in fig. 13 -3 and fig. 13 - 4. The standard deviation of TGA results for Coating B and Coating S were 1 and 2%, respectively. Therefore, a standard deviation of 2% was employed in this study.

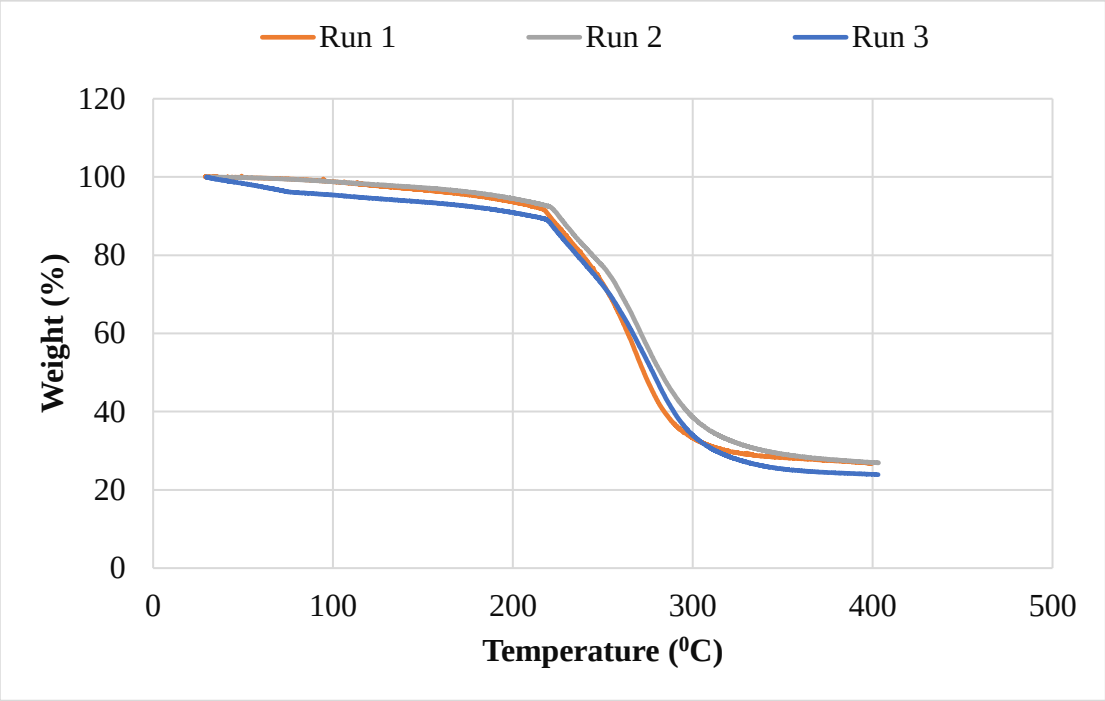

Fig.13 - 4: Repeatability and reproducibility study of TGA curves on Coatings S.

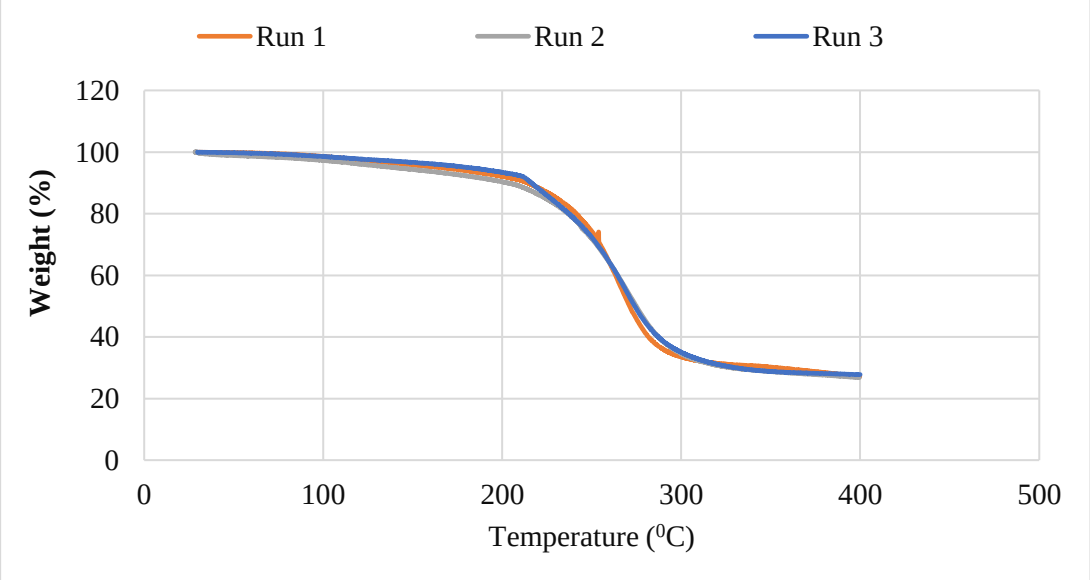

Fig.13 - 5: Repeatability and reproducibility study of TGA curves on Coatings S.

APPENDIX C: CHEMICAL ANALYSIS OF PLASTICERAM BLACK.

MICROSTRUCTURAL ANALYSIS ON STEEL WHEN COATING B IS THE TOPCOAT

Elemental mapping was essential for identifying differences of inorganic compositions between coating B and Coating S. Fig. 13 - 6. shows a micrograph from which elemental analysis on the cross-section of the coated steel was conducted. There were four layers identified on the cross-section of a coated steel, namely: steel surface, galvanising layer; primer coating and the topcoat. Fig. 13 – 7 allocates the elements on the steels tested samples

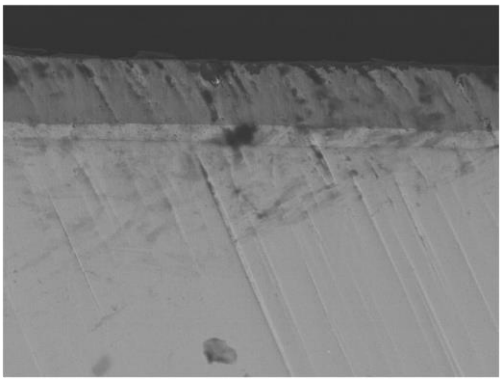

Fig.13 - 6: Micrograph of coated steel from which elemental mapping was derived with Coating X as the topcoat layer.

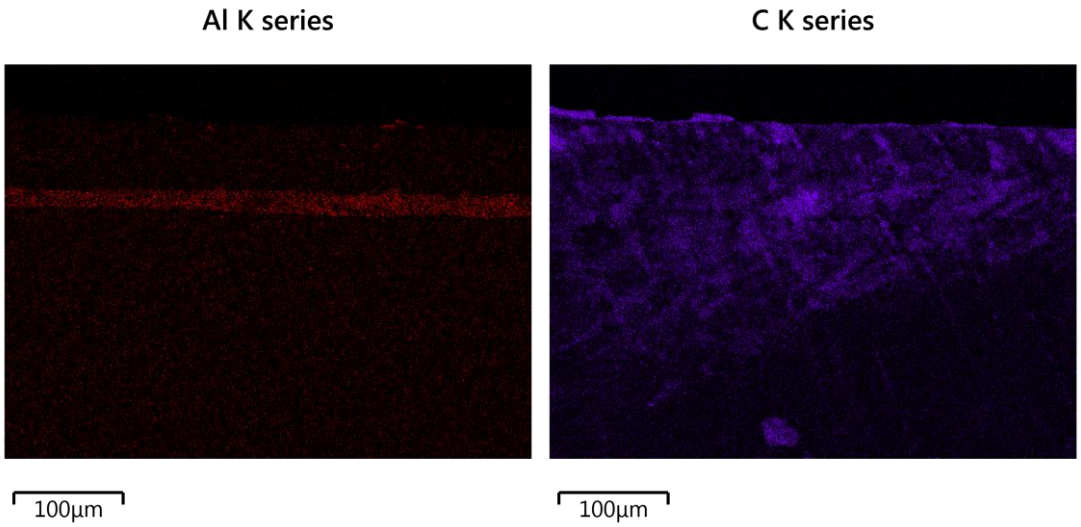

B K series

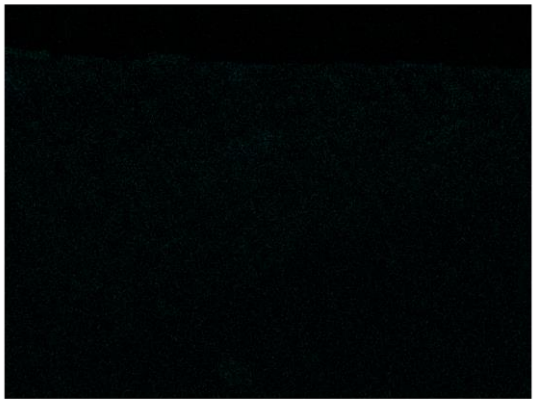

Ca K series

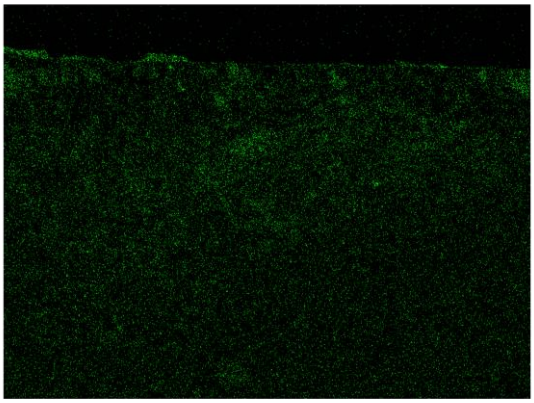

Cl K series

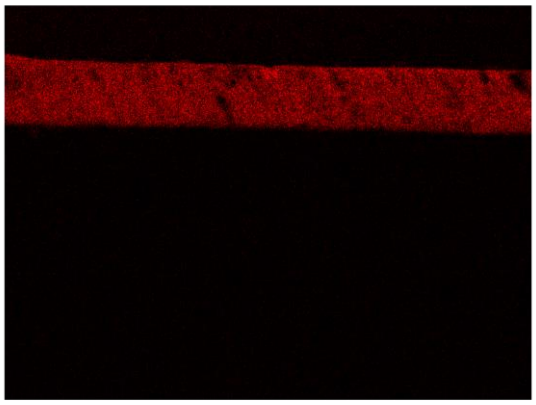

Cr K series

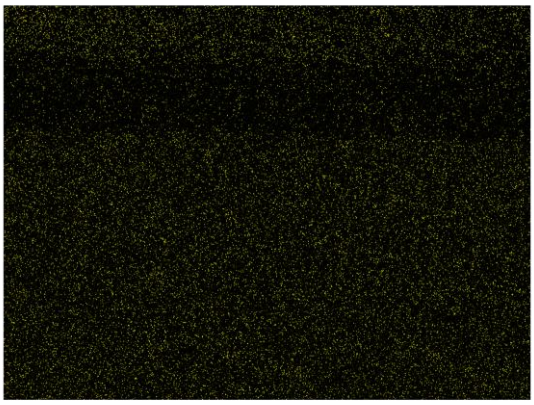

Fe K series

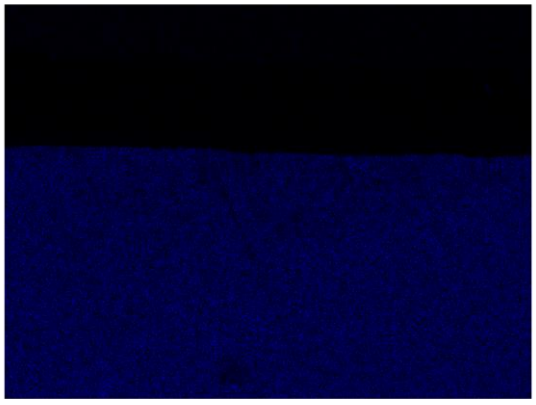

Si K series

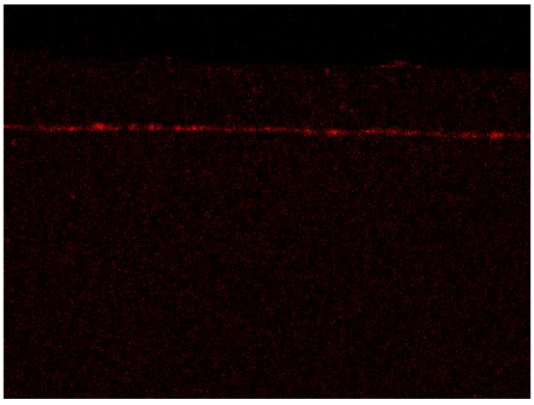

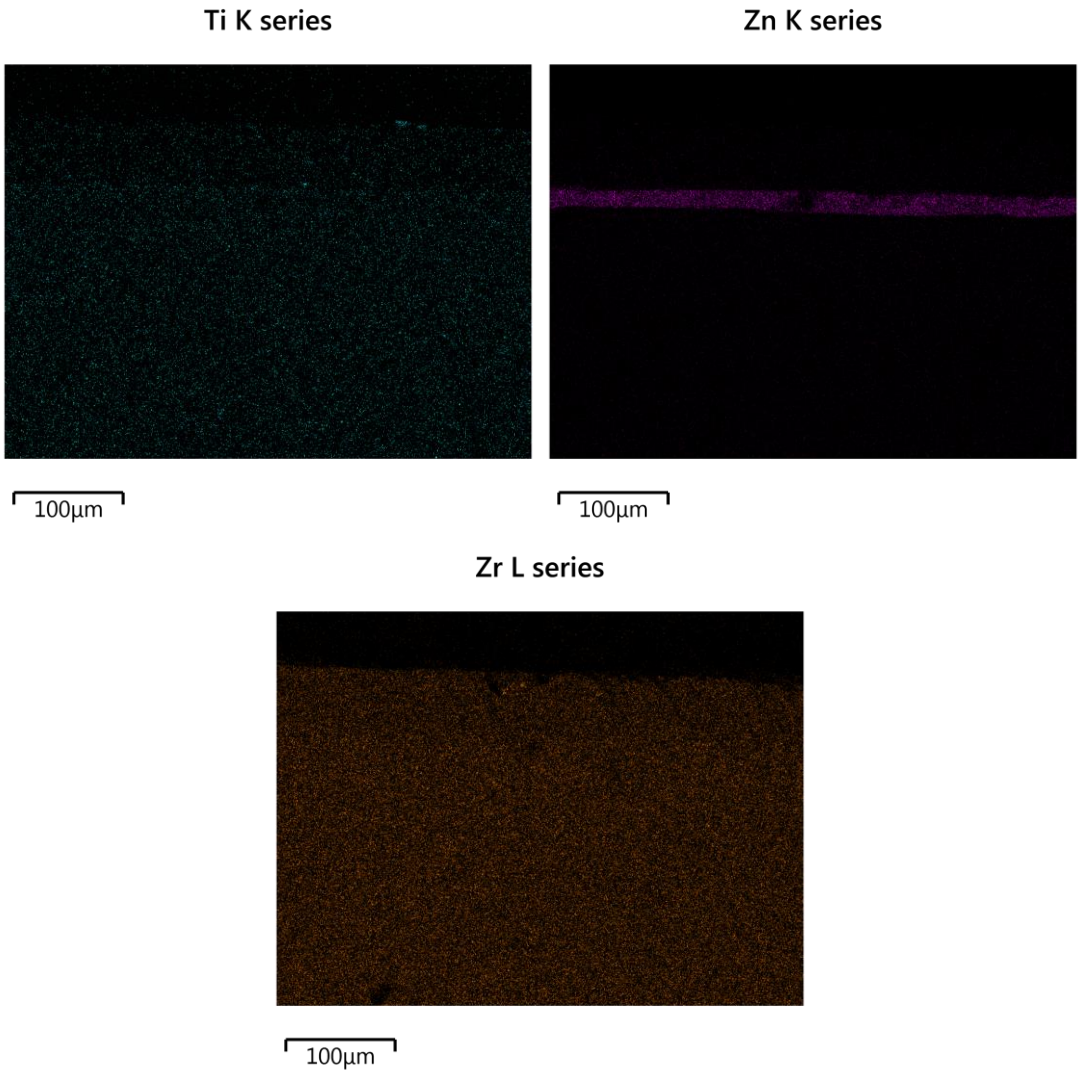

Fig.13 - 7: Electron mapping of cross-section of coated steel from which electron mapping was derived with Coating B as the topcoat layer

Steel surface: traces of Iron (Fe), carbon (C), Calcium (Ca) was traced back to steel layer, chromium (Cr), Titanium (Ti), and Zinc (Zn). Ti presence in steel layer was believed to have leaked from other layers during grinding and polishing process.

Galvanised layer: Silicon (Si) and Zinc (Zn) were observed and this was ascribed to the magi-zinc application.

The third layer: Traces of carbon (C), Chromium (Cr), Aluminium (Al), Titanium (Ti), Zinc (Zn), calcium (Ca), traced back to the primer coating. Al was believed to have leaked into other layers during sample preparation process.

Primer layer: Carbon (C), Boron (b), Chlorine (Cl) and Sodium (Na)

Topcoat layer: Carbon (C), Boron (b), Chlorine (Cl) and Silicon (Si)

MICROSTRUCTURAL ANALYSIS FOR COATING S

Fig. 13 – 8 shows the layers of coating on a steel surface. For coating X The same elements observed for Coating B were the same as those observed for Coating S, as seen in fig. 13 – 9.

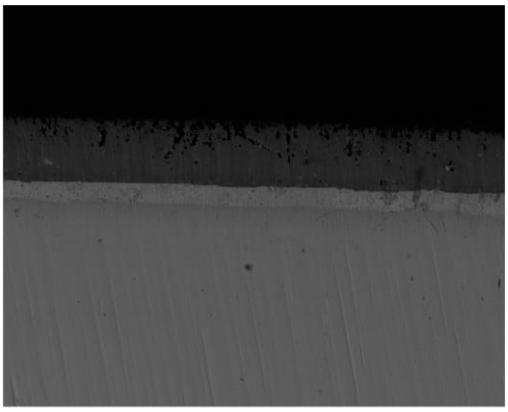

Fig.13 - 8: Micrograph of coated steel from which elemental mapping was derived with Coating X as the topcoat layer.

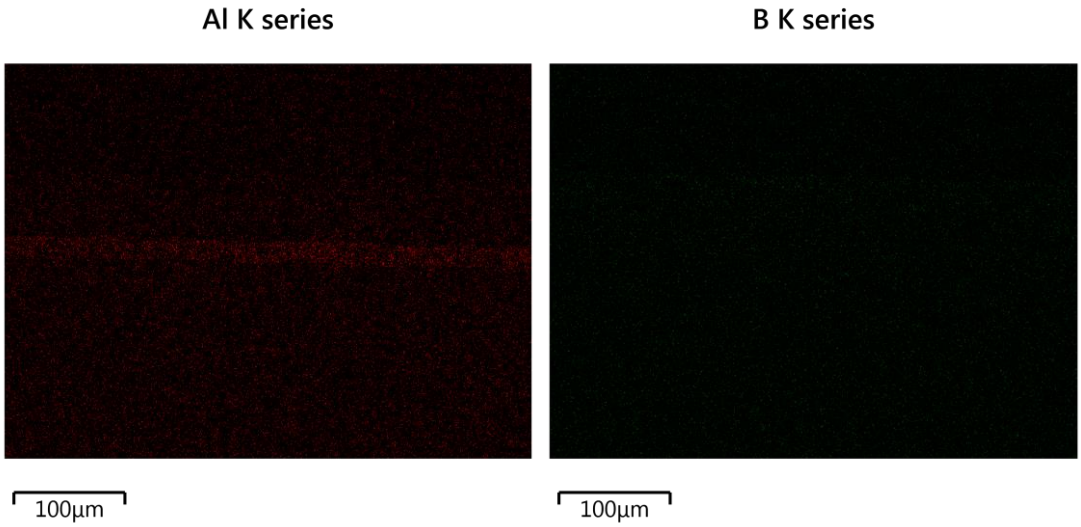

C K series

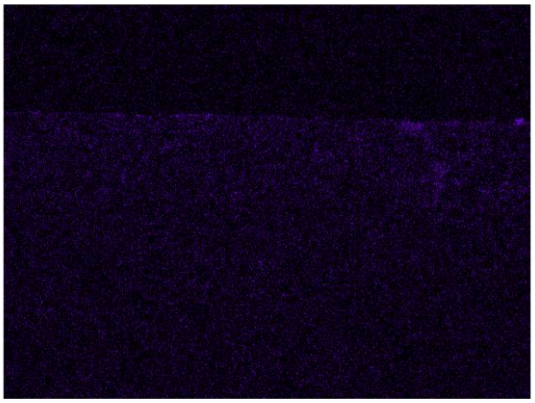

100μm

Ca K series

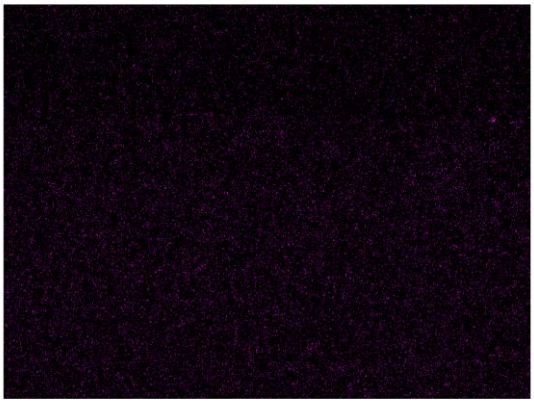

100μm

Cl K series

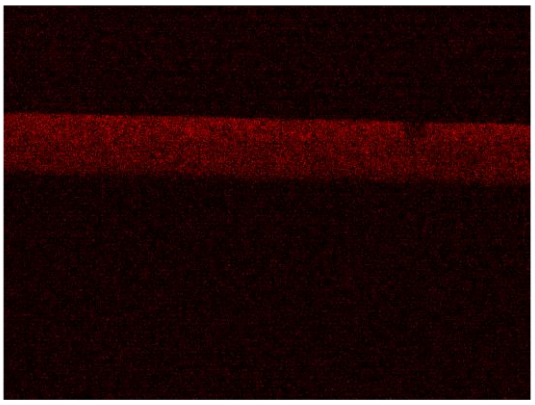

100μm

Cr K series

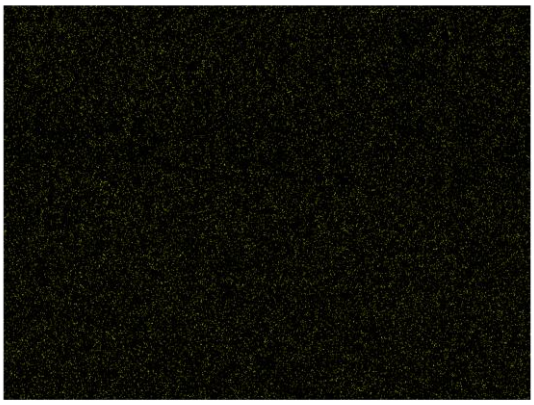

100μm

Fe K series

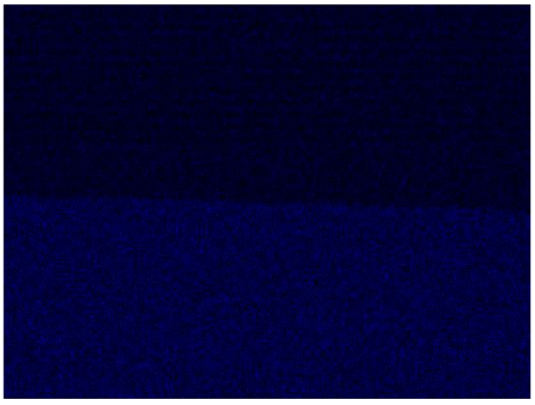

100μm

O K series

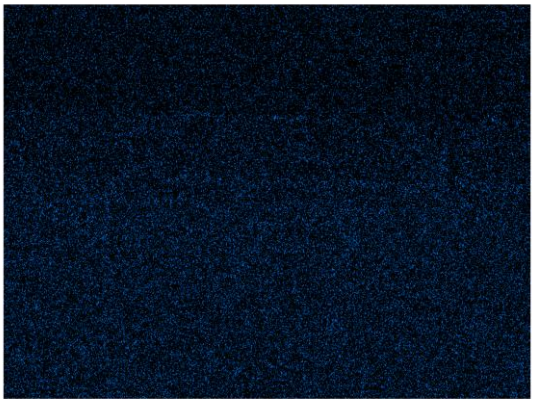

100μm

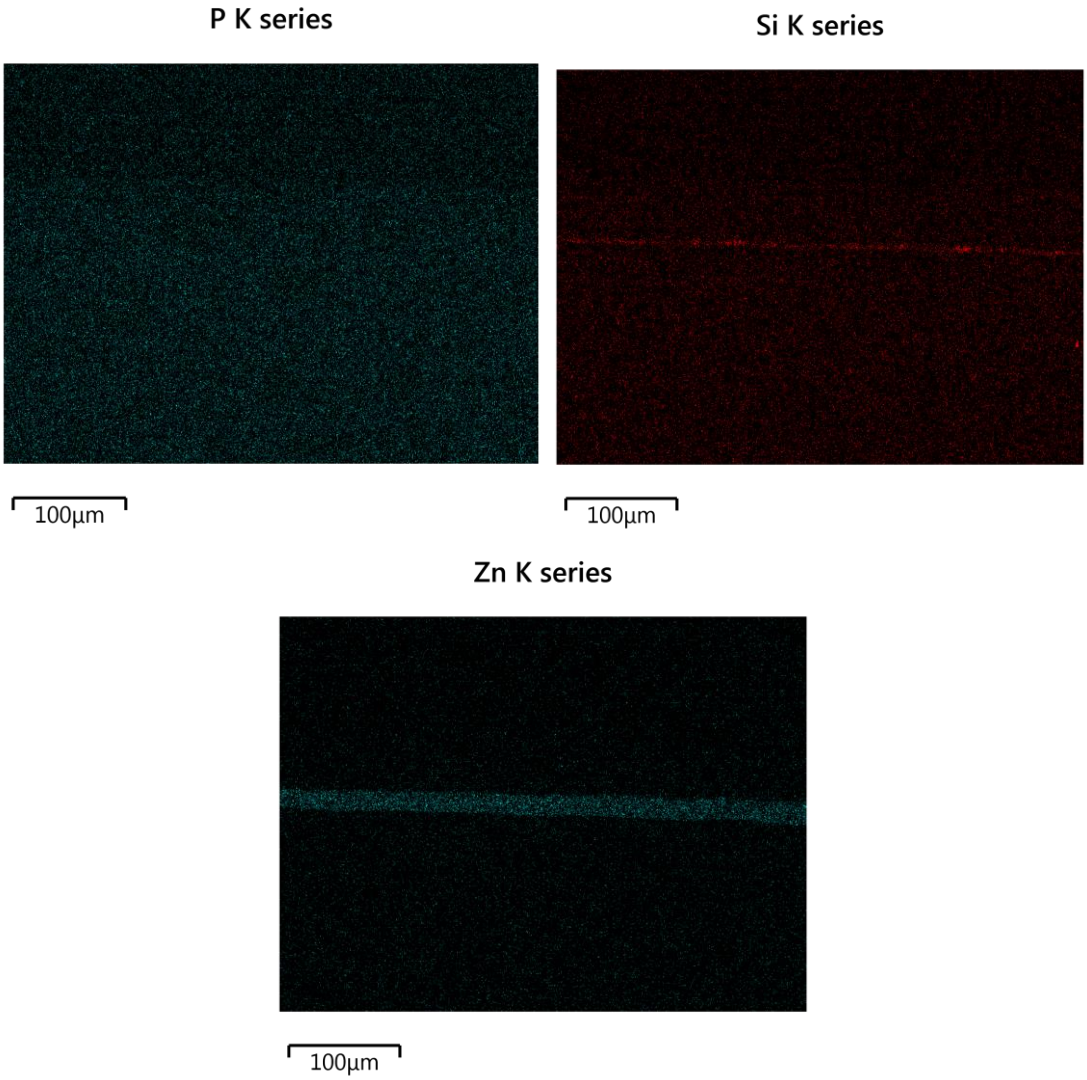

Fig.13 - 9: Electron mapping of cross-section of coated steel from which electron mapping was derived with Coating S as the topcoat layer

APPENDIX D: CHEMICAL ANALYSIS OF PLASTICERAM SUN MERLIN

MICROSTRUCTURAL ANALYSIS ON STEEL WHEN COATING X

There were no differences in elements observed between Coating X (See Fig. 13 – 10) and Coating Y (See Fig. 13 – 11)., the same elements with Plasticeram Black coatings were also observed in Plasticeram sun Merlin

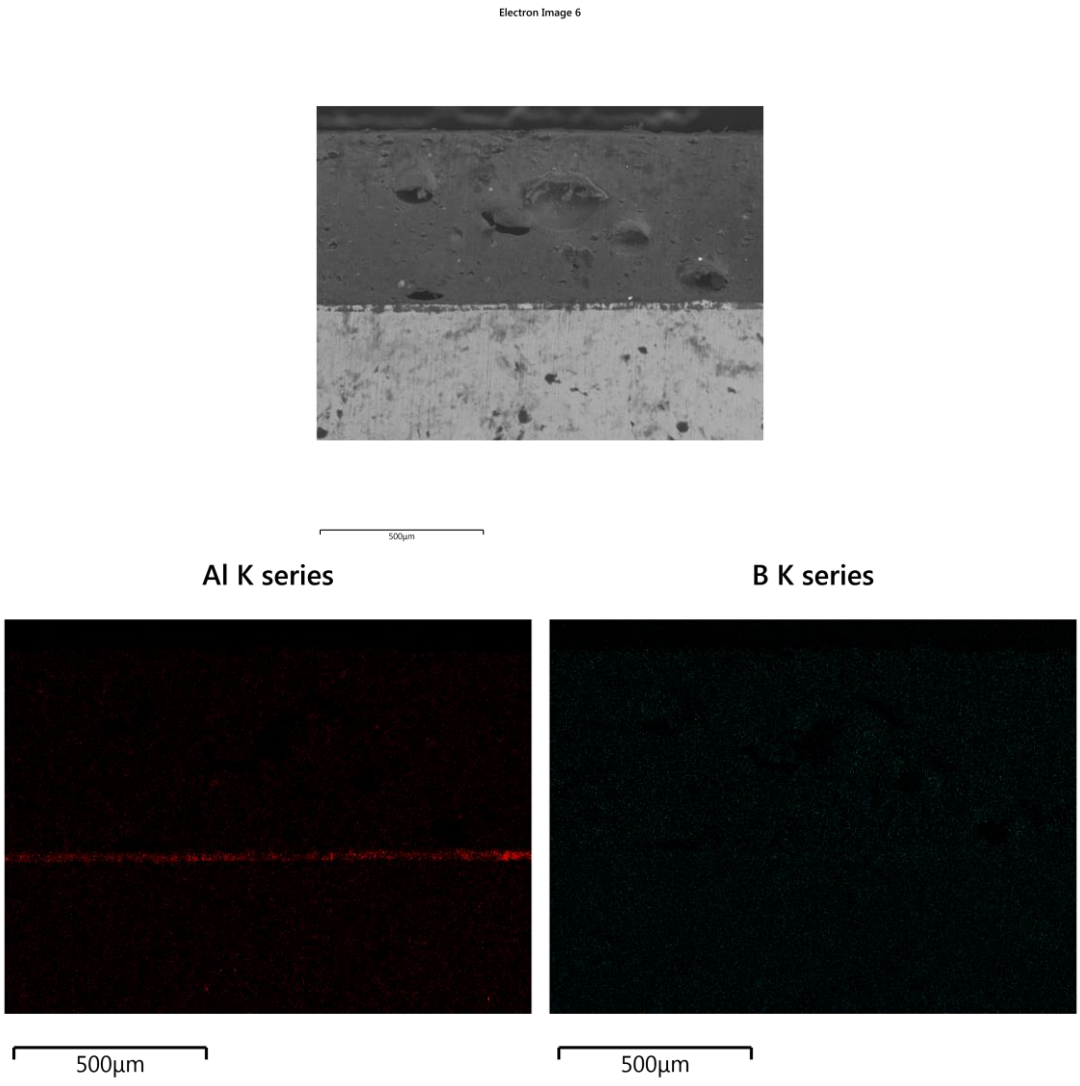

C K series

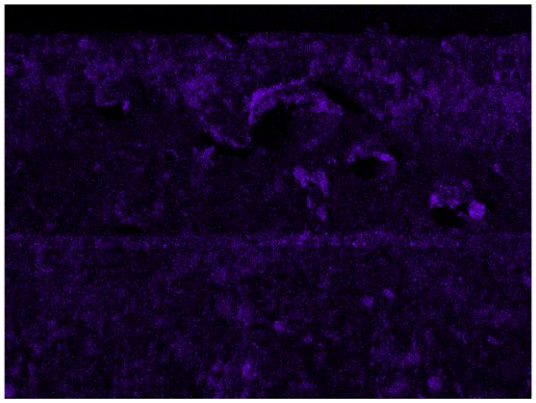

500µm

Ca K series

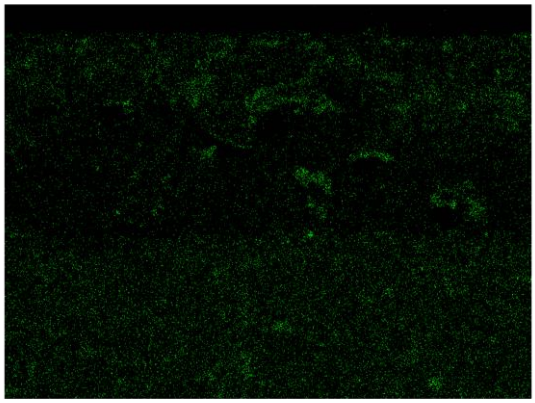

500µm

Cl K series

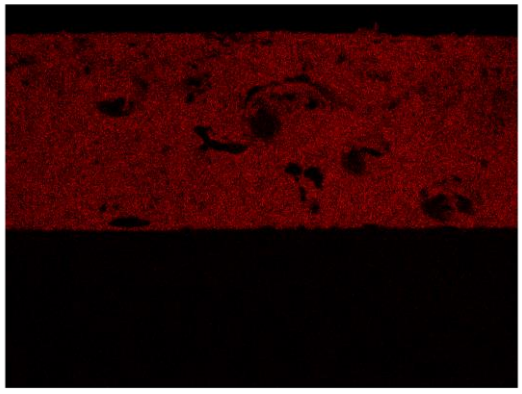

500µm

Cr K series

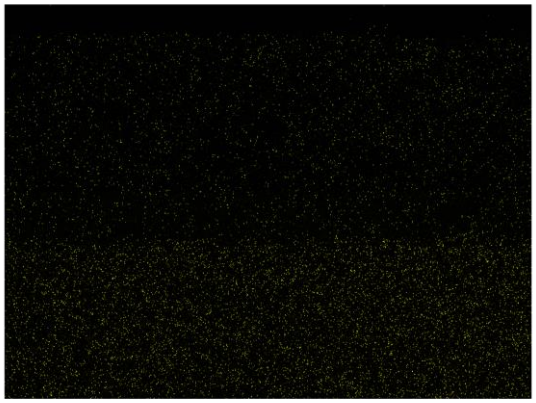

500µm

Fe K series

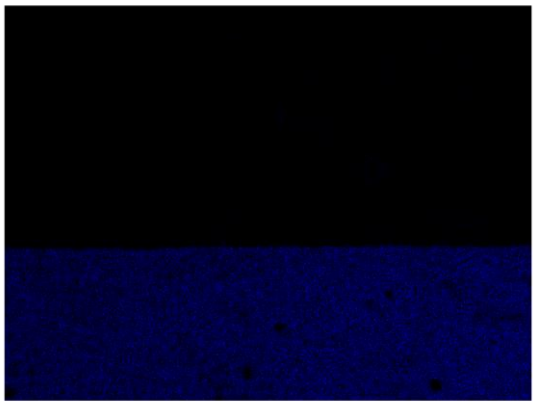

500µm

Mn K series

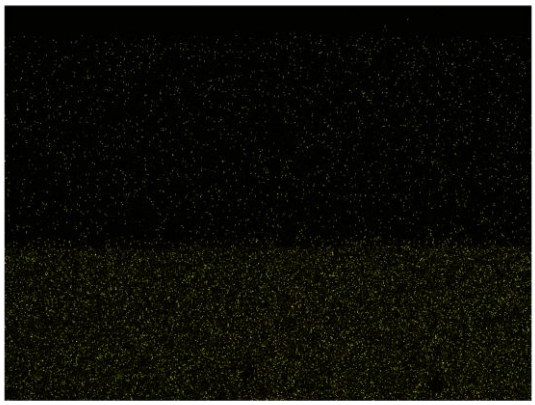

500µm

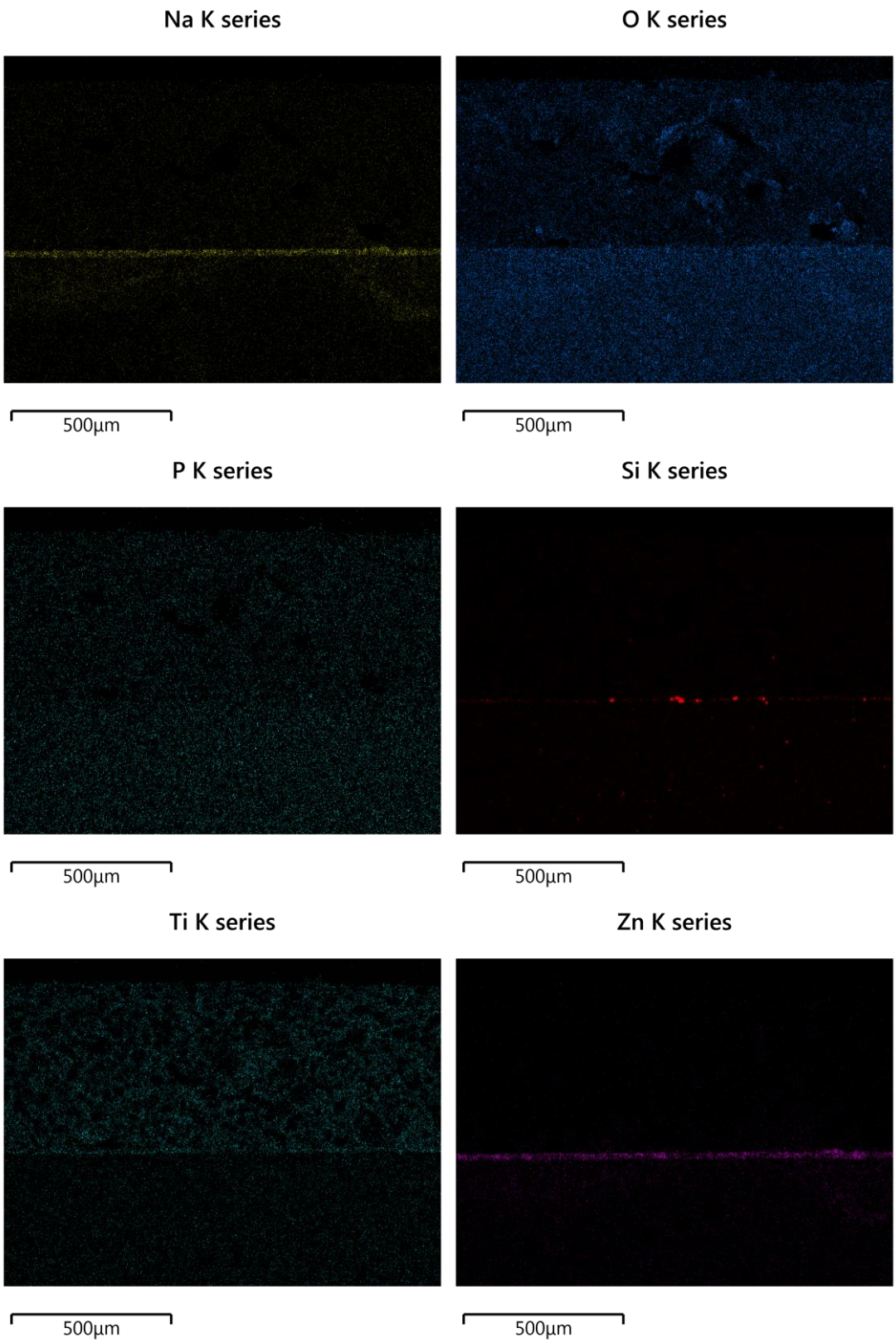

Fig.13 - 10: Electron mapping of a cross-section of coated steel from which electron mapping was derived with Coating X as the topcoat layer

COATING Y

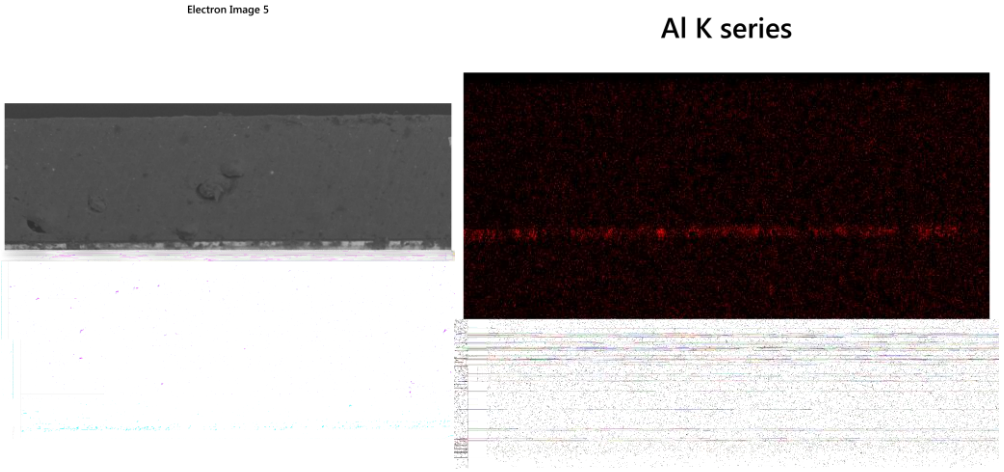
Electron Image 5
Al K series

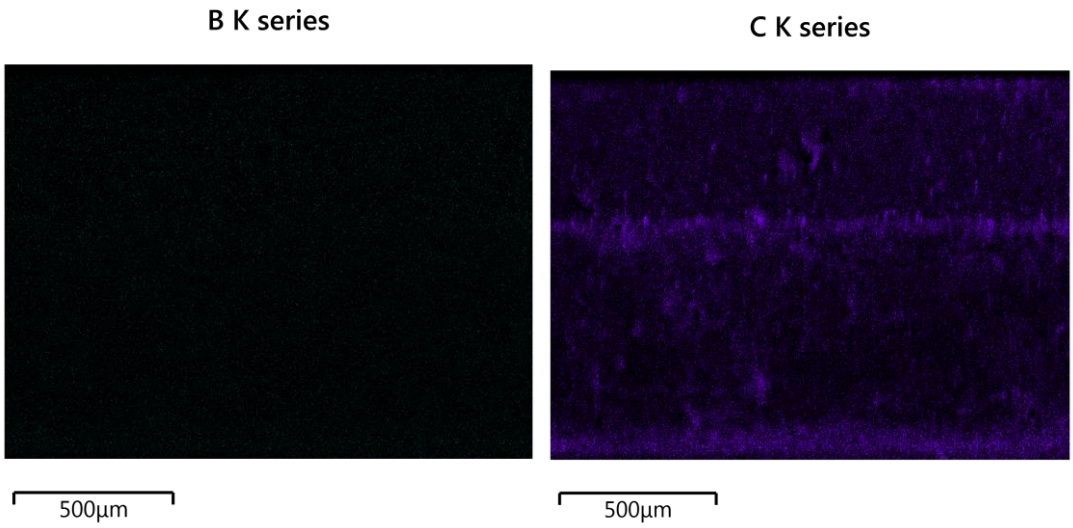
B K series
C K series
500µm
500µm

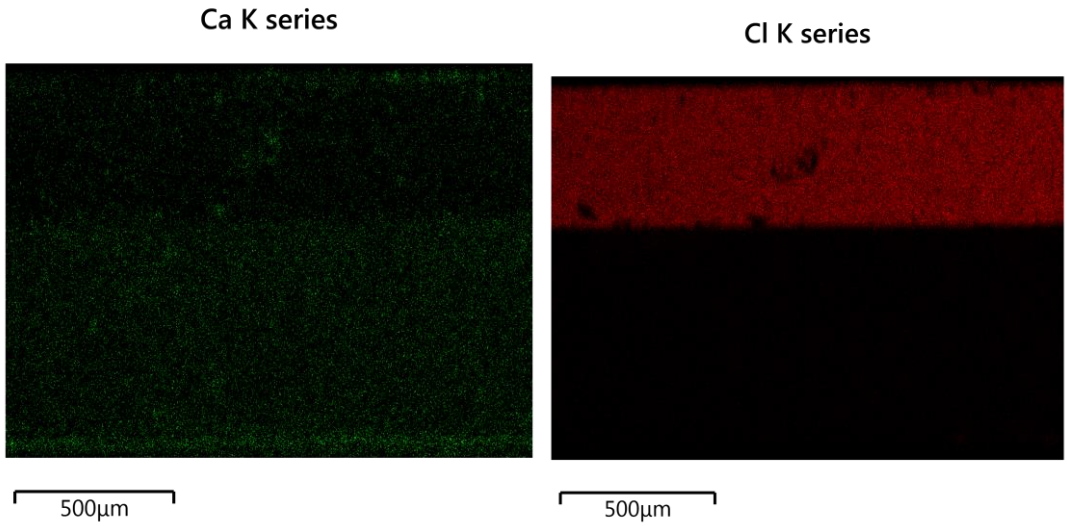
Ca K series
Cl K series
500µm
500µm

Cr K series

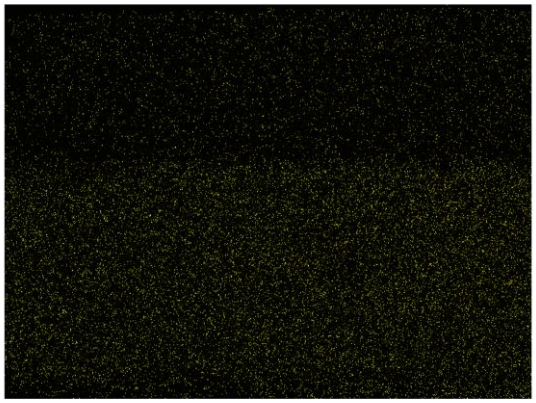

Fe K series

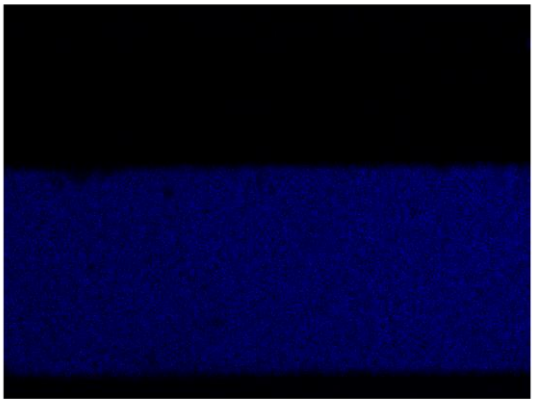

Mn K series

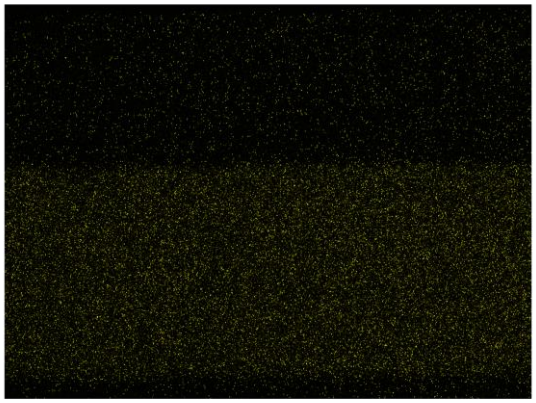

Na K series

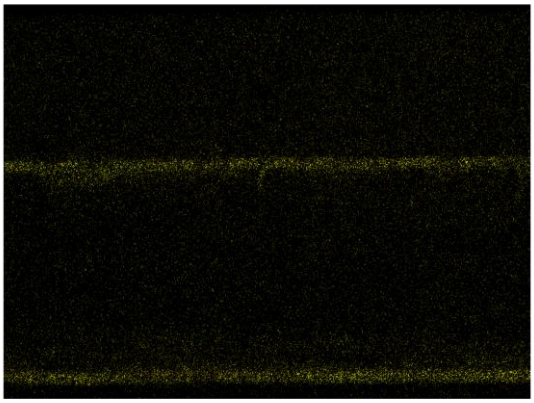

O K series

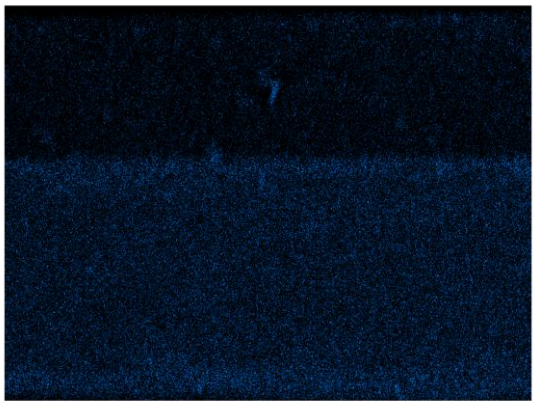

P K series

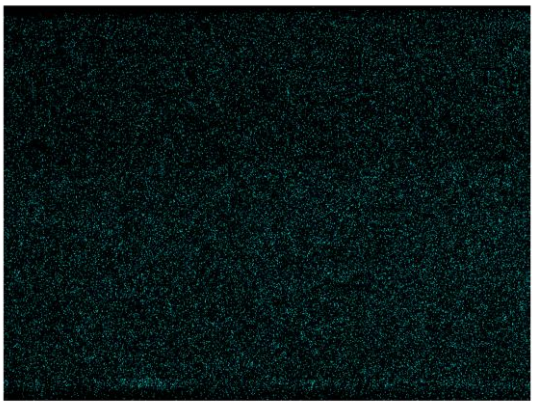

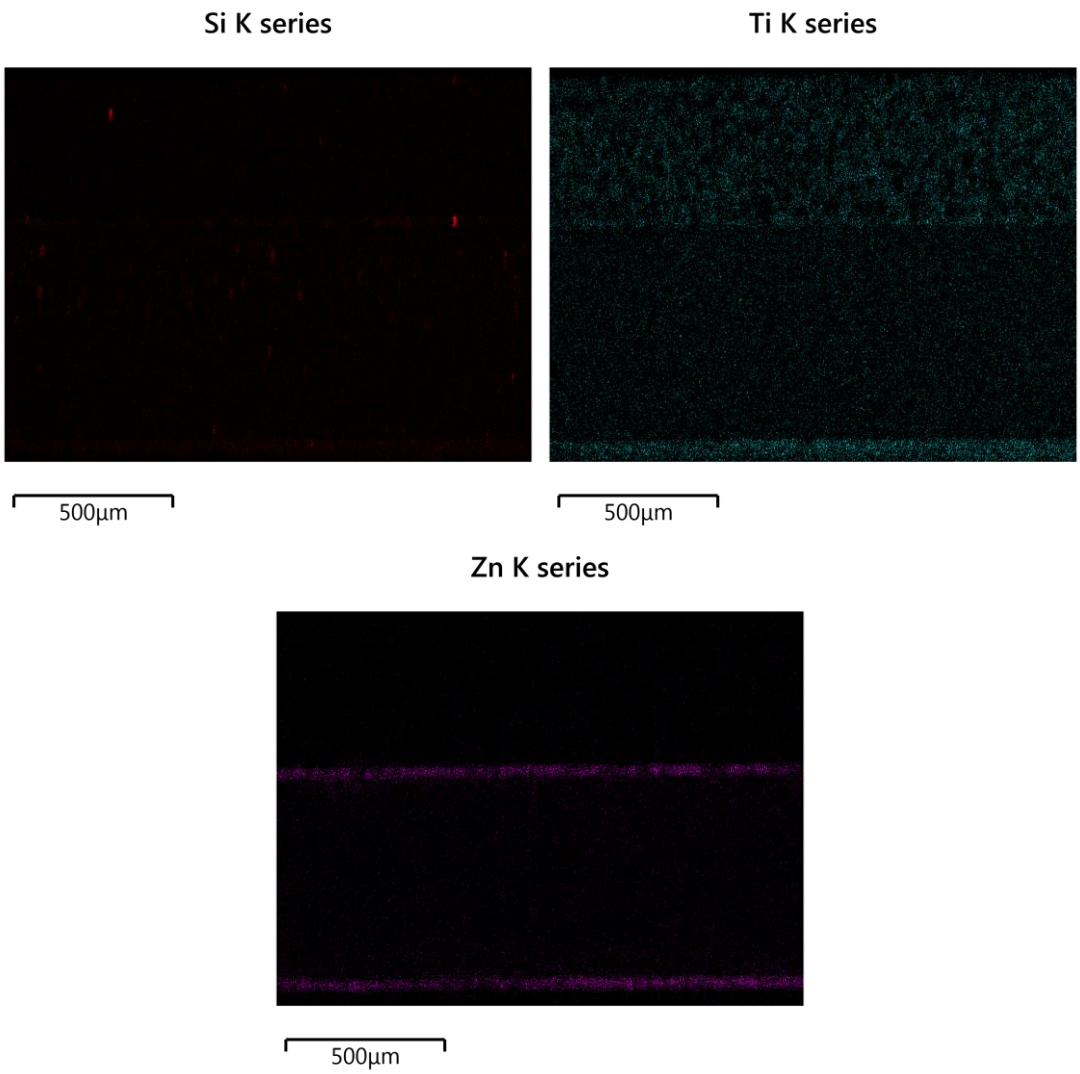

Fig.13 - 11: Electron mapping of a cross-section of coated steel from which electron mapping was derived with Coating Y as the topcoat layer

.

APPENDIX E: SURFACE TENSION AND SURFACE ENERGY

DETERMINING CONTACT ANGLE ON THE PICK-UP ROLL, FROM THE POINT OF IMPACT ON THE NIP

Roller coating process is constantly is a dynamic mode. Therefore, dynamic roller coating process was conducted with consideration of coating rotation from the pick- up trough (point A) to the middle of nip gap (point B) in fig. 13 – 12 below.

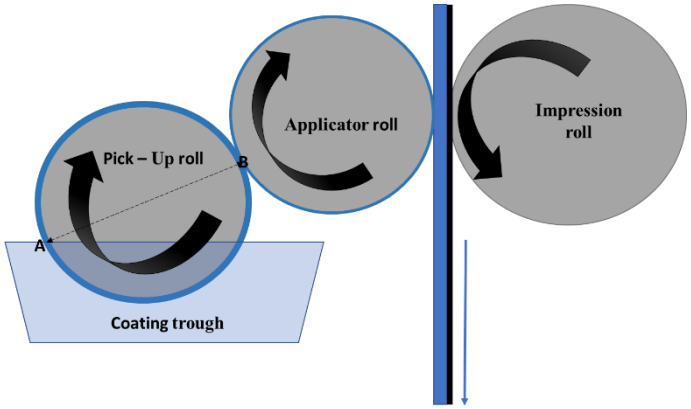

Fig.13 - 12: Determination of contact on the pick - up roll

Note: 60 seconds = 1 minutes

Therefore, Line speed of 90 m/min = 1.5 m/s, and 70 m/min = 1.17 m/s

Pick - up roll speed = 70 m/min (1.17 m/s) and 90 m/min (1.5 m/s)

The diameter of a pick-up roll is 256 mm (0.256 m)

Pick up roll speed = Applicator roll speed = Line speed

Surface speed $= \frac{Rotational\ speed}{Pick\ up\ roll\ Radius}$

Rotational speed = Surface speed x Pick up roll radius

$Coating\ material\ travelling\ a\ distance\ of\ \pi, from\ the\ point\ of\ impact\ to\ nip\ gap$

Also:

$\pi radians = 3.14 = 180$ degrees

AT LINE SPEED OF 90 M/ MIN

$$Rotational\ speed = \frac{90\ m/min}{60 seconds}\ x\ 0.256m$$

Rotational speed = 11.7 rad/s

Travelling time = $\frac{\pi\ rads}{11.7\ rad/s}$

Travelling time* = 0. 27 *seconds

AT LINE SPEED OF 90 M/ MIN

$$Rotational\ speed = \frac{70\ m/min}{60 seconds}\ \ x\ 0.256m$$

Rotational speed = 9.11 rad/s

Travelling time = $\frac{\pi\ rads}{9.11\ rad/s}$

Travelling time =0.34 seconds

SURFACE ENERGY AND DYNAMIC CONTACT ANGLE MEASUREMENTS

Fig. 13 - 13 shows surface energy of Polyurethane and Acrylic primer coated Steel substrate, and Clean ECCS and Unclean ECCS (ECCS with 5 nm organic layer of DOS) –as a representation of the pick - up roll with and without a layer of coating.

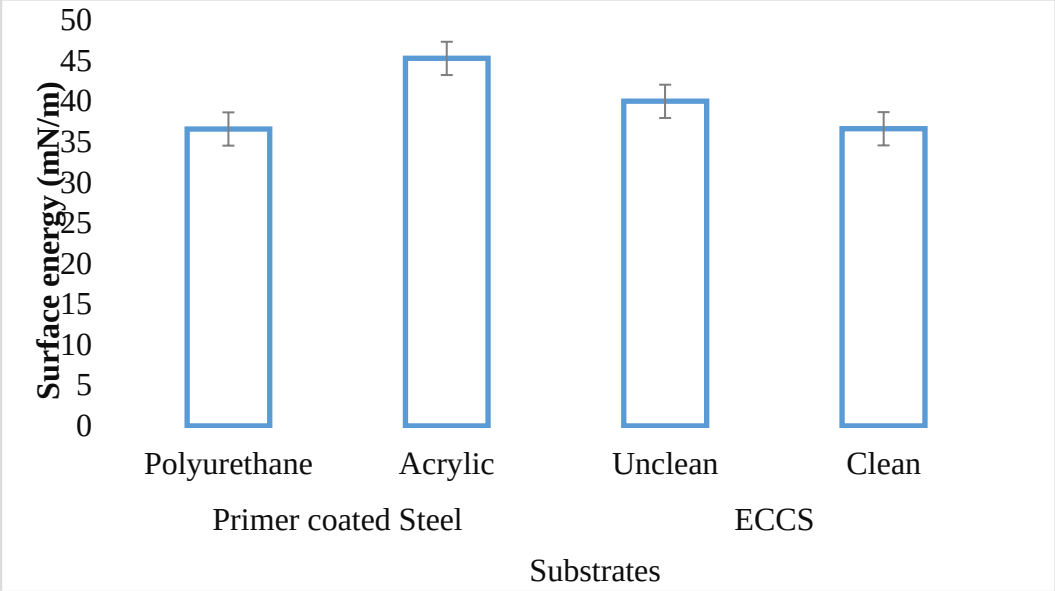

Fig.13 - 13: Surface energy of different surfaces

The pick - up roll achieved great wetting with the presence of organic layer compared to a clean pick - up roll; ECCS with organic layer exhibited a surface energy of 40 mN/m whereas a clean ECCS has a surface energy of 37 mN/m. The materials under study showed surface tension values of 35 and 27 mN/m for Coating B and Coating S, respectively. The results depicted that ECCS with organic layer has higher surface energy to bring about the distortion of the droplet shape, and subsequently achieving good wetting. This was attributed to the fact that cohesive forces are created between the

deposited material (organic coating) and organic layer already settling on the primer coated steel. Similarly, Acrylic primer - coated steel showed higher surface energy than Polyurethane primer coated steel with a surface energy of 45 and 37 mN/m, respectively.

APPENDIX F: SHEAR RHEOLOGY OF PLASTICERAM BLACK COATINGS

DETERMINATION OF FLOW PROPERTIES

Flow indices were determined using a natural log – log plot (fig. 13 – 14) based on the power-law model in section 2.3.

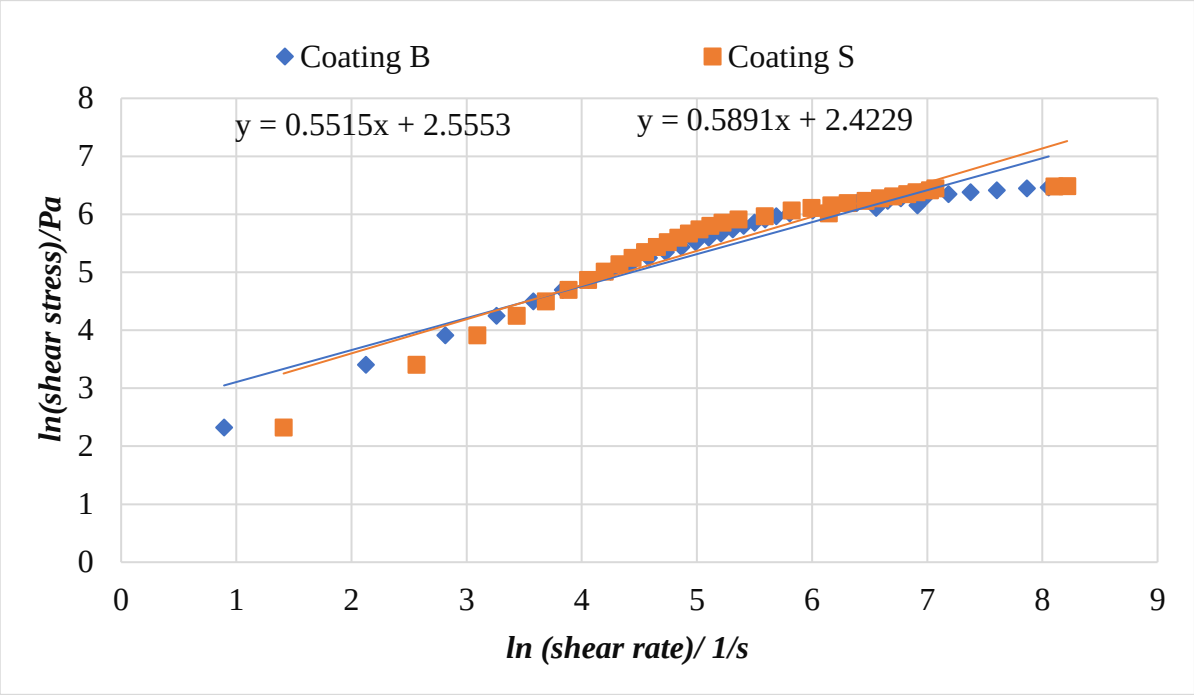

Fig.13 - 14: ln – ln plot of shear stress Vs shear rate

Table 13 - 1: Flow properties of Coating B and Coating S

	Gradient	**Exp. (intercept)]**	**R^2**
Coating B	0.555	18.2	0.93
Coating S	0.589	15.6	0.93

CALCULATION OF POWER LAW FLOW PROPERTIES OF DYNAMIC SHEAR RHEOLOGY

To determine the power-law parameters of the elastic modulus Vs frequency, a natural log-log plot of elastic modulus against frequency employed – Fig. 13 – 15.

$$\ln (G') = \ln k + n' \ln (\omega) \qquad (13 - 2)$$

COATING B:

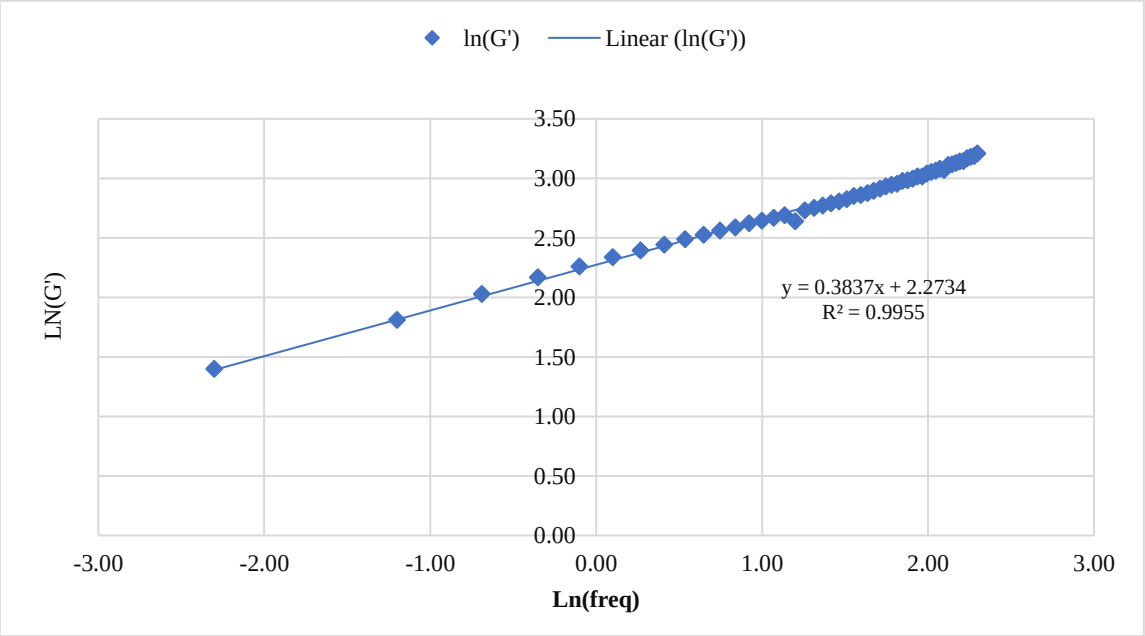

Fig.13 - 15: ln-ln plot of G' Vs Frequency of Coating B

To determine the power-law parameters, a natural log-log plot of viscous modulus against frequency employed. – Fig. 13 – 16, based on Eqn. (13 – 3)

$$\ln (G'') = \ln K'' + n'' \ln (\omega) \qquad (13 - 3)$$

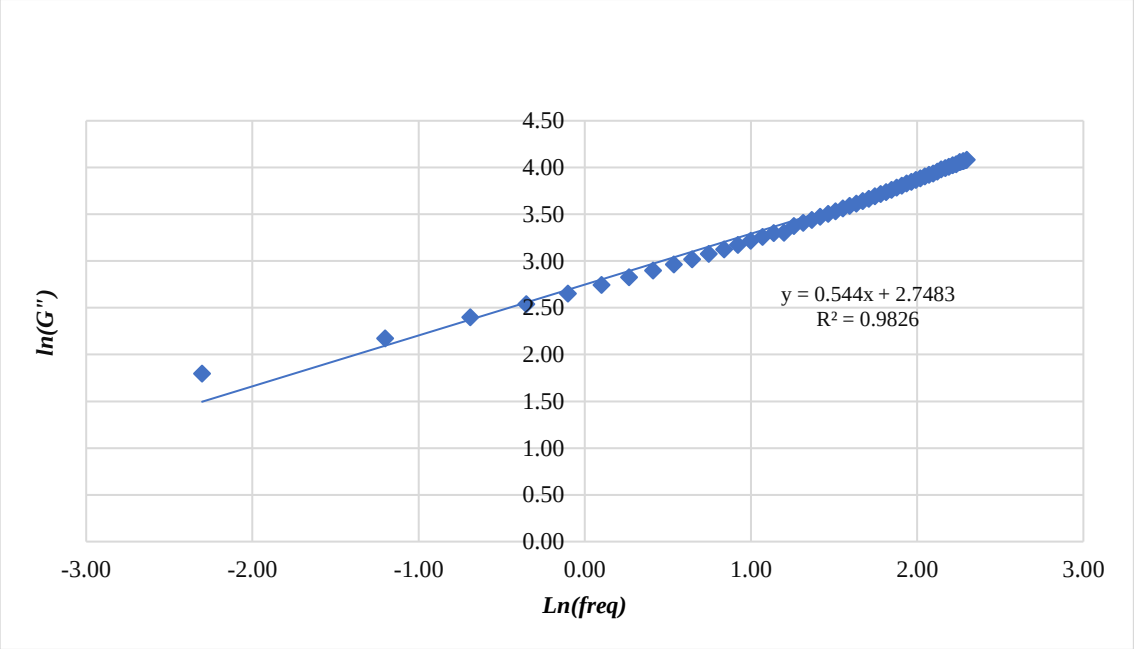

Fig.13 - 16: Ln-ln plot of G" Vs Frequency of Coating B

To determine the power-law parameters of a natural ln-ln plot of Viscous modulus against frequency employed, Fig. 13 – 17, based on Eqn. (13 – 4).

$$\ln(v^*) = \ln K^* + n^* \ln(\omega) \qquad (13 - 4)$$

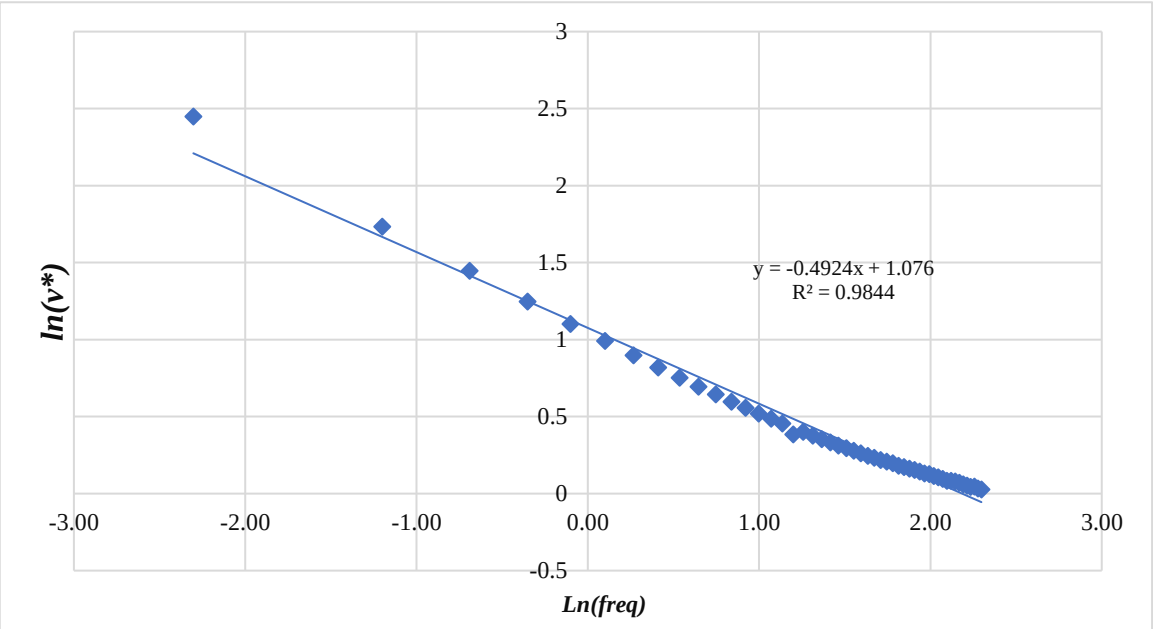

Fig.13 - 17: ln - ln plot of V* Vs Frequency of Coating B

A summary of derived flow properties for Coating B are presented in Table 13 - 2 below.

Table 13 - 2: Dynamic flow properties of Coating B

K': (EXP(Intercept)')	**n': Slope**	**R^2**
9.71	0.38	0.99
K": (EXP(Intercept)'')	**n": Slope**	**R^2**
15.14	0.54	0.98
V*: (EXP(Intercept)*)	**n*: Slope**	**R^2**
2.9	0.51	0.989

COATING S

To determine the power-law parameters of the elastic modulus Vs frequency, a natural log-log plot of elastic modulus against frequency employed – Fig. 13 - 18

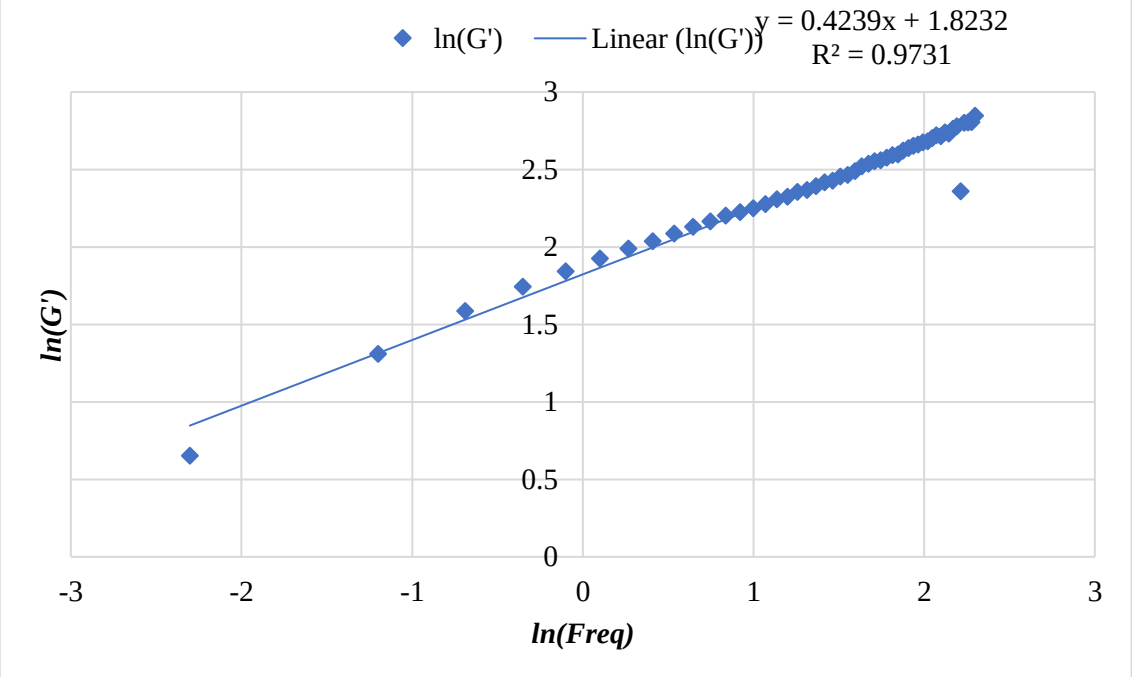

Fig.13 - 18: ln-ln plot of G' Vs Frequency of Coating S

To determine the power-law parameters in a natural log-log plot of viscous modulus against frequency employed. Fig. 13 - 19

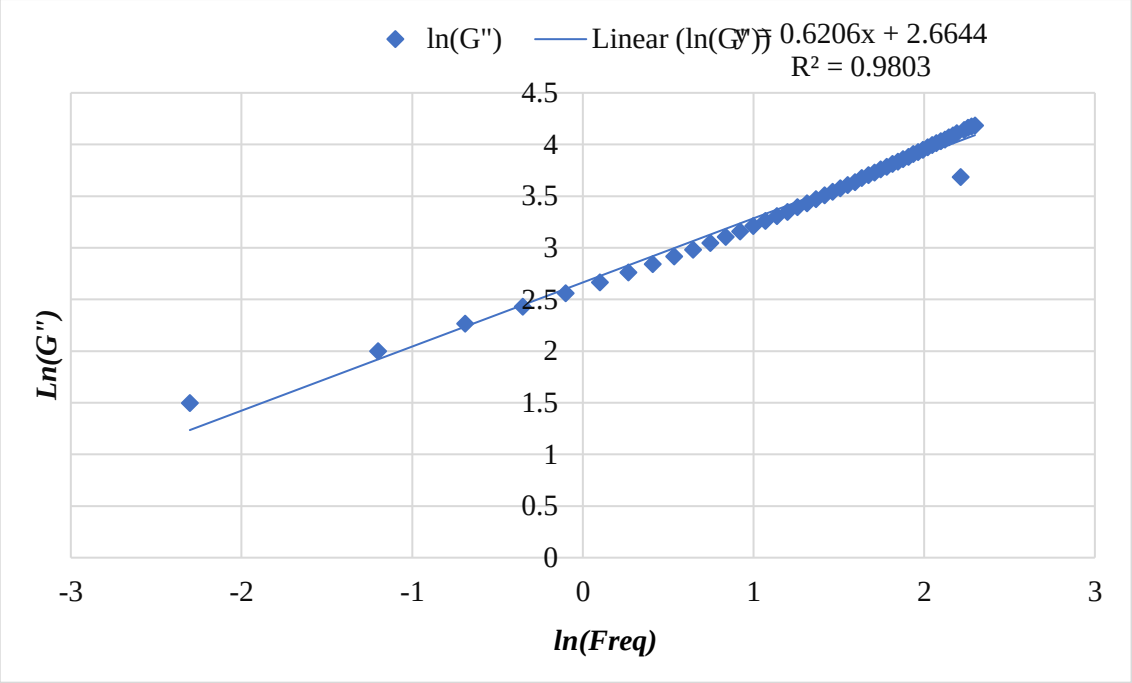

Fig.13 - 19: ln-ln plot of G" Vs Frequency of Coating S

To determine the power-law parameters of a natural ln-ln plot of Viscous modulus against frequency employed, Fig. 13 – 20.

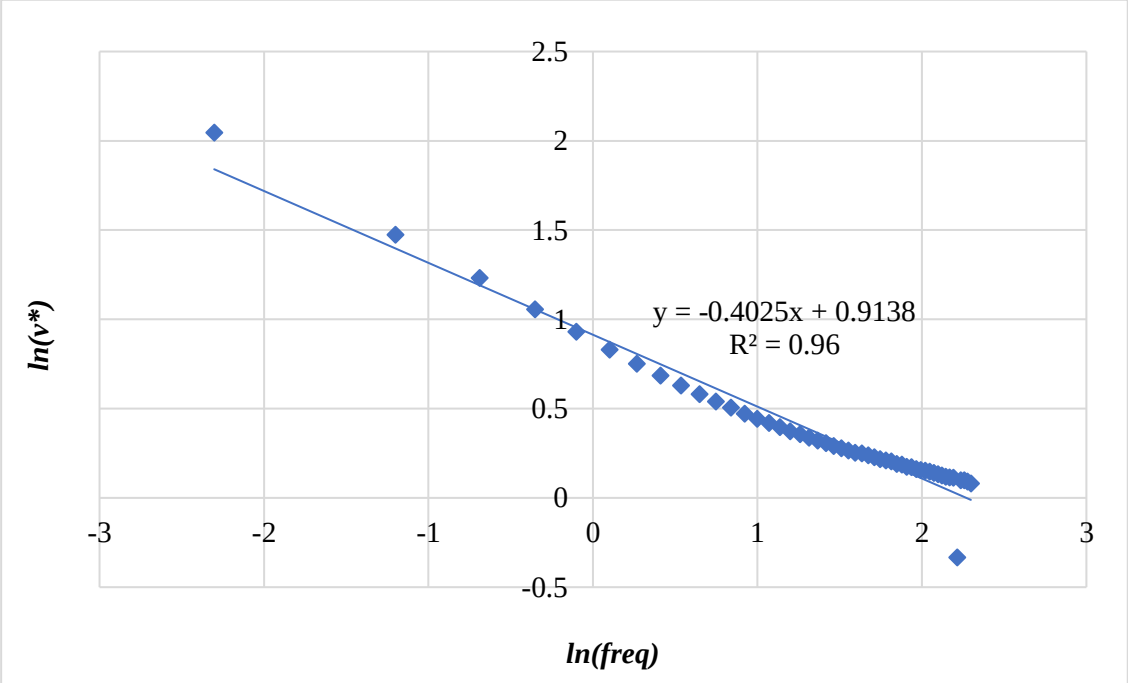

Fig.13 - 20: ln - ln plot of V* Vs Frequency of Coating B

Table 13 - 3: Flow properties of Coating S

K': (EXP(Intercept)'	n': Slope	R^2
6.2	0.6	0.970
K": (EXP(Intercept)''	**n": Slope**	**R^2**
14.4	0.4	0.980
V*: (EXP(Intercept)*	**n*: Slope**	**R^2**
1.9	0.6	0.980

APPARENT WALL SLIP INVESTIGATION: GEOMETRY SIZE VISCOSITY DEPENDENCE COATING B AND COATING S

Investigation of geometry size viscosity dependence was investigated on parallel plate diameters of 20, 40 and 60 mm – see Fig. 13 - 21. The ratio of gap size to diameter was kept constant at 10. It is seen that geometry size has the negligible effect of geometry sizes on the obtained shear viscosity. Therefore, a 40 mm diameter was chosen for subsequent investigation of apparent wall slip (AWS).

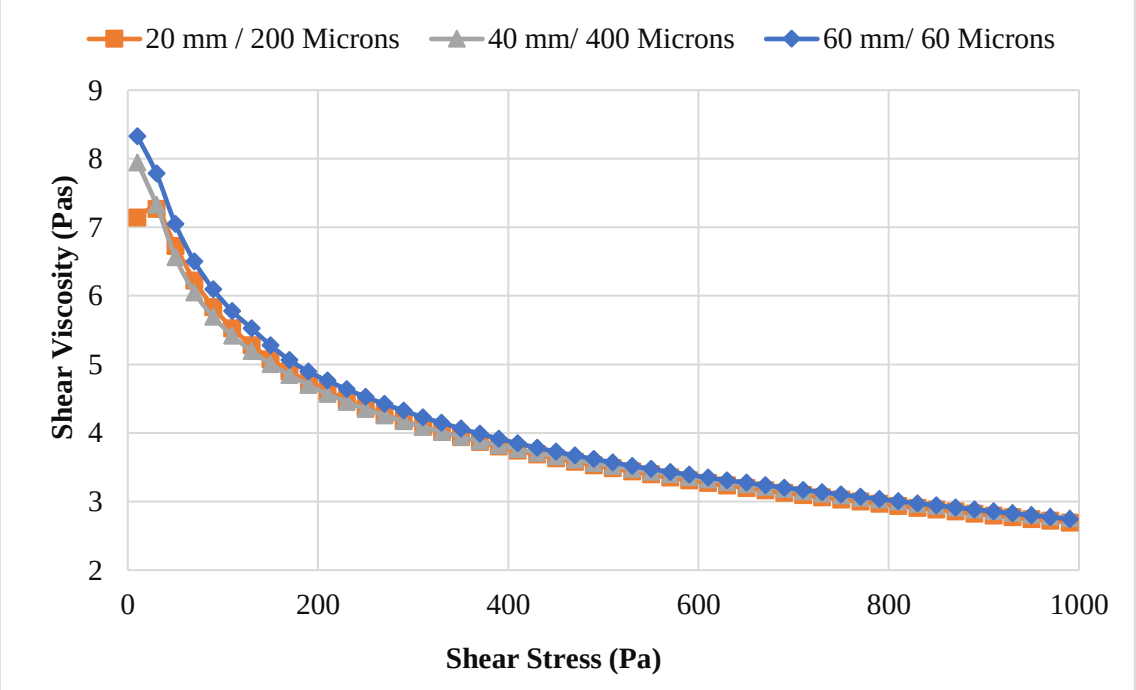

Fig.13 - 21: Geometry size effect on shear viscosity.

APPARENT WALL SLIP INVESTIGATION: GAP SIZE VISCOSITY DEPENDENCE COATING B AND COATING S

Fig.13 – 22 to fig. 13 - 27show apparent shear rate against inverse separation gap for Coating B, while fig. 13 - 28 to fig. 13 - 33 show apparent shear rate against inverse separation for Coating S. For both coatings, flow curves shifted at varying shear stresses, illustrating AWS effects on the flow curves.

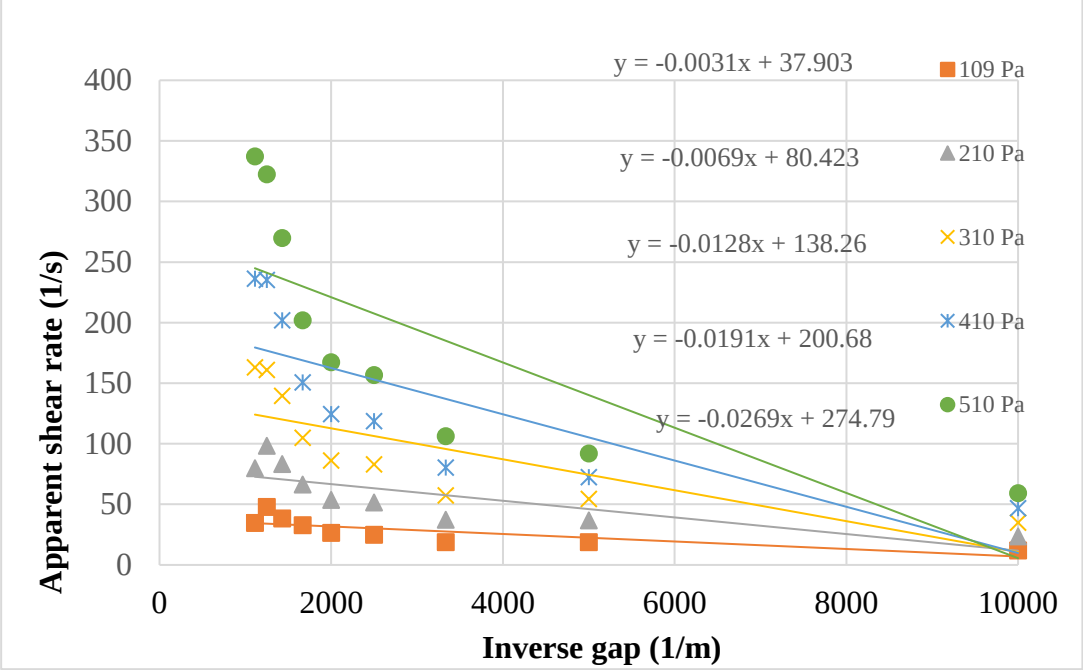

Fig.13 - 22*:* Apparent shear rate against inverse gap flow curves Coating B, shear stress range 109 – 510 Pa.

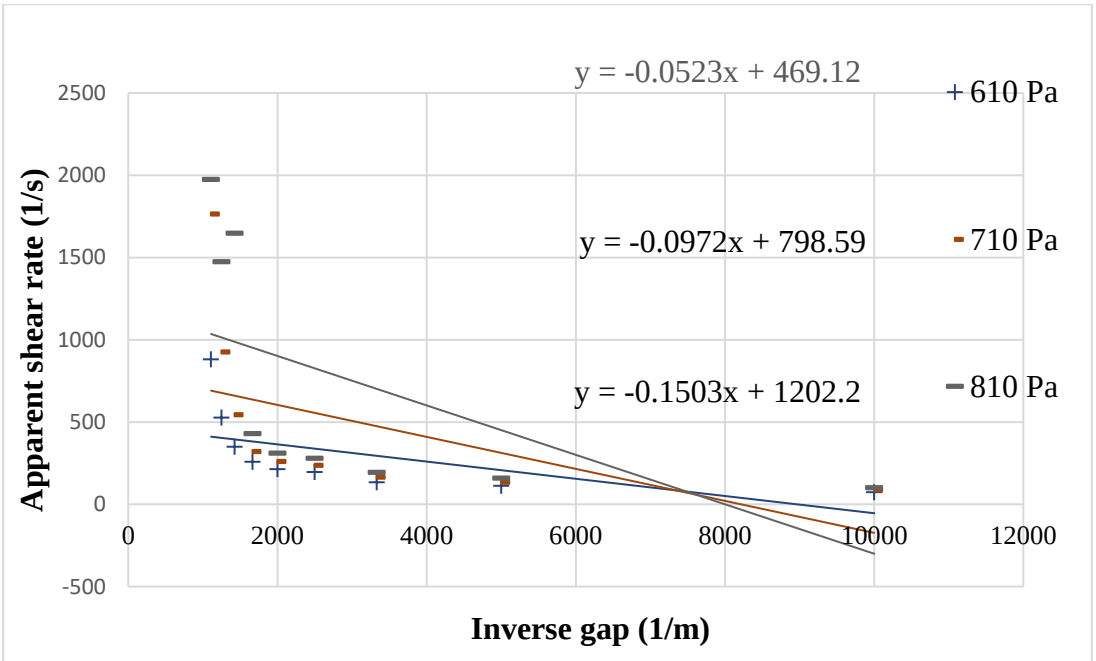

Fig.13 - 23*:* Apparent shear rate against inverse gap flow curves Coating B, shear stress range 610 – 810 Pa.

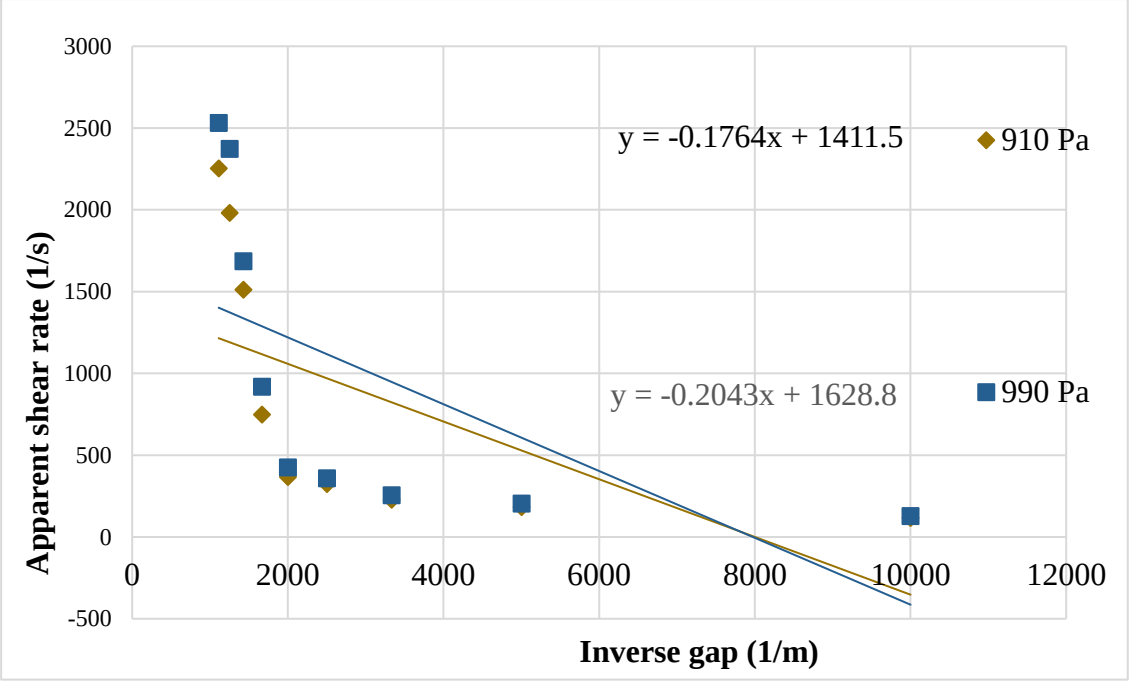

Fig.13 - 24: Apparent shear rate against inverse gap flow curves Coating B, shear stress range 910 – 990 Pa.

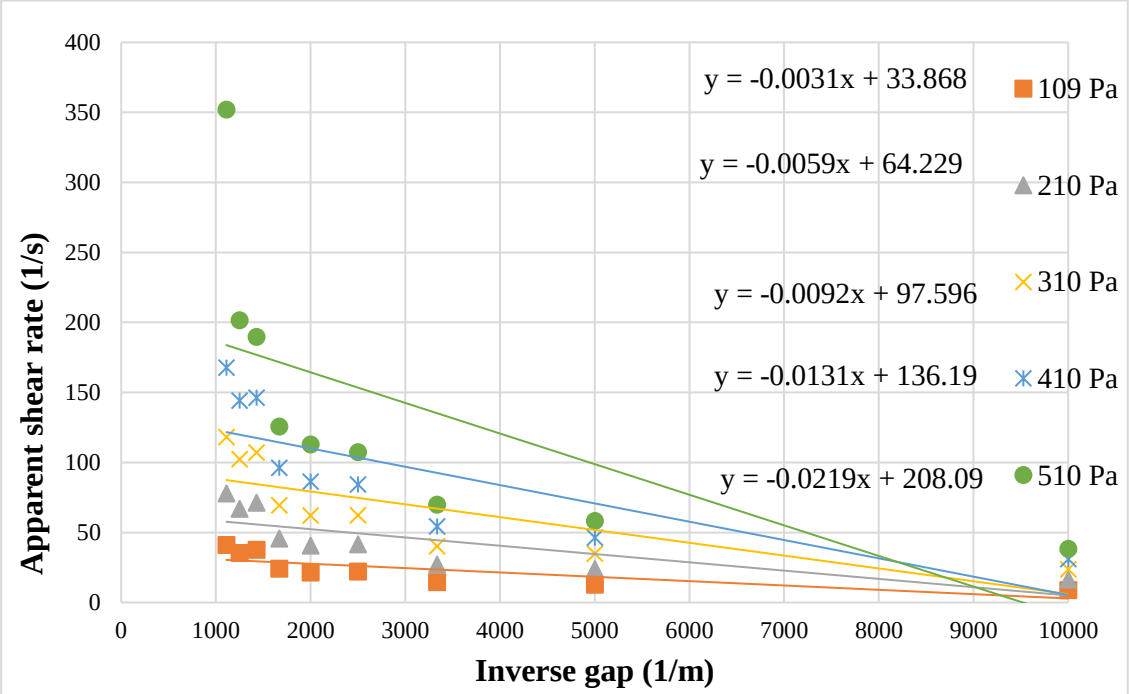

Fig.13 - 25: Apparent shear rate against inverse gap flow curves Coating S, shear stress range 109 – 510 Pa.

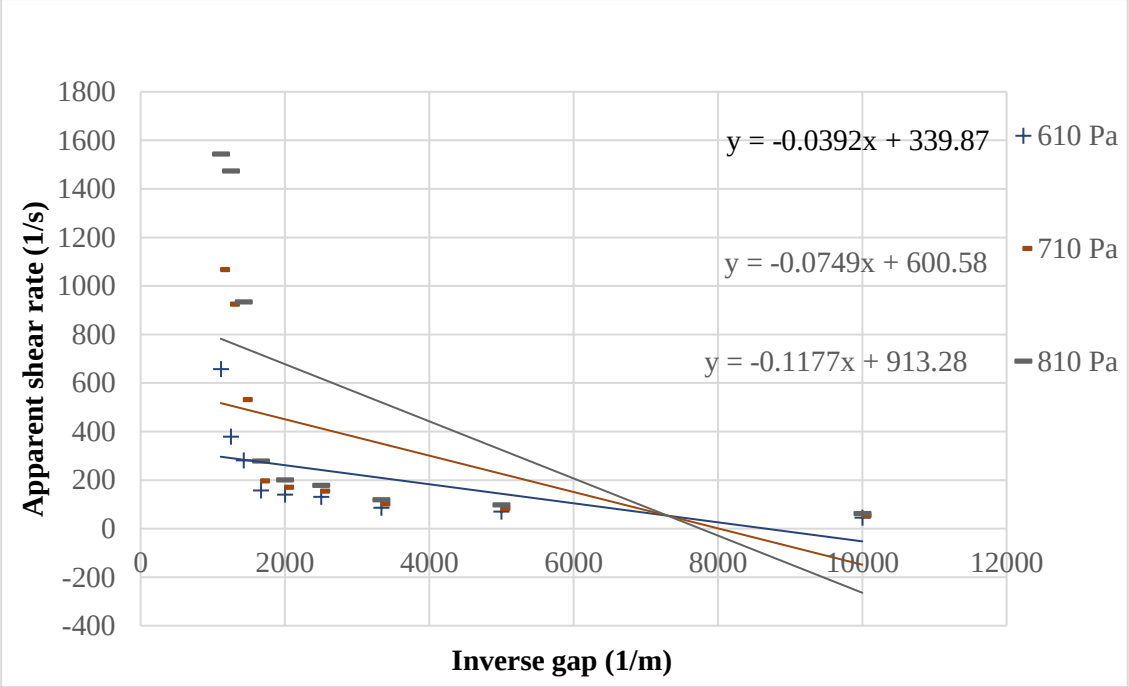

Fig.13 - 26: Apparent shear rate against inverse gap flow curves Coating S, shear stress range 610 – 810 Pa.

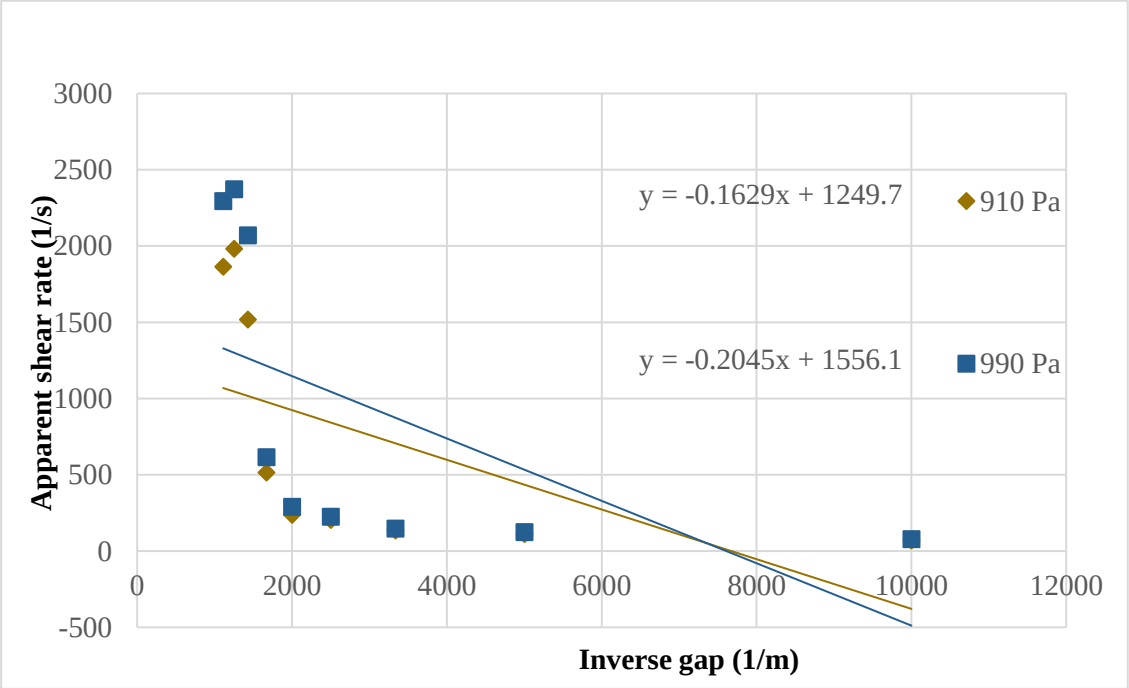

Fig.13 - 27: Apparent shear rate against inverse gap flow curves Coating S, shear stress range 910 – 990 Pa.

APPENDIX G: PLASTICERAM SUN MERLIN - SHEAR RHEOLOGY

Power law properties OF Plasticeram grey samples were determined through steady-state curves and dynamic oscillatory rheometry using the same methodology as Plasticeram black coatings.

Apparent wall slip/ stick investigation: Apparent shear rate against shear stress

COATING X

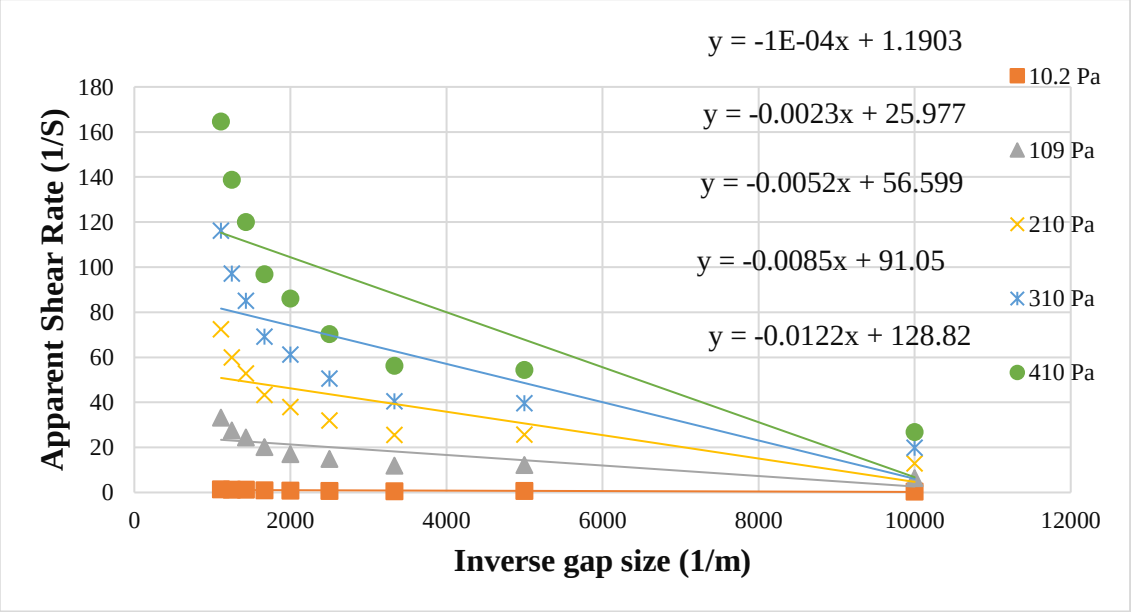

Fig. 1: Apparent shear rate against inverse gap flow curves Coating X, shear stress range 109 – 410 Pa.

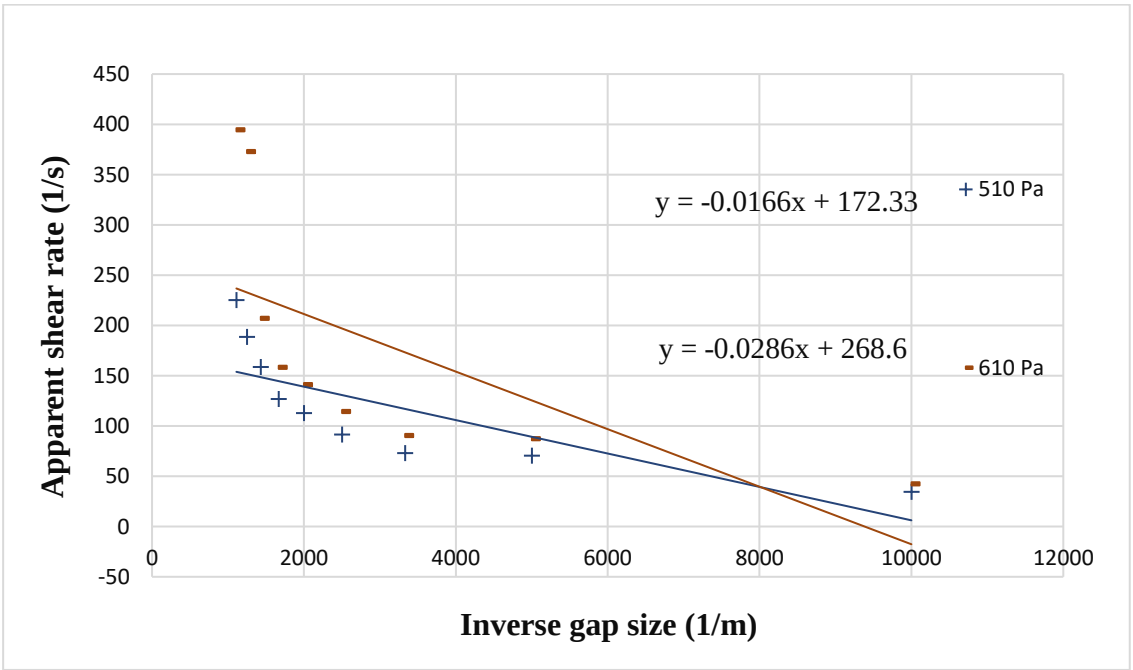

Fig.13 - 28: Apparent shear rate against inverse gap flow curves Coating X, shear stress range 510 – 610 Pa.

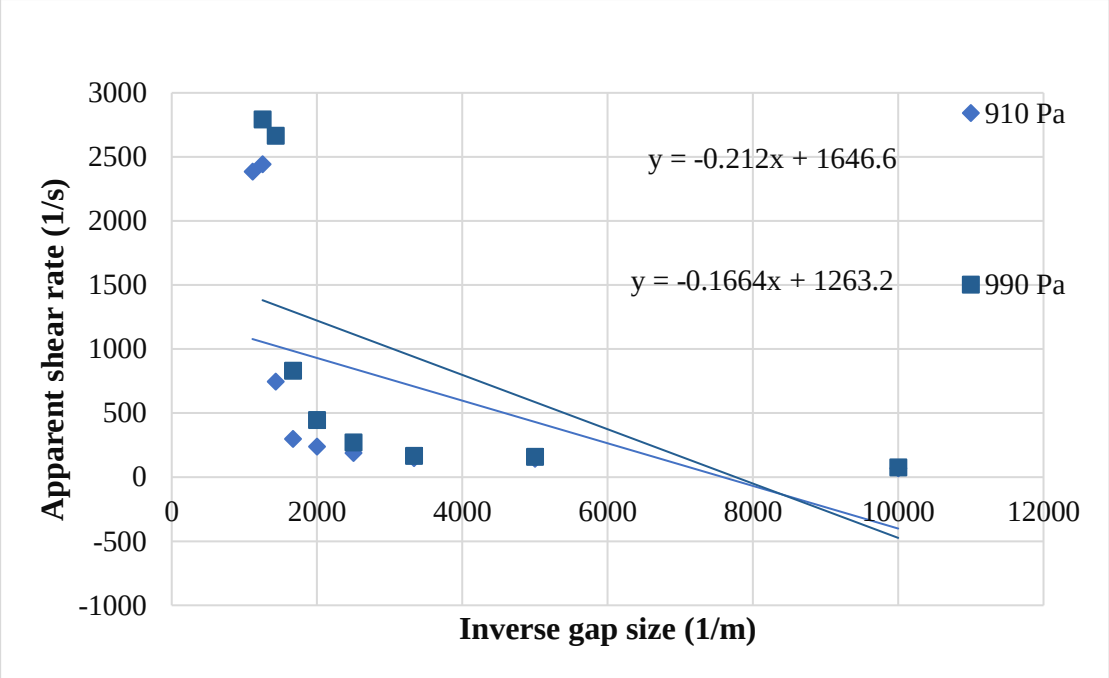

Fig.13 - 29: Apparent shear rate against inverse gap flow curves Coating X, shear stress range 910 - 990 Pa.

COATING X

The same behaviour was seen for coating Y. It was therefore concluded that the Mooney analysis was a poor fit for commercial coatings.

APPARENT WALL SLIP/ STICK INVESTIGATION: ANOMALOUS LAYER THICKNESS

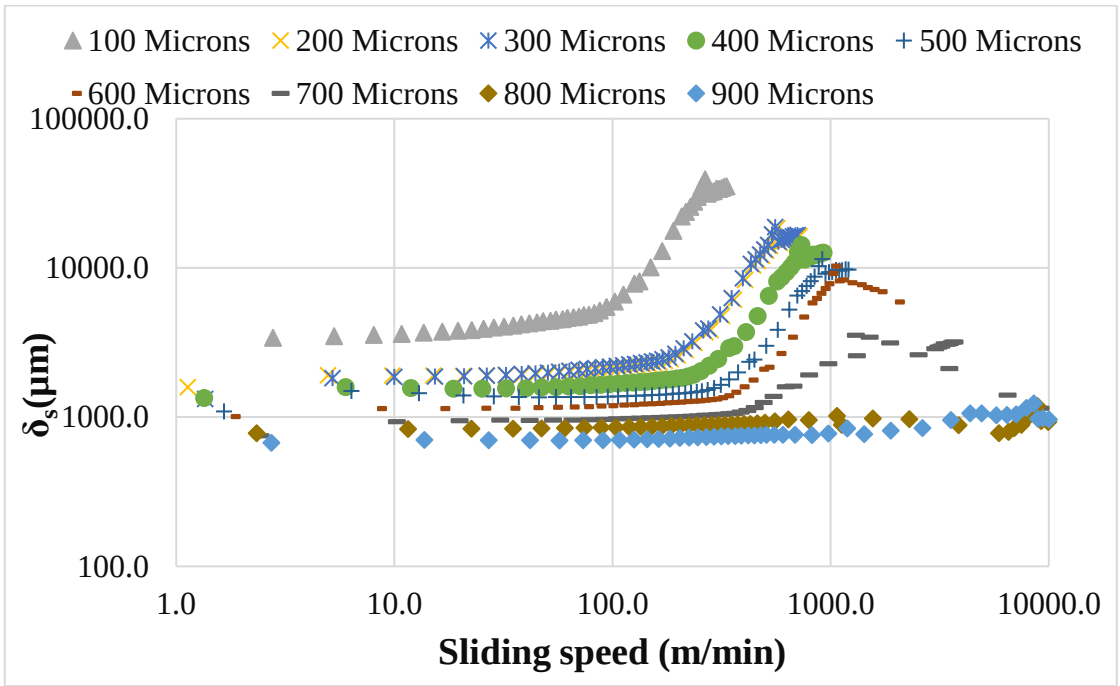

Fig.13 - 30: Anomalous layer thickness with sliding speed for Coating X

ANOMALOUS LAYER THICKNESS FOR COATING Y

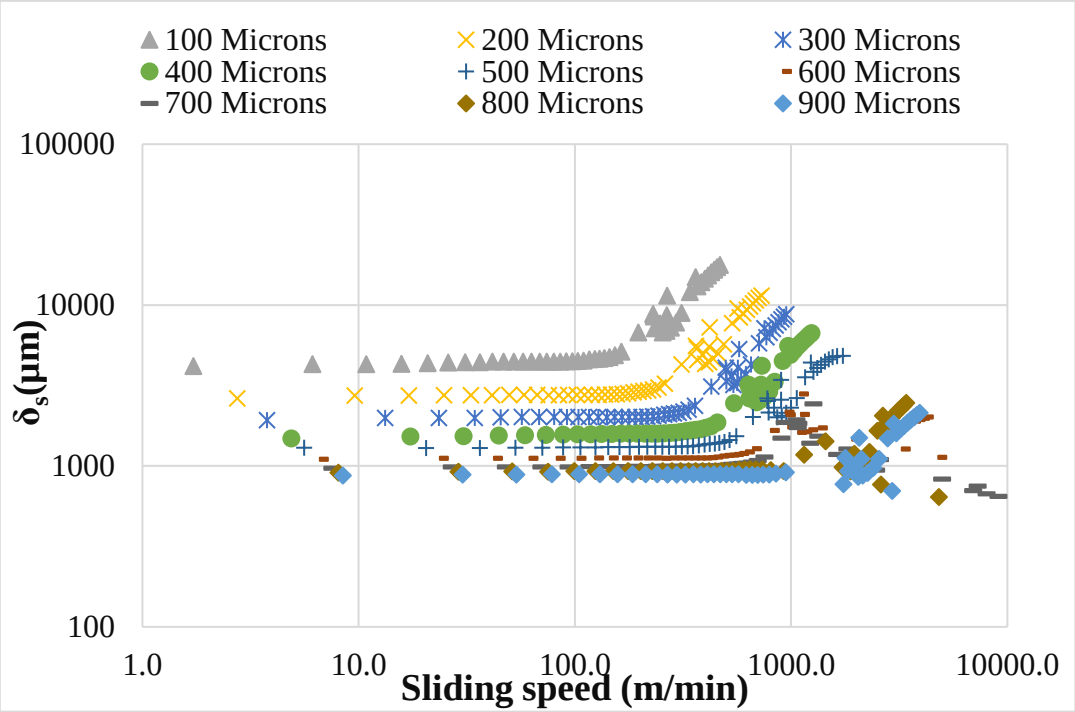

Fig.13 - 31: Anomalous layer thickness with sliding speed for Coating y

The anomalous layer thickness was larger than the gap size. This shows a breakdown of the Mooney analysis. The physical response makes scientific sense.

APPENDIX H: PLASTICERAM SUN MERLIN – EXTENSIONAL RHEOLOGY

(1) Progressive thinning of filament radius with time

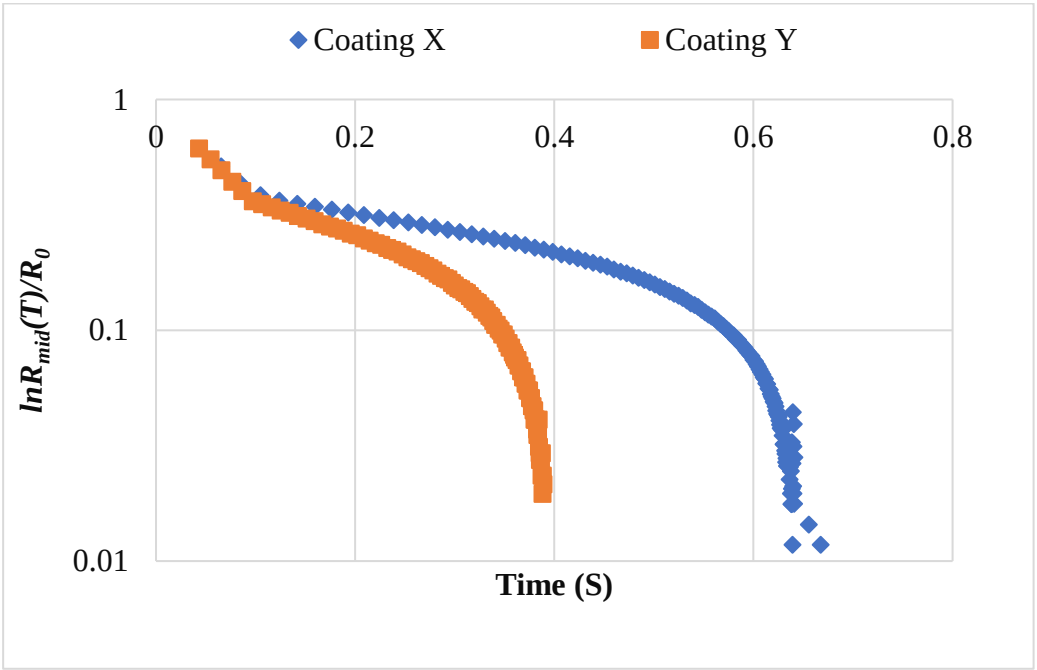

Fig.13 - 32: Progressive thinning of filament radius as a function of time

A delayed filament break was observed for Coating X than Coating Y. Therefore, coating X has a higher extensional viscosity than coating Y.

APPENDIX I: SURFACE TENSION AND DESNISTY OF MODEL PVC COATINGS

(1) Density and surface tension of Model PVC coatings

Table 13 - 4 and Table 13 - 5 summaries surface tension and density measurement of 0.7 and 1.7 wt.% pigment concentration. As expected, density measurement increased with pigment concentration due to higher solid content.

Table 13 - 4: Surface tension and density of pigmented model fluids

Pigment concentration [wt.%]	**Surface tension [mN/m]**	**Density [kg/m^3]**
0.7	18.5	1184
1.7	13.3	1230

Table 13 - 5*:* surface tension and density solvated model PVC coatings

Solvent (wt. %)	**Density [kg/m^3]**	**Surface tension [mN/m]**
0	1030	22.9
4	1219.6	28.4
8	1085.3	28.9
12	1094	24.4

APPENDIX J: EXTENSIONAL RHEOLOGY OF MODEL PVC COATINGS

BOND NUMBER AGAINST DIMENSIONLESS NUMBER

The bond number against filament radius for pigment concentration in fig. 13 -33 and fig.13 – 34. The bond number increased with increased filament radius; however, a steeper gradient was for highly pigmented fluids than highly solvated PVC coatings.

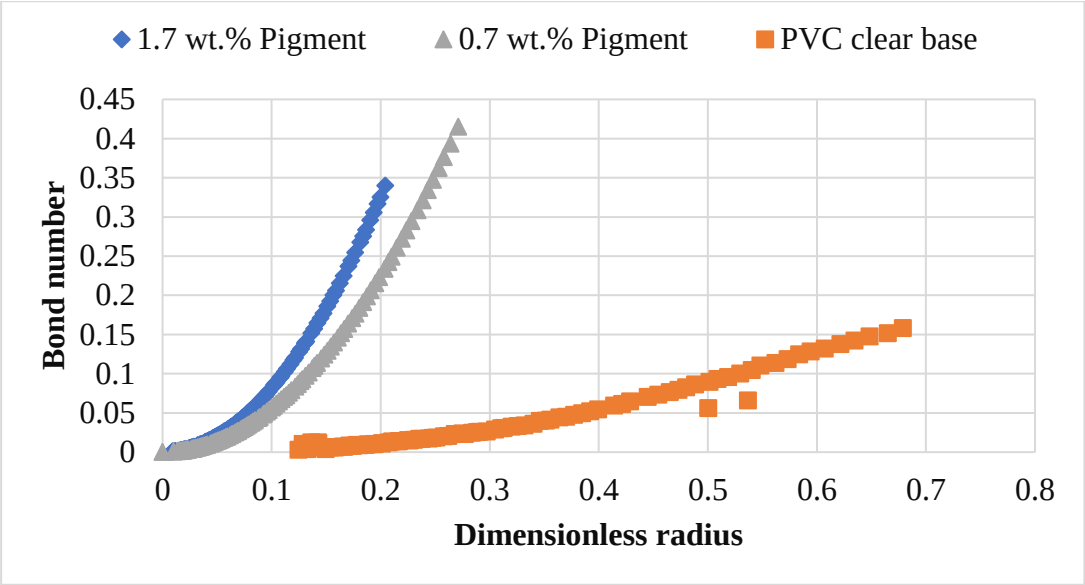

Fig.13 - 33: Bond number against filament radius for Solvated PVC coatings

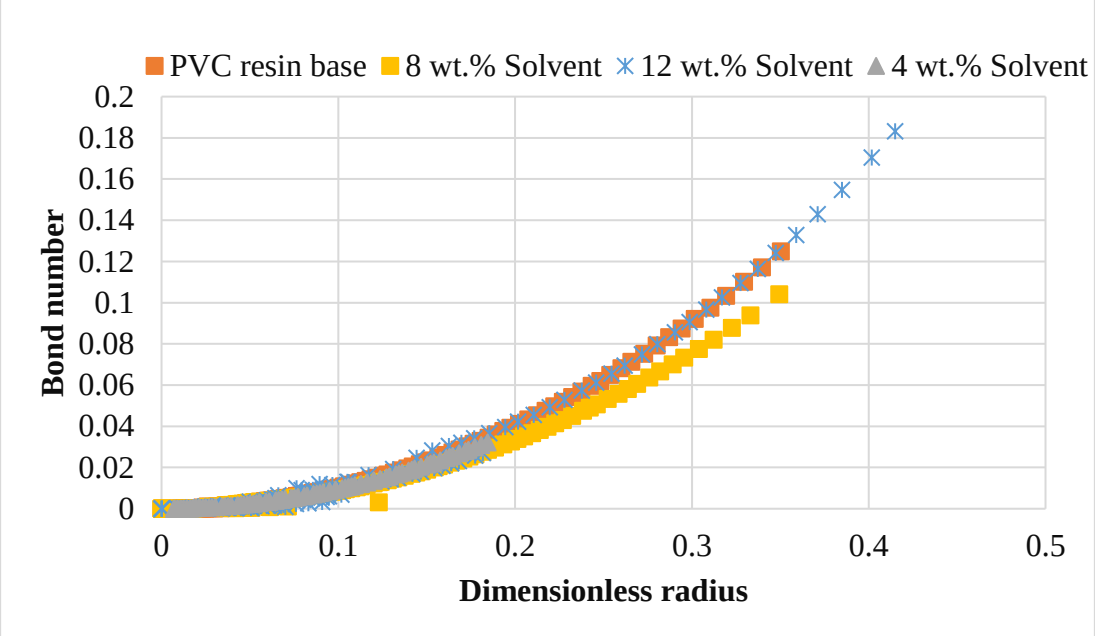

Fig.13 - 34: Bond number against filament radius for pigmented PVC coatings

APPENDIX K: PARAMETRIC STUDIES USING A ROLL COATING RIG

RIG CALIBRATION

Fig.13 – 35 to 13 - 38 show calibration studies conducted on the pick- up roll coater rig. The presence of background noise during pick-up roll rotation and when in the motionless state was observed in this study. This was also considered during data analysis.

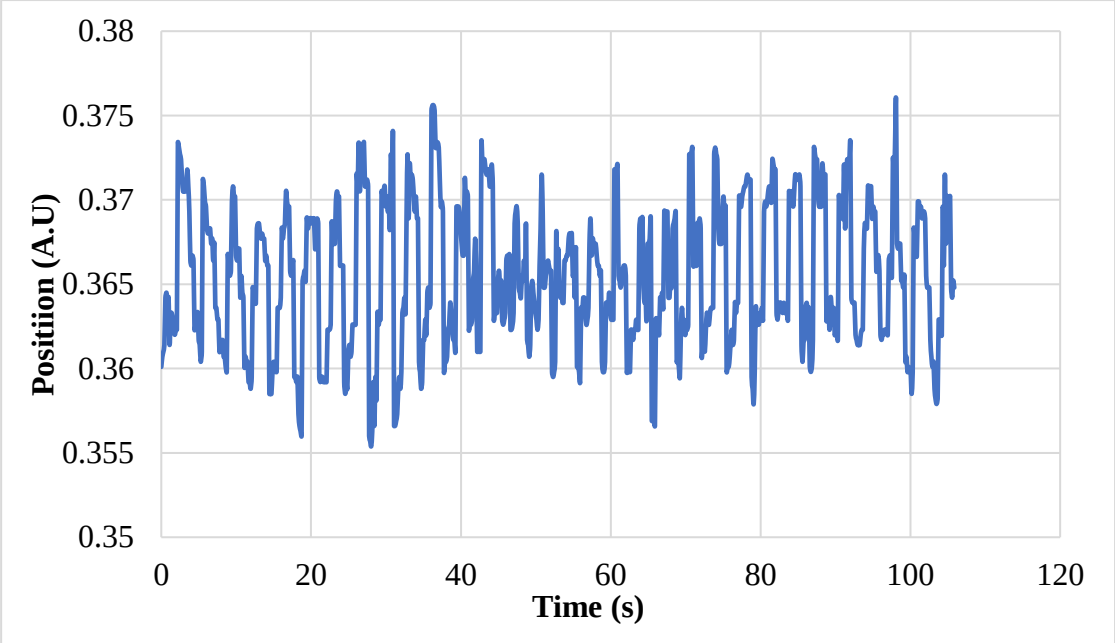

Fig.13 - 35: This is a test of running for over 100s to test the laser measurement system when the roll is rotating at 113.0 m/min

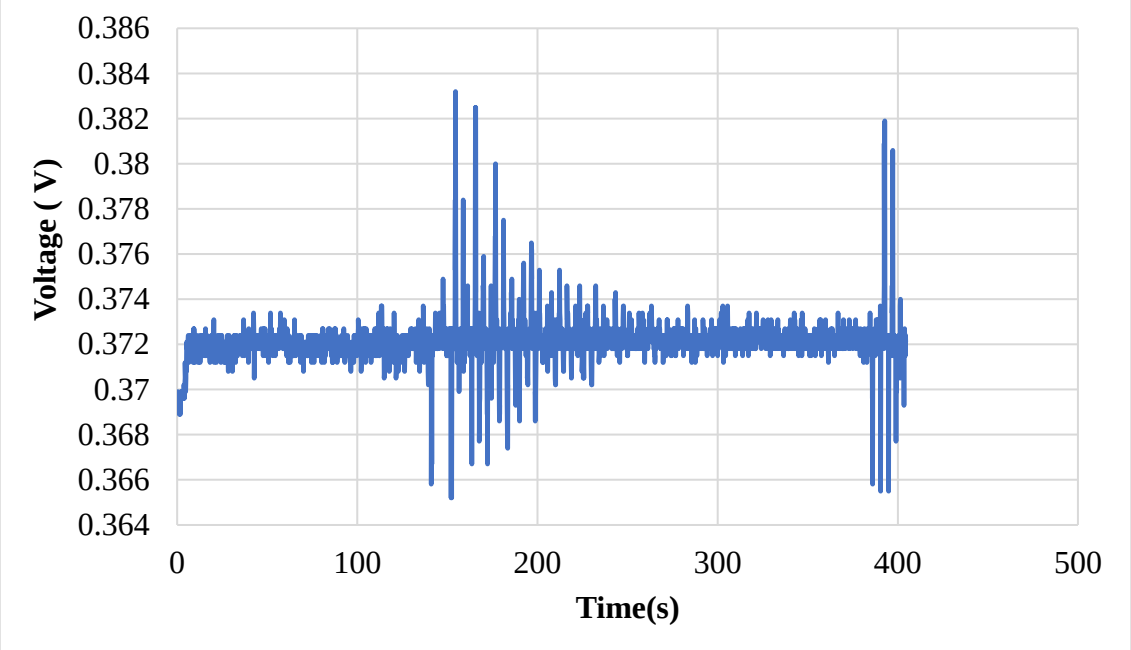

Fig.13 - 36: A test without any movement of the roll, just background noise

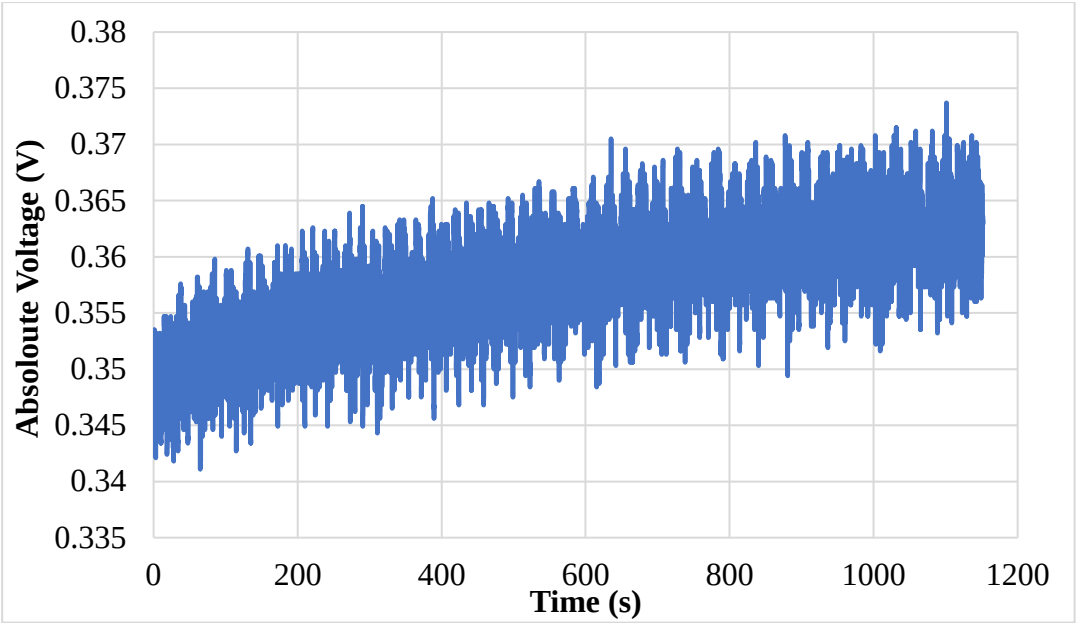

Fig.13 - 37: A test without any movement of the roll, just background noise

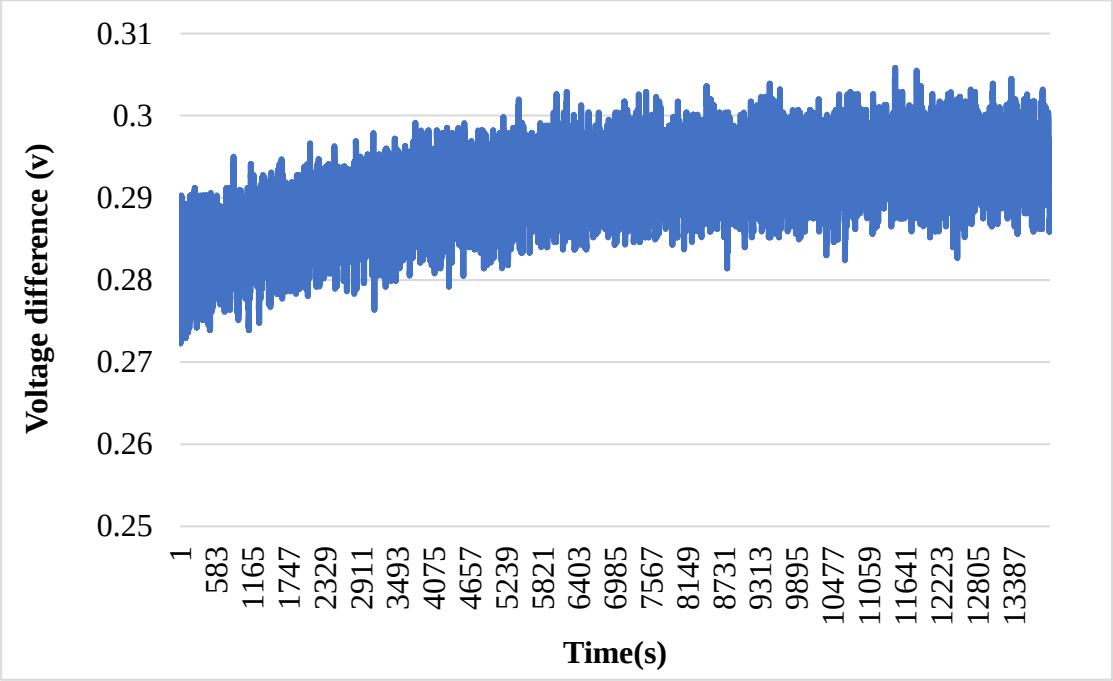

Fig.13 - 38: This is a test of running for over 100s to test the laser measurement system when the roll is rotating at 113.0 m/min

Fig.13 – 39 shows the determination of the standard deviation of the voltage against layer thickness. For every 1µm thickness, the standard deviation is 6.3 mV.

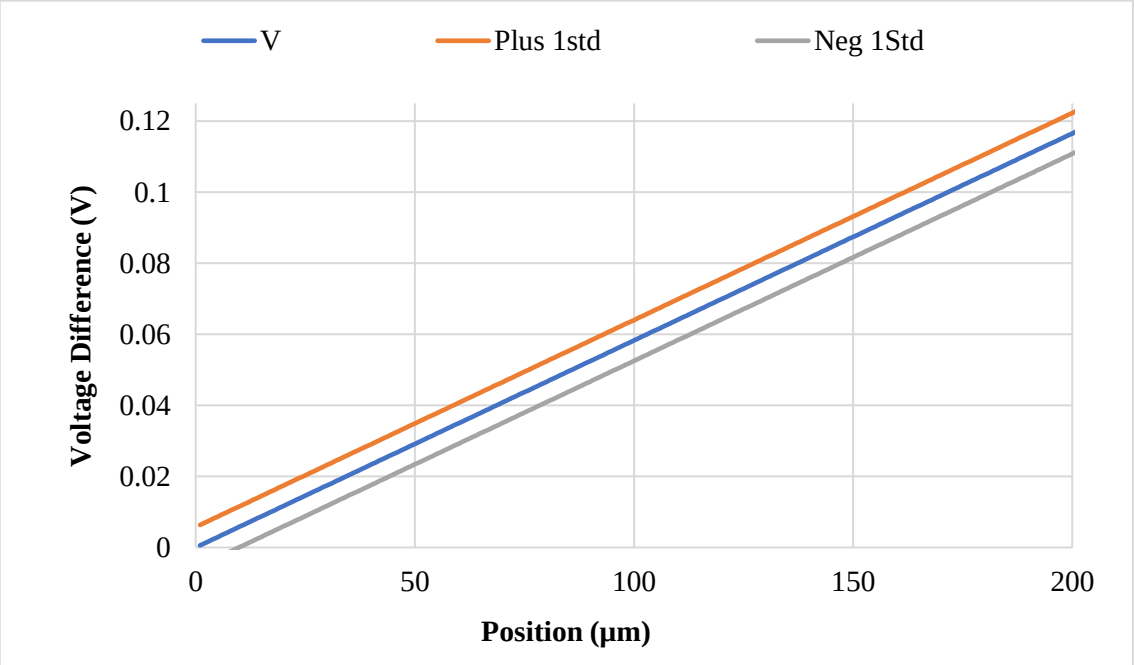

Fig.13 - 39: Relationship between Voltage differences and position

Fig. 13 – 40 shows the relationship between voltage and substrate thickness. There is a direct proportionality between voltage output and substrate thickness. The equation derived this relation was employed in the determination of coating thickness and roll speeds.

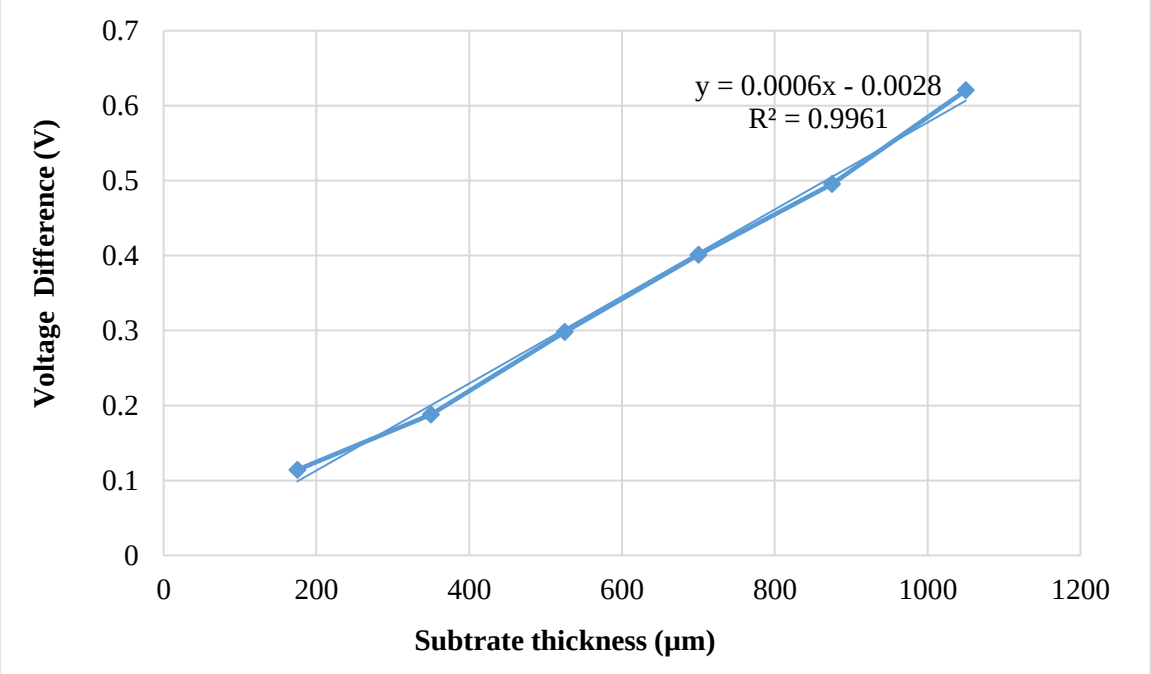

Fig.13 - 40: Relationship between Voltage differences and substrate thickness

APPENDIX L: PARAMETRIC STUDIES USING COMPUTATIONAL FLUID DYNAMICS (CFD) MODEL OF A RIG AS A MODEL

The initial aim of the laboratory scale investigations was to parametrically investigate the impact of coating liquid properties and operational parameters on the coating pick up mechanism. While this was partially successful, the presence of ribbing introduced some additional difficulties into the investigation. The inability to accurately mimic on the laboratory scale (geometry reduced by a factor of 8.5) the full-scale coating roll and coating trough were attributed to scale. By reducing the geometrical size of the rig, while maintaining the physical properties of the coating, maintaining even simple Reynolds number similarity becomes difficult without increasing the speed by the same ratio. This was impractical due to rotational speed limits and spray and thus factors as extension rates and surface effects would also differ. To fully understand the interactions, it is likely that a full-scale roll in coating trough is used. This adds significantly to the capital and operational cost as well as the volumes of liquid coating required.

An attempt was made to model the phenomena (to account for changes in scale) using the commercial finite element code within the Ansys environment, Fig.13 - 41, which examined a rotating roll in a fixed geometry coating trough.

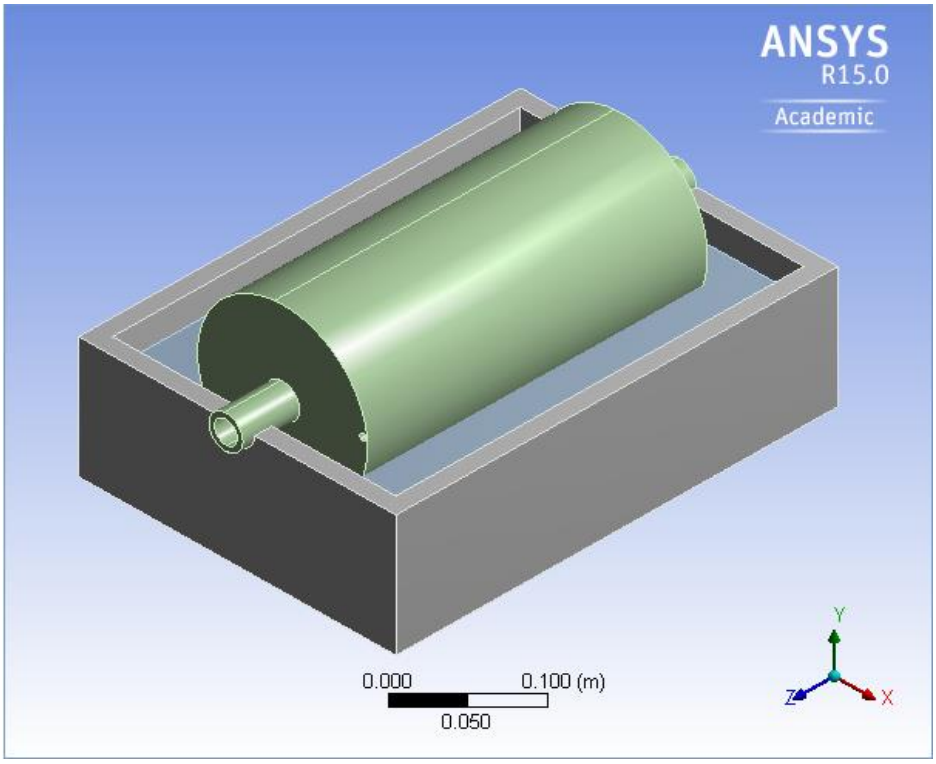

Fig.13 - 41: Model of the coating trough designed in Solid works and simulations run in Ansys fluent

The model aimed to numerically investigate the relationship between the material properties, process parameters and the wider fluid flow in the coating trough, including the pick-up ability of the rotating roll. The model was designed in three parts, namely; coating trough made from steel, pick-up roll made from steel and the liquid – material properties varied depending on the rheological properties previously obtained from shear rheology.

After many modifications to the model and an exploration of the operational ability, this work was terminated as it became evident that an alternative software solution was required where custom solution domain and physical models would need to be adjusted/ developed. This would need to deal with the free surface flows, near-wall sticking phenomena and introduce some of the unique material properties.

Although this was not deemed an appropriate use of time within the current project, there is merit in developing a numerical solution of the coater as a standalone project using the data generated in this thesis. Fig. 13 – 42 and Fig. 13 – 43 show the generated contour plots of shear stress (left) and the resultant Shear rate (right) distribution in the coating trough of Coating B and 3.52 wt. % pigmented PVC coating.

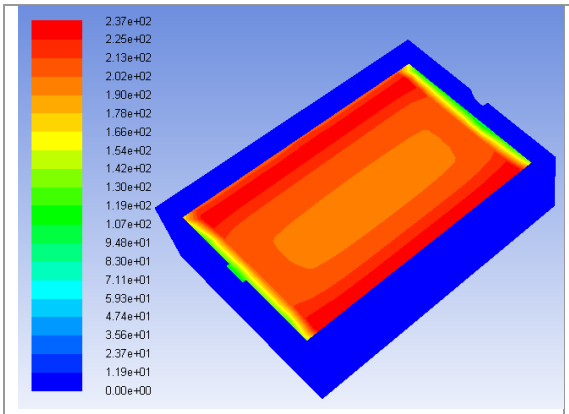

(a) Shear stress distribution at 3.75 rad/s

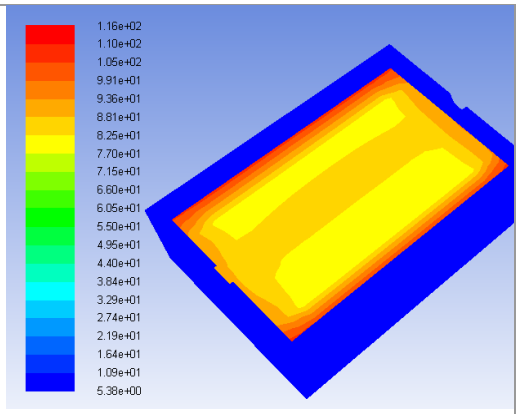

(b) Shear rate distribution at 3.75 rad/s

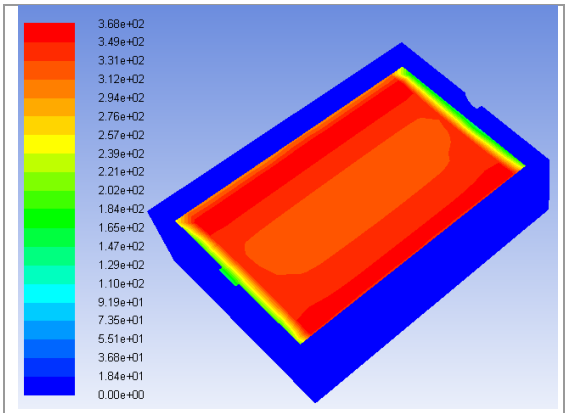

(c). Shear stress distribution at 7.5 rad/s

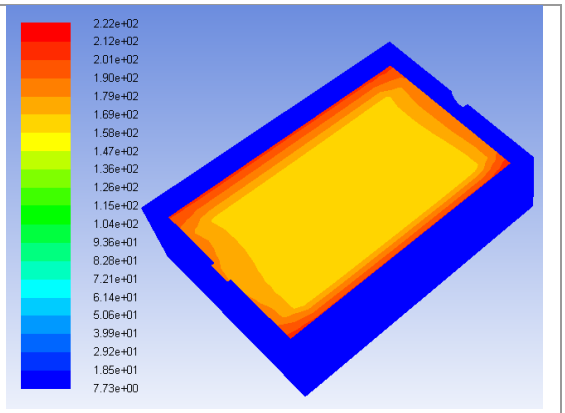

(d). Shear rate distribution at 7.5rad/s

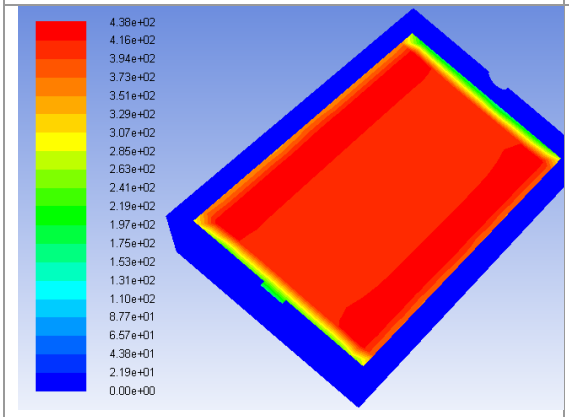

(e). Shear stress distribution at 10 rad/s

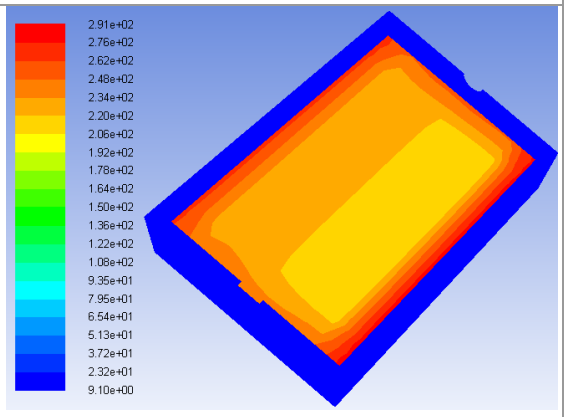

(f). Shear rate distribution at 10 rad/s

Fig.13 - 42: CFD modelling of Coating B flow in the coating trough at different rotational speeds

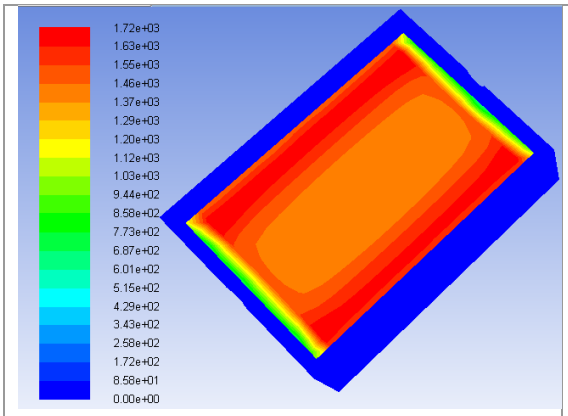

(a) Shear stress distribution at 3.75 rad/s

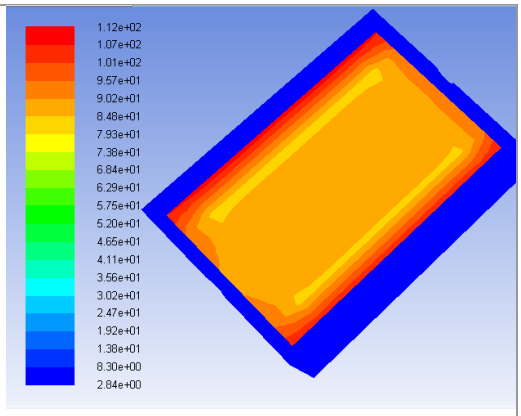

(b)Shear rate distribution at 3.75 rad/s

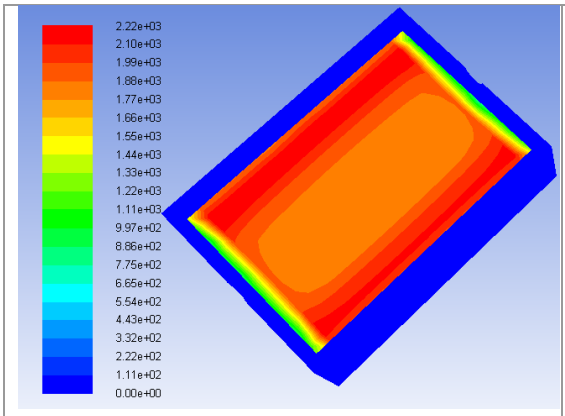

©. Shear stress distribution at 7.5 rad/s

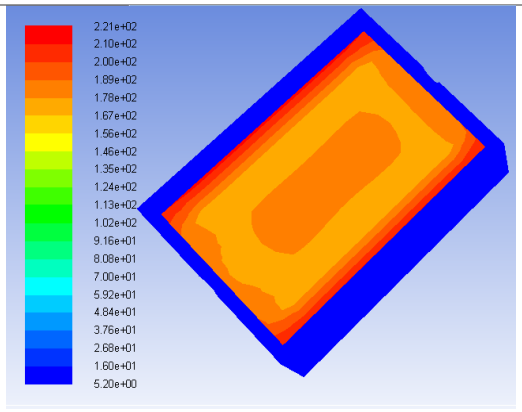

(c) Shear rate distribution at 7.5rad/s

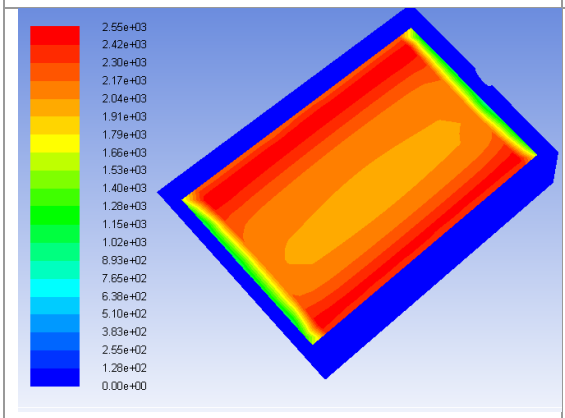

(e) Shear stress distribution at 10 rad/s

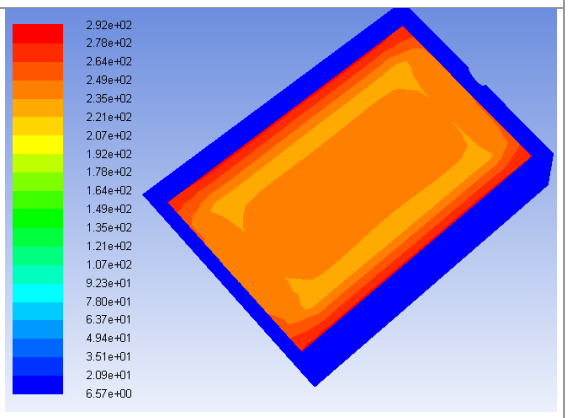

(d). Shear rate distribution at 10 rad/s

Fig.13 - 43: CFD modelling of 3.5 wt. % of Pigmented PVC coating flow in the coating trough at different rotational speeds

Pick up rotational speeds of 3.75, 7.5 and 10 rad/s were investigated. It was seen that pigment concentrations affected the distribution of shear stress and shear rate. And for materials that are prone to AWS, intermittent stagnant and lubricating layers are likely to occur near the pick-up roll thus PMD.